

Electronic Thesis and Dissertation Repository

---

9-19-2017 1:00 PM

## 3D Printing of Functional Materials: Surface Technology and Structural Optimization

Dongxing Zhang, *The University of Western Ontario*

Supervisor: Jun, Yang, *The University of Western Ontario*

A thesis submitted in partial fulfillment of the requirements for the Doctor of Philosophy degree in Mechanical and Materials Engineering

© Dongxing Zhang 2017

Follow this and additional works at: <https://ir.lib.uwo.ca/etd>



Part of the [Manufacturing Commons](#), [Other Materials Science and Engineering Commons](#), and the [Structural Materials Commons](#)

---

### Recommended Citation

Zhang, Dongxing, "3D Printing of Functional Materials: Surface Technology and Structural Optimization" (2017). *Electronic Thesis and Dissertation Repository*. 4976.

<https://ir.lib.uwo.ca/etd/4976>

This Dissertation/Thesis is brought to you for free and open access by Scholarship@Western. It has been accepted for inclusion in Electronic Thesis and Dissertation Repository by an authorized administrator of Scholarship@Western. For more information, please contact [wlsadmin@uwo.ca](mailto:wlsadmin@uwo.ca).

## ABSTRACT

There has been a surge in interest of 3D printing technology in the recent 5 years with respect to the equipment and materials, because this technology allows one to create sophisticated and customized parts in a manner that is more efficient regarding both material and time consumption. However, 3D printing has not yet become a mainstream technology within the established manufacturing routes. One primary factor accounting for this slow progress is the lack of a broad variety of 3D printable materials, resulting in limited functions of 3D printed parts.

To bridge this gap, I present an integrated strategy to fabricate a variety of functional materials/devices through the post-printing surface modification and target-motivated structural topology. A reusable 3D printed filter was first demonstrated to remove metal ions from water. This filter was functionalized with a layer of bio-adsorbent grown on its surface using post-printing modification, and the capacity was improved through structural optimization. To further improve the working efficiency, a customized 3D all-in-one printable material system was employed, which uses only one 3D printing material, but can realize various functionalities through a post-printing process. This material system is applicable for all types of photo-polymerization based 3D printing routes, including DLP, SLA, polyjet and other emerging technologies. It has significantly extended the capacity of current 3D printing technology. The 3D printed structures were converted into useful devices with new functions or new structural metamaterials with novel properties, that are attributed to both their materials composition and structural design. For example, we have showcased the magnetically manipulated robot, strength-enhanced lattice materials with high effective strength, ultralight metal materials and mechanical-metamaterials.

In this thesis, a new generation of initiator-integrated material system was also developed. Beyond being able to successfully 3D print functional devices/materials with desirable

properties, I also demonstrated that this initiator-laden material can be utilized to locally repair the surface damage, allowing a self-healing ability.

In general, the developed 3D printing process that incorporates surface modification and structural topology enables a new class of functional devices/materials to be produced, and opens a door for further research and development of an increasing variety of 3D printing applications. Through the work presented in this dissertation, I substantially build upon and further establish the strategy and material system for 3D printing functional devices/materials, keeping in mind components, design, engineering and application.

Keywords: 3D printing, functional materials, post-printing modification, target-motivated structural optimization, metal ion removal, initiator-integrated material, magnetically driven robot, strength-enhancement, ultralight metallic material, mechanical meta-material, polydopamine initiated modification.

## CO-AUTHORSHIP

This doctoral thesis has been carefully prepared according to the regulations for an integrated-article format thesis stipulated by the Faculty of Graduate and Postdoctoral Studies at Western University, and has been co-authored as follows:

### **CHAPTER 2: 3D printing of reusable chitosan-coated filter for metal ions removal and structural optimization**

All the preparation for experimental testing and set-up was undertaken by D.X. Zhang under the supervision of Dr. J. Yang. Theoretical analyses were conducted by D.X. Zhang under the supervision of Dr. J. Yang. Experimental testing was performed by D.X. Zhang under the supervision of Dr. J. Yang. Chapter 2 was drafted by D.X. Zhang and reviewed by supervision of Dr. J. Yang. A paper co-authored by D.X. Zhang, J.F. Xiao, Q.Q. Guo and J. Yang is to be submitted.

### **CHAPTER 4: Magnetic objects by i3DP and the structural optimization**

All the preparation for experimental testing and set-up was undertaken by D.X. Zhang under the supervision of Dr. J. Yang. Theoretical analyses were conducted by D.X. Zhang under the supervision of Dr. J. Yang. Experimental testing was performed by D.X. Zhang under the supervision of Dr. J. Yang. Chapter 4 was drafted by D.X. Zhang and reviewed by supervision of Dr. J. Yang. A paper co-authored by D.X. Zhang, J.F. Xiao, Y.J. Q, Q.Q. Guo and J. Yang has been published on IEEE Transaction on Magnetics.

### **CHPATER 5: Strength-enhanced cellular materials by i3DP and the optimal design**

All the preparation for experimental testing and set-up was undertaken by D.X. Zhang under the supervision of Dr. J. Yang. Theoretical analyses were conducted by D.X. Zhang under the supervision of Dr. J. Yang. Experimental testing was performed by D.X. Zhang

under the supervision of Dr. J. Yang. Chapter 5 was drafted by D.X. Zhang and reviewed by supervision of Dr. J. Yang. A paper co-authored by D.X. Zhang, J.F. Xiao, Q.Q. Guo and J. Yang is to be submitted.

#### **CHAPTER 6: Ultralight, super-elastic, hierarchical metallic meta-materials by i3DP**

All the preparation for experimental testing and set-up was undertaken by D.X. Zhang under the supervision of Dr. J. Yang. Theoretical analyses were conducted by D.X. Zhang under the supervision of Dr. J. Yang. Experimental testing was performed by D.X. Zhang under the supervision of Dr. J. Yang. Chapter 6 was drafted by D.X. Zhang and reviewed by supervision of Dr. J. Yang. A paper co-authored by D.X. Zhang, J.F. Xiao, C. Moorlag, Q.Q. Guo and J. Yang has been published by Nanotechnology.

#### **CHAPTER 7: Mechanical meta-materials by i3DP and the integrated properties**

All the preparation for experimental testing and set-up was undertaken by D.X. Zhang under the supervision of Dr. J. Yang. Theoretical analyses were conducted by D.X. Zhang under the supervision of Dr. J. Yang. Experimental testing was performed by D.X. Zhang under the supervision of Dr. J. Yang. Chapter 7 was drafted by D.X. Zhang and reviewed by supervision of Dr. J. Yang. A paper co-authored by D.X. Zhang, J.F. Xiao, Q.Q. Guo and J. Yang is to be submitted.

#### **CHAPTER 8: New generation of initiator-integrated 3D printable material (i3DP II)**

All the preparation for experimental testing and set-up was undertaken by D.X. Zhang under the supervision of Dr. J. Yang. Theoretical analyses were conducted by D.X. Zhang under the supervision of Dr. J. Yang. Experimental testing was performed by D.X. Zhang under the supervision of Dr. J. Yang. Chapter 7 was drafted by D.X. Zhang and reviewed by supervision of Dr. J. Yang. A paper co-authored by D.X. Zhang, J.F. Xiao, Q.Q. Guo and J. Yang is to be submitted.

## ACKNOWLEDGEMENTS

It is a pleasure to acknowledge the meaningful contribution from everyone who supported to make this work possible.

First and foremost, I would like to sincerely thank my supervisor-Prof. Jun Yang for his enlightening guidance, meticulous suggestions, astute criticism and words of encouragement throughout my PhD period. I really appreciate that I have the opportunity and privilege to be working under a supervision of such brilliant and innovative mind. I also would like to thank my supervisor committees, Prof. Andy Sun and Prof. G.K. Knopf, for their co-supervision and guidance.

Many thanks also go to my colleagues in Yang's MNBS team, for their stimulating discussions with me, help with experimental setup and general advice. I also want to give special thanks to Dr. Guo for his insight suggestions in both research and life.

I am also thankful to my friends at Western University, the ones that are here and the ones that have left, not only for their support and comments that made my research work better but also for an enjoyable and pleasant time at the University. I am extremely grateful for your friendship. It is you guys that make my life full of varieties and interests. Special thanks here go to Dr. Sun and Zhao, I really appreciate your support in the past four years.

I would not have been able to do this if it were not for the support of my parents, my siblings and my siblings in law. They have encouraged me, stood by my decisions and for that I am eternally gratefully. It simply would not have been possible without you.

## Table of Contents

ABSTRACT .....	I
CO-AUTHORSHIP .....	III
ACKNOWLEDGEMENTS.....	V
Table of Contents .....	VI
List of Tables .....	X
List of Figures.....	XI
Glossary of Terms .....	XXIV
Chapter1 .....	1
1 Introduction to 3D printing and materials .....	1
1.1 What is 3D printing? .....	1
1.1.1 A brief history of 3D printing.....	1
1.1.2 3D printing techniques and categories .....	5
1.1.3 State-of-the-art 3D printing: new materials, methods and concepts.....	13
1.1.4 Advantages and drawbacks of 3D printing .....	18
1.2 Review of functional materials/devices by 3D printing .....	22
1.2.1 Material modification enables the functions.....	24
1.2.2 Surface modification enables the functions .....	31
1.2.3 Structural modification enables the functions.....	34
1.3 Challenges, opportunities and objectives.....	47
1.4 Outline of the thesis .....	50
Chapter 2.....	53
2 3D printing of reusable chitosan-coated filter for metal ions removal and structural optimization .....	53
2.1 Introduction.....	53
2.2 Experimental setup.....	57
2.2.1 Materials .....	57
2.2.2 Fabrication of the chitosan filter .....	57
2.2.3 Adsorption and desorption .....	59
2.2.4 Characterization .....	60
2.3 Results and discussion .....	61
2.3.1 Working principle.....	61
2.3.2 XPS analysis .....	63
2.3.3 Adsorption and desorption .....	65
2.3.4 Mechanism analysis .....	75
2.4 Conclusion .....	76
Appendix 1 .....	77
Chapter 3.....	79

3	Development of an initiator-integrated 3D printable material system (i3DP).....	79
3.1	Introduction.....	79
3.2	Working principles .....	81
3.3	Preparation of initiator-integrated resin .....	81
3.4	Characterization .....	83
3.5	Printability.....	84
3.6	Mechanical properties .....	87
3.7	Functionalization.....	89
3.7.1	Experiment setup .....	89
3.7.2	Characterization .....	90
3.7.3	Results and conclusion.....	91
3.8	Extending functions based on the polymer grafting .....	93
3.8.1	Metallization of 3D printed objects .....	93
3.8.2	Conductive hydrogel enabled by SI-ATRP .....	96
3.9	Conclusion .....	98
Chapter 4	.....	100
4	Magnetic objects by i3DP and the structural optimization.....	100
4.1	Introduction.....	100
4.2	Experimental setup.....	103
4.2.1	Materials .....	103
4.2.2	3D printing and ATRP .....	104
4.2.3	Magnetic control .....	105
4.2.4	Characterization .....	106
4.3	Results and discussion .....	106
4.3.1	XPS of ATRP Process .....	106
4.3.2	Magnetism properties.....	107
4.3.3	Fluidic Kinematics .....	109
4.3.4	Magnetic control .....	112
4.3.5	Optimization of spiral structure .....	115
4.3.6	Effect of viscosity on the swimming properties.....	120
4.3.7	Effect of rotating magnetic field. ....	121
4.4	Conclusion .....	124
Chapter 5	.....	125
5	Strength-enhanced cellular materials by i3DP and the optimal design .....	125
5.1	Introduction.....	125
5.2	Optimal design and the effective properties .....	127
5.2.1	Effective relative density .....	127
5.2.2	Effective moduli.....	128
5.2.3	Comparison of effective properties among various lattice .....	130
5.3	Metallization via post-printing modification .....	131
5.3.1	Experimental setup.....	131

5.3.2 Results and discussion .....	134
5.3 Conclusion .....	144
Chapter 6.....	145
6 Ultralight, super-elastic, hierarchical metallic meta-materials by i3DP .....	145
6.1 Introduction.....	145
6.2 Experimental setup.....	148
6.2.1 Materials .....	148
6.2.2 Fabrication of metallic structures.....	148
6.2.3 Characterization .....	149
6.3. Results and Discussion .....	149
6.3.1 ATRP grafting.....	149
6.3.2 Structural controlling of the hollow metallic microlattices .....	152
6.3.3 Characterization of mechanical properties.....	156
6.4 Conclusion .....	168
Chapter 7.....	170
7 Mechanical meta-materials by i3DP and the integrated properties .....	170
7.1 Introduction.....	170
7.2 Experimental setup.....	172
7.2.1 Materials .....	172
7.2.2 Initiator-integrated 3D printing.....	172
7.2.3 Characterization .....	173
7.3. Results and Discussion .....	174
7.3.1 Computation of re-entrant structure.....	174
7.3.2 Mechanical properties .....	178
7.3.3 Poisson's ratio upon metal thickness. ....	183
7.4. Conclusion .....	184
Chapter 8.....	186
8 New generation of initiator-integrated 3D printable material (i3DP II) .....	186
8.1 Introduction.....	186
8.2 Experimental setup.....	190
8.2.1 Chemicals and materials. ....	190
8.2.2 3D Printing of dopamine-Integrated Architectures .....	190
8.2.3 In-suit polymerization of PDA.....	190
8.2.4 PDA-assisted ELP .....	191
8.2.5 Characterization .....	192
8.3 Results and discussion .....	192
8.4 Conclusion .....	202
Chapter 9.....	203
9 Summary, conclusions, and future directions .....	203
9.1 Summary of 3D printing of functional materials.....	203
9.2 Future directions .....	208

References.....	210
Curriculum Vitae.....	226

## List of Tables

### CHAPTER 1

Table 1-1. Summary of 3D printing processes.....	9
Table 1-2. Comparison chart of additive and traditional manufacturing.....	21
Table 1-3. structural flexibility of different 3D printing approaches for architecture materials. Approaches are listed with decreasing maturity from left to right.....	39

### CHAPTER 2

Table 2-1. Expected and XPS measured molar concentration ratios of chitosan .....	65
Table 2-2. Comparison of adsorption capacities of chitosan-base materials for the removal of Cu (II) from aqueous solutions.....	71

### CHAPTER 3

Table 3-1. Comparison of the printability after the integration of initiator. ....	86
--	----

### CHAPTER 4

Table 4-1. Series of robots with different spiral shape, $l=25\text{mm}$ , $r=5\text{mm}$ , $h1=4\text{mm}$ ....	117
--	-----

### CHAPTER 5

Table 5-1. Effective properties of several lattice materials.....	130
Table 5-2. Summary of lattice properties and the composed bulk material.....	140

### CHAPTER 6

Table 6-1. Summary of structural parameters and mechanical properties of the fabricated microlattices.....	155
--	-----

### CHAPTER 7

Table 7-1. Summary of structural parameters and mechanical properties of the fabricated microlattices.....	181
--	-----

# List of Figures

## CHAPTER 1

Fig. 1-1. Schematic illustration of 3D printing process. A digital model of the interested object is created. Then, the 3D model is converted into a .STL format and subsequently converted to a G-code file. Finally, the G-code is read by 3D printer to print material layer-by-layer until an entire object is created.....	5
Fig. 1-2. The working process of SLA and DLP. SLA utilizes a laser to draw a polymer layer, while DLP projects layers as a flat image.....	7
Fig. 1-3. Top-down and bottom-up configurations of photo-polymerization based 3D printing. (A) In a top-down configuration, the 3D objects are created successively by lowering the solidified layers. (B) In a bottom-up configuration, the 3D objects are obtained by moving up the solidified layers.....	8
Fig. 1-4. Deposition-based 3D printing. (A) Schematic illustration of FDM. Two nozzles are employed to supply the building material and supporting material, respectively. (B) Robocasting (direct ink writing, DIW) utilizes a dispenser to deposit materials of viscous liquid state layer-by-layer..	10
Fig. 1-5. Powder-based 3D printing technology. (A) Binder jetting 3D printing employs a powder supply system to distribute a thin layer of powder material, and an inkjet dispenser deposits the liquid adhesives to the exposed layer. A 3D object is created by repeating the distribution and deposition process. (B) Selective laser sintering or melting (SLS or SLM) uses a laser beam to sinter or fuse the particles locally according to the layer design..	12
Fig. 1-6. (A) Selective inhibition sintering (SIS) process. (1) printing sintering inhibitor; (2) laying a thin powder layer; (3) creation of a boundary to contain part; (4) heating and compression; (5) bulk sintering in an oven. (B) Laminated object manufacturing (LOM) works for materials in a sheet form. Once the excess material is removed by a cutting system, a new sheet is loaded with a laminating roller until an entire 3D object is created..	13

Fig. 1-7. 3D printing of fused silica glass. (A) UV-curable monomer is mixed with SiO <sub>2</sub> nanoparticles, and then polymerized through SLA. Finally, a fused silica glass is obtained after debinding and sintering the polymerized composite at 1300 °C. (B-C) Examples of printed glass structures. (D) Demonstration of the high thermal resistance of the printed fused silica glass..	15
Fig. 1-8. Varieties of wire-deposition 3D printing. (A) Wire-arc-welding based 3D printing technologies, including (a) gas metal arc welding, (b) gas tungsten arc welding, and (c) plasma arc welding. (B) Schematic of electron beam freeform fabrication with a wire feed system. (C) Schematic of wire-laser 3D printing.....	16
Fig. 1-9. Continuous liquid interface production (CLIP) allows a faster printing process by layerless part construction. (A) Schematic of CLIP printing system. (B) Printed objects by CLIP. (C) Ramp test patterns printed at the same speed at different slicing thickness (100 μm, 25 μm, and 1 μm).....	16
Fig. 1-10. CLIP avoids sequential steps from traditional photopolymerization processes (SLA/DLP).....	17
Fig. 1-11. Microfabrication based multi-photon polymerization. (A) A typical experimental setup of microfabrication system. (B) microstructures with extremely detailed features enabled by the direct laser writing approach..	18
Fig. 1-12. Additive manufacturing vs. subtractive manufacturing. (A) Subtractive manufacturing uses material-removing process to fabricate a final 3D object, resulting in a large amount of residual material. (B) Additive manufacturing employs a layer-by-layer fashion to fabricate a final 3D object from a starting material (powder, liquid, filament, etc.); only a required amount of material is used.....	20
Fig. 1-13. A typical example of functional materials realized by surface modification and structural design. Superhydrophobic materials are prepared by constructing micro/nano structures or hierarchical structures on the flat substrate.....	23
Fig. 1-14. A modification of printing materials in the fabrication of functional materials. Traditionally used metal powder for energy-based and powder-based 3D printing is	

substituted by ink composed of metal oxide powder which is extruded by an ink-jetting 3D printing approach. The printed object is then reduced and sintered to form the final metallic architectures through H<sub>2</sub> thermochemical reduction.....25

Fig. 1-15. Stereolithography of polymer-derived ceramics. (A) UV-curable preceramic monomers are mixed with a photoinitiator to accomplish the modification of printing material. (B) the UV-curable resin is polymerized by exposure to UV light. (C) polymer structure is obtained. (D) the polymer is converted into a ceramic structure via pyrolysis. (E-H) examples of 3D printed ceramics by the described approach.. .....26

Fig. 1-16. Modification of graphene materials for 3D printing. (A-G) Coagulation treatment by a chemical reduction of GO-ABS in a NMP solution or a hydrazine hydrate at 95°C for 1 h. (H) Schematic illustration of the FDM process of GO composite. Inset is a graphene-based filament winding on a roller. (I) 3D printed characters using GO composite as the filaments, scale bar: 1 cm.....28

Fig. 1-17. Fabrication of graphene-based microlattices through DIW. (A) Schematic illustration of a modification of GO-based ink and the following 3D printing process. (B-E) Optical and SEM images of a 3D printed graphene aerogel microlattice. (F) 3D printed graphene aerogel microlattices of different thickness and (G) 3D printed graphene aerogel honeycomb. Scale bars, 5mm (B), 200 mm (C), 100nm (E, F), 1 cm (G).....29

Fig. 1-18. DIW of epoxy-based ink with high-aspect-ratio fiber fillers. (A) Illustration of the progressive alignment of high aspect ratio fillers during composite ink deposition. (B-C) Tensile fracture surfaces of longitudinally and transversely printed SiC/C-filled specimens. (D-F) A triangular honeycomb structure composed of SiC/C-filled epoxy, which has highly aligned carbon fibers oriented along the print direction. The scale bars in (E-F) are 500 μm. (G-H) High magnification of fiber fillers in the printed specimen, scale bars: 20 μm.. .....30

Fig. 1-19. Sketch of experimental setup of 3D printing of complex conductive structures through post UV photoreduction.. .....32

Fig. 1-20. Surface modification of ultralight magnetic materials. (A) illustration of the

fabrication from a polyacrylic acid-grafted polyurethane sponge. Resulted ultralight $\text{Fe}_2\text{O}_3/\text{C}$ foam could be manipulated by a magnet bar (B) and stand on a dandelion (C). The superhydrophobic foam can be used to remove lubricating oil..	33
Fig. 1-21. Influence of structural characteristics in the scaling of mechanical properties with density interpreted by stretching-dominated and bending-dominated behavior..	36
Fig. 1-22. Examples of sandwich panels with periodic cellular cores. (A) Illustration of a sandwich panel used in lightweight design under loading. (B-J) examples of periodic cellular cores..	38
Fig. 1-23. (A) Schematic illustration of the energy absorption performed by lattice structure which lowers the impulse intensity and eliminates the transferring pressure. (B) The ideal response of a cellular energy absorbing material. (C) The actual mechanical behavior of a cellular lattice structure..	40
Fig. 1-24. Comparison of energy-absorption performance of different materials. (A) Extruded polystyrene foam, (B) Open-cell Al foam, (C) Solid Al microlattice, (D) Pre-crushed Al honeycomb, (E) Thermoplastic polyurethane twin hemispheres, and (F) Hollow Ni microlattice..	42
Fig. 1-25. Illustration of the pentamode metamaterial ideal suggested by Milton and Cherkaev in 1995 (the artificial crystal with lattice constant $a$ has diamond symmetry) and the first metallic penta-mode meta-material based on the same design and manufactured at Additive Manufacturing Laboratory of TU Delft using selective laser melting..	43
Fig. 1-26. Architecture, design, and microstructure of alumina mechanical-metamaterial. (A) CAD image of the octet-truss design used in the study. (B) Cutaway of hollow octet-truss unit cell. (C) Hollow elliptical cross section of a microlattice tube. (D) SEM image of fabricated octet-truss microlattice. (E-H) Microlattice demonstrates a slow, ductile-like deformation, local shell buckling, and recovery of the structure after compression..	44
Fig. 1-27. The performance of (A) cold plates, (B) heat pipes, and (C) heat exchangers can be improved by introducing architected cellular cores enabled by emerging additive manufacturing techniques..	45

Fig. 1-28. Architectural optimization of clinical scaffolds for breast reconstruction..	46
Fig. 1-29. Graphical illustration listing several of the important material and structural characteristics that have a significant impact on the overall functionality of the 3D printed functional materials.....	49

## CHAPTER 2

Fig. 2-1. Schematic model of 3D printed filter and the structural parameters. 3D printed filters were designed with close-arranged hexagon holes (A), round holes (B), square holes (C) and skewed hexagon holes (D). Inset illustrated the feature size.....	58
Fig. 2-2. Schematic illustration (A) and experimental setup (B) of the chitosan-deposited filter.....	59
Fig. 2-3. Schematic illustration of the fabrication of complex 3D architecture coated with chitosan for metal ion removal. ....	61
Fig. 2-4. SEM images show the change of surface morphology before and after the deposition process. Before deposition (A and C), the 3D printed object shows relatively smooth surface and with cavities distributed. After the deposition (B, D-F), a thin crinkly layer was produced. ....	62
Fig. 2-5. XPS survey spectra of 3D printed cellular before and after GMTPS grafting and subsequent deposition of chitosan. The inset is the Si 2p high resolution spectra of GMTPS grafted object. ....	63
Fig. 2-6. High-resolution XPS C1s spectra of original 3D printed cellular, GMTPS modified and final chitosan-modified cellular (A-C). Representative high-resolution XPS peaks of O 1s (D) and N 1s(E) in a chitosan-modified sample. ....	64
Fig. 2-7. Schematic illustration of metal ion (Cu(II)) removal and absorption-desorption repeating cycles.....	66
Fig. 2-8. EDS of the desorption results by EDTA. (A) EDS data just after Cu(II) ions removal; (B) EDS data after desorption of EDTA.....	67
Fig. 2-9. (A) Effect of temperature (pH = 5.5) and (B) pH on the adsorption (T = 25 °C) of	

Cu(II) on the chitosan-modified 3D filter.....	68
Fig. 2-10. Comparisons of experimental results and fitted results according to pseudo-first-order kinetics model (A) and pseudo-second-order kinetics model (B).....	70
Fig. 2-11. Adsorption isotherms of Cu (II) by chitosan-coated filter (A), and the Freundlich (B) and Langmuir (C) isotherm plots.....	73
Fig. 2-12. (A) Desorption capacity of EDTA to the Cu (II), T=25°C, pH=5.5. (B) Reusability profile of the chitosan-modified material in adsorption and desorption repetition with the optimum working condition (T=25°C, pH=5.5).....	74
Fig. 2-13. SEM images of the chitosan-loaded surface before (A) and after five adsorption-desorption cycles (B). .....	74
Fig. 2-14. Comparison of adsorption capacity of filters with different hole shapes (T=25°C, pH=5.5). .....	75
Fig. 2-15. FTIR spectra of chitosan-modified cellular before and after Cu(II) ions absorption.....	76

### CHAPTER 3

Fig. 3-1. Schematic illustration of the preparation of initiator-integrated UV-curable resin and the surface modification of 3D printed object via SI-ATRP. ....	82
Fig. 3-2. Experiment used DLP 3D printer, and the 3D printing process via a layer-by-layer sequence.....	83
Fig. 3-3. XPS spectra of UV-cured sample. (A) UV-curable resin before and after initiator-integrated. (B) Br signal from the outmost surface and the internal part. ....	84
Fig. 3-4. Printability of initiator-integrated resin. (A). CAD model. (B) 3D object by original clear resin. (C) 3D printed object of clear initiator-integrated resin. (D-E) 3D printed objects by initiator-integrated resin with the addition of pigments. ....	85
Fig. 3-5. SEM images of feature arrays to investigate the printing resolution. (A-B) Side view and top view of square trusses. (C) Circular holes. (D) Rectangular holes. Scale bars: A 50 μm, B 100 μm, C and D 150 μm. ....	86

Fig. 3-6. Test specimen for axial tension experiment. ....	87
Fig. 3-7. Influence of the initiator on the mechanical properties of 3D printed parts. (A) Stress-strain curve of the initiator-integrated specimen under axial tensile test. (B) Comparison of the tensile strength of the samples with and without initiator-integrated. (C) Comparison of Young's modulus of the samples with and without initiator-integrated....	88
Fig. 3-8. XPS spectra of two representative polymer coatings growing by SI-ATRP. (A) XPS spectrum of poly(PFMA). (B) high resolution spectra of C 1s. (C) XPS spectrum of PMETAC.....	92
Fig. 3-9. Hydrophobicity of poly (PFMA) grafted micromesh. Inset is the SEM of hexagonal mesh holes. ....	93
Fig. 3-10. Ni- and Cu-coated microlattices through polyelectrolyte-brush assisted metal deposition. (A-B) Ni-coated microlattice and SEM image of the Ni coating. (C-D) Cu-coated microlattice and SEM image of the Cu coating.....	94
Fig. 3-11. Functional 3D printed hydrogel-microlattices. (A) 3D printed PEGDA (60%) microlattice. (B) Microlattice with P(Py-co-FPy) grafted. (C-D) High resolution SEM image of the P(Py-co-FPy) brush. Scale bar of C: 200 $\mu\text{m}$ , D: 10 $\mu\text{m}$ . ....	98
Fig. 3-12. Semilogarithmic plot of I/V measurements and resistance evaluation for P(Py-co-FPy) coated object (a plate was fabricated via the same procedures as the microlattices). ....	98

## CHAPTER 4

Fig. 4-1. Schematic illustration of the procedures of magnetic-driven robot by initiator-integrated 3D printing with subsequent SI-ATRP and electroless plating for the magnetic layer.....	103
Fig. 4-2. CAD model of the designed robot and the spiral characteristics. ....	104
Fig. 4-3. Magnetic manipulator used to magnetically drive the robot. ....	105
Fig. 4-4. XPS survey spectra of 3D printed robots. (A) robot integrated with initiator and regular robot with base resin. (B) High resolution XPS of Br 3d on outmost surface and	

2mm beneath. (C) Sample with PMETAC brush before and after ion exchange with $\text{PdCl}_4^{2-}$ . (D) High resolution XPS spectra in Pd 3d region of poly(METAC) grafted sample after ion exchange. ....	107
Fig. 4-5. (A) Magnetic material coated robot with a major axis of 12.5mm and minor axis of 5mm. (B) Surface morphology. (C) The EDX spectrum of the surface coating. ....	108
Fig. 4-6. VSM measurement of the magnetic coating (powder scraped from the surface of i3DPed object) .....	109
Fig. 4-7. Flow field around swimming robot. ....	110
Fig. 4-8. Kinematic analysis of the robot swimming in liquid. ....	112
Fig. 4-9. Qualitative motion behavior of magnetic-driven based on equation (2). $a_{1,2}$ and $a_{2,2}$ are the entries of matrix A. ....	114
Fig. 4-10. The relationship between the thrust force $F_a$ and swimming velocity $u$ at three different rotation speed, 150r/min, 90 r/min and 60 r/min. The other parameters were set as $\theta=30^\circ$ , $\beta=0.2$ , $\gamma=1$ , $h_2=2$ mm, $r=5$ mm, $\eta=1$ Pa·s, $l=25$ mm. ....	116
Fig. 4-11. Relationship between the design parameters and the swimming velocity. (A) Spiral angle $\theta$ , (B) spiral width coefficient $\beta$ and (C) height coefficient $\gamma$ . ....	117
Fig. 4-12. Effect of spiral shape (A. spiral angle, B. spiral width, C. spiral height) on the swimming velocity. ....	119
Fig. 4-13. Robot (M1) rotates along its long axis in an empty plastic tube (A) and full of distilled water (B). The inset shows the schematic of magnetic force applying to the rotor. ....	121
Fig. 4-14. Axial swimming and radial swimming in rotating magnetic field. ....	123
Fig. 4-15. Axial swimming of the magnetic robot. Red dash line and blue dash line represent the fitted curve of step-out and break-away, respectively. ....	123
Fig. 4-16. Frequency of the rotating magnetic field vs. distance of the robot the rotation axis during radial swimming. ....	124

## CHAPTER 5

Fig. 5-1. Cellular materials with octet-truss core (A) and pyramidal core (B).....	127
Fig. 5-2. Comparison of the effective Young's modulus (A) and shear modulus (B) as a function of relative density for octet-truss and pyramidal core structures.....	131
Fig. 5-3. Schematic illustration of the fabrication of metallic cellular lattices. Both octet-truss and pyramidal lattices are based on the same approach. ....	132
Fig. 5-4. 3D printed octet-truss cellular materials (A. polymer, B. Cu-coated, C. Ni-coated) and pyramidal cellular materials (D. polymer, B. Cu-coated, C. Ni-coated).....	134
Fig. 5-5. Surface morphology of Ni-coated octet-truss lattice in the z (A) and x, y direction. ....	135
Fig. 5-6. SEM images showing the surface of the Ni-coated lattice obtained at 15 min (A, B), 30 min (C), and 180 min (D) of ELP. The thickness of Cu layer is c.a. 120 nm, 300 nm, and 1500 nm, respectively. The Ni film obtained at 15 min of ELP was not uniform and had some defects (A). ....	136
Fig. 5-7. SEM images showing the surface of the Cu-coated lattice obtained at 10 min (A, inset shows the thickness), 15 min (B), and 20 min (C) of ELP. The thickness of Cu layer is c. a. 100 nm, 140 nm, and 230 nm, respectively. The Cu film obtained at 10 min of ELP was not uniform and had some defects (A). ....	137
Fig. 5-8. Compression setup of octet-truss lattice and the stress-strain curve. ....	138
Fig. 5-9. Compression setup of pyramidal lattice and the stress-strain curve. ....	138
Fig. 5-10. Simplified representation of idealized stress state in an octet-truss lattice. The solid struts are assumed to only experience uniaxial tensile or compressive stresses. ....	138
Fig. 5-11. Comparison of effective properties between octet-truss and pyramidal lattices. (A) Comparison of effective strength. (B) Comparison of effective Young's modulus. .	139
Fig. 5-12. (A) Octet-truss lattice after compression test. (B) SEM image of the fracture status at nodes. ....	140
Fig. 5-13. Strength-enhancement of mechanical properties of the octet-truss lattice. (A) Stress-strain curves of Ni-coated lattices of different ELP time. (B) Young's modulus of Ni-coated lattices vs. the thickness of metal film. (C) Stress-strain curves of Cu-coated	

lattices of different ELP time. (D) Young's modulus of Cu-coated lattices vs. the thickness of metal film.....142

Fig. 5-14. After 60 min of ELP, the lattice collapses along the maximum shear stress face. When the metal layer is thick enough, the nodes can bear a higher loading force form fracture than the maximum shear stress action face of the entire material. ....143

## CHAPTER 6

Fig. 6-1. Schematic illustration of the fabrication of metallic cellular material by initiator-integrated 3D printing and the subsequent surface initiated atomic transfer radical polymerization (SI-ATRP) assisted ELP followed by etching.....148

Fig. 6-2. (A) Comparison of XPS survey spectra of 3D printed samples with and without initiator integrated. The inset is the comparison of high-resolution spectra of Br 3d distributed on the outermost surface and inner part. (B) XPS survey spectra of poly(METAC) before and after an exchange in  $(\text{NH}_4)_2\text{PdCl}_4$  aqueous solution. The inset is the high-resolution spectra of Pd 3d. (C) High resolution spectra of Cl 2p shift after ion exchange for loading  $\text{PdCl}_4^{2-}$  moieties on PMETAC-sample surface. ....151

Fig. 6-3. Metallic 'Eiffel Tower' as an example of hierarchical structure composed of hollow Ni-tubes. (A) polymer-template of 'Eiffel Tower', (B) Metallic 'Eiffel Tower' after ELP and the subsequent etching of polymer core, (C) SEM image of hollow NiP tube. 152

Fig. 6-4. (A-D) Demonstration of as-fabricated ultralight metallic microlattices along with a breakdown of the hierarchical elements. (E) Ultralight metallic materials suspending on a flower .....153

Fig. 6-5. Structural characteristics of the pyramidal microlattices. ....154

Fig. 6-6. SEM images showing the surface of the Ni layer obtained at 5 min (A), 10 min (B), 0.5 h (C, D), and 1 h (E, F) of ELD. The thickness of Ni layer is c.a. 530 nm and 1.52  $\mu\text{m}$  after 0.5 and 1 h's deposition. The film obtained at 5 and 10 min of ELP was not uniform and had obvious defects (A and B). ....155

Fig. 6-7. Cyclic and monotonic uniaxial compression is used to detect the mechanical

behavior of the microlattices. (A) Experimental setup, microlattice (sample 12 in Table S1) before compression (B), after 15% compression (C), 50% compression (D), nearly recover to its original shape (E). .....157

Fig. 6-8. Mechanical response of microlattices upon loading/unloading cycles (Samples 7, 5, 13 from Table 6-1) at progressively increasing wall thickness.....159

Fig. 6-9. Mechanical properties evolution of microlattices upon loading/unloading cycles (Samples 7, 5, 13 from Table 6-1) at progressively increasing wall thickness.....160

Fig. 6-10. SEM images of microlattice (sample #11 in Table S1) in cyclic compression testing of 50% strain and two corresponding mechanisms demonstrate the microlattices can bear large global compression without plastic deforming. From left to right, (A) strut of original microlattice, (B) cracking occurs at the node after the first loading cycle, corresponding model of partial fracture of a node with subsequent rotation (C), nearly no enlarging of crack after second loading cycle (D), (E) and (F) show the node rotation of a remnant ligament and the corresponding mechanical model.....162

Fig. 6-11. Critical maximum strain varying with the wall-thickness-to-diameter ratio (A) and truss angle (B) to obtain complete recovery after the compression, insets are the comparison of theoretic prediction and experimental data. ....165

Fig. 6-12. Evaluation of the mechanical efficiency of the microlattices by plotting the relative compressive strength (A) and elastic modulus (B) as functions of the relative density. The compressive strength scales quadratically with the relative density over the ultralight region but sharply changes to  $\sim \bar{\rho}^{2.5}$ . For the elastic modulus, the microlattices show a quadratic scaling through the entire range of relative density. ....167

## CHAPTER 7

Fig. 7-1. CAD model of re-entrant structure and the structural parameters .....173

Fig. 7-2. Deformation of re-entrant cell by inclined cell member bending. ....174

Fig. 7-3. Poisson's ratios vary with strain for a re-entrant cell with geometric parameters of different  $a$  and re-entrant angle  $\theta$ . ....176

Fig. 7-4. Relationship of PR with re-entrant angle $\theta$ (A) and strut ratio $\alpha$ (B) at the limit value of small deformation. ....	177
Fig. 7-5. Auxetic architecture of metallic hollow microlattices after etching of polymer core. (A) Polymer template was fabricated by the initiator-integrated 3D printing. (B) Metallic cellular template was achieved by SI-ATRP-assisted ELP of Cu. (C) Metallic hollow structure was obtained after the etching of polymer core. (D) Unit cells along with a breakdown of the relevant architectural hierarchy. ....	178
Fig. 7-6. Compression experiments on the re-entrant lattices of three material systems. (A) Image of the polymer sample before compression. (B) Load displacement data that show compression to 35% strain. (C) Post-deformation of the polymer sample. (D) Image of the composite polymer and 190-nm Cu sample before compression. (E) Load displacement data that show 17.5% strain. (F) Post-deformation image of the composite sample. (G) Image of the hollow 1.9 $\mu\text{m}$ walled Cu sample before compression. (H) Load displacement data that show compression to 20% strain. (I) Post-deformation image of the hollow sample .....	179
Fig. 7-7. Mechanical model of inclined beams rotating around the node.....	181
Fig. 7-8. PR of three material systems versus the thickness metal layer. ....	183

## CHAPTER 8

Fig. 8-1. Schematic illustration of the processing of complex architectures by dopamine-integrated 3D printing with subsequent electroless plating for the metallic layer. A dopamine-integrated photo-curable resin was polymerized by a DLP style 3D printing to be a solid part. After the treatment in tris-pH 8.5, a layer of PDA was in-situ grown on the surface of the 3D structure. And the subsequent ELP initiated by the catalyst function of PDA deposits a layer of metal coating on the surface. ....	189
Fig. 8-2. FTIR spectra of the photo-curable resin before and after the mixture of dopamine .....	193
Fig. 8-3. Optical photographs of complex metallic-architecture fabricated via dopamine-	

integrated 3D printing. (A-D) Ag-coated Eiffel tower and its surface morphology in the x, y, and z direction, the inset shows the thickness of the Ag coating, scale bar: 1  $\mu$ m; (E-G) Metallic Eiffel tower of Ni-Co, Cu, and Ni coating, the dimension of the model is 28 x28 x72mm. (H) Microlattice of Au-coating (20 x20 x15mm). .....195

Fig. 8-4. (A) Deformation behavior of dopamine initiated sample. (B) Comparison of tensile strength of the samples with and without mixture of dopamine-initiator .....195

Fig. 8-5. SEM of the silver film growing on the 3D printed object, the reaction time is 5 min for (A-B) and 30 min for (C-D), respectively.....196

Fig. 8-6. Tape test of the Au- and Ag-coated surface to verify the adhesion of the metal coating generated by the dopamine-integrated 3D printing.....197

Fig. 8-7. EDX spectrum of the Ni-Co alloy coating consisting of 65% Ni, 28% Co and 7% P.....198

Fig. 8-8. VSM measurement of the Ni-Co alloy coating. Inset is a cellular structure with Ni-Co alloy coating adsorbed by a magnet.....199

Fig. 8-9. Demonstration of regeneration of the Cu metal film. (A) A plate with Cu coating was used as electrode to light the LED. (B) After peeling off the coating in middle area, the LED turned down. (C) The Cu coating was regenerated to connect the circuit again. Insets are the electrode made of Cu-coated plate.....200

Fig. 8-10. Comparison of the conductivity of deposited metal coatings and the bulk materials.....201

Fig. 8-11. SEM images showing the thickness of the (A) Cu-coated substrate at 30 min, (B) Ag-coated substrate at 30 min, (C) Au-coated substrate at 30 min. ....201

## CHAPTER 9

Fig. 9-1. Workflow of 3D printing functional material through the incorporation of surface modification and structural optimization. ....203

## Glossary of Terms

AM	additive manufacturing
RP	rapid prototyping
SLA	stereolithography
DLP	digital light processing
SLS	selective laser sintering
SLM	selective laser melting
SIS	elective inhibition sintering
FDM	fused deposition modeling
.STL	STereoLithography File
LOM	laminated Object Manufacturing
CLIP	continuous liquid interface production
DIW	direct ink writing
DLW	direct laser writing
MPP	multi-photon polymerization
GO	graphene oxide
CNTs	carbon nanotubes
PR	Poisson's ratio
NPR	negative-Poisson's-ratio
FTIR	Fourier transform infrared spectroscopy
SEM	scanning electron microscopy
XPS	X-ray photoelectron spectroscopy
EDS	energy dispersive X-ray spectrometer
ATRP	atom transfer radical polymerization
SI-ATRP	surface-initiated atom transfer radical polymerization
BrMA	2-(2-bromoisobutyryloxy) ethyl methacrylate
EDTA	ethylenediaminetetraacetic acid
PFMA	1H,1H,2H,2H-perfluorodecyl methacrylate
METAC	2-(methacryloyloxy)ethyl-trimethylammonium chloride
PMETAC	poly(METAC)
ELP	electroless plating/deposition
P(Py -co-FPy)	poly(pyrrole-co-formyl pyrrole)
VSM	vibrating sample magnetometer
PDA	polydopamine

## Chapter1

### 1 Introduction to 3D printing and materials

3D (three-dimensional) printing technology has been employed in a wide range of fields. Significant research and financial contributions are being invested to improve its capability for more practical applications, focusing on functional 3D printing. By taking the advantage of 3D printing in building complex geometries, it is possible to fabricate materials and structures with novel properties assisted with proper material or surface modification and structural control. The theme of this thesis is to develop 3D printing technology's ability in designing and fabricating different kinds of functional materials, and simultaneously establish the theories and models for their functional behaviors. This chapter will review the research background including the status of current 3D printing technology, the working materials and current strategies of functionalization, and then identify the research opportunities and objectives.

#### 1.1 What is 3D printing?

##### 1.1.1 A brief history of 3D printing

Additive manufacturing, commonly known as 3D printing or rapid prototyping (RP), has obtained huge advancements since the first 3D system was introduced in the late 1980s [1-3]. This novel manufacturing process is usually used to fabricate customized and complex structures that are often difficult or even impossible for traditional fabrication technologies to accomplish. Due to its advantages of fast manufacturing and ability to form complex geometries, 3D printing technology has attracted great attention from various emerging applications, including physical prototypes, functional evaluation of product designs, health care products and even end-use products [4-9].

Apparently, the terms “additive manufacturing” and “3D printing” are still under debate even today for what should be considered as the exact definition of this layer-by-layer fabrication process. Normally, “additive manufacturing” is mostly used in industry, while “3D printing” is more acceptable for the public especially when discussing this technology generally. For understanding this work well and the purpose of consistence, the terms “additive manufacturing” and “3D printing” are used interchangeably. This study is mainly focused on the 3D printing technology of photo-polymerization based principle, targeting for the industrial AM technologies.

3D printing technology has emerged recently as a prevalent method to fabricate customized and complex structures, although this incremental fabrication method has existed for almost 40 years. The conception of 3D printing can be traced back to 1976 when the inkjet printer was invented. The adaptations and advances on the inkjet concept then inspired the leap from a planar printing with ink to a three-dimensional printing with materials. In 1984, the first 3D printing processes were developed by Charles Hull (later the co-founder of 3D SYSTEM) [10], who invented stereolithography (SLA) and selective laser sintering (SLS). Fused deposition modeling (FDM) was subsequently developed, and it was patented rapidly and commercialized by Stratasys Inc. These processes make it possible to create a tangible 3D object from digital data. Here, the file type (STereoLithography, .STL) which is still used in 3D printing technology to date, was also invented by Hull. These technologies allow users, for the first time, to test a design before investing in a large practical manufacturing. Soon afterwards, many derivative technologies were developed and patented by Hull and his colleagues.

Until the expiration of these patents in the late 2000’s, the social media and the open digital environment began to popularize the terms “3D printing” and “additive manufacturing”. The RepRap project established in 2005 by Dr. Adrian Bowyer of Bath

University (UK) as an open source of hardware and software was a milestone in popularizing this technology [11]. From this point onwards, tremendous developments in 3D printing have been achieved within technology upgrades, applications, working materials and so forth. The following section lists some representative developments.

In 1999, the first lab-grown organ of a 3D printed scaffold with human cells fostered on the surface was implanted in a young patient's body. The scientists at Wake Forest Institute for Regenerative Medicine developed this technology, and opened up new areas of 3D printing organs [12].

In 2002, a miniature kidney was functionalized to filter blood and diluted urine in an animal. This project was also conducted by scientists at Wake Forest Institute for Regenerative Medicine. The direct printing of organs and tissues by 3D printing technology had begun[7].

In 2005, an open-source collaboration with 3D printing was proposed by Dr. Adrian Bowyer of Bath University to build a 3D printer that could print most of its own components. This project opened an era of democratized manufacturing by cheaply distributing RepRap units to individuals everywhere, and enable the public to create products on their own [13].

In 2006, a SLS machine which used a laser to sinter materials into 3D objects became viable. This was a breakthrough that opened a door for mass customization and on-demand manufacturing of industrial parts [4, 14]. In the same year, 3D printing machines which were capable of printing multiple materials, such as elastomers and polymers, became available, and enabled a single part to be made with a variety of material properties [15].

In 2008, the first self-replicating printer which was able to print the majority of its own components was released by RepRap. Thus, 3D printer users could duplicate their 3D

printers to spread the use of 3D printing technology [16]. Simultaneously, a DIY co-creation service was launched by Shapeways, which allowed a private beta for artists, architects and designers to make their 3D designs as physical objects inexpensively [13, 17]. In the same year, the first 3D printed prosthetic leg was implanted into a human's body, and worked well for walking. This prosthetic leg was printed without any assembly but contained all functional parts, including the knee, foot, and socket, in a whole complex structure. This breakthrough prompted the creation of Bespoke Inc, which is a manufacturer of prosthetic devices [18]. Two years later, the first 3D printed prosthetic jaw was implanted into an 83-year old woman. And this technology is currently being explored to promote the growth of new bone tissues [19].

In 2009, the first blood vessel was printed by Organovo, a bioprinting innovator relying on Dr. Gabor Forgacs's technology [20, 21].

When it comes to the 2010s, a large number of breakthroughs in 3D printing began to emerge. For example, the first 3D printed robotic aircraft was printed by engineers at the University of Southampton. 3D printing technology enabled the plane to be built with elliptical wings in an economical way, resulting in an improvement of aerodynamic efficiency and drag reduction [22].

In 2013, President Obama said 3D printing had "the potential to revolutionize industry" in his State of the Union Address, which gave a big boost to the development of 3D printing [23].

In 2015, a groundbreaking 3D printing technology which was 25-100 times faster than the at-that-time available commercial 3D printers was released by Carbon3D. This new 3D printing process was named "Continuous Liquid Interface Production" or "CLIP". It had similarities with the working process of DLP and SLA, but can complete an object in a fast-continuous flow of UV-curable which was enabled by an additional

oxygen permeable layer [24].

In 2016, Daniel Kelly's lab announced their ability to 3D print bones, which paved the way to 3D bio-print cartilages and organs, and made it possible to reduce the need for donors [25, 26].

### 1.1.2 3D printing techniques and categories

The process of 3D printing is performed as joining materials layer by layer to transform complex 3D model designs into objects, as shown in **Fig. 1-1** [27]. The virtual model can be established by using either computer-aided design (CAD), three-dimensional scanner (to copy an existing object), or photogrammetry which reconstitutes the model by combining object's images taken from different positions [28, 29]. Then, the 3D model is converted to a standard file (.STL) which stores the information as a list of coordinates of triangulated sections [30]. This file format is then converted to a G-code file after the slicing process by the 3D printer software. The G-code consists of all the 2D cross section data of an entire object, and guides the 3D printer to deposit materials following a successive sequence of 2D patterns with one layer on top of the other until a desired 3D object is formed.

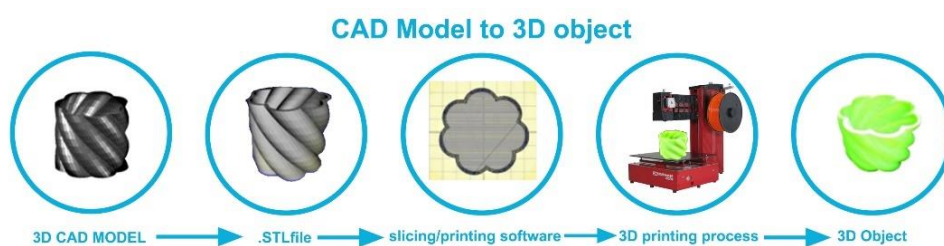


**Fig. 1-1. Schematic illustration of 3D printing process. A digital model of the interested object is created. Then, the 3D model is converted into a .STL format and subsequently converted to a G-code file. Finally, the G-code is read by 3D printer to print material layer-by-layer until an entire object is created.**

Reprinted with permission from ref. [27].

According to the differences of manufacturing process and working material, 3D printing technology includes a number of established manufacturing techniques and experimental technologies [5]. Different 3D printing techniques build and consolidate layers in different ways. Some utilize energy-based sources (lasers, electron beams) to form materials by polymerizing, melting or sintering. Others are mainly based on a deposition principle, which uses inkjet-type printing heads to accurately spray binder or solvent onto powdered materials. **Table 1-1** summarizes the major 3D printing processes [29] according to the printing routes, such as photo-polymerization, extrusion, powder-based deposition and lamination. Each technique has its own characteristics and applications in producing prototype models. Among them, photo-polymerization based 3D printing which uses optics to polymerize photoresists is the most prevalent technique. This technology was also one of the first employed mechanisms for additive manufacturing [31]. Typically, it works as, a layer of liquid polymer is solidified upon the exposure to UV light, then, this solidified layer is lifted in a controlled way to successively solidify the following layers, and a final 3D object is fabricated by stacking one solidified layer on top of another with good adhesion. This technology has been developed in several varieties, which include laser-based stereolithography (SLA), Digital Light Processing (DLP), and the latest developed continuous liquid interface printing (CLIP) and Two-photo polymerization (more details will be discussed in later section).

SLA is the first commercialized technique, which employs a UV laser to polymerize liquid UV-curable polymers (photopolymer), while DLP uses a light projector to project voxel data to polymerize the photopolymer. **Fig. 1-2** shows the working difference between these two techniques [32]. SLA employs two motors—one of each in X and Y axis—to rapidly draw a laser beam to the print area and solidify the photo-curable resin as the laser beam goes along. Differently, DLP projects a single image of each layer at once by a digital projector screen. Each image layer is composed of small rectangular

bricks called voxels. The layer of polymerization is, therefore, related to the square pixel of the projector.

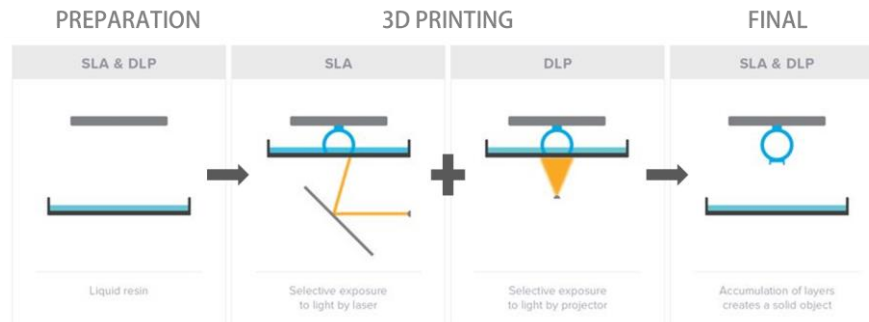


**Fig. 1-2. The working process of SLA and DLP. SLA utilizes a laser to draw a polymer layer, while DLP projects layers as a flat image. Reprint with permission from ref. [32].**

Up to now, the photo-polymerization based 3D printing has been developed into several configurations including top-down, bottom-up and material jetting. For the top-down one, the polymerization process occurs at the liquid surface and the stage moves downwards after each layer is solidified (**Fig. 1-3A**). The bottom-up one obtains the final object from the bottom, and a transparent window is used to separate the resin with optics upon layer formation (**Fig. 1-3B**). Compared to the top-down configuration, the bottom-up one is more suitable to print objects when the polymer resin is in a limited quality. The material jetting method which works similar to the inkjet approach deposits curable materials followed immediately by full area UV light exposure [33]. Because all these approaches are based on the UV-polymerization mechanism and have advantages in fast manufacturing, high printing quality and affordability, they are getting more and more attention in fields of research, products development and household life.

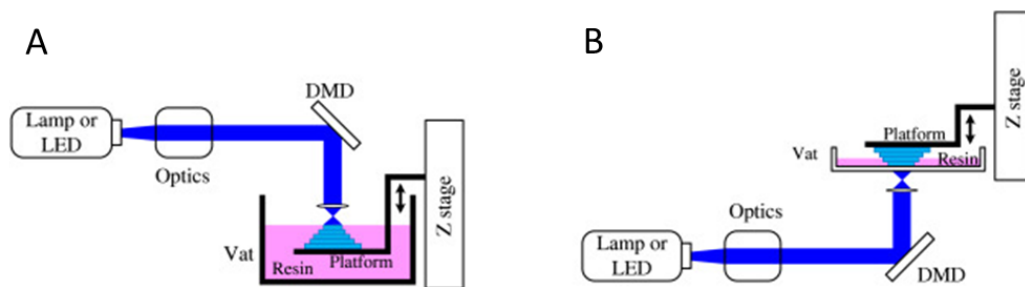


**Fig. 1-3. Top-down and bottom-up configurations of photo-polymerization based 3D printing. (A) In a top-down configuration, the 3D objects are created successively by lowering the solidified layers. (B) In a bottom-up configuration, the 3D objects are obtained by moving up the solidified layers. Reprint with permission from ref. [34].**

**Table 1-1. Summary of 3D printing processes. Reprint with permission from ref. [29].**

3D printing processes	techniques	Materials	Advantages	Limitations
Photo-polymerization	Stereolithography (SLA& DLP) Material jetting Continuous liquid interface printing (CLIP) Two-photon polymerization (2PP)	Photopolymers Photopolymers UV-curable resins UV-curable resins	Simple Multimaterial structures High speed Sub-100 nm resolution	Single material High cost Single material Low yield of production
Extrusion	Fused deposition modeling (FDM)  Robocasting (DIW)	Thermal plastics (ABS, PLA, PC, PA, etc.); glass (new); metal (new) Plastics, ceramic, food, living cells, composites	Simple, multi-material structures, low cost versatile	High cost for glass and metal Requires post-processing, low resolution
Powder based	Selective laser sintering (SLS)  Selective laser melting (SLM) Electron beam melting (EBM) Binder jetting  Selective inhibition sintering (SIS)	Thermal plastics, metals  Metals Metals Any materials in particulate form  Metal	No need for support material  No need for support material No need for support material No need for support material; lower cost than laser based methods Sintering is performed only once after printing; lower cost than laser-based methods	Limited mechanical properties; high cost High cost High cost Limited mechanical properties Low resolution; limited mechanical properties
Lamination	Laminated object manufacturing (LOM)	Paper, metal, plastic, etc. as laminated sheets	versatile	Limited mechanical properties; some design limitations

Different from the photo-polymerization processes, extrusion-based 3D printing technology generally prints objects by depositing materials directly from a nozzle head dispenser. FDM is the most common method employed in this technology, and mainly works for thermoplastic materials or eutectic metals, including polylactic acid (PLA), acrylonitrile butadiene styrene (ABS), polycarbonate (PC), polyamide (PA), etc. The materials are usually used in a filament form to make it easy to extrude. During the printing process, structures are fabricated by extruding small beads of fused materials which immediately bond to the layer below. What is more, multiple nozzles can be employed to deposit different materials during a single printing process, allowing a multi-material structure (**Fig. 1-4A**) [29].

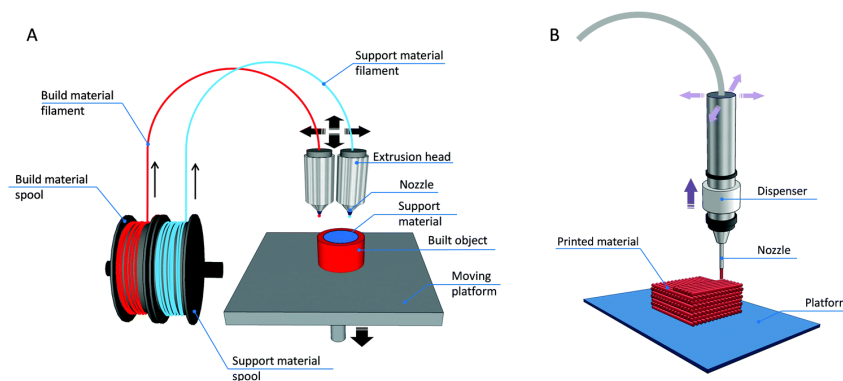
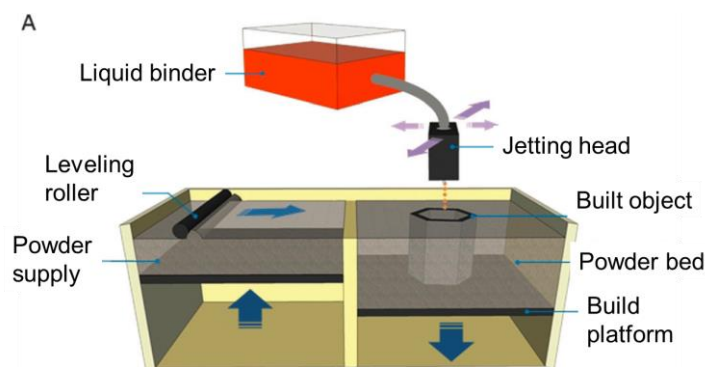


**Fig. 1-4. Deposition-based 3D printing. (A) Schematic illustration of FDM. Two nozzles are employed to supply the building material and supporting material, respectively. (B) Robocasting (direct ink writing, DIW) utilizes a dispenser to deposit materials of viscous liquid state layer-by-layer. Reprint with permission from ref. [29].**

Because this method uses heat as the forming tool, the printing resolution is strongly restricted by the melted plastic flow dynamics rather than the optics and radical polymerization kinetic. That means, FDM not only provides a narrow material spectrum but also has a limitation of low printing quality [35, 36]. The newly proposed robocasting (or direct ink writing, DIW) adopts a similar working principle to that of

FDM, but it can deposit a much wider variety of materials or a combination of materials provided in a form of highly viscous ‘ink’ which can retain its shape after deposition (**Fig. 1-4B**) [29, 36]. This printing approach applies to extremely versatile materials ranging from ceramic, plastics, and glass to living cells [36]. However, the preparation of the materials and necessity of complex post-processing limit its application significantly.

Powder-based 3D printing is a fabrication approach similar to SLA but uses a binding source (liquid glue, laser beam, etc.) to fabricate product. It works for materials that are in a powder state and provides opportunities to form materials of high melting point, such as thermoplastic, metal, ceramic or glass powders. Technically, a binder system is directed applied to the powder and links the particles at the exact position according to the cross-sectional model design [29]. As shown in **Fig. 1-5**, the binder source can be either a liquid glue to adhere the particles or a high-energy beam, like a laser, to sinter the particles just below the melting point (selective laser sintering, SLS) or over the melting temperature (selective laser melting, SLM) [37, 38]. Alternatively, the high-energy beam can also be an electron beam (electron beam melting, EBM) to achieve a higher temperature. Despite a large variety of materials can be fabricated in forms of plaster, ceramics, wood, marble, and metal powders, the powder-based 3D printing is still restricted by the low printing resolution due to the drawbacks similar to the FDM [4].



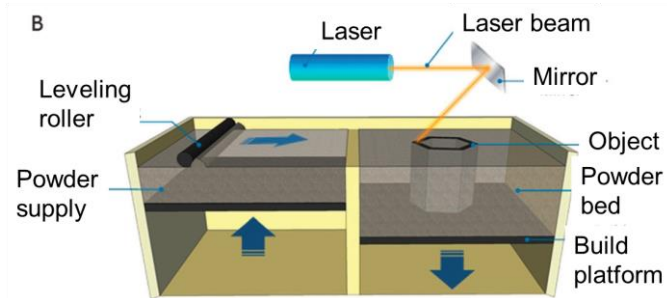


**Fig. 1-5. Powder-based 3D printing technology. (A) Binder jetting 3D printing employs a powder supply system to distribute a thin layer of powder material, and an inkjet dispenser deposits the liquid adhesives to the exposed layer. A 3D object is created by repeating the distribution and deposition process. (B) Selective laser sintering or melting (SLS or SLM) uses a laser beam to sinter or fuse the particles locally according to the layer design. Reprint with permission from ref. [29].**

Other 3D printing techniques are also developed to accommodate special materials or processing requirements. For example, selective inhibition sintering (SIS) was developed to printing oxygen-sensitive materials (such as Cu), which employs a different approach from general methods, like SLS and SLM. It first deposits particles in a layer-by-layer sequence to form an inhibitor which outlines the desired object, and a container to keep the materials. Once the inhibitor and the container are completed, the green part is then solidified in the oven. The process is described as **Fig. 1-6A** [39]. This technology can significantly reduce the cost because employs a much cheaper system, and also make it possible to form special materials that have to be sintered in an environment without air.

In addition, Laminated Object Manufacturing (LOM) was developed to fabricate 3D structures by gluing and laser-cutting layers of paper or plastic film. Depending on the working materials (paper, metal, plastic, etc.), each layer is bonded to the preceding one using adhesives or welding techniques, and a laser-cutting is subsequently used to

outline the cross section of each layer. Finally, an entire 3D object is created by repeating this process (**Fig. 1-6B**) [40].

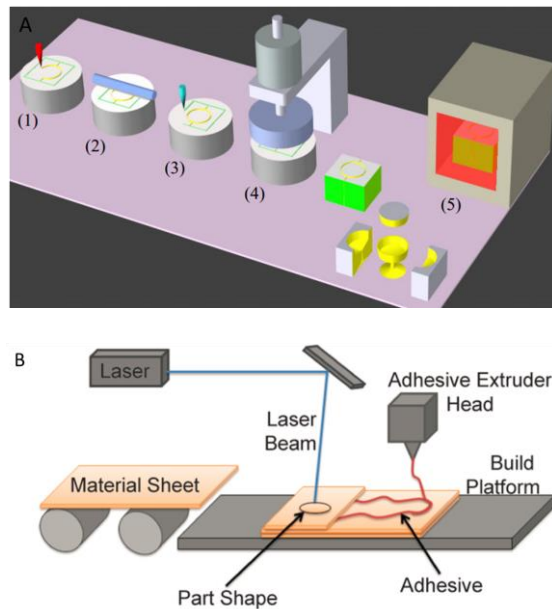


**Fig. 1-6. (A) Selective inhibition sintering (SIS) process. (1) printing sintering inhibitor; (2) laying a thin powder layer; (3) creation of a boundary to contain part; (4) heating and compression; (5) bulk sintering in an oven. (B) Laminated object manufacturing (LOM) works for materials in a sheet form. Once the excess material is removed by a cutting system, a new sheet is loaded with a laminating roller until an entire 3D object is created. Reproduced with permission from ref. [39, 40].**

### 1.1.3 State-of-the-art 3D printing: new materials, methods and concepts

Recently, numerous researchers are attempting to push forward the development of 3D printing technology. They are trying to introduce new concepts into 3D printing technology, aiming to create faster, cheaper, and smaller printing systems, enhance printing definition and fabricate objects using materials which would normally be processed only by traditional manufacturing. Typically, the current advancements in 3D

printing technology are mainly progressing in three possible directions [29]: 1. printing systems accommodating new materials; 2. high printing speed by introducing new working concepts; and 3. High printing resolution of micro-nanoscale. The following lists some of the recent advancements in 3D printing technology:

To overcome the difficulties of printing transparent glass, a research team at MIT recently demonstrated a full extrusion printer, which has a similar working process to the FDM technique[29, 41]. In this 3D printer, a special heating system was adopted to liquefy glass and control the spatial deposition according to CAD design. This printer allowed a direct fabrication of real glass materials, obtaining extremely fragile objects. In 2017, a research team in Karlsruhe Institute of Technology (KIT) also demonstrated a compatible approach to 3D print high-quality fused silica glass components. This approach employed a photopolymerization-based mechanism instead of the above deposition process, shown as **Fig. 1-7** [42]. A mixture of UV curable resin and silica nanopowder was prepared and polymerized in a SLA system. The resulting 3D objects were then turned into fused silica glasses through thermal debinding and sintering. This process not only made it possible to fabricate glass, one of the most difficultly machined materials, by the modern 3D printing techniques, but also allows the construction of complex geometries in either macro- or microscale.

3D printing of metals enables one to create metallic products with highly desirable structures (e.g., using highly refined particles), which could not otherwise be achieved by using conventional approaches. The additive manufacturing of metal materials is, therefore, always a hot research topic. Recently, a novel extrusion-based approach, which uses a metal wire feed system instead of sintering powder and metal particles by high-energy beam, is proposed to 3D print metal objects. Similar to FDM process, this technology is equipped with a heating system to locally melt a solid metal wire, creating a sort of pool of molten metal. Three varieties have recently been developed

according to the energy system [43]: electron beam freeform fabrication **Fig. 1-8A**, wire-laser **Fig. 1-8B**, and wire-arc-welding additive manufacturing **Fig. 1-8C**.

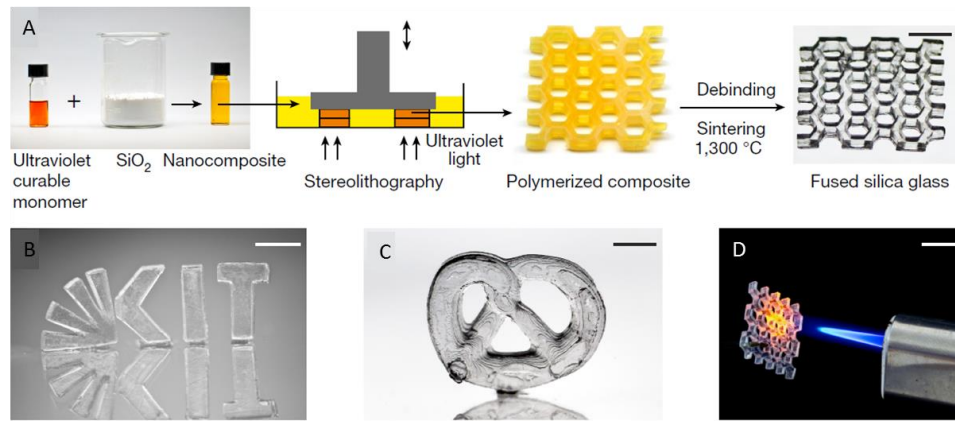


**Fig. 1-7. 3D printing of fused silica glass. (A) UV-curable monomer is mixed with SiO<sub>2</sub> nanoparticles, and then polymerized through SLA. Finally, a fused silica glass is obtained after debinding and sintering the polymerized composite at 1300 °C. (B-C) Examples of printed glass structures. (D) Demonstration of the high thermal resistance of the printed fused silica glass. Reprint with permission from ref. [42].**

Fabrication speed has always been one of the most important issues in the manufacturing. To increase the printing speed, Carbon3D recently introduced a new 3D printing technology, which can achieve a printing speed 25 to 100 times to even the most advanced SLA or poly-jet machines [24]. This groundbreaking 3D printing technology is named as “continuous liquid interface production (CLIP)”. It is equipped with an oxygen-permeable window below the ultraviolet image projection plane, thus, the photopolymerization is inhibited between the window and the polymerizing part because of the oxygen inhibition to radical polymerization (**Fig. 1-9**). A thin uncured liquid layer (oxygen-containing “dead zone”) between the window and the cured part surface allows a continuous liquid interface printing. Compared to other photopolymerization-based 3D printing processes which rely on the step-by-step layer formation, this approach accelerates significantly the production speed by a layerless-

construction approach (Fig. 1-10) [24].

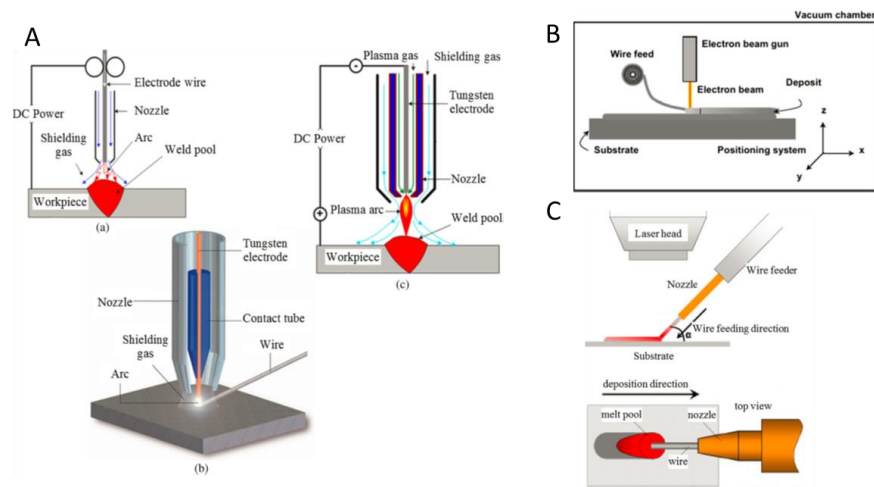


**Fig. 1-8. Varieties of wire-deposition 3D printing. (A) Wire-arc-welding based 3D printing technologies, including (a) gas metal arc welding, (b) gas tungsten arc welding, and (c) plasma arc welding. (B) Schematic of electron beam freeform fabrication with a wire feed system. (C) Schematic of wire-laser 3D printing.**

Reproduced with permission from ref. [43].

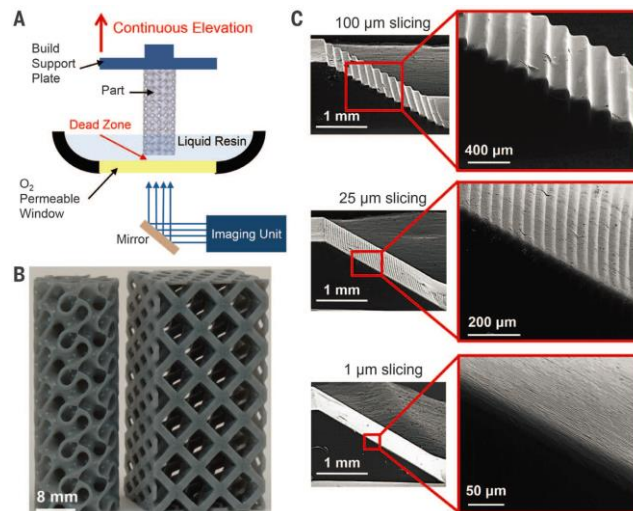


**Fig. 1-9. Continuous liquid interface production (CLIP) allows a faster printing process. (A) Schematic of CLIP printing system. (B) Printed objects by CLIP. (C) Ramp test patterns printed at the same speed at different slicing thickness (100 μm, 25 μm, and 1 μm). Reprint with permission from ref. [24].**

Additionally, extraordinary progress has been made to improve the fabrication resolution of 3D printing technology. Recently, a technology known as direct laser writing (DLW) allowed the fabrication of complex structures with high resolution of  $\sim 50$  nm. This technology is based on the multi-photon polymerization (MPP), which means monomers begin to polymerize only when absorbing more than one photons. Technically, the polymerization is enabled by an ultrafast laser (such as femtosecond laser). By focusing a laser spot inside a transparent photoresist, a submicron-size model can be fabricated according to the CAD design. New technologies including piezoelectric actuators and galvanometric mirrors are currently employed in this 3D printing technique to enhance the positioning and scanning speed [44]. **Fig. 1-11** shows a typical experimental setup of a micro-fabrication system equipped with a femtosecond laser.

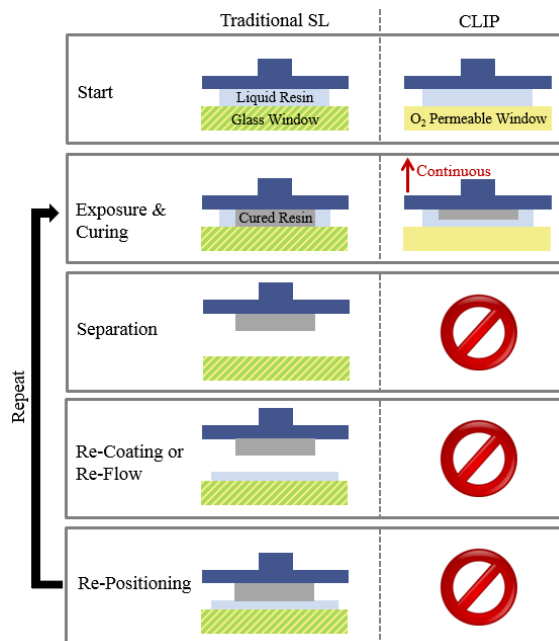


**Fig. 1-10. CLIP avoids sequential steps from traditional photopolymerization processes (SLA/DLP). Reprint with permission from ref. [24].**

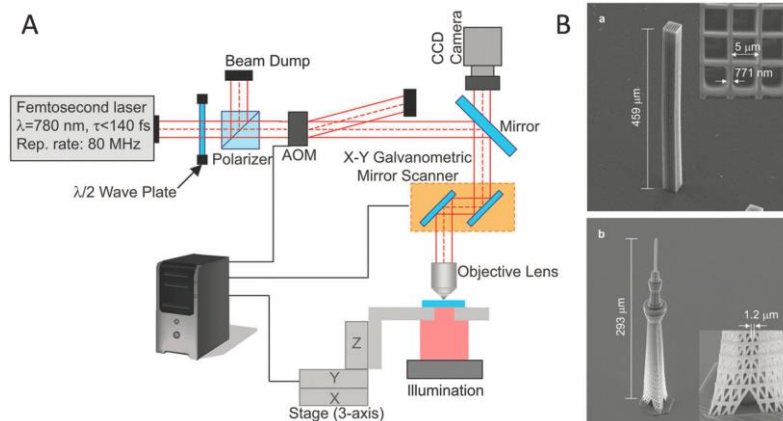


**Fig. 1-11. Microfabrication based multi-photon polymerization. (A) A typical experimental setup of microfabrication system. (B) microstructures with extremely detailed features enabled by the direct laser writing approach.**

**Reprinted with permission from ref.[45].**

#### 1.1.4 Advantages and drawbacks of 3D printing

Although 3D printing technology consists a number of established manufacturing techniques and experimental approaches according to the manufacturing process and working materials [16], all the techniques share a common defining feature of being able to produce a 3D object in a manner of bottom-up rather than the top-down manner of traditional subtractive manufacturing. 3D printing follows an opposite fabrication process to that of subtractive manufacturing, which needs to use various material-removal processes, like drilling, milling, sawing and broaching. Therefore, the factors that primarily differentiate the two methods lie in the geometrical complexity and the material waste of parts being created.

**Fig. 1-12** [29] indicates the difference between the 3D printing process and the subtractive manufacturing. Subtractive methods often require an expensive tooling, which must be designed specifically according the precise nature of the objects being created. It is also required to create the tooling before producing the object of interest. Thus, the subtractive manufacturing always presents a constraint in design flexibility

and fabrication speed. In contrast, 3D printing process typically produces parts in a layer-by-layer way, which is unnecessary to use an expensive tooling. The fabrication manner determines there are crucial benefits for the production cycle as one needs only to alter a software design, such as CAD, to optimize the object, rather than designing and reproducing new tooling. It allows a high efficiency for the design-to-product life cycle, and provides an unprecedented degree of user customization. Also, the 3D printing approaches produce less waste materials than subtractive manufacturing routes. **Table 1-2** lists the main comparisons between additive manufacturing and traditional manufacturing [46].

In summary, 3D printing technology has advantages as the following:

1. *Material efficiency.* 3D printing uses raw materials efficiently by constructing objects layer-by-layer. The leftover materials can often be reused with minimum processing.
2. *Resource efficiency.* 3D printing does not require auxiliary resources, such as jigs, fixtures, cutting tools..., and can produce parts through small manufacturers, resulting in an opportunity for improving supply chain dynamics.
3. *Object flexibility.* 3D printing does not require to sacrifice parts' functionality to ease the manufacturing process, and makes it possible to fabricate a single part with integrated mechanical properties. Thus, it provides more opportunities for innovation.
4. *Production flexibility.* The small batch production of 3D printing makes it easier to synchronize the fabrication process with customer demand. Furthermore, the drawbacks of line balancing and production bottlenecks are virtually eliminated because complex parts are produced in a single piece.

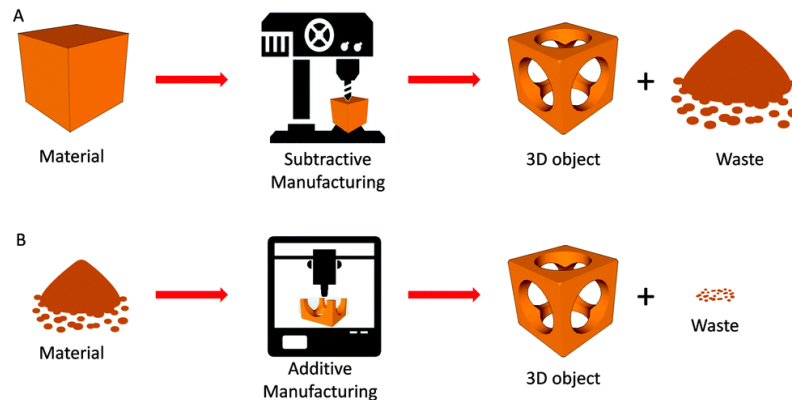


**Fig. 1-12. Additive manufacturing vs. subtractive manufacturing. (A) Subtractive manufacturing uses material-removing process. (B) Additive manufacturing employs a layer-by-layer fashion to fabricate a final 3D object from a starting material (powder, liquid, filament, etc.); only a required amount of material is used. Reprint with permission from ref. [29].**

However, 3D printing technology still cannot fully compete with traditional manufacturing, especially for the mass production field because of the following drawbacks:

1. *Materials limitation.* Currently, liquid polymers, powder comprised of resin or plaster are still the main working materials for most 3D printers. Although it is becoming more commonplace to printing other materials, such as metal, only high-end printers are capable to fulfill.
2. *Size limitation.* Because of a limited building area for 3D printing, large scale objects are often impractical due to the extended amount of time need to complete the build process.

Researchers have been working on improving 3D printing to overcome the mentioned drawbacks. Even though it is unlikely that 3D printing technology will obsolete the traditional manufacturing processes, it is still reasonably expected that 3D printing will play an increasingly important role in manufacturing as a complementing technology.

**Table 1-2. Comparison chart of additive and traditional manufacturing. Reprint with permission from ref. [46].**

<b>Process</b>	<b>principle</b>	<b>Specification</b>	<b>Advantages</b>	<b>Disadvantages</b>
SLS & SLM	Laser fusion in powder materials	Layers: 0.06-0.15 mm Features: 0.3mm Surface: rough Print speed: average	Strong Complex part, Large build volume, Parts can be stacked in build volume, Living hinges and snap features possible	Grainy surface finish
SLA & DLP	UV initiated-polymerization	Layers: 0.01-0.2 mm Features: 0.05mm Surface: smooth Print speed: average	Fine detail, Smooth surface finish	Weak parts, Susceptible to sunlight and heat
Poly-jet	Jetted droplets of UV cross-linked polymer	Layers: 0.016-0.032 mm Features: 0.2mm Surface: smooth Print speed: fast	Fine detail, High accuracy, Multi-material capabilities	Low material strength Susceptible to sunlight and heat
Binder Jetting	binding powder materials using binder	Layers: 0.05-0.15 mm Features: 0.4mm Surface: rough Print speed: fast	Multicolor prints, Fast print speed	Very weak parts Rough surface finish
FDM	Extrusion of thermoplastic	0.1-0.3 mm layers Surface: very rough finish, Print speed: slow	High part strength, Low cost	Poor surface finish Slow printing
Injection Molding	Material heated and forced into a mold	Surface: excellent finish Tolerance: 50 $\mu$ m	Broad material selection, High volume, High tolerance, Great surface finish	High start-up cost Long lead time Thin walled parts only
CNC Machining	removal of materials	Surface: smooth Feature: 25 $\mu$ m	All materials compatible, Very high tolerances, Reasonable turnaround	Difficulty with complexity, High equipment cost, Lot of scraps
Plastic Forming	Stretched and formed plastic sheets or tubes	Surface: smooth Tolerance: typical 1mm	Very large parts, Affordable price	Plastics materials only Limited shape complexity,
Plastic Joining	Welded or adhered plastic parts	Dependent on semi-finished products	Nearly all materials	Time-consuming, High labor cost

## 1.2 Review of functional materials/devices by 3D printing

Recently, the term “functional” is often used to describe the newly prepared materials/devices to indicate their potential for certain applications or to simply attach more importance to them. “Functional materials” are generally characterized as those materials that possess particularly native properties and functions of their own. Actually, almost every material could somehow be designated as a functional one and it is not possible to fabricate any materials with no any kind of functions or functionalities. Therefore, functional materials could be expressed as those being prepared by a target-motivated approach, that is, all their properties are adjusted and optimized to serve a specific purpose [47]. Because of their designed properties, a functional material can always work like a device to provide the required functions, for example, ferroelectricity, piezoelectricity, magnetism or energy storage. Thus, the mentioned “functional materials” and “functional devices” are often used interchangeably. For the purposes of this work, the term “functional materials” will be used in this dissertation to represent the combination of functional materials and functional devices.

To exhibit functions, a material has to present chemical or physical functionalities. For example, metals’ plasmonic properties at optical frequencies assume a particular importance in optical applications. Electro- and magnetocaloric materials which have energy storage and solar harvesting functions have a great potential for energy production. Therefore, although every material does exhibit some specific properties, it displays its function only when it is purposefully designed to possess specific properties. Two examples are the super-hydrophobic surface and “Eiffel Tower”. The former is usually realized through surface modification to create structures of micro and nano roughness, or hierarchical structures on a substrate **Fig. 1-13** [48]. It was found that the hierarchical structures can not only keep a high contact angle of droplet but also provide

an essential stability of the water-solid and water-air interfaces (the composite interface). Eiffel Tower is a notable example being hierarchically engineered structures [49], which can provide 2-3 times strength as strong as mild structural steel, although it has a relative density  $1.2 \times 10^{-3}$  times to that of iron. Recently, the functional materials have already been applied to a number of different areas, ranging from the personalized implants, more efficient and conformal cooling systems, or lightweight and cost-saving components for the aviation and automotive industry to bioprinting of tissues, electronics and sensors, and biologically inspired and shape-morphing materials [33].

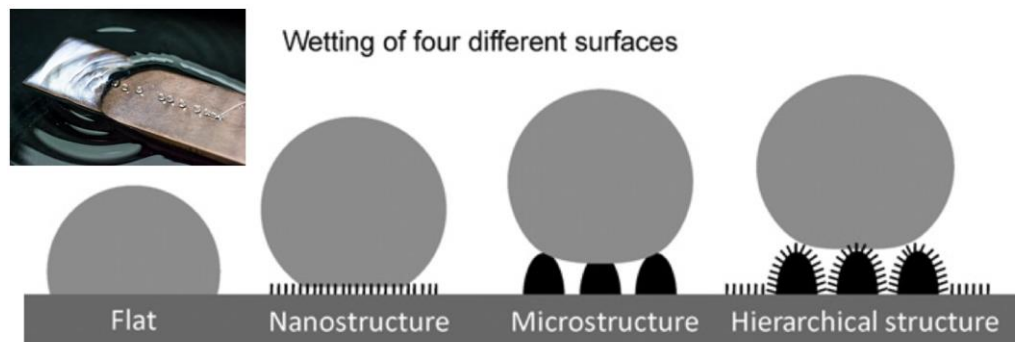


**Fig. 1-13. A typical example of functional materials realized by surface modification and structural design. Superhydrophobic materials are prepared by constructing micro/nano structures or hierarchical structures on the flat substrate. Reprint with permission from ref. [48].**

Accordingly, it should be noted that the realization of functions relies on the physical and chemical properties of the material itself, as well as the geometry of the structure. Therefore, a target-motivated approach to design and fabricate functional material is reasonable to include two main aspects: 1. the fabrication of functional materials base on the chemical modification of material which is in a microscale range, including material modification and surface modification; 2. the fabrication of functional materials based on the structural design which is in a relative macroscale range. In the following sections, I will review the current advancements of fabricating functional

materials including these two aspects.

### 1.2.1 Material modification enables the functions

A typical example of fabricating functional materials via modification of materials is the construction of metallic architecture by metal oxide. Among many established approaches to create metallic architectures, the most used methods are employing a high energy source (a laser or an electron beam) to directly bind the metal particles through either sintering or melting. Despite of a high effectiveness in producing metallic objects, the cost of preparing desired metal powder and the related equipment are always unaffordable. What is more, this approach is not suitable for oxygen-sensitive metals, such as copper. Therefore, although the established 3D printing approaches offer advantages of design and manufacturing flexibility and efficiency, they still suffer from numerous manufacturing limitations, in addition to being compatible with only a narrow range of materials.

Metal oxide powders are proposed to substitute the pure metal powders in 3D printing metallic objects because of their numerous advantages including reduced cost, availability in sub-micrometer size, and a lack of reactivity and pyrophoricity. A typical process is described in **Fig. 1-14**, where a metallic object is formed by ink-jetting 3D printing metal oxide and other metal components, and the subsequent reduction process [50]. This approach is based on the modification of materials and can greatly expand the variety of materials to other particle-based materials, such as ceramics and composites, as well as potentially yet-to-be-discovered advanced materials. It also demonstrates that the modification of printing materials shows potential to overcome the manufacturing shortcomings of the long established, energy-based and powder-bed printing approaches.

A similar situation happens to the 3D printing of ceramic functional materials. Because

of the hard machinability of this brittle material which is crucial for the processes by either casting or machining, 3D printing potentially offers a big leap in the fabrication of functional ceramics. However, the extremely high melting point adds challenges to 3D print ceramics when comparing with metals and polymers. The approaches that use a laser or an electron beam are restricted for potentially causing disadvantageous structures including enclosed, hollow, and tightly porous architectures because of the rapid sintering or melting process of material powders. Additional deficiencies include the need for expensive, energy-intensive equipment, slow building rate, significant thermal gradients during printing.

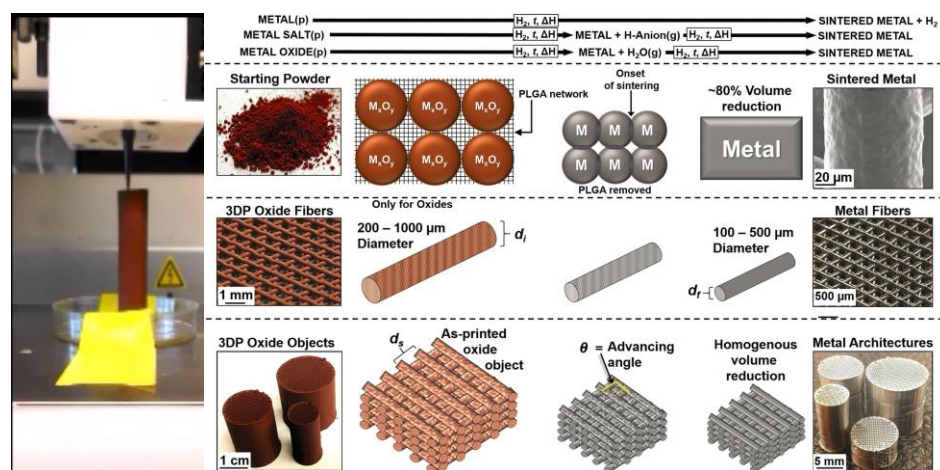


**Fig. 1-14. A modification of printing materials in the fabrication of functional materials. Traditionally used metal powder for energy-based and powder-based 3D printing is substituted by ink composed of metal oxide powder which is extruded by an ink-jetting 3D printing approach. The printed object is then reduced and sintered to form the final metallic architectures through  $H_2$  thermochemical reduction. Reprint with permission from ref. [50].**

The concept of polymer-derived ceramics opens an opportunity to 3D print ceramic in a more effective approach just by a modification of the printing material. Zak C. E. and his colleagues [51] developed a series of preceramic monomers which can be cured by

ultraviolet light in a SLA 3D printer. The resultant 3D polymer structures can possess very complex shapes and cellular architectures, which can be pyrolyzed to a real ceramic structure with uniform shrinkage and virtually no porosity. Typical experimental setup is described in **Fig. 1-15**. In their work, the modification of ceramic materials allowed the fabrication of ceramic by a SLA 3D printing, and significantly expanded 3D printed objects' ability by taking advantage of ceramics' impressive properties, including high-temperature capability, environmental resistance, and high strength, which have potential applications from the microscale—e.g., in microelectromechanical systems (MEMS)—to the macroscale—e.g., in propulsion or thermal protection systems.

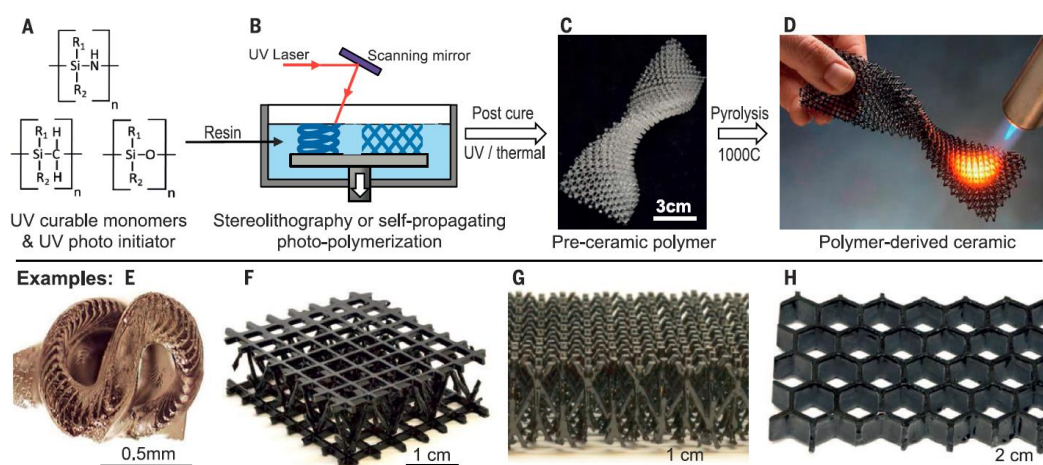


**Fig. 1-15. Stereolithography of polymer-derived ceramics. (A) UV-curable preceramic monomers are mixed with a photoinitiator to accomplish the modification of printing material. (B) the UV-curable resin is polymerized by exposure to UV light. (C) polymer structure is obtained. (D) the polymer is converted into a ceramic structure via pyrolysis. (E-H) examples of 3D printed ceramics by the described approach. Reprint with permission from ref. [51].**

Carbon materials, currently as one of the most popular materials for energy-related applications, are widely studied in 3D printing due to their good chemical stability.

However, the carbon materials themselves are not printable, because of their physical properties, such as agglomeration nature. Modification of the material is necessary to make it suitable for the 3D printing process. For example, it is critical to modify the materials to have a high viscosity and shear-thinning behavior for DIW.

Typically, the modification is usually conducted by mixing carbon materials as fillers, such as graphene oxide (GO), carbon nanotubes (CNT), carbon blacks, with solvent, pre-polymers and other additives. CNTs and carbon black require the assistance of polymers to adjust the ink viscosity to achieve proper printability, while GO has shown good printing capabilities with unique viscoelastic properties in aqueous solution, even without the addition of polymers to control the viscosity [52]. Wei et al. [53] demonstrated a method to 3D print graphene-based functional materials. A commercial FDM printer was used to produce conductive 3D carbon materials from a mixture of GO, acrylonitrile–butadiene–styrene (ABS) and poly (lactic acid) (PLA) (**Fig. 1-16**). This is one of the first attempts to directly print graphene related materials in a 3D fashion.

In another work, Zhu et al. [54] used DIW to fabricate periodic graphene aerogel microlattices which possess a ultralight property. To prepare the GO inks with suitable rheological properties for printing, gelation of concentrated GO suspensions was synthesized under basic conditions (for example, addition of ammonium hydroxide) and cross-linked using organic sol-gel chemistry (for example, in a resorcinolformaldehyde (R-F) solution), followed by the addition of hydrophilic fumed silica powders to impart additional increase of viscosity (**Fig. 1-17**). This approach enables one to fabricate graphene aerogels which are lightweight, highly conductive and exhibit super-compressibility (up to 90% compressive strain). Moreover, the mechanical property was improved significantly when comparing with the bulk graphene. For example, the elastic modulus of the graphene microlattice showed an

order of magnitude improvement. The modification of graphene materials enabled the 3D printing of functional materials in forms of complex aerogel architectures which have a broad range of applications.

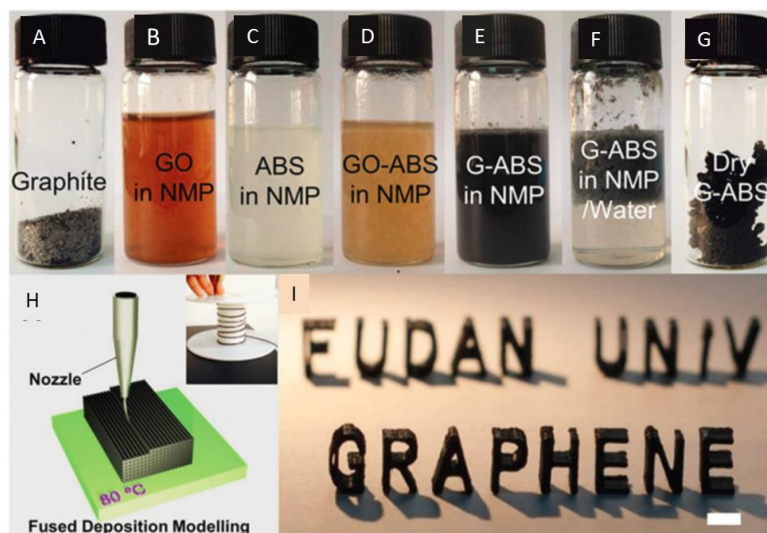


**Fig. 1-16. Modification of graphene materials for 3D printing. (A-G) Coagulation treatment by a chemical reduction of GO-ABS in a NMP solution or a hydrazine hydrate at 95°C for 1 h. (H) Schematic illustration of the FDM process of GO composite. Inset is a graphene-based filament winding on a roller. (I) 3D printed characters using GO composite as the filaments, scale bar: 1 cm. Reprint with permission from ref. [53].**

Brett G. et al. [55] reported a new epoxy-based ink for the 3D printing of functional cellular materials, which had a structure of multi-scale and high aspect ratio fiber reinforcement. Unlike the previous ink design which requires solidification via gelation, drying, or on-the-fly photopolymerization, this approach utilized the nature of epoxy of initially low viscosity and increasing viscosity with time to fabricate structures of high strength. This epoxy based ink can exhibit a desired viscoelasticity and a long pot-life at the absence or presence of highly anisotropic fillers. **Fig. 1-18** shows the DIW process of the modified ink and the printed wood-inspired functional materials of lightweight property. The elastic modulus of these materials exhibited an order of

magnitude improvement over those materials obtained by thermoplastics and photocurable resins developed by commercial 3D printing methods.

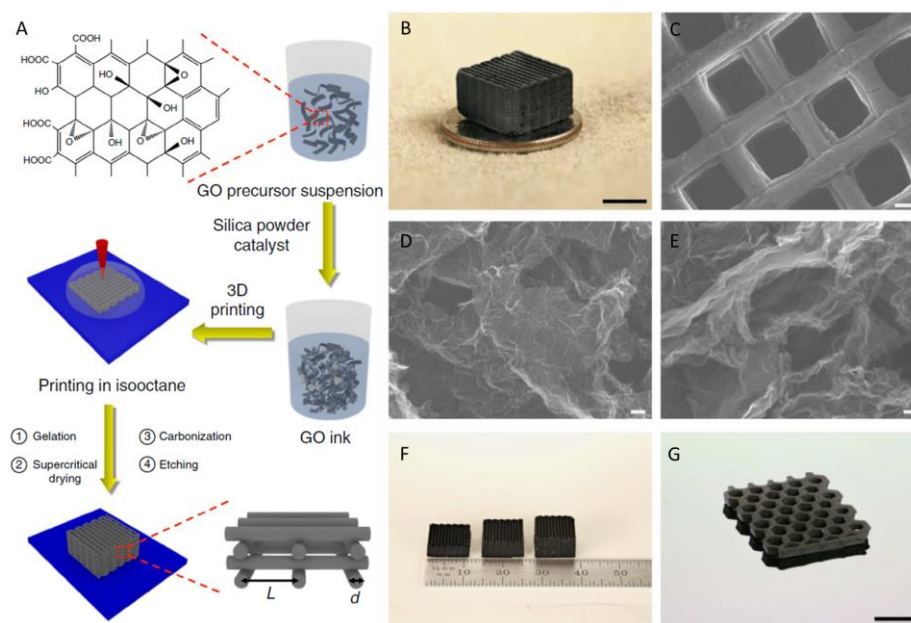


**Fig. 1-17. Fabrication of graphene-based microlattices through DIW. (A) Schematic illustration of a modification of GO-based ink and the following 3D printing process. (B-E) Optical and SEM images of a 3D printed graphene aerogel microlattice. (F) 3D printed graphene aerogel microlattices of different thickness and (G) 3D printed graphene aerogel honeycomb. Scale bars, 5mm (B), 200  $\mu$ m (C), 100nm (E, F), 1 cm (G). Reprint with permission from ref. [54].**

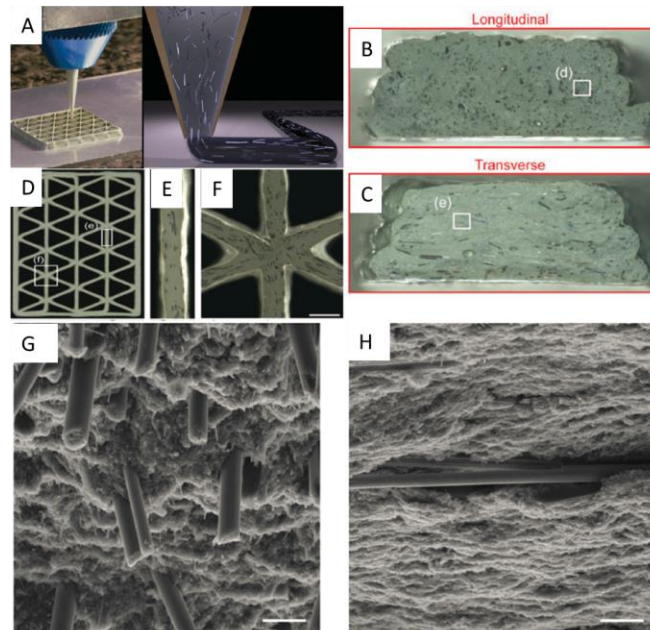


**Fig. 1-18. DIW of epoxy-based ink with high-aspect-ratio fiber fillers. (A) Illustration of the progressive alignment of high aspect ratio fillers during composite ink deposition. (B-C) Tensile fracture surfaces of longitudinally and transversely printed SiC/C-filled specimens. (D-F) A triangular honeycomb structure composed of SiC/C-filled epoxy, which has highly aligned carbon fibers oriented along the print direction. The scale bars in (E-F) are 500  $\mu\text{m}$ . (G-H) High magnification of fiber fillers in the printed specimen, scale bars: 20  $\mu\text{m}$ .**

**Reprint with permission from ref. [55].**

In conclusion, the above examples demonstrate that material's modification adds new dimensions of 3D printing, and enables the functional materials/devices to be built in a target-motivated route. However, certainly for all of the promises associated with the development of the printing materials, they currently remain in an insufficient state due to the lack of versatile modification methods and the specific compatibility with different 3D printing technologies. It is imperative to exploited more expansive 3D printable materials for the fabrication of functional materials of more novel properties.

### 1.2.2 Surface modification enables the functions

Except for the pre-modification, post-printing surface modification is another effective approach to add functions to the 3D printed objects. One of the main challenges for artificial functional materials/devices is to find the suitable materials to meet the crucial requirements in practical applications. Both the physical and chemical properties of the materials are of great importance for practical applications. Between the natural and synthetic materials, the latter are getting more attention because their parameters can be tuned to tailor the performance in terms of different requirements. To get the right choice of materials, it needs a thoughtful consideration of both physical properties and chemical properties, which can be tailored through either the material modification or the surface modification, it is therefore, beyond the structural integrity and mechanical properties, the surface properties are also crucial for the fabrication of functional materials/devices. An effective strategy is developing the printing structural materials along with post-printing surface modification, providing a highly-desirable, cost-effective and time-saving method for 3D printing.

Recently, various surface technologies were developed to endow the 3D printing capacity of fabricating functional materials/devices. E. Fantino [56] proposed a new method to obtain 3D printed polymer-based nanocomposites. The result provides a novel approach for the preparation of 3D conductive complex structures by coupling the photoreduction of metal precursors with the photopolymerization, resulting in functional materials with metal nanoparticles and organic polymers integrated together. Specifically, the 3D conductive structures were fabricated by adding silver salt to the UV-curable pre-monomers and exposing them to the UV light. As shown in **Fig. 1-19**, the UV irradiation provides an effective post surface modification to grow a layer of silver nanoparticles on 3D samples.

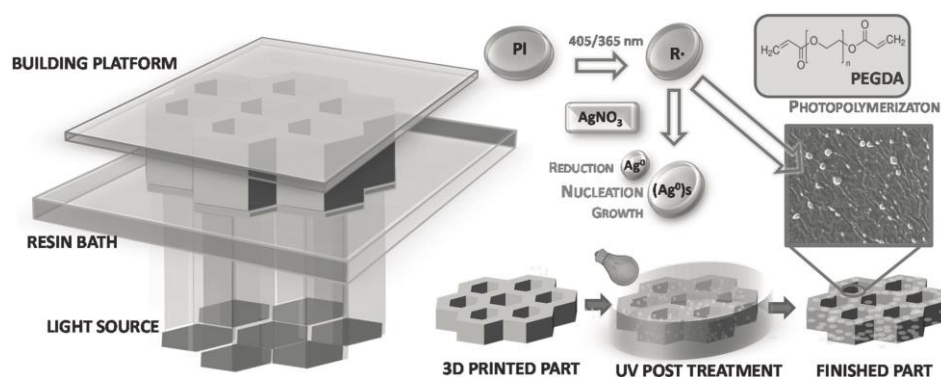


**Fig. 1-19. Experimental setup of 3D printing of complex conductive structures through post UV photoreduction. Reprint with permission from ref. [56].**

Based on this study, they also adopted the contemporary sintering to thermally reduce the silver nanoparticles. Firstly, 3D structures were printed by integrated metal salts in the starting formulation, which was exposed to a DLP 3D printing system. Secondly, the 3D printed object with silver salt embedded was conducted by a thermal treatment, in order to induce the in-situ generation of metal nanoparticles (NPs) in the polymer matrix. Both of the above post printing surface modification methods enable the 3D printed objects to have electrical properties. The in-situ thermal generation of the silver nanoparticles does not cause any negative effect on the stability of the polymeric structures, and also provides a possible alternative of the UV generation method.

Surface modification was also used to obtain ultralight magnetic materials, which can be applied to separate oil-water. As shown in **Fig. 1-20** [57], ultralight magnetic  $\text{Fe}_2\text{O}_3/\text{C}$ ,  $\text{Co}/\text{C}$ , and  $\text{Ni}/\text{C}$  materials were fabricated by pyrolyzing commercial polyurethane sponge grafted with polyelectrolyte layers. The ultralight materials consisted of 3D interconnected hollow tubes, forming hierarchical structures from macroscopic to nanometer length scales. More importantly, the wall thickness and morphology of the microtubes can be tuned by controlling the acrylic acid concentrations and the metallic cations. After surface modification with low-surface-energy polysiloxane, the ultralight materials present superhydrophobicity and

superoleophilicity, which can have an oil absorption capacity 100 times of the material's. This surface modification is also extendable to fabricate a variety of functional materials desirable for electrode materials, catalyst support etc., by controlling the composition and conformation of the grafted organic layers.

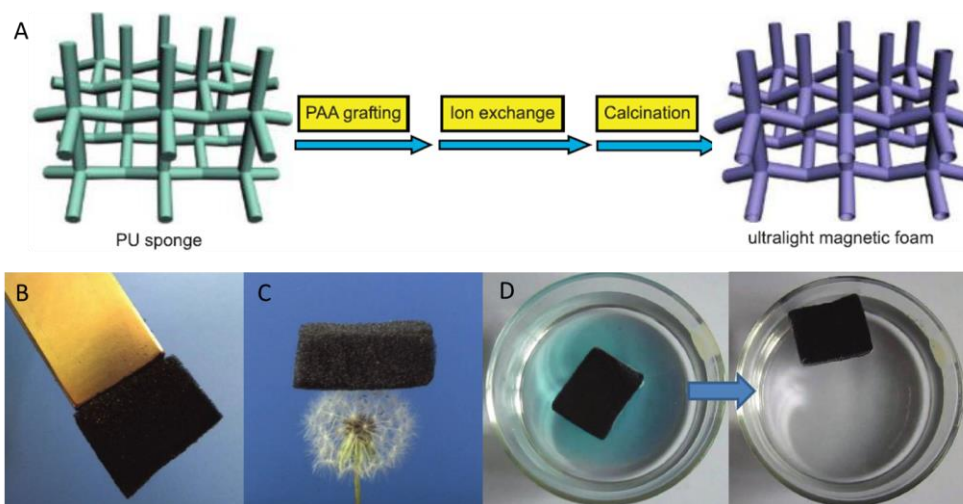


**Fig. 1-20. Surface modification of ultralight magnetic materials. (A) illustration of the fabrication from a polyacrylic acid-grafted polyurethane sponge. Resulted ultralight  $\text{Fe}_2\text{O}_3/\text{C}$  foam could be manipulated by a magnet bar (B) and stand on a dandelion (C). The superhydrophobic foam can be used to remove lubricating oil. Reproduced with permission from ref. [57].**

One of the main application of surface modification is to realize the metallization of plastic surface. Therefore, many latest studies have been reported to develop low-cost and environmentally friendly surface technologies to enhance the adhesion between metal coatings and the substrate. D. Chen [58] proposed a layer by layer electroless deposition method to fabricate adhesion-enhanced metallic coatings on plastic surfaces, by modifying the polymeric substrate to form surface-bonded active groups. Ag- and Cu-coated polymer materials were successfully prepared. Recently, to replace the high cost Pd catalyst in the conventional electroless plating process, palladium-free surface activation processes were developed [59-62]. Typically, these methods apply a semi-

interpenetrating polymer network film on the surface of the plastic materials, and then immobilize the catalyst to the pretreated substrate via N-Ni chemical bond, the grafted catalyst can initiate the subsequent electroless metal plating on the plastic substrate.

Beyond all doubt, the surface modification provides a robust method to endow the 3D printed objects with various surface properties. It is also believed that it is high-desirable, cost-effective and time-saving to print structural materials along with post-printing surface modification for 3D printing of functional materials. More importantly, surface modification will not only retain the desired bulk properties of printed architectures but also offer new functionality. However, all the surface modification methods described above are limited to serve specific applications. Each needs a specific design of the experimental setup. To the best of our knowledge, a 3D printed structural material, with a functionalized surface that can be easily modified, has been addressed rarely to date. X. Wang, et al. [63] developed a new polymerization-based 3D printing approach which was achieved by modifying the UV-curable resin to induce a generic post-printing modification for the printed objects. This initiator-induced modification provided the 3D printed materials with tunable surface properties. This feasible method was also expected to make 3D printed objects possible with a wide range of desired surface functions. It is, therefore, necessary to further develop this generic, versatile, yet simple approach to make 3D printable material subjectable to various surface modifications.

### 1.2.3 Structural modification enables the functions

Except to the effective modification of printing materials, structural characteristics also concerns significantly the construction of functional materials. The materials' architecture determines the mechanical properties and density, and can influence a wide range of other properties, e.g., acoustic, thermal, and biological properties. A typical example is the tissue engineering scaffolds, which must have both the appropriate

material and structures, not only allowing the relevant cell types to adhere and remain viable, but also directing the cell's behavior towards the characteristics of the appropriate tissue or organ [20]. Because all my work in this dissertation is focusing on the 3D printing of functional materials, and 3D printing is highly advantageous for tailoring the structural characteristic, I describe the structural modification as the design, optimization and fabricating of structural materials. In this section, I will review the field of structural design for functional materials with an emphasis on 3D printing of cellular materials, and discuss the recent developments of architected materials.

***Mechanics of structural design of functional materials.*** The mechanical properties of architected materials are determined not only by the constituent materials but also by the spatial configuration of void and solid, that is cellular architecture. By introducing certain ordered lattice-type cellular architectures, the functional materials can have nearly optimal force-distributing properties. **Fig. 1-21** [64] illustrates the influence of structural characteristics on the scaling of mechanical properties. At very low density, even small difference in scaling can result in a significant difference of mechanical properties, such as modulus and strength. Compared to the honeycomb and foam structure, the carefully designed octet truss can perform the best mechanical scaling of density. Therefore, a proper introduction of lattice type (i.e., stretching-dominate or bending-dominate lattice) can enable one to design materials with desired mechanical properties.

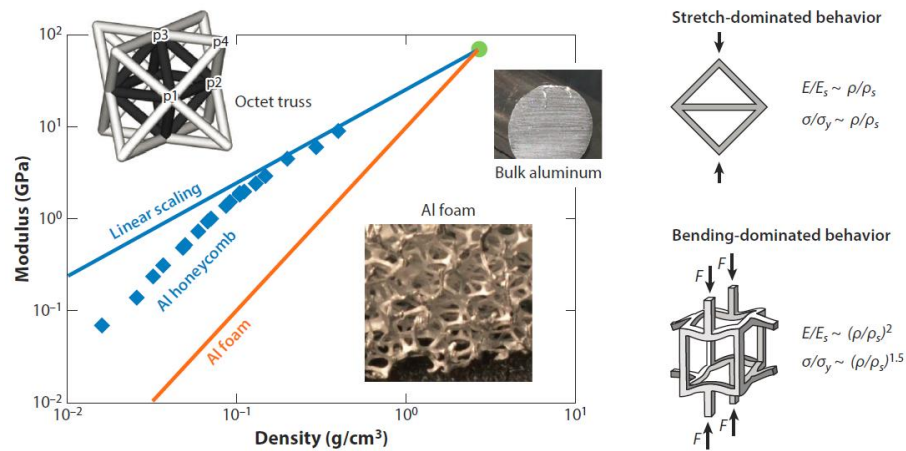


**Fig. 1-21. Influence of structural characteristics in the scaling of mechanical properties with density interpreted by stretching-dominated and bending-dominated behavior. Reprint with permission from ref. [64].**

Structures with sophisticated structural characteristics are difficult to be fabricated by traditional manufacturing. 3D printing offers new avenues to realize the fabrication of complex architectures. **Table 1-3** summarizes and compares the capacity of most common 3D printing approaches for fabricating architecture materials. According to the required functions, I will present the current advancements of structural modification as following.

**Functional materials of lightweight property.** In most cases where architected cellular materials are bearing a load, facesheets are attached to a robust lightweight core. Take a sandwich structure by attaching facesheets to a cellular material core for an example, the facesheets carry in-plane and bending loads, whereas the core structure carries transverse shear and transverse compression loads. The design that the core acts as a key component to separate the facesheets, provides the structure with a high area moment of inertia.

**Fig. 1-22** [64] shows some examples of sandwich panels with periodic cellular cores. The weight-to-performance benefits can be achieved using complex-shaped structural

cores with spatially graded properties. Design by a location-specific principle makes the structural core matched to the local loads, and also realizes a substantial weight saving with uniform density and properties. Currently, although honeycomb cellular architecture is the most widely used core material, lightweight materials with alternative core have been studied, such as tetrahedral and pyramidal truss structures which provide the most compelling properties of high effective strength [65]. Especially the recent arising of hollow truss structures offers an improved compressive and shear strength relative to honeycomb structures, due to the suppression of buckling. The complexity of lightweight structures is growing to satisfy the increasing structural, aerodynamic, and packaging requirements; however, it is also challenging the manufacturing. The emerging 3D printing technology now offers new avenues to fabricate structures that cannot be achieved with traditional processes, and offers advantages over conventional honeycomb or foam manufacturing with the ability to deliberately design net shape cores with complex curvature, or with graded cellular architectures.

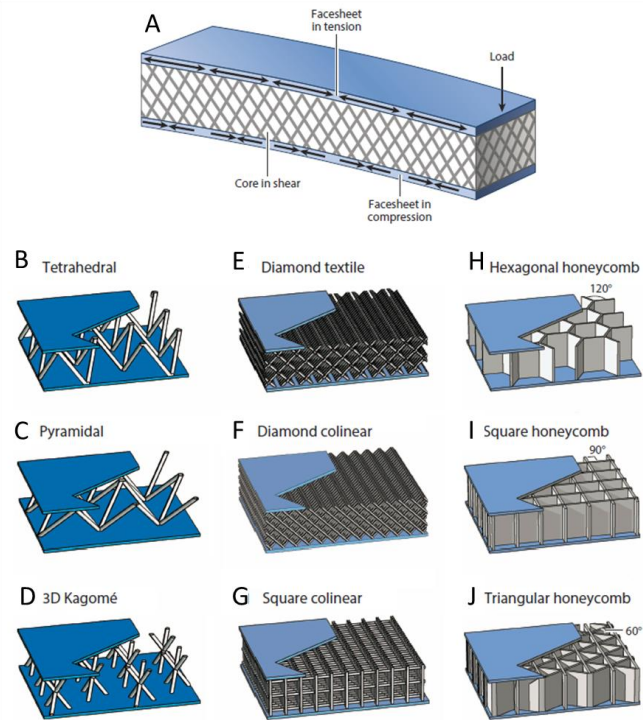


**Fig. 1-22. Examples of sandwich panels with periodic cellular cores. (A) Illustration of a sandwich panel used in lightweight design under loading. (B-J) examples of periodic cellular cores. Reprint with permission from ref. [64].**

**Table 1-3. structural flexibility of different 3D printing approaches for architecture materials. Approaches are listed with decreasing maturity from left to right. Reproduced with permission from ref. [64].**

3D printing Structural flexibility	FDM	SLS	EBM	Polyjet printing	SLA	Binder printing/ jetting	2PP	Wire or textile layup	Deformed perforated sheet lattice	Waveguide polymerization	Projection-Micro-SLA	DIW
Lattice type	Periodic or aperiodic	Periodic or aperiodic	Periodic or aperiodic	Periodic or aperiodic	Periodic or aperiodic	Periodic or aperiodic	Periodic or aperiodic	Periodic	Periodic	Periodic	Periodic or aperiodic	Quasi 3D
Arbitrary geometry	Yes, with support structure	Yes, with support structure	Yes, with support structure	Limited angle	Limited angle	yes	yes	Bonded wire only	Limited to lattice core	Limited to extend lattice	yes	Yes, with support structure
Minimum feature size	~250 $\mu\text{m}$	~200 $\mu\text{m}$	~200 $\mu\text{m}$	~100 $\mu\text{m}$	~25 $\mu\text{m}$	~150 $\mu\text{m}$	~2000 nm	~50 $\mu\text{m}$	~150 $\mu\text{m}$	~50 $\mu\text{m}$	~5 $\mu\text{m}$	~500 $\mu\text{m}$
Fabrication area	~0.5 $\text{m}^2$	~0.2 $\text{m}^2$	~0.2 $\text{m}^2$	~0.2 $\text{m}^2$	~0.5 $\text{m}^2$	~0.5 $\text{m}^2$	~0.005 $\text{m}^2$	~0.1 $\text{m}^2$	~1 $\text{m}^2$	~0.5 $\text{m}^2$	~0.03 $\text{m}^2$	~0.1 $\text{m}^2$
height	1 m	30 cm	30 cm	30 cm	30 cm	30 cm	1 mm	10 cm	10 cm	2 cm	0.1 cm	5 cm
Potential for graded properties	yes	yes	yes	yes	yes	yes	yes	limited	limited	yes	yes	yes
Application performance	prototype	Final part	Final part	prototype	prototype	Research material	Research material	Research material	Research material	Research material	Research material	prototype
Production rate	medium	low	low	Low	Low	low	Very low	medium	high	medium	low	low

**Functional materials for energy absorption.** Energy-absorbing materials are of extensive interest in protecting persons or structures from impulsive loads in automotive, sporting, and defense applications, due to their ability to lower the intensity of an impulse by extending its duration. To achieve an effective absorption, an intervening medium is required to reduce the initial impulsive pressure to a level below the damage threshold [66]. The medium material must be capable of large volume decrease at constant pressure, shown as **Fig. 1-23**. It is, therefore, the damage threshold or injury criterion that determines the maximum allowable stress transmitted through the energy absorber.

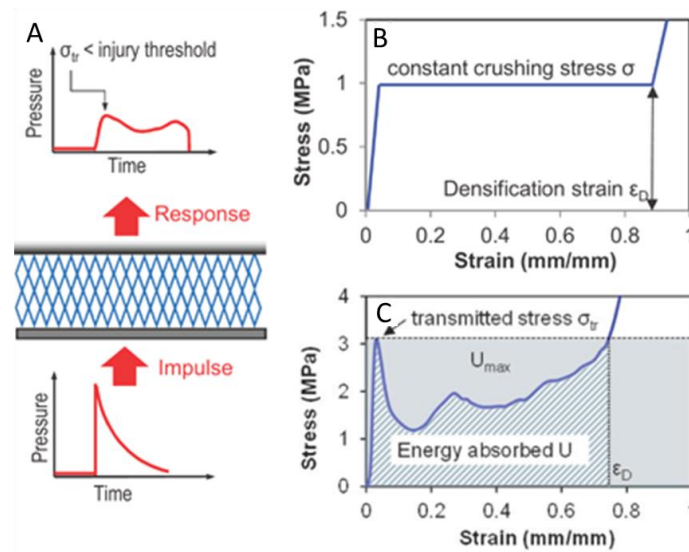


**Fig. 1-23. (A) Schematic illustration of the energy absorption performed by lattice structure which lowers the impulse intensity and eliminates the transferring pressure.**

**(B) The ideal response of a cellular energy absorbing material. (C) The actual mechanical behavior of a cellular lattice structure. Reprint with permission from ref.**

**[66].**

Although foams are the most used energy-absorption materials, emerging capability of well-

defined and ordered structures opens up opportunities to create energy absorption materials with highly desired properties [67]. The sophisticatedly designed materials with ordered structures consider fully the space limitations and lightweight-demand, which typically make a material capable to have the maximum energy absorption per unit volume and unit mass.

**Fig. 1-24** [64] compares the performance of a range of designed materials used as energy absorbers, including conventional metal foam and metal honeycomb, and the newly developed energy absorption materials of more complex architectures. The comparison results indicate that the architected materials present a new class of energy absorption materials which offer more flexibility in tailoring the response to impulsive loads than conventional materials. It is believed that, further optimization of architected materials, guided by numerical modeling and fabricated by flexible manufacturing like 3D printing, will provide more new generations of energy absorption and protection materials.

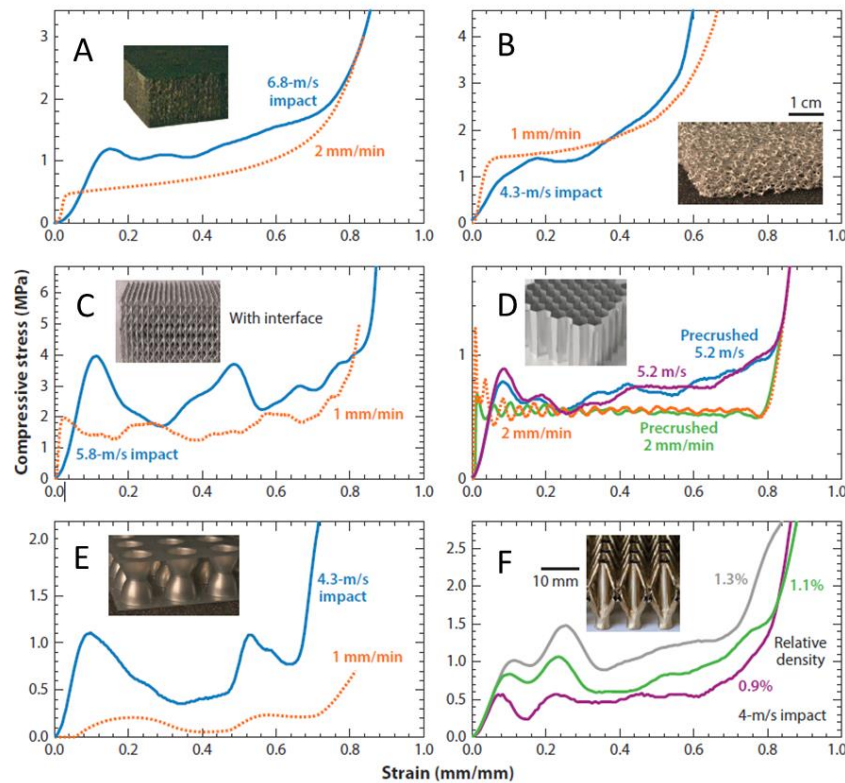


**Fig. 1-24. Comparison of energy-absorption performance of different materials. (A) Extruded polystyrene foam, (B) Open-cell Al foam, (C) Solid Al microlattice, (D) Precrushed Al honeycomb, (E) Thermoplastic polyurethane twin hemispheres, and (F) Hollow Ni microlattice. Reprint with permission from ref. [64].**

**Metamaterials.** Metamaterials are a new class of designed multiscale materials, for which the unusual physical properties are defined by the cellular architectures rather than compositions. Metamaterial has recently attracted significant interest within the research community because of its intrinsic capability of exhibiting unusual properties, such as thermal, acoustic, elastic, and irreversible nonlinear mechanical effects, which have a broad range of potential applications [68]. By tailoring the architecture, the properties of metamaterials can be rationally designed to achieve unprecedented properties. However, because the corresponding wavelength and length scale usually range from micrometer to

centimeter, the fabrication limitation is critical for the manufacturing [69]. The pentamode metamaterial is a typical example, which was proposed years ago, and has been realized only recently by 3D printing, shown as **Fig. 1-25**. This material was enabled to have a unique property like a fluid, which has a close to zero shear modulus; it also opened new possibilities in transformation acoustics [70].

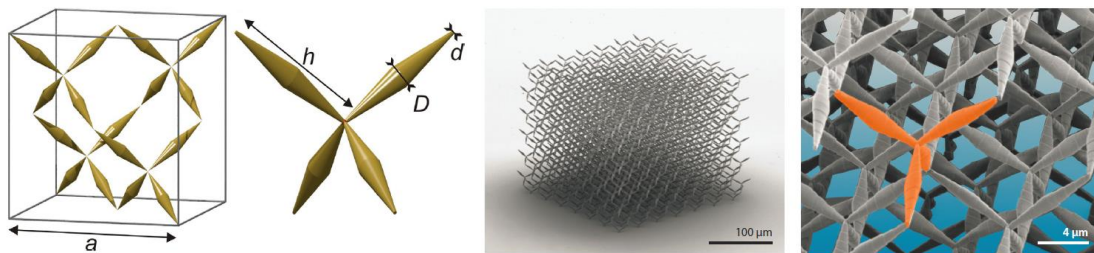


**Fig. 1-25. Illustration of the pentamode metamaterial ideal suggested by Milton and Cherkaev in 1995 (the artificial crystal with lattice constant  $a$  has diamond symmetry) and the first metallic penta-mode meta-material based on the same design and manufactured at Additive Manufacturing Laboratory of TU Delft using selective laser melting. Reprint with permission from ref. [70].**

In addition, rationally designed cellular architectures also enable the realization of mechanical metamaterials which exhibit reversible deformation by their architecture rather than by their constituent materials. For example, microlattices composed of extremely thin-walled hollow tubes buckle upon loading and recover upon unloading immediately [71]. A microlattice formed from brittle ceramic, as an example, is shown as **Fig. 1-26**, which demonstrates a slow, ductile-like deformation and a local shell buckling, resulting in a recovery after significant compression over 50%.

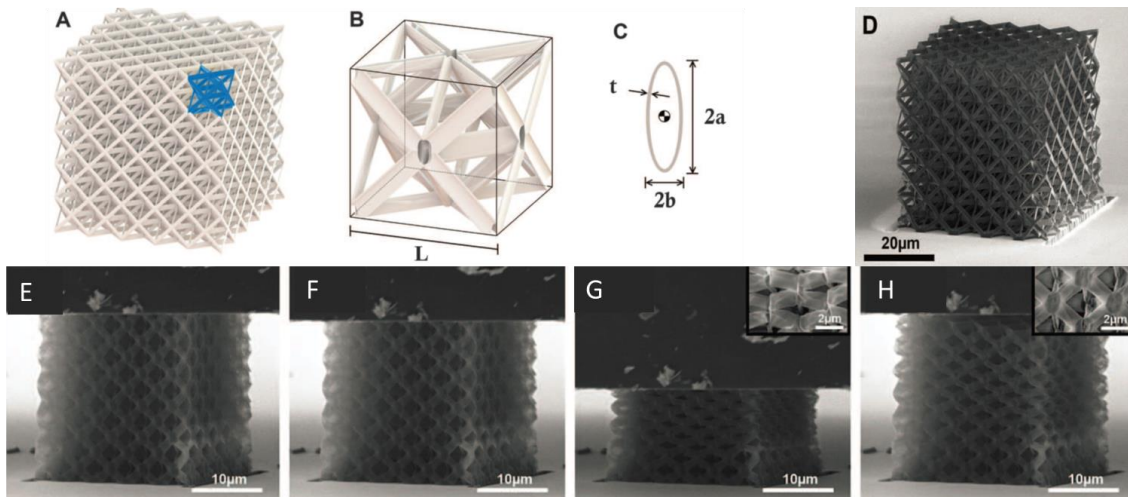


**Fig. 1-26. Architecture, design, and microstructure of alumina mechanical-metamaterial. (A) CAD image of the octet-truss design. (B) Cutaway of hollow octet-truss unit cell. (C) Hollow elliptical cross section of a microlattice tube. (D) SEM image of fabricated octet-truss microlattice. (E-H) Microlattice demonstrates a slow, ductile-like deformation, local shell buckling, and recovery of the structure after compression. Reprint with permission from ref. [71].**

Assisted by 3D printing, as well as theoretical and numerical analysis, researchers can exploit more material and geometric nonlinearities to add new properties to the metamaterials, for example, negative-Poisson's-ratio (NPR) behavior induced by an elastic instability [72].

**Functional materials for other applications.** Cellular and periodic materials also provide a function of heat exchange, especially when it is required to optimize multiple objectives, such as maximizing heat transfer rate and minimizing pumping energy input, temperature drop and mass. Because the architected materials can be designed with feature size in microscale, they have inherent advantages due to the fact that heat transfer per unit area scales inversely with characteristic channel width, and surface area-to-volume ratio increases with device size, allowing an enhanced efficiency per unit volume [64]. **Fig. 1-27** illustrates

examples of architected cellular materials used in heat exchange. In the future, synergies between maturing 3D printing techniques and the computational simulation for mechanics and fluid flow are expected to allow the architected materials with more improved performance [73-75].

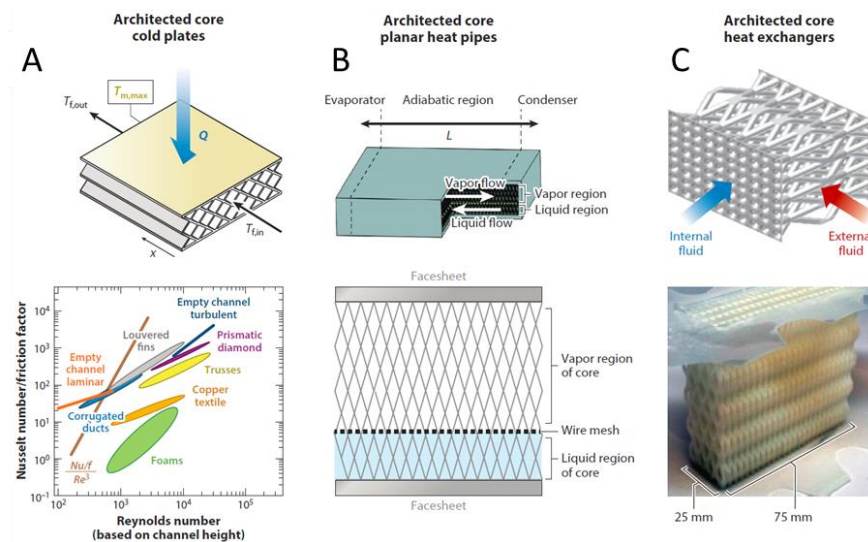


**Fig. 1-27. The performance of (A) cold plates, (B) heat pipes, and (C) heat exchangers can be improved by introducing architected cellular cores enabled by emerging additive manufacturing techniques. Reproduced with permission from ref. [73-75].**

Architected materials can also be applied as medical bioscaffolds which can be used to repair and implant tissues, cartilages and bones. In terms of tissue defect size, geometry and biological features, highly advantageous 3D printing offers the possibility to rapidly produce interconnected pore network for cell growth and flow transport of nutrients and metabolic waste, which are crucial to meet patients' specific requirements [76]. Since bioscaffolds, in addition to possessing a biocompatibility and suitable surface properties for cell attachment, also require proper mechanical properties to match the tissues at the implantation site, the architecture needs to be optimized rationally for medical application. **Fig. 1-28** shows an

example of optimized clinical scaffolds for breast reconstruction. The pore size and porosity can be tailored by controlling the density of seeding points in the creation of the tetrahedron mesh, as well as by choosing an appropriate strut thickness.

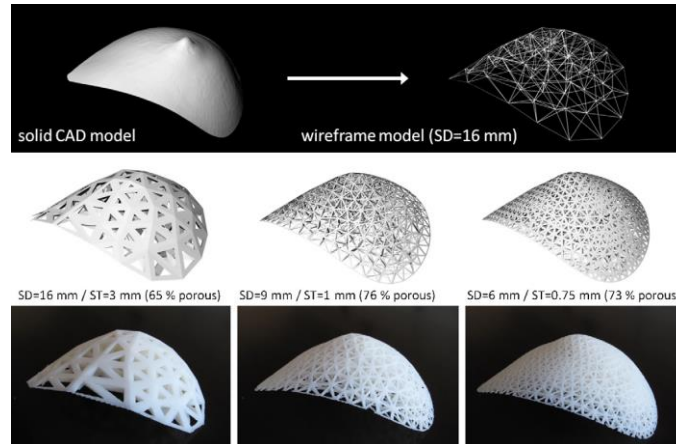


**Fig. 1-28. Architectural optimization of clinical scaffolds for breast reconstruction.**

**Reprint with permission from ref. [77].**

In conclusion, the recent advances in architectural design and 3D printing technology are giving a boost to the fabrication of architected materials. Fabrication of increasingly complex cellular architectures is enabled. Numbers of applications currently under research and developing are expected to be commercially available, and additional applications are bound to arise. Therefore, more breakthroughs of architected cellular materials in the future are expected to be yielded along with the new optimization techniques combined with increasing computational power, which is aiding the design of multiscale cellular architectures to fulfill multiple objectives.

### 1.3 Challenges, opportunities and objectives

Although there are lots of advantages and promise associated with 3D printing technology, it is still limited by the lack of material compatibility and functional fabrication capability. The development of 3D printing technology has reached a stage where we can say that it is able to 3D print a variety of materials including metals, ceramics, polymers, and composites, but it is still far from the point where expansive varieties of existing materials can be printed with ease. As stated in **Table 1-1**, each of the 3D printing processes has its advantages and disadvantages. Each method is only compatible with the fabrication using certain materials, whereas it may be completely incompatible with other materials. Especially, for metal based printing, the price is prohibitive for most of the users. It is for this reason why 3D printing has not yet become a fully revolutionizing industrial, research, and consumer technology.

Significant research and financial contributions are being invested to improve the 3D printing technology, such that they are incrementally better and compatible with more materials. A majority of the efforts are focusing on developing specific printing strategies together with many different material/ink systems, which is quite costly and time-consuming. In addition, current research is mainly working towards expanding printing capabilities targeting to 3D print an object to possess the same properties as that produced via traditional manufacturing. In this work, special attention is being given to employ 3D printing to assist the creation of new material systems with advantageous and unique functionalities specially enabled by 3D printing technology, so called “3D printing functional materials”. A comprehensive strategy is focusing on the developing of ‘all-purpose’ 3D printable materials along with surface modification to endow the materials of desired functions and properties.

Here, as an all-purpose 3D printable material, it is required the surface of the 3D printed parts by this material own the feasibility for various surface modification so that the 3D printed parts can be convert into functional materials/devices with novel or desired surface properties. Among all the probable approaches, integrating active components into 3D printing is proven to be a promising method to enable this all-purpose 3D printable material. Recently, 3D reactionware for chemical synthesis and analysis were allowed by integrating conductive carbon black and catalyst into the 3D printing material [78, 79]. Also, the integrating of Ag nanoparticles, as metal precursor allowed the fabrication of conductive 3D hybrid structures [56, 80]. All these are evident that the integrated strategy is capable of allowing all-purpose 3D printable materials to various application by simple selecting different additives as an initiator to work together with the present 3D printing materials. Particularly, a robust initiator that is versatile to induce various surface modifications is promising for it can induce a generic post-surface modification to in situ interested surface properties, thus it will improve the functionalization efficiency by avoiding the individual development for specific application. Therefore, we are aiming to developing a generic, versatile, yet simple approach by the integration of initiator to make 3D printable materials that can be subjected to various surface modifications.

Simultaneously, more attention will also be given to the design of material architecture due to the unlimited structural capability of 3D printing. With a proper structural design, material properties can be altered to form a meta-structure or meta-material, which can realize various desired properties and functions that are no existed in nature, and maximize the capability for target applications. Additionally, powerful computational tools can be incorporated to optimize structures for properties efficiency, allowing the best structural efficiency assisted by the additive manufacturing process.

Therefore, in this study, the research is particularly focused on the 3D printing of functional materials through a comprehensive strategy considering two incorporated aspects: modification of constituent materials through surface modification, and architectural improvement through structural optimization, summarized as **Fig. 1-29**. Upon further integrations, a whole spectrum of applications and functionalities based on these two leading aspects could be exploited.

Comprehensively, the strategy of 3D printing functional materials aims to produce materials with both desired chemical properties through proper post-printing modification and physical properties through structural design. Based on the established surface properties, a vast attention will simultaneously be given on structural design, thereupon, material properties can be altered throughout a part in such a way that the target application can be maximally enabled.

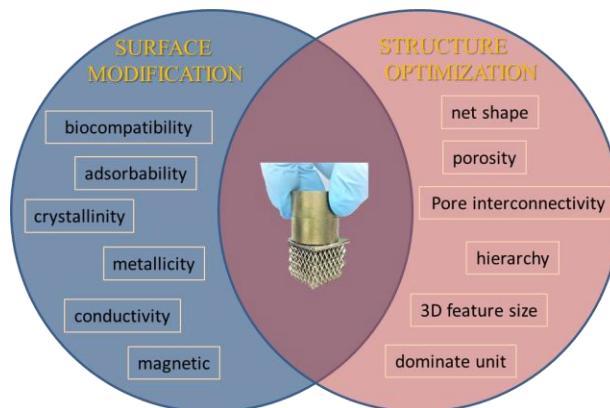


**Fig. 1-29. Graphical illustration listing several of the important material and structural characteristics that have a significant impact on the overall functionality of the 3D printed functional materials.**

## 1.4 Outline of the thesis

In what follows, the dissertation will be organized in an outline as:

In the current Chapter, we have reviewed the research background, the state-of-the-art of 3D printing technology, the working materials and current strategies of functionalization initiated by materials modifications, surface modifications and architectural optimizations, and finally, identified the research opportunities and objectives.

A reusable 3D porous adsorbing filter is demonstrated in Chapter 2 following the proposed functionalization strategy of surface modification and structural optimization. The filter was fabricated by integrating 3D printing technique with a natural adsorbent. It provides a low cost and highly effective solution for heavy metal removal. The function was established by using the 3D printing technology to achieve superiority in 3D porous geometric construction with a large surface area, and growing chitosan to form a “filter” for highly efficient removal of Cu(II) ion.

A robust material system—initiator-integrated printable material (i3DP I)—was further developed in Chapter 3 to serve for a wide variety of function demands. This material system is an improvement on the printed filter so that modifications do not need to be developed individually for specific applications. A bromine-containing acrylate was added into 3D printing resin, as an initiator, to allow polymer brushes to grow on the printed surface. The printed 3D structures can then be grafted with a variety of functional coatings and turned into useful devices with new functions or new structured metamaterial with novel properties, attributed to both their materials composition and structural optimization.

With the intention to apply the material system described in Chapter3, a functional magnetic

robot was developed in Chapter 4 with an effective spiral structure for application of remote controlling. The robot with Ni-rich magnetic coating was functionalized with a soft-magnetic property. The magnetic manipulation demonstrated that the ellipsoid robot was successfully magnetized, and could rotate synchronously with the magnetic field. The swimming properties under magnetic control are affected by the spiral shape, liquid viscosity and the controlling manner. The rotational movement can transfer efficiently to linear movement by carefully designing the spiral structure and the strategy of magnetic controlling.

In Chapter 5, metal-coated cellular materials inspired by the magnetic coating in Chapter 4 were prepared by using the initiator-integrated material. The strength-enhanced property was also investigated. The relationship between mechanical properties and structural characteristics, and the metal film's thickness was demonstrated. Two typical stretching-dominated lattices (octet-truss unit and pyramidal lattice), were exemplified to demonstrate the structural influence on the mechanical properties.

In Chapter 6 we step further towards the fabrication of metallic ultralight materials via the proposed strategy of surface modification and structural optimization. This strategy provides an effective platform for the optimized design of materials, which leads the materials with the best geometric parameters and desired mechanical performances. In this study, a series of ultralight metallic materials composed of 3D interconnected hollow tubes were fabricated to have features spanning three scale orders. The resultant materials can achieve an ultralight density of as low as  $5.1 \text{ mg/cm}^3$  and can nearly recover after significant compression over 50%.

In Chapter 7, the design and fabrication of mechanical-metamaterials were studied based on the results described in the previous two chapters. By combining the strength-enhanced

properties and fabrication of ultralight metallic materials, mechanical-metamaterials with tunable negative Poisson's ratio was fabricated. The subsequent measurement and theoretical analysis were utilized to demonstrate the fabrication flexibility.

We have so far always demonstrated a fixed material system which has been successfully applied in the studies in above chapters. In Chapter 8, we are focusing on developing a new generation of initiator-integrated material system (i3DP II) for the functional 3D printing. A bio-inspired initiator was introduced to prepare the 3D printable materials. Metallization of 3D printed objects was demonstrated to verify the efficiency. This newly developed material can simplify the functionalization process by omitting the nitrogen/argon protection because the functional layer of polydopamine comes from a natural oxidation process, and no critical condition is required.

In Chapter 9 we conclude the thesis and give perspectives on future research.

## Chapter 2

### 2 3D printing of reusable chitosan-coated filter for metal ions removal and structural optimization

In this study, a reusable 3D porous adsorbing filter was fabricated by integrating 3D printing technology and a natural chitosan, which is a low cost and highly effective biocompatible material for heavy metal removal. A facile two-step process was applied to graft functional chitosan brushes firmly onto the 3D filter. It uses the 3D printing technology to achieve 3D porous geometric construction with a large surface area, and uses surface modification to grow chitosan forming a layer of adsorbent for highly efficient removal of Cu(II) ions. XPS was utilized to monitor the fabrication process. Furthermore, spectrophotometry was conducted to investigate the adsorbability and desorbability. The results demonstrated that the 3D chitosan filter could provide a comparable capability of removing Cu(II) ions and had a great reusability. In addition, Fourier transform infrared spectroscopy (FTIR) was used to verify the role of functional groups,  $-NH_2$  and  $-OH$ , during the adsorption of Cu(II) ions.

#### 2.1 Introduction

Toxic heavy metal pollution has become a significant ecotoxicological hazard for ecosystem due to their accumulation in living organism [81, 82]. Especially with the rapid development of industries, the environment is suffering from increasing accumulation of heavy metals getting into water streams. This phenomenon is particularly severe in developing countries where they are dedicated to developing highly polluting industries

such as mining, metal plating, fertilizer and paper industries [83-85]. The treatment of heavy metals is of special concern and necessity due to the stringent regulations. Therefore, it is imperative to improve the efficacy of treatment to meet the increasing demand of heavy metal ions processing from industrial effluents.

The current methods for purifying the heavy metal contaminated aqueous solution include chemical, physical and biological treatments, such as chemical precipitation, ion-exchange, electrochemical treatment, membrane filtration and bio-adsorption [86-88]. Among all the possible methods, chemical precipitation is the most widely used technique in the industry due to its simplicity and economic benefit [82]. However, it is limited by generating large volumes of low-density sludge, and it also cannot coordinate the amphotericity for mixed metal ions. Furthermore, the sulfide precipitation can cause the evolution of toxic H<sub>2</sub>S fumes in acid conditions [89, 90]. Physical treatment involves material adsorption including activated carbon adsorbents [91], carbon nanotube adsorbents [92] and other porous materials [93]. Although it can offer flexible design and operation, its adsorption efficiency is over-dependent on the working environment, and the oxidation initiated by acid will decrease its adsorption capacities significantly [94, 95].

Biosorption has been proved as a new and promising process for heavy metal ion removal. It presents advantages in high effectiveness, inexpensive resources and its particularly outstanding biocompatibility [96, 97]. Typical biological adsorbents, such as living or dead microorganisms, can carry out heavy metal ions. Chitosan is an outstanding representative of natural bio-adsorbents for the removal of metal ions from wastewater [98, 99], and it is also an attractive biomaterial owing to its effective biological properties such as gene delivery and antibacterial activity. A typical process, which uses chitosan to remove metal ions, is performed by dissolving chitosan or chitosan derivatives in acidic solution,

followed by an ultrafiltration process after reacting with metal ions. Chitosan in this process, however, is usually for one-time use or requires complex processing to recycle, and the scaling up is very complex. In addition, it often suffers from blockage during the treatment of industrial effluents due to clogging effects [100]. Preconditioning, like de-agglomeration procedure, frequently requires to control the hydrodynamic condition. Thus, it will increase the complexity and incur a significant loss of adsorption efficiency [101].

An effective strategy to avoid clogging effect is to modify the chitosan chemically as chitosan derivatives or physically to be grafted or adhered on a support while maintaining the reactivity. Recent research has demonstrated that structured adsorbents, especially in the form of monolithic structures, have advantages of mass production, high stability, controllable pore structure and operational efficiency [102, 103]. Compared with the developed pellets and beads [104-106], an oriented porous structure can dramatically reduce attrition and pressure drop of the adsorption column, resulting in a more cost-effective adsorption process. However, the developed technology of a flow-through structure is still limited, which is often material dependent [107], thus inevitably limiting their availability.

The emerging 3D printing technology provides an effective manufacturing method for complex structural construction, enabling the optimal design of monolithic bio-adsorbent. Although developing a printable chitosan derivative is obviously tedious, simple modification of current 3D printing technology enables one to obtain both structural support with excellent porosity and functional surface with desired properties [108-110]. Recent research demonstrated success in producing functionalized materials/devices by simple modifications of current 3D printing technology allowing construction of intricate structures with functional surfaces [63, 111-113]. Taking advantage of 3D printing and

targeted surface modification, the 3D printed complex architectures can be converted into useful devices with new functions. It is, therefore, promising to employ and extend such hybrid 3D printing technique to fabricate a 3D chitosan-laden structure for heavy metal ion removal.

Herein, we developed an integrated strategy to make a reusable chitosan filter that can adsorb metal ions from solutions multiple times with an optimal structure design to maximize the surface area for adsorption. This integrated strategy combined the advantage of 3D printing for the optimal porous structure, and surface modification techniques for growing chitosan brush layers, which is completed by the epoxide-amine reaction between epoxide group and primary amine of D-glucosamine in chitosan [114]. By directly applying a coupling agent on the 3D printed materials, one end of the coupling agent ensures a good adhesion on the surface of 3D printed structure, while the other end is able to grow dense and uniform amino-polysaccharide molecular with primary amine functional groups via regio- and stereoselective ring opening of epoxides. A chitosan-laden 3D porous structure was finally fabricated, and the high content of amine and hydroxyl groups can take the role of adsorbing metal ions due to its polymer chelation properties. In this study, a water purification ‘filter’ was demonstrated with superiority of less diffusion resistance, high adsorption capacity and fast separation for large volumes of solution. Notably, this 3D printed purification-used cellular structure is potential to remove multiple heavy metal ions because of chitosan’s high content of amino and hydroxyl groups [100]. In this study, the removal of Cu (II) is taken as an example to demonstrate the filter’s capability and reusability.

## 2.2 Experimental setup

### 2.2.1 Materials

The acrylate-based UV-curable resin was purchased from Asiga. (3-Glycidyoxypropyl) trimethoxysilane (GPTMS,  $\geq 98\%$ ), chitosan flakes (85% deacetylated, 140000-220000 g/mol), (3-Aminopropyl) trimethoxysilane (APS) and Ethylenediamine-tetraacetic acid (EDTA) were supplied from Sigma-Aldrich.  $\text{CH}_3\text{OH}$  (anhydrous, 99.8%), Isopropyl alcohol (IPA) and  $\text{CH}_3\text{COCH}_3$  (99.8%) were purchased from Caledon. All chemicals were used as received except specially noted.

### 2.2.2 Fabrication of the chitosan filter

To prepare the polymer cellular structure, a customized 3D model was designed first using a CAD software (SOLIDWORKS). After slicing the CAD model to 2D layers, a DLP 3D printer (PICO2, Asiga) was used to create 3D structures by photo-polymerizing the resin in a layer-by-layer sequence until an entire 3D object was printed. Afterwards, the finished object was ultrasonically rinsed in ethanol for 10 min to avoid any resin and small molecule residual on the surface. Finally, a cylinder filter with a diameter of 20 mm and height of 15 mm was printed. To maximize the working area and water adsorption time, four structures were designed with close-arranged hexagonal holes (**Fig. 2-1A**), round holes (**Fig. 2-1B**), square holes (**Fig. 2-1C**) and hexagonal holes with a slight skewing between every 200  $\mu\text{m}$  layer (**Fig. 2-1D**), which can allow the fluid to have a better chance of contacting the surface. In this study, the minimum dimension  $a$  of the hexagonal hole was determined to be 300  $\mu\text{m}$  by the chitosan functionalization process (calculated as **Appendix S1**), which can be further decreased by lowering the viscosity and surface tension of processing solution if desired. According to the geometric relationship between these four structures, it is easy

to calculate the feature size of the rest filters.

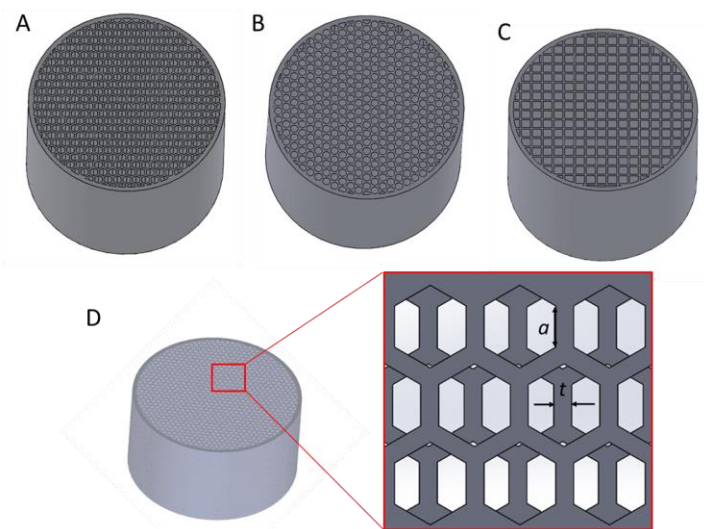


**Fig. 2-1. Models of 3D printed filter and the structural parameters. 3D printed filters were designed with close-arranged hexagon holes (A), round holes (B), square holes (C) and skewed hexagon holes (D). Inset illustrated the feature size.**

A layer of coupling agent was coated before grafting the chitosan brushes. Here we used epoxy-based silane, GPTMS, as the coupling agent to graft chitosan brushes through epoxide-amine reaction. Briefly, an alkali treatment was performed on the cleaned object by immersing into a 30% NaOH aq. solution at 60 °C for 5 min. This process is to prepare a hydroxylated surface for covalent bonding of -Si-OH group. Then, the sample was coated with a layer of silane by immersing into the coupling agent solution. The solution was prepared by dissolving 3 ml GPTMS into 6 ml IPA, 1 ml APS and 1 ml DI water. After that, the treated sample was air-dried and then post-cured at 100 °C for 20 min. Next, ultrasonic cleaning was performed for the deposited sample in IPA to remove the physically adsorbed molecules and impurities on the surface. The samples were then washed with DI water and finally dried in the air.

The immobilization of chitosan was carried out on the epoxide-derivative surface according to Lee's report [115]. Briefly, the treated sample was immersed into 2 wt% aqueous solution (PH~5) of chitosan and the water was evaporated slowly at 60°C overnight ( $\geq 10$  hours). The sample was then rinsed with an acid solution (PH~5) and DI water to remove polymers and impurities physically adsorbed on the surface.

### 2.2.3 Adsorption and desorption

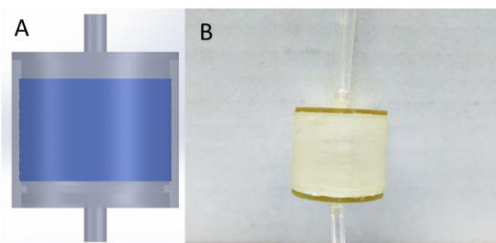


**Fig. 2-2. Schematic illustration (A) and experimental setup (B) of the chitosan-deposited filter**

To demonstrate the adsorption process, a metal ion removal device was assembled by integrating the treated filter into a 3D printed enclosure (**Fig. 2-2**). Cu(II) solution of 100 mg/L was prepared initially to investigate the concentration change before and after filtration. The initial pH was adjusted by using 0.1 M HCl and 0.1 M NaOH. The adsorption process was performed repeatedly as filtration cycles, and after each cycle, the Cu(II) concentration of filtered solutions was analyzed via UV/vis spectroscopy. The adsorbed amount of Cu(II) per unit weight of chitosan-coated material  $K$  was calculated from mass balance equation as follows:

$$K=(C_0-C_1)V/m \quad (1)$$

where  $C_0$  and  $C_1$  denote the initial and final concentration of Cu(II) respectively,  $V$  is the

volume of the passing flow of Cu(II) solution, and  $m$  is the weight of modified 3D structure.

For the desorption studies, EDTA aqueous solution (0.02 M) was used as an eluent to desorb the Cu (II) from the filter. The adsorbed amount is described above as a final concentration  $C_1$ , and the desorbed amount was determined by the concentration of Cu (II) ions  $C_2$  in the EDTA solution. The desorption ratio  $\tau$  was calculated by the decrement of Cu(II) ions from the filter. Moreover, to verify the reusability, this sorption-desorption process was repeated through the same chitosan modified filter.

Lastly, the desorption ratio  $\tau$  can be calculated as follows:

$$\tau = \frac{C_2 V_2}{(C_0 - C_1) V} \quad (2)$$

where  $V_2$  is the volume of the EDTA solution.

#### 2.2.4 Characterization

The morphology of the chitosan modified 3D printed sample was observed by scanning electron microscopy (SEM, Hitachi S-4500) at a 10 Kv accelerating voltage. XPS was conducted by using an Axis Ultra spectrometer (Kratos, UK) to obtain the chemical composition of the 3D object during each procedure. For the spectroscopy, a monochromatic Al  $K\alpha$  radiation resource was utilized with reference to a binding energy of C 1s at 284.8eV. Fourier transform infrared spectroscopy (FTIR, Nicolet 6700 FT-IR Spectrometer) was used to verify the grafting of polymer groups as well as to identify the functional groups involved in adsorbing Cu(II) ions. The presence of Cu(II) adsorbed on the surface of the cellular structure was detected by energy dispersive X-ray spectrometer (EDS).

## 2.3 Results and discussion

### 2.3.1 Working principle

**Fig. 2-3** describes the fabrication process of the chitosan-grafted 3D printed filter. Following the fabrication procedure, the commercial UV-curable resin was polymerized to be a highly cross-linked network, and was finally converted into a highly porous 3D structure via 3D printing. Subsequently, the -Si-OH functional group in the coupling agent was bonded to the substrate covalently. Afterwards, the outmost epoxide group of the coupling served as an initiator to grow chitosan via epoxide-amine reaction. Because of the formation of covalent C-N bonds between chitosan and the epoxy films, the epoxy-terminated surface was specifically modified. Finally, a chitosan-coated object with complex geometry was obtained.

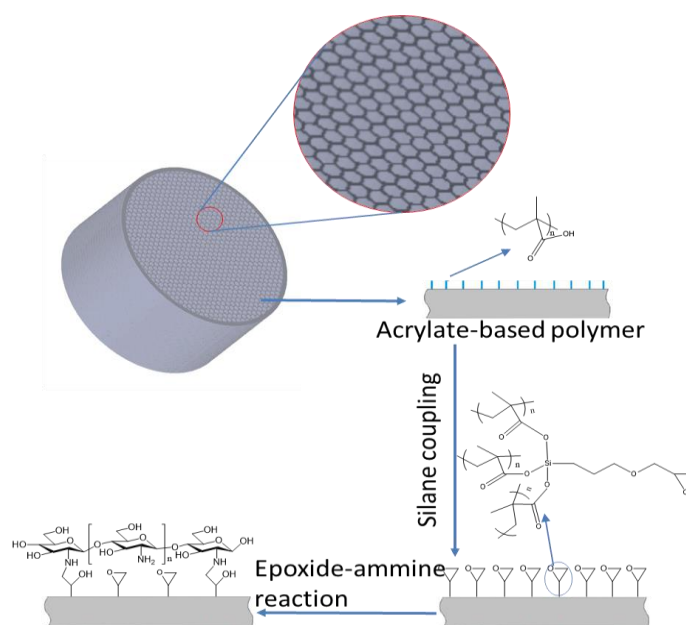


**Fig. 2-3. Schematic illustration of the fabrication of complex 3D architecture coated with chitosan for metal ion removal.**

SEM was used to demonstrate the morphology change before and after the deposition of chitosan. The morphology comparison of the untreated (**Fig. 2-4A and C**) and treated objects (**Fig. 2-4 B**) is evident that the surface of the original object immediately after printing is smoother, and distributed with small cavities due to the shrink during the polymerization process. While the crack shown in **Fig. 2-4E** indicates the deposited object was covered with a thin layer which is  $\sim$ micron thick and present in form of folding status (**Fig. 2-4F**). It is noteworthy that the crack of chitosan described here is an extremely individual phenomenon. The adhesion between the chitosan layer and substrate is strong enough to withstand the adsorption of metal ions which will be justified in later discussion.

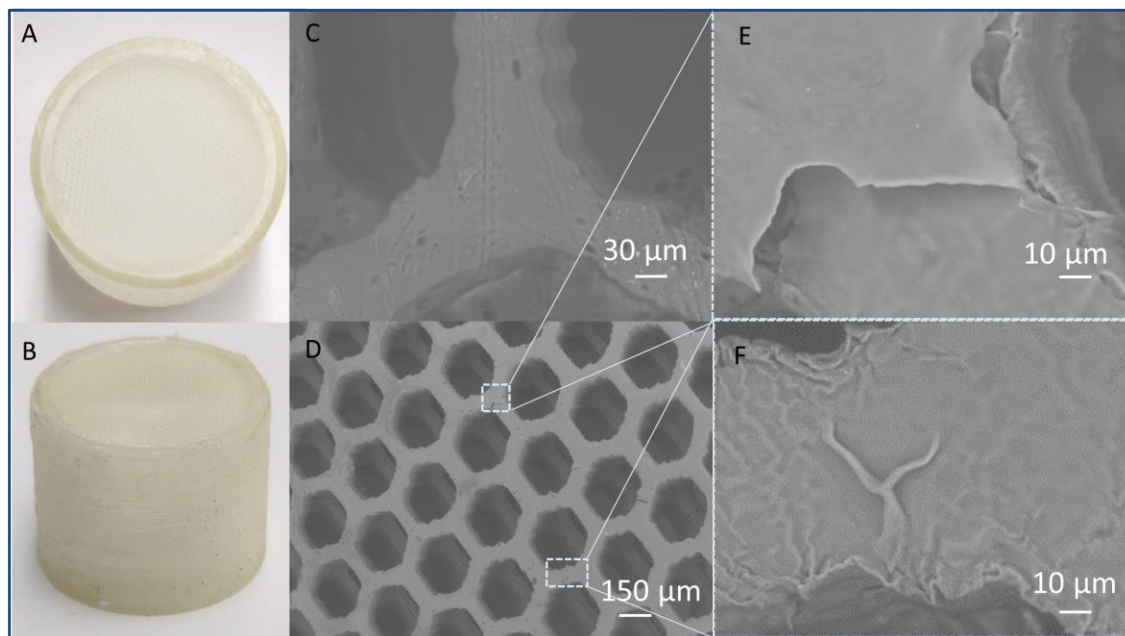


**Fig. 2-4.** SEM images show the change of surface morphology before and after the deposition process. Before deposition (A and C), the 3D printed object shows relatively smooth surface and with cavities distributed. After the deposition (B, D-F), a thin crinkly layer was produced.

### 2.3.2 XPS analysis

XPS was utilized to monitor the fabrication process from the original 3D printed object to the final functional material, as **Fig. 2-5**. As mentioned in **Fig. 2-3**, functional groups were attached to the acrylate-based substrate via a media of terminal epoxide moieties due to the silanization of GPTMS molecules. Obvious peaks of Si 2s and Si 2d show up after the reaction with a coupling agent containing GMTPS, and they are completely absent in the spectrum of the original object after printing, indicating the grafting of GMTPS on the surface. The deposited GMTPS enabled the outmost layer of epoxy groups to act as a medium to carry out the epoxy-amine reaction with chitosan. The signal of N 1s which presents at 396.35 eV and increases from 0.9% to 5.1% verifies the existence of amine groups, and indicates a successful formation of chitosan layer on the surface. In addition, the Si 2p signal also decreases sharply from 6.3% to 0.7%, due to the shroud formed by chitosan. All the evidence demonstrates a uniform and dense chitosan layer was deposited on the surface of 3D printed subject.

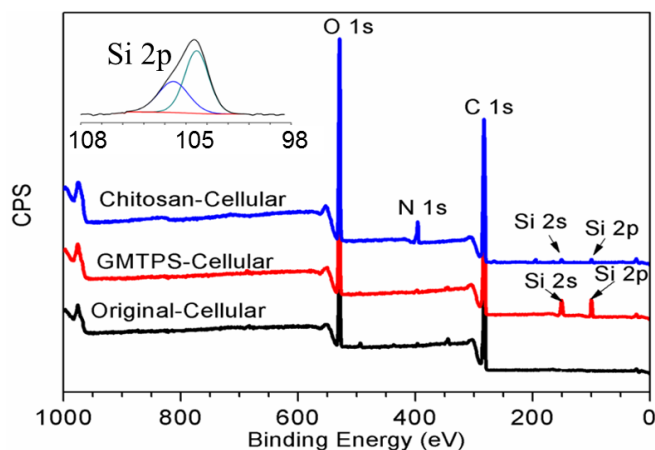


**Fig. 2-5. XPS survey spectra of 3D printed cellular before and after GMTPS grafting and subsequent deposition of chitosan. The inset is the Si 2p high resolution spectra of GMTPS grafted object.**

High resolution C 1s XPS (**Fig. 2-6A-C**) provides a more detailed insight into the chemical binding state before and after grafting of GPTMS. It is evident that the epoxy-modified surface shows a completely different spectrum from that of the acrylate-based substrate. The spectrum is fitted with four components: C-O which features intensely at  $286.5 \pm 0.3$  eV are ether moieties and epoxide rings respectively [116], and C-C/C-H peaks at 285.0 eV. The other two components (C=O/O-C=O) and the additional contributions of (C-C/C-H) are contributed to the acrylate-based substrate (**Fig. 2-6D**). It is noteworthy that, the susceptibility of C-O-containing material to X-ray exposure is the main reason for the underestimation of C-O peak area compared to theoretical data.

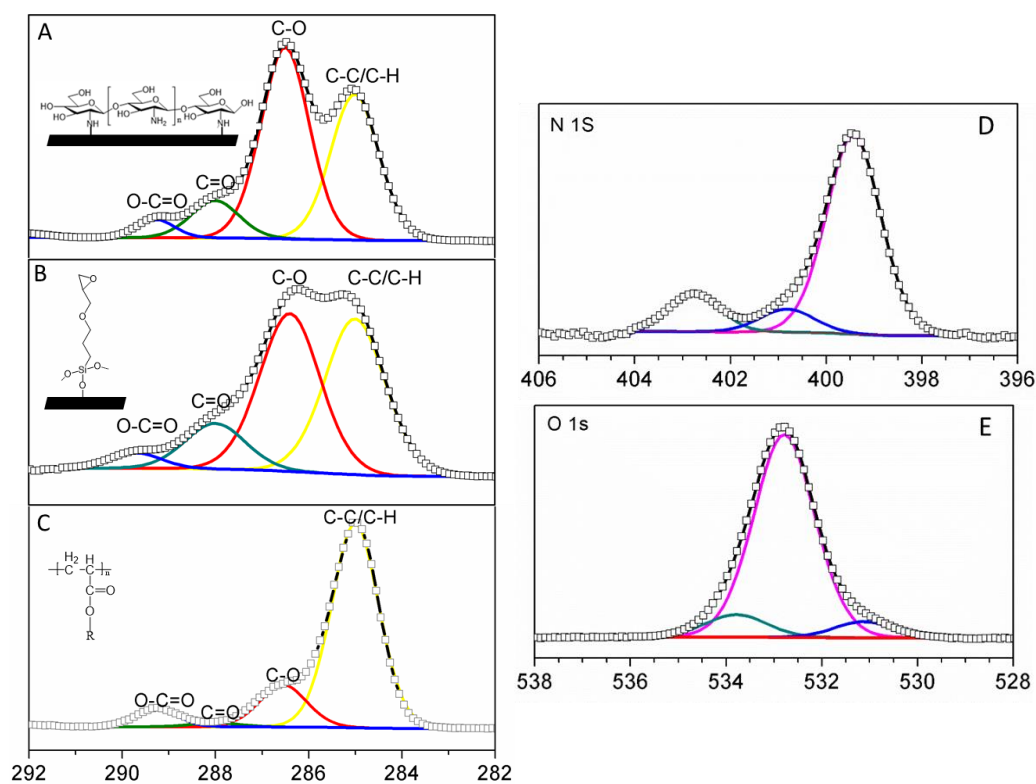


**Fig. 2-6. High-resolution XPS C1s spectra of original 3D printed cellular, GMTPS modified and final chitosan-modified cellular (A-C). Representative high-resolution XPS peaks of O 1s (D) and N 1s(E) in a chitosan-modified sample.**

In addition, the percent of Si and O which presents in a ratio of nearly 1:5 also verifies the successful integration of epoxy group onto the surface of the 3D cellular structure. Representative high resolution XPS of N 1s, O 1s and C 1s shown in **Fig. 2-6A, D and E** demonstrate the chemical binding state of chitosan. The spectrum of C 1s consists of three components: main component peaking at 286.5 eV indicates the single bond of C-O or C-N, while the smaller peak (284.8 eV) shows the typical bound of carbon and carbon to hydrogen (C-C/C-H). The smallest cover area near 288.0 eV is attributed to the acetal and amide groups. The major O 1s peaking at 532.5 eV represents the oxygen of polysaccharide backbone, whereas another peak at 531.0 eV is due to the amide of acetylated function. The N 1s XPS spectrum which consists of a main component at 399.5 eV and an affiliated contribution near 401.5 eV suggests the presence of non-protonated amine and protonated amine. Moreover, **Table 2-1** compares the theoretical and measured ratios between molar concentrations of elements and functions, and further verifies the success of chitosan grafting.

**Table 2-1. Expected and XPS measured molar concentration ratios of chitosan**

Elements	Theoretical	XPS data
N/C <sub>286.5</sub>	0.20	0.17
N/C <sub>288.0</sub>	0.84	0.83
O/C <sub>286.5</sub>	0.84	0.83
C <sub>287.7</sub> /C <sub>286.5</sub>	0.24	0.20
(O+N)/C <sub>286.5</sub>	1.04	1
(O+N)/(C <sub>286.5</sub> +C <sub>280.0</sub> )	0.84	0.84
C <sub>285.0</sub> /C <sub>total</sub>	0.3	0.32
N/C <sub>288.0</sub>	0.84	0.85

### 2.3.3 Adsorption and desorption

After the fabrication of chitosan-grafted filter, the efficiency of this material for metal ions

removal was investigated. In this study, a lab-made filtration device (**Fig. 2-2**) was used to remove the Cu(II) ions (the size of the filter was 20 mm in diameter and 15 mm in height). As shown in **Fig. 2-7**, the experimental setup was composed of two circulations. One was the adsorption by flowing the solution with high concentration through the functional filter. The other was the desorption process to desorb the metal ions from the filter by using an eluent solution. To test the adsorbability and reusability, each circulation was repeated according to the instructions prementioned. Both the adsorbability and desorbability were finalized by repeating the filtration process until there was no change of the solution concentration.

EDS was used to measure the existence of Cu(II) ions on the cellular structure. The change of concentration of Cu(II) ions in the solution was also detected through spectrophotometry. The EDS spectrum of each element after the Cu(II) ion removal was also conducted as **Fig. 2-8**. A Cu signal shows up in the sample (6.89 wt%) after the adsorption procedure, but was absolutely absent in the original chitosan-grafted sample. This EDS spectrum provides direct evidence for the adsorption by the material. EDS spectroscopy was also performed on the material after the lavation of EDTA, as shown in **Fig. 2-8B**, only a small amount of Cu(II) ions were residual on the material.

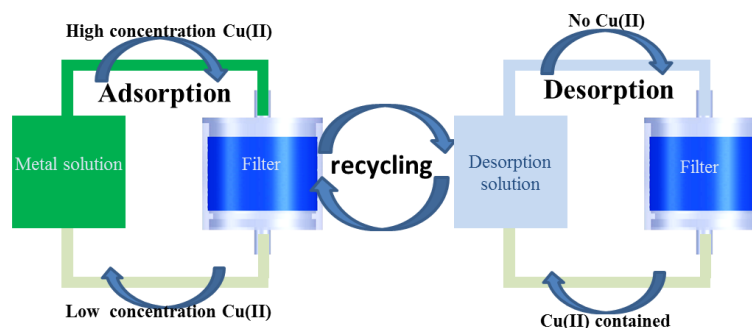


**Fig. 2-7. Schematic illustration of metal ion (Cu(II)) removal and adsorption-desorption repeating cycles.**

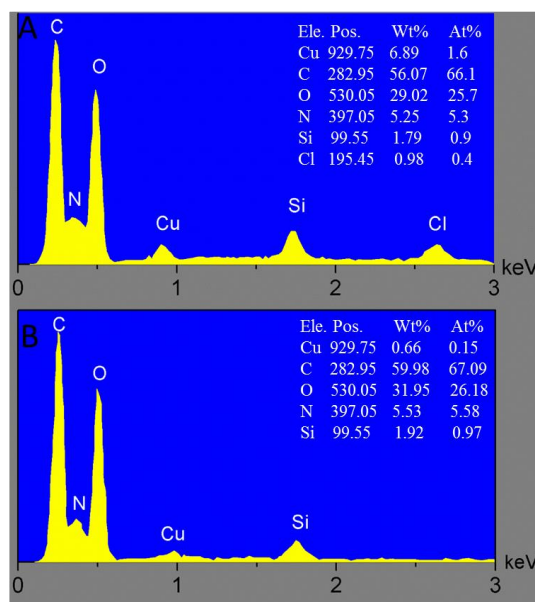


**Fig. 2-8. EDS of the desorption results by EDTA. (A) EDS data just after Cu(II) ions removal; (B) EDS data after desorption of EDTA.**

***Influence of temperature and pH.*** The adsorption experiments were carried out by passing 50mL of 100 mg/L Cu(II) solution through the filter with a pre-optimized flow rate of 0.12 ml/min. To optimize the adsorption process, we first investigated the effect of temperature and pH on the adsorption efficiency. Because the optimal temperature and pH do not change with filter's hole shape of, here, we take the skew-hexagon filter which has the largest porosity as the target object. The results in **Fig. 2-9A** shows that the Cu(II) adsorption on the chitosan-coated filter decreases from 92% to 75% when increasing the temperature from 25 to 100°C. This shows a great agreement with other reports [117, 118] and can be explained by the fact that the reaction of metal ion removal is an exothermic process due to the negative  $\Delta H^\circ$  values during the adsorption reaction [119]. The mobility of metal ions is expected to increase with the increase of temperature, resulting in desorption and dechelation from the adsorbent.

pH is one of the most important variables which affect the ionization and surface characteristics of the chitosan. The optimum pH for the adsorption of metal ions by chitosan and chitosan derivatives has previously been investigated, and was found in a range of 2.0 ~ 6.0 [120]. In this study, we investigated the optimum pH by adjusting the initial pH of the solution using 0.1 M HCl and 0.1 NaOH. It is noted that the temperature was kept at 25°C to eliminate the temperature influence according to the results above. The optimum pH was observed to be 5.5, as shown in **Fig. 2-9B**. The low adsorbability in lower pH range can be explained in two aspects. For one, the abundance of H<sup>+</sup> in the low pH solution may compete with the metal ions for the limited functional sites on the adsorbent. For another, the functional groups of chitosan-coated material are easily protonated and will be positively charged. Thus, the metal ions will show electrostatic repulsion to the material surface at low pH. And the fact that higher pH will neutralize or precipitate the metal ions and hydroxide will then adversely affect Cu(II) adsorption.

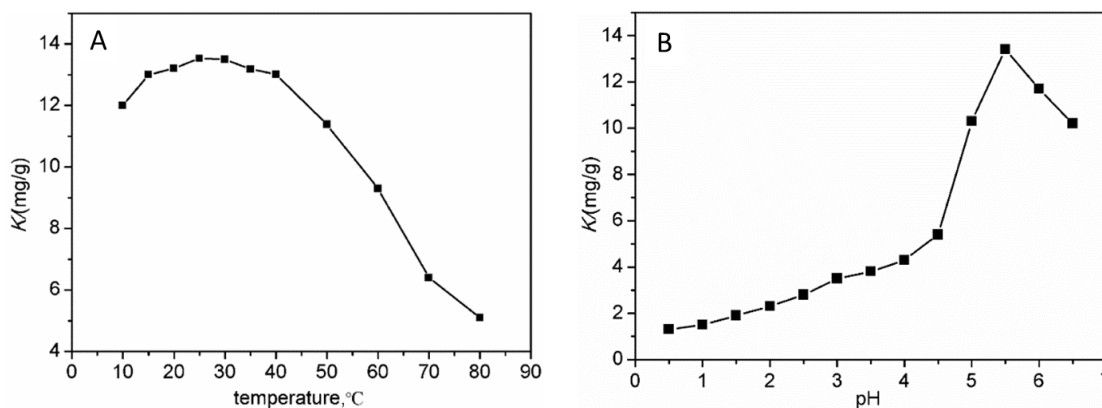


**Fig. 2-9. (A) Effect of temperature (pH = 5.5) and (B) pH on the adsorption (T = 25°C) of Cu(II) on the chitosan-modified 3D filter.**

**Adsorption kinetics.** The adsorbability with multiple filtration repetitions was investigated to find the optimum processing. **Fig. 2-10a** shows the measurement results under optimized

working condition of pH = 5.5, T = 25 °C. The removal capacity increased with the reaction time, and the adsorption rate slowed down with time elapsed until reaching a platform after 75 min adsorption. Thus, 75 min was selected as a preset time interval for studies on adsorption equilibrium in following. Compared with several hours for adsorption equilibrium reported frequently, this monolithic structure with oriented porosity has a fast adsorption kinetics indicating a high-performance adsorbent (**Table 2**). As shown in **Fig. 2-10a**, the equilibrium adsorption for Cu (II) is 13.7 mg/g of chitosan-coated filter, implying a universal practicability for heavy metal ions removal.

A comprehensive analysis of adsorption rates is helpful to guide the practical operation. Therefore, a quantitative kinetic analysis was conducted to get an insight of the adsorption rate and the adsorption mechanism. The pseudo-first-order equation (PFO, Eq.3) and the pseudo-second-order equation (PSO, Eq.4), which are the most frequently used in the kinetic analysis of adsorption, were adopted here to analyze the filter's performance.

$$\ln(q_e - q_t) = \ln q_e - k_1 t \quad (3)$$

$$\frac{t}{q_t} = \frac{1}{k_2 q_e^2} + \frac{1}{q_e} t \quad (4)$$

where,  $q_e$  and  $q_t$  are the adsorption capacities at equilibrium and at time  $t$  (min), respectively.  $k_1$  and  $k_2$  are the rate constant of PFO adsorption and PSO adsorption. Here, the rate constants  $k_1$ ,  $k_2$  and equilibrium capacity  $q_e$  were calibrated together to get a convincing evaluation result based on the correlation coefficient. And the deviation between the calculated  $q_e$  and experimental data was adopted to evaluate the preferred equation. According to **Fig. 2-10**, although both PFO and PSO describe the fast adsorption stage very well, PFO model can obtain a  $q_e$  closer to the experimental data than that from PSO model,

and evidently, gives a better fit for the experimental kinetic data.

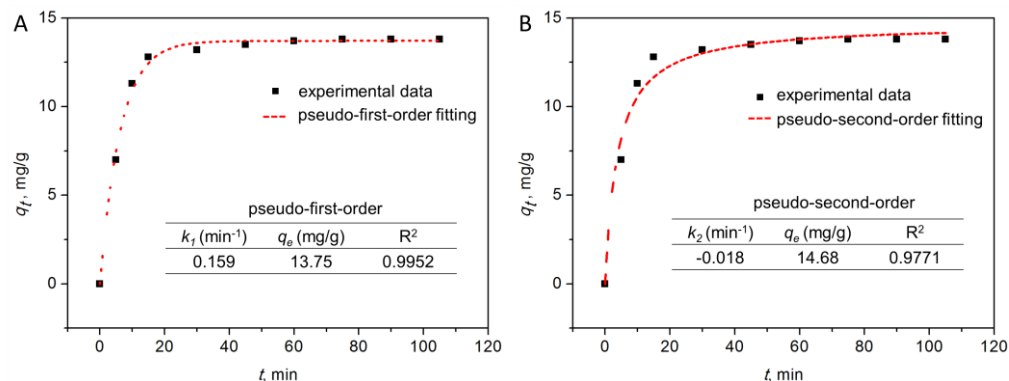
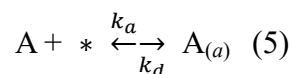


**Fig. 2-10. Comparisons of experimental and fitted results according to pseudo-first-order kinetics model (A) and pseudo-second-order kinetics model (B).**

Generally, the adsorption and desorption of adsorbates (denoted as A) in solution can be described as [119]:



$k_a$  is the adsorption rate constant, while  $k_d$  is the desorption rate constant, and  $*$  stands for the vacant site of the working material. According to Azizan's theory [121], this general equation can convert to either a PFO model at a high initial concentration of solute or a PSO model at a short contact time. The validity of the PFO may support the surface adsorption as a rate-controlling mechanism, for the initial concentration in our experiments was relatively high and the concentration change during adsorption was small. The initial adsorption rate can be calculated from  $k_1 \cdot q_e$  according to **Fig. 2-10a**, that the adsorption rate of Cu (II) is 2.2 mg/(g·min), indicating a superior adsorption kinetics compared with literatures [122-125].

Moreover, compared with the developed pellets and beads which have drawbacks of

complicate synthesis, low yield and technical complexity for adsorption, the 3D printed monolithic structure takes advantages of high yields, fast reaction and easy scale-up, leading to a more practical application in wastewater treatment. **Table 2-2** representatively compares the adsorption capacities of chitosan-based materials for the removal of Cu (II) from aqueous solutions. It is noted that, although chitosan takes up a weight proportion nearly two orders of magnitude lower that of other adsorbents, the 3D printed filter present a comparable equilibrium adsorption capacity, indicating a high advantage of working efficiency.

**Table 2-2. Comparison of adsorption capacities of chitosan-base materials for the removal of Cu (II) from aqueous solutions.**

Materials	Form	Q <sub>e</sub> (mg/g)	k <sub>1</sub> ·q <sub>e</sub> (mg/g·min)	Production / h	Reaction time	Reference
Carboxymethylated CS-bound Fe <sub>3</sub> O <sub>4</sub> nanoparticles	nanoparticles	21.5	20	~mg	1-60min	[126]
Chitosan-coated sand	particles	8.18	0.01	~mg	~24h	[127]
Chitosan-coated magnetic particles	Nanoparticles	35.5	-	~mg	~8h	[128]
CS-MWCNTNH	membrane	12.89	9.9	~mg	~24h	[129]
N-HAP/chitosan	microparticles	113	0.57	~mg	~24h	[118]
CS- filter	monolithic structure	13.7	2.2	g - kg	75 min	This study

**Adsorption isotherms.** A serial of adsorption equilibrium experiments were further conducted at the optimal working condition to establish the relationship between the adsorption capacity and Cu (II) concentration, as shown in **Fig. 2-11a**. The experimental data were then used to fit the Freundlich (Eq.6) and Langmuir isotherm model (Eq. 7), which are the most frequently used isotherm models, as **Fig. 2-11b**.

$$\ln q_e = \ln K_F + n \cdot \ln C_e \quad (6)$$

$$\frac{C_e}{q_e} = \frac{1}{q_m b} + \frac{C_e}{q_m} \quad (7)$$

where  $q_e$  (mg/g) is the adsorption capacities at equilibrium,  $C_e$  (mg/L) is the Cu (II) concentration at equilibrium,  $K_F$  (L/mg) is the Freundlich constant,  $n$  is the heterogeneity factor.  $b$  (L/mg) and  $q_m$  (mg/g) are the Langmuir coefficients, indicating an adsorption equilibrium constant and a monolayer capacity, respectively. Freundlich model describes the adsorption on an energetically heterogeneous surface where the adsorbed molecules are interactive, while Langmuir model interprets a monolayer adsorption on an energetically uniform surface where the adsorbed molecules are not interactive [119].

All the calibrated results are listed in the **Fig. 2-11a**, and the fitting behaviors are described as **Fig. 2-11b**. It is found that the adsorption of Cu (II) fits the Langmuir model better than the Freundlich model, the former presents a square error  $R^2$  as  $> 0.99$ , while the latter is just  $\sim 0.90$ . The reason for the better agreement with Langmuir isotherm model lies in: 1. the dominant interaction for adsorption is a short-range interaction same to chemisorption; 2. the active sites on the filter distribute homogeneously.

**Desorption and reusability study.** For the desorption process, EDTA (0.02 M) was used as the chelating agent to desorb the metal ions from the filter. According to **Fig. 2-12a**, it was found that, due to the high chelation ability to metal ions, EDTA can desorb  $> 90\%$  desorption of Cu(II) ions from the filter after 15 min, and finally obtains the maximum desorption capacity of 92%. What is more, the used EDTA can be further recycled after the precipitation of the metals by a well-established procedure using combination of  $\text{Na}_2\text{S}$  with  $\text{Ca}(\text{OH})_2$  [130].

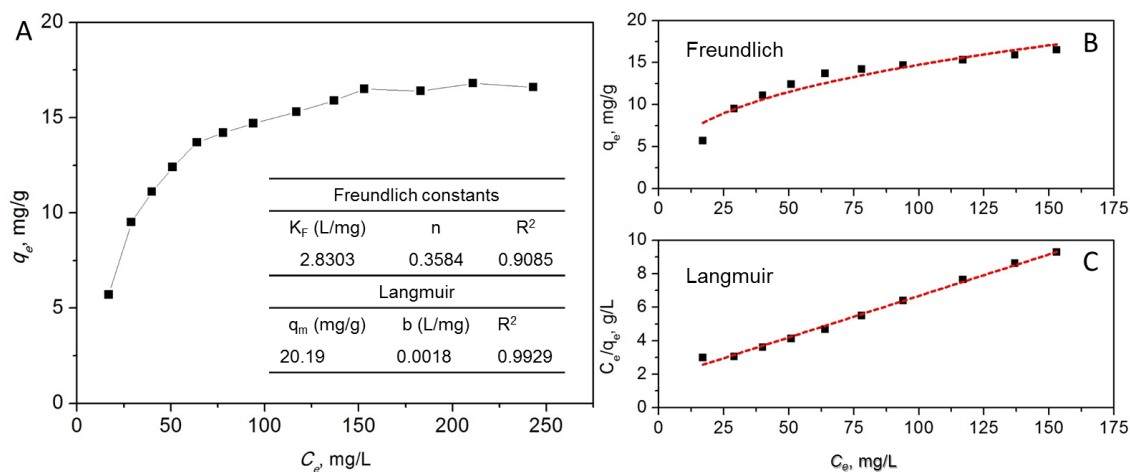


**Fig. 2-11. Adsorption isotherms of Cu (II) by chitosan-coated filter (A), and the Freundlich (B) and Langmuir (C) isotherm plots.**

The adsorption–desorption cycles were performed to investigate the potential of chitosan-coated filter for real applications. **Fig. 2-12b** shows the reusability of the chitosan-modified filter. It is clear to see that the material presented the best adsorption during the first filtration and the efficiency become steady from the second filtration. The efficiency of desorption remains around 91%, indicating that there are still metal ions residual on the filter after the desorption, and the saturation of ions adsorbed onto the limited functional sites will limit further adsorption. Therefore, the following filtration can present a relatively constant adsorbability from the second adsorption. **Fig. 2-12b** shows the adsorbability  $K$  of a filter decreases slightly from an initial adsorbability of 13.7 mg/g to around 11 mg/g in the following 4 repetitions of the absorption-desorption process and then keeps relatively steadily, which is also comparable with the other adsorbents. Also, the surface change before and after the five adsorption-desorption cycles was compared to verify the durability of this chitosan-loaded surface.

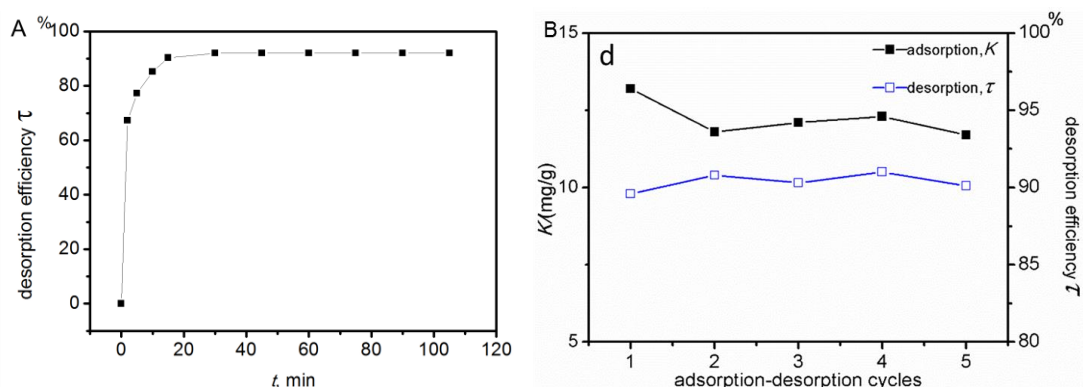


**Fig. 2-12. (A) Desorption capacity of EDTA to the Cu (II), T=25°C, pH=5.5. (B) Reusability profile of the chitosan-modified material in adsorption and desorption repetition with the optimum working condition (T=25°C, pH=5.5)**

As shown in **Fig. 2-13**, the chitosan layer has no obvious change after cycles of purification because the covalent C-N bonds between chitosan and the epoxy films are strong enough to withstand the dissolution at acidic condition, leading to a robust adsorption performance.

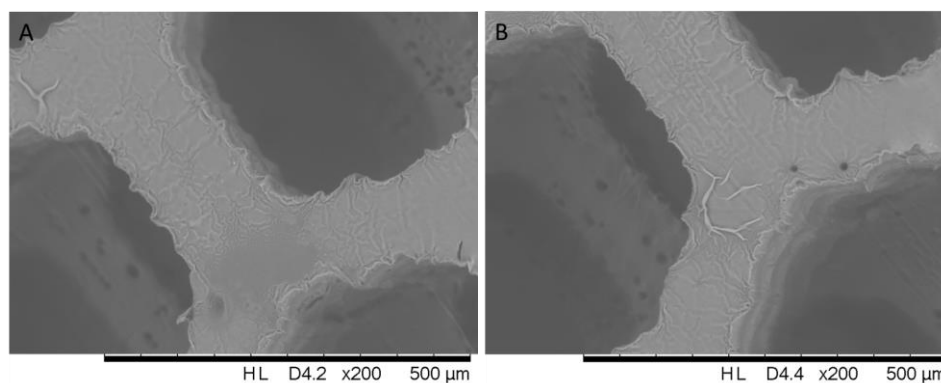


**Fig. 2-13. SEM images of the chitosan-loaded surface before (A) and after five adsorption-desorption cycles (B).**

**Structural influence on the adsorbability.** The adsorbability is expected to increase with filter's porosity. To verify the assumption, we repeated the adsorption experiment on the filters of four hole shapes. For each filter, three samples were prepared to get the average

maximum adsorbability. Briefly, all the filters were tested by passing Cu(II) solution of 100 mg/L. And the temperature and pH were kept at the optimum conditions  $T = 25\text{ }^{\circ}\text{C}$ ,  $\text{pH} = 5.5$ , respectively. **Fig. 2-14** shows the filter of skew-hexagon holes provides the largest adsorbability of 13.2 mg/g, while the filters of round and square holes can only reach to 9.3 mg/g and 9.8 mg/g, respectively. The results present a positive correlation with the filter's porosity, and verify the assumption that the adsorbability increases with filter's porosity. That is because the effective area increases with the porosity, and results in a proportionate increase of the working chitosan.

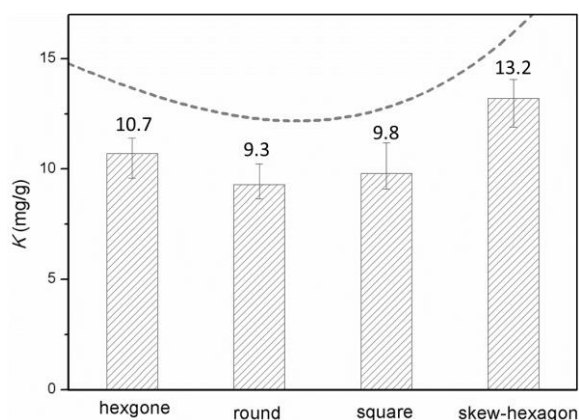


**Fig. 2-14. Comparison of adsorption capacity of filters with different hole shapes ( $T=25^{\circ}\text{C}$ ,  $\text{pH}=5.5$ ).**

#### 2.3.4 Mechanism analysis

FTIR analysis was conducted to analyze the mechanism of metal ion adsorption, and confirm whether it is the amine and hydroxyl groups that work to adsorb the metal ions, and then eliminate the possibility of physical absorption. **Fig. 2-15** shows the FTIR spectra of the chitosan-coated sample before and after ion adsorption. It clearly shows that the -N-H peak at  $1630\text{ cm}^{-1}$  shifts to  $1614\text{ cm}^{-1}$ , and  $3420\text{ cm}^{-1}$  shifts to  $3370\text{ cm}^{-1}$  after the absorption of Cu(II), indicating that  $\text{NH}_2$  plays a role in adsorbing metal ions. Furthermore,

a new peak also appears at  $1324\text{ cm}^{-1}$  in the spectrum of the sample after Cu(II) adsorption, which presents the characteristic band of the association between chitosan and Cu(II). Since the peak of  $1324\text{ cm}^{-1}$  corresponds to C-N stretching vibration [131], the Cu(II) adsorption is implied to affect the bonds of the N atom. All these evidences verify that -NH<sub>2</sub> and -OH are involved in the adsorption of metal ions.

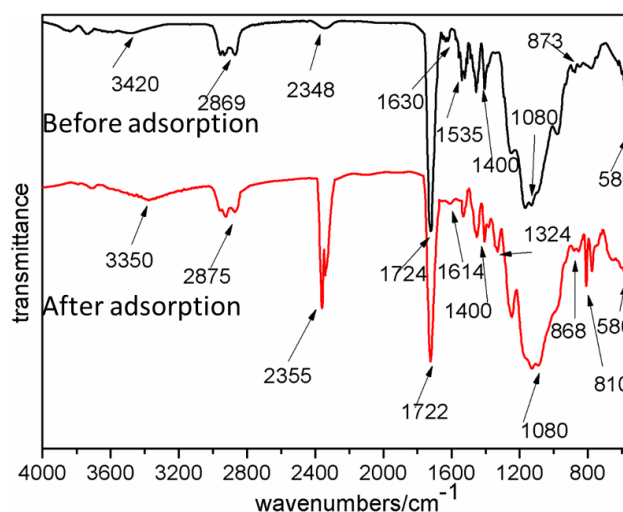


**Fig. 2-15. FTIR spectra of chitosan-modified cellular before and after Cu(II) ions adsorption.**

## 2.4 Conclusion

In this study, an effective method was demonstrated for heavy metal ion removal by integrating a hybrid 3D printing technology with bio-adsorption. By combining the advantages of 3D printing for geometry construction and the high efficiency of bio-adsorption in heavy metal ion, it enables to fabricate a 3D chitosan ‘filter’ with great reusability. Four kinds of filters were prepared to obtain the optimal structural design, and it was found the filter of skew-hexagon holes provides the largest adsorbability. Compared to conventional bio-sorbents, it offers advantages of simplified manufacturing,

customized design and fast treatment. Furthermore, it can achieve a considerable adsorption capability of up to 13.7 mg/mg in the optimal working condition at  $T = 25^{\circ}\text{C}$  and  $\text{pH} = 5.5$ , which shows promising prospect in a mass application of wastewater treatment. By repeating the adsorption-desorption process, the adsorbability remains relatively steadily in repeated filtrations, with only a slight reduction of  $\sim 2$  mg/g after the first filtration cycle. FTIR spectra indicate that it is the  $-\text{NH}_2$  and  $-\text{OH}$  groups of chitosan that facilitate the adsorption process and shows potential compatibility of adsorbing other metal ions [120]. Therefore, the application in this study can be employed for the removal of more kinds of heavy metal ions.

## Appendix 1

The minimum dimension  $a$  of the hexagonal hole (**Fig. 2-1**) was determined by the surface tension of chitosan solution. Suppose a drop of chitosan solution has a radius  $r$ ; then the pressure difference between the inside of the drop and the outside is:

$$\Delta P = 2\gamma / r \quad (1)$$

Where  $\gamma$  is the surface tension of chitosan solution.

To calculate the hole size of the 3D printed filter, one needs to work out the pressure at the hole and equate it to the pressure (1). The pressure working on the surface of the object depends on the immersion depth when depositing the 3D printed object in chitosan solution. It is calculated as  $\rho gh$ , where  $\rho$  is the density of the chitosan solution (measured as  $1.22 \text{ g/cm}^3$ ) and  $g$  is the acceleration due to gravity ( $9.81 \text{ m/s}^2$ ). Let the two pressures equal to each other, it has

$$\rho gh = 2\gamma / r \quad (2)$$

According to the measurement  $\gamma = 193 \text{ mN /m}$ , and supposing the immersion depth as 30 cm, the minimum radius of the hole is calculated as 200  $\mu\text{m}$ . Thus, the feature size  $a$  was determined as 300  $\mu\text{m}$ . Based on the resolution of the 3D printer, the distance  $t$  was set to 120  $\mu\text{m}$ .

## Chapter 3

### 3 Development of an initiator-integrated 3D printable material system (i3DP)

In this chapter, a 3D printable material system was developed by introducing an initiator into a customized UV-curable resin for functional 3D printing. Surface-initiated atom transfer radical polymerization (SI-ATRP) is employed to enable a generic post-printing modification for the fabrication of functional materials. By taking advantage of both 3D printing and SI-ATRP, with one material system, it is feasible to fabricate complex architectures along with obtaining desired functions for various applications. Compared with other 3D printing technology, like the printed filter in Chapter 2, this technology is an all-in-one 3D printing method to fabricate objects with a modifiable surface that can be easily tuned to realize various functionalities.

#### 3.1 Introduction

3D printing technology has emerged as a powerful manufacturing tool, allowing one to create sophisticated, customer-required and low-cost products, which were either impossible to manufacture or traditionally fabricated using complicated procedures and facilities. Different types of printer and printing technology are being developed to meet various demand. However, a universal 3D printing process, which can meet multiple requirements for various applications by one 3D printing approach, is nearly impossible. Two possible approaches are suggested to address the challenge, one is developing specific printing strategies together with many different material systems, and the other is

developing a new 3D printing material system to produce all functional materials/devices. The former is obviously costly and time-consuming, which also requires the support of 3D printer, while the latter is verified to be accessible through an integrated strategy. As a matter of fact, the very recently developed integrated 3D printing approach [78, 79, 132], has verified this strategy in applications of biomedical science, composite and electronics.

As identified in the *Introduction* part, embedding fillers in a polymeric matrix could improve the 3D printed objects properties but usually causing the printing process more difficult. Considering this drawback, we proposed a strategy to obtain desired functional materials/devices by in situ generation of functional surface after the printing process. Compared to the existing technologies that can only server for a specific application by developing treatments individually, this integrated strategy can enable the printed parts with modifiable surfaces which can easily be formed to functional materials with various properties. For example, a vinyl-terminated halide that can induce atom transfer radical polymerization can enable the 3D printed object to have an easily modifiable surface by growing various polymer brushes via surface-initiated polymerization. These resultant polymer brushes can either act as a medium to grow other organic or inorganic functional coating, or even as a functional coating directly. Particularly, all these functional coating can be induced upon the same surface-initiated polymer, indicating the 3D printing material itself plays a role as a “stem cell” for making 3D architectures with desired surface properties in a cost-effective manner.

In this study, a customized 3D printable material system is developed, which is applicable for all types of photo-polymerization based 3D printing routes, including DLP, SLA, polyjet and other emerging technologies. It has significantly extended the capacity of current 3D printing technology.

According to the comparison of different 3D printing processes described in Chapter 1, the photo-polymerization based approach has combined the advantage of easy-to-use and high resolution, along with a relatively large area and an acceptable cost. More importantly, for industrial application, the photo-polymerization method has made a great progress, which has great potential to become a new manufacturing technique in the coming world of Industry 4.0. It is therefore, in this study, the newly developed material system is based on a 3D printing technology of photo-polymerization principle.

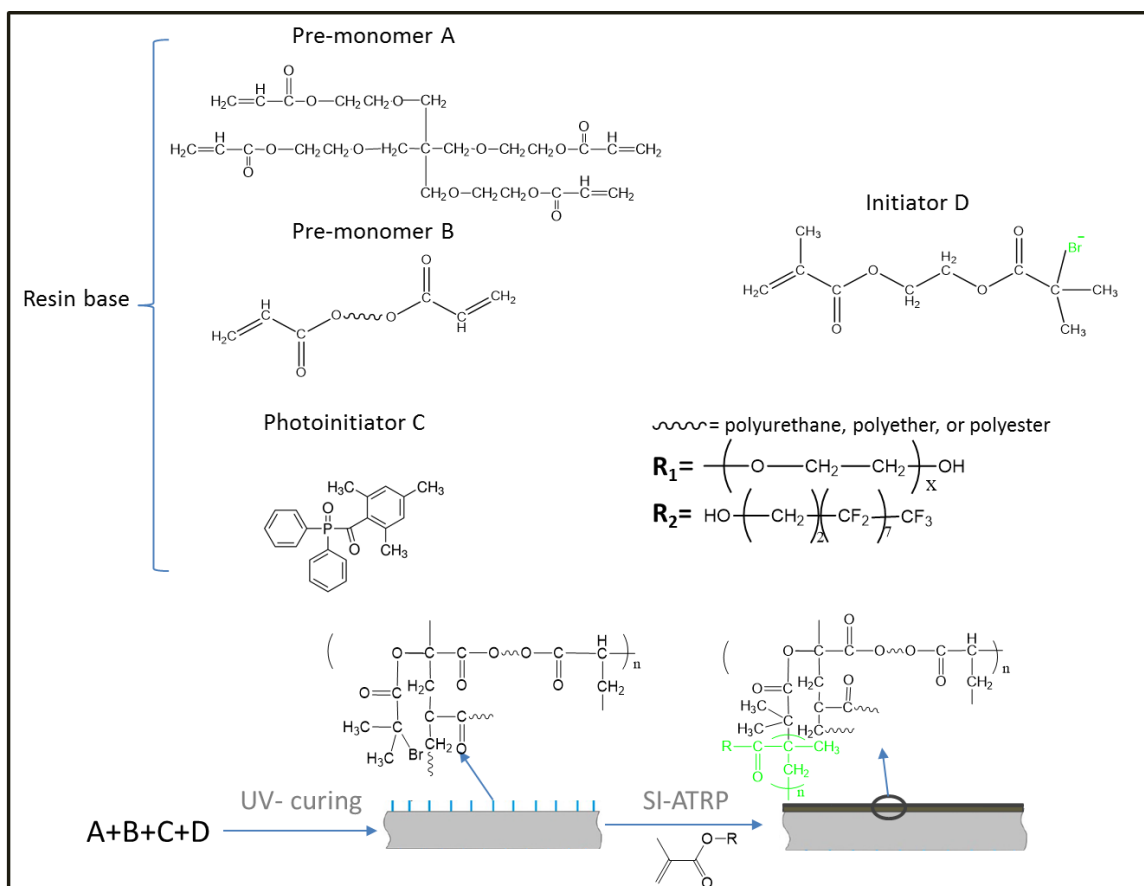
## 3.2 Working principles

Fig. 3-1 The material is developed according to the principle of atom transfer radical polymerization (ATRP), which has been proven to be robust and widely used to grow multifunctional surface [133-135]. Typically, a vinyl-terminated halide as the initiator (part D) is added into the UV-curable resin which is mainly composed of acrylate-based pre-monomer (part A, part B), cross-linking agents and phosphine oxide-based photoinitiator (part C). Herein, to exemplify the working capability, a vinyl-terminated initiator (2-(2-bromoisobutyryloxy) ethyl methacrylate (BrMA) was mixed with resin base composed of pentafunctional monomer, diacrylate oligomer and Diphenyl(2,4,6-trimethylbenzoyl) phosphine oxide (**Fig. 3-1**). The mixed resin will be polymerized to highly cross-linking networks after 3D printing process and result in a 3D printed object with initiator both exposed on the surface and in the structure. Subsequently, the outmost Br will initiate the ATRP process to grow a variety of polymer brushes with desired functions.

## 3.3 Preparation of initiator-integrated resin

The resin base was composed of pre-polymers including 39.5 wt.% di(trimethylolpropane)

tetraacrylate, 39.5 wt% uethoxylated pentaerythritol tetraacrylate and 20 wt.% 2-[(butylcarbamoylethyl)oxy] ethyl acrylate with 1.0 wt.% (2,4,6-Trimethylbenzoyl-diphenylphosphineoxide) as the photo-initiator. From the view point of ATRP, 5 wt.% 2-(2-bromoisobutyryloxy) ethyl methacrylate BrMA is the minimum concentration to prepare the initiator-integrated resin for a successful grafting for the polymer brushes [133]. Thus, the customized resin was prepared by adding 5 wt.% BrMA which is a standard mixing concentration in the following study, into the acrylate-based pre-polymers, mixed well, and degassed for 1h in the dark.



**Fig. 3-1. Schematic illustration of the preparation of initiator-integrated UV-curable resin and the surface modification of 3D printed object via SI-ATRP.**

### 3.4 Characterization

The objective is to achieve a robust integration of the initiator with the 3D printed object for the following functionalization. To verify the effectiveness of this initiator-integrated material, X-ray photoelectron spectroscopy (XPS) was utilized to detect the chemical component of the 3D printed object from both basic resin and the customized resin.

A DLP 3D printer as **Fig. 3-2** [136] (PICO2, Asiga) was used to print architectures via photo-polymerizing the acrylate-based liquid resin. A digital projector screen was used to flash a single image of each layer and a final 3D architecture is formed by repeating this process. After printing, both structures were thoroughly cleaned with methanol in an ultrasonic bath to remove the physical residual groups on the surface and ensure the accuracy of characterization. **Fig. 3-3** clearly shows that, the initiator-integrated object has a rising characteristic peak of Br, which was absent in the object printed by the basic resin. In addition, the distribution of Br in the printed object was also analyzed in the internal structure, which was cut off from different locations. The results in **Fig. 3-3B** indicate that the initiator distributes in both the outmost surface and all the locations inside the structure. Therefore, uniform coverage of the initiator throughout the whole object guarantees the following grafting of polymer brushes.

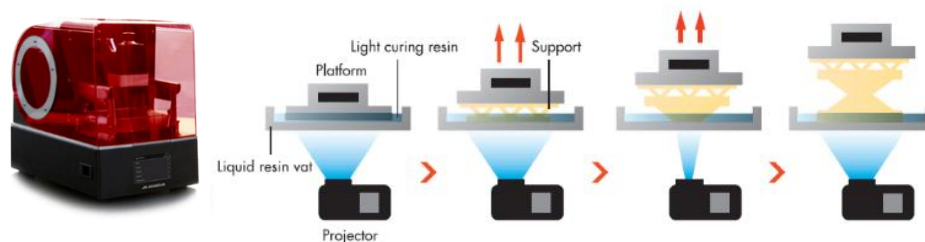


**Fig. 3-2. Experiment used DLP 3D printer, and the 3D printing process via a layer-by-layer sequence. Reproduced with permission from [136].**

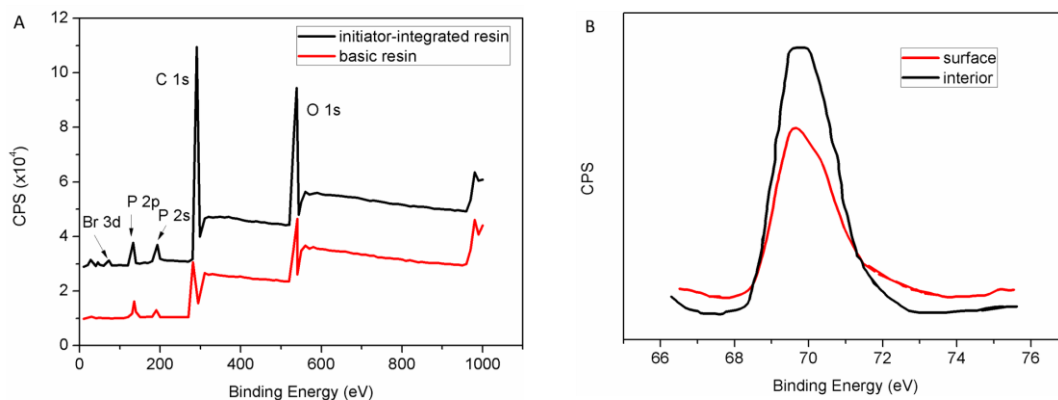


**Fig. 3-3. XPS spectra of UV-cured sample. (A) UV-curable resin before and after initiator-integrated. (B) Br signal from the outermost surface and the internal part.**

### 3.5 Printability

It is crucial to investigate the influence of the integrated initiator on the printability, and find out the optimal concentration for 3D printing and functionalization use. It is expected that the newly customized resin will have the same printability as that of original resin. Here, the printability is determined by the printing quality compared to the control resin which is without initiator integrated. The transparent initiator in the pre-polymers is assumed to have a minimum or no influence on the absorption of UV light. A standard test model was designed and fabricated as **Fig. 3-4A** to verify the assumption by comparing the printability of original resin and the initiator-integrated resin. The test model contained five areas of different printing features arrays, including square trusses, rectangular-shaped holes and circular holes. Specifically, in area 1, the square trusses were aligned with the printing direction, and the smallest dimension was 50  $\mu\text{m}$  for side length and 5 mm for height. All the features in the rest areas were designed to be perpendicular to the printing direction. In area 2, circular holes were distributed with diameters from 100  $\mu\text{m}$  to 1 mm, and with a depth of 4 mm. Area 4 was distributed with similar circular holes to area 2, but

the depth was designed to be 1.5 mm. Area 3 and 5 were distributed with rectangular holes, for which the smallest dimension was 100  $\mu\text{m}$ , 1 mm and 1.5 mm for width, length and depth.

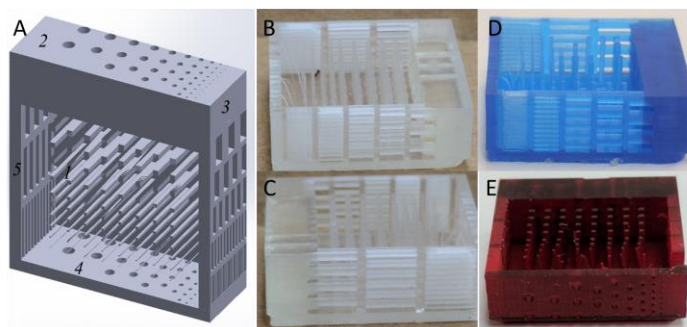


**Fig. 3-4. Printability of initiator-integrated resin. (A). CAD model. (B) 3D object by original clear resin. (C) 3D printed object of clear initiator-integrated resin. (D-E) 3D printed objects by initiator-integrated resin with the addition of pigments.**

After printing, no visible difference was found between the control part (**Fig. 3-4B**) and initiator-integrated part (**Fig. 3-4C**). The printing process of both resins were conducted by the same setting, allowing one to analyze the influence on the absorption of UV-light. **The results** further imply that, it is the structural design and 3D printing process itself that result in the blocked holes rather than the addition of initiator, and initiator does not cause a negative effect on the printability.

Table 3-1 summarizes the printability comparison of UV-curable resin with and without initiator-integrated. It verifies our speculation that the introduction of initiator does not affect the printability, and implies that the initiator-integrated resin can work under the same printing setting as the original resin which does not have initiator.

Scanning electron microscopy (SEM) was also conducted to detect the printing resolution

as shown in **Fig. 3-5**. It was found that the smallest holes in both objects were not through. Two main reasons for the blocked holes are that, the printing direction will influence the resin's flow in the holes and the scattering property of light will cure the resin in the perpendicular direction. The latter can be optimized through adding additives, like pigment, to enhance the printing resolution [137]. **Fig. 3-4D** and **Fig. 3-4E** are examples of 3D printed objects with pigment added, which also demonstrate initiator's compatibility in preparing colorized resin. The results further imply that, it is the structural design and 3D printing process itself that result in the blocked holes rather than the addition of initiator, and initiator does not cause a negative effect on the printability.

**Table 3-1. Comparison of the printability after the integration of initiator.**

features	Control resin	Initiator-integrated resin	note
Area1 ( $\mu\text{m}$ )	80	80	
Area2 ( $\mu\text{m}$ )	100	100	Not through
Area3 ( $\mu\text{m}$ )	100	100	Not through
Area4 ( $\mu\text{m}$ )	100	100	Not through
Area5 ( $\mu\text{m}$ )	100	100	

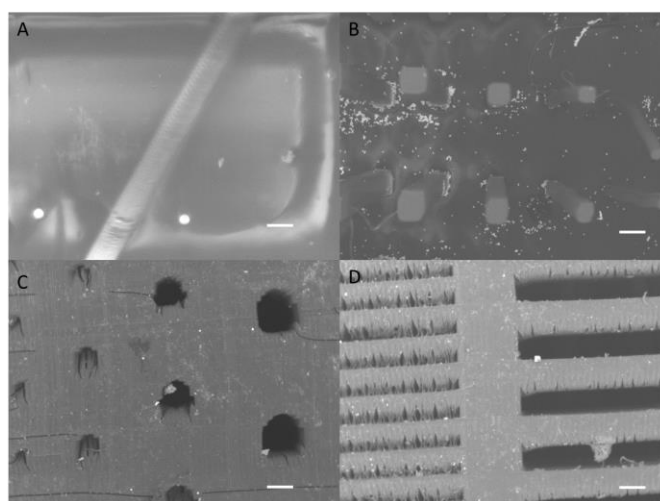


**Fig. 3-5. SEM images of feature arrays to investigate the printing resolution. (A-B) Side view and top view of square trusses. (C) Circular holes. (D) Rectangular holes.**

**Scale bars: A 50  $\mu\text{m}$ , B 100  $\mu\text{m}$ , C and D 150  $\mu\text{m}$ .**

### 3.6 Mechanical properties

Mechanical properties are also of great significance when developing a new material. Desired modifications are regarded as those which will not sacrifice one property to enhance another. We assume that, although the attachment of initiator to cross-linkers would decrease the degree of cross-linking more or less, one could reduce the influence by carefully choosing the ratio of A/B/C/D and introducing a proper content of initiators into the network. In fact, as a random cross-linking process, the network formation during the polymerization is not 100% completed even without the initiator added, but always has a small amount (<5%, w/w) of unreacted functional groups left [138]. It is expected that the introduction of initiator will not cause a significant change of the mechanical property because: 1. The initiator only takes up a small proportion to the material system; 2. the vinyl-groups contained in initiator are expected to take part in the photo-polymerization process and cross-link with acrylate-based monomers [63].

To verify our speculation, uniaxial tensile tests were conducted to compare the mechanical behaviors of the objects printed by original resin and customized resin. Standard test samples designed as **Fig. 3-6** were fabricated to conduct the tensile test. All tests were performed with a servo-electric INSTRON 8862 frame, equipped with a FastTrack 8800 controller and a National Instrument SCXI Data Acquisition system.



**Fig. 3-6. Test specimen for axial tension experiment.**

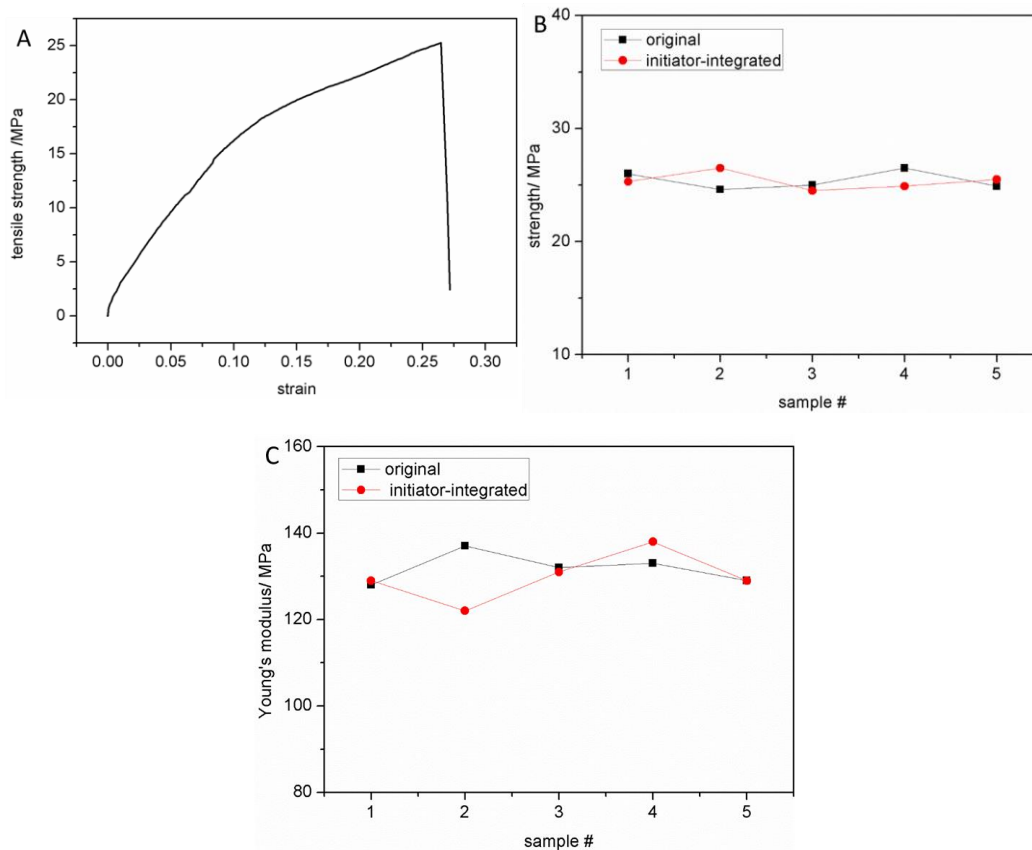


**Fig. 3-7. Influence of the initiator on the mechanical properties of 3D printed parts. (A) Stress-strain curve of the initiator-integrated specimen under axial tensile test. (B) Comparison of the tensile strength of the samples with and without initiator-integrated. (C) Comparison of Young's modulus of the samples with and without initiator-integrated.**

The deformation behavior of initiator-integrated sample is shown in **Fig. 3-7A**, which describes a typical mechanical behavior of elastic deformation and was constant with the sample containing no initiator. In addition, the elongation remains  $\sim 0.27$  which is relatively unchanged after the addition of initiator. **Fig. 3-7B** and **C** plot the quantitative comparison of the tensile strength and Young's modulus. Apparently, the addition of initiator does not cause a side influence same as other reports in which the addition of small molecular

usually result in a negative influence on the mechanical properties [139-141]. In conclusion, the mechanical test verifies that the addition of initiator causes no obvious change on the mechanical property of the initiator-integrated 3D object.

## 3.7 Functionalization

The distribution of Br in the 3D object enables the SI-ATRP process to grow polymer coatings. Here we take two representative monomers as examples to demonstrate initiator's capacity of growing polymer brushes on the surface. One is 1H,1H,2H,2H-perfluorodecyl methacrylate (PFMA) which is expected to result in a surface with low surface energy, and the other is 2-(methacryloyloxy)ethyl-trimethylammonium chloride (METAC) which can act as a polyelectrolyte layer to assist the electroless plating process.

### 3.7.1 Experiment setup

**Materials.** The customized resin was prepared as that described in 3.3. Briefly, 5 wt% BrMA was mixed well with the resin base composed of acrylate-based pre-polymers (Asiga), and degassed for 1h in the dark. All other chemicals and solvents were obtained from Sigma Aldrich and used as received except that CuBr was purified by reflux in acetic acid. PFMA and METAC were passed through an aluminum oxide column to remove inhibitors prior for use.

**Initiator-integrated architectures by 3D printing.** The initiator-integrated objects were 3D printed following the instruction described in 3.4. Briefly, a 3D model was first designed by Solidworks (Dassault Systèmes), and then digitally sliced into 2D layers for the subsequent solidification, which was conducted in a DLP 3D printer. Since the initiator has no negative effect on the printability, the initiator-added resin was polymerized with the

same parameters as the commercial resin base. After ultrasonically rinsing for 5 min in ethanol, the 3D printed objects were dried by a mild nitrogen flow and UV-post cured for 5 min.

***SI-ATRP process.*** For the grafting of PFMA, 1.56 g of PFMA was added in 15 mL of dimethylformamide (DMF) under stirring with Argon protection for 20 min. Then, 78 mg of N,N,N',N'',N'''-pentamethyldiethylenetriamine and 42 mg of CuBr were added to the solution. The mixture was then degassed by Argon flow under stirring for 20 min before syringing into Schlenk tube where a 3D printed object was already placed. 2 h of polymerization was conducted. After the polymerization, all the samples were ultrasoundly rinsed with methanol and water, dried using Ni flow, and heated at 60 °C in vacuum overnight.

For the grafting of METAC, a typical process follows as: commercially available METAC was dissolved in methanol at 20 °C by a weight ratio of 1:1, and the resultant solution was degassed for 20 min by passing a continuous stream of dry N<sub>2</sub>. Then 2,2-Dipyridyl (24 mg/ml) and CuBr (6 mg/ml) were added to the solution. After stirring and degassing the mixture with a N<sub>2</sub> stream for 15 min, the 3D printed initiator-integrated samples were carefully immersed into the solution. The polymerization was performed at 60 °C under N<sub>2</sub> protection for 4 h. Once completed, the resultant samples were washed with methanol and water, and then dried with a stream of N<sub>2</sub>.

### 3.7.2 Characterization

Surface information of chemical composition was obtained by X-ray photoelectron spectroscopy (XPS). The measurement was carried out by a Kratos Axis Ultra spectrometer using a monochromatic Al K $\alpha$  radiation source. The binding energy was referred to the C

1s line at 284.8 eV from an adventitious carbon.

### 3.7.3 Results and conclusion

**Fig. 3-8** is the XPS spectra of PFMA and METAC grafted objects via SI-ATRP. As shown in **Fig. 3-8A**, the strong F 1s signal at 689.4 eV and the high-resolution spectrum of C 1s which demonstrates the atom% of the initiated chemical components by SI-ATRP is very close to the theoretical values of poly(PFMA) [63], suggest a successful grafting of poly(PFMA). In addition, the P decreases sharply from 4.0% to almost zero (compared to **Fig. 3-3**) further implies that a dense layer of poly(PFMA) was covering the object's surface.

As shown in **Fig. 3-8C**, the presence of N is attributed to the formation of poly(METAC) coating, for the sharp increase of N signal from 1.0 to 6.5% indicates the growing of a PMETAC coating on the surface of 3D printed object. In addition, the atom % of P nearly disappears from 4.0%, suggesting that a dense PMETAC surface coating was formed. All these evidence indicate that a uniform and dense PMETAC coating was grafted on the 3D printed object through the SI-ATRP.

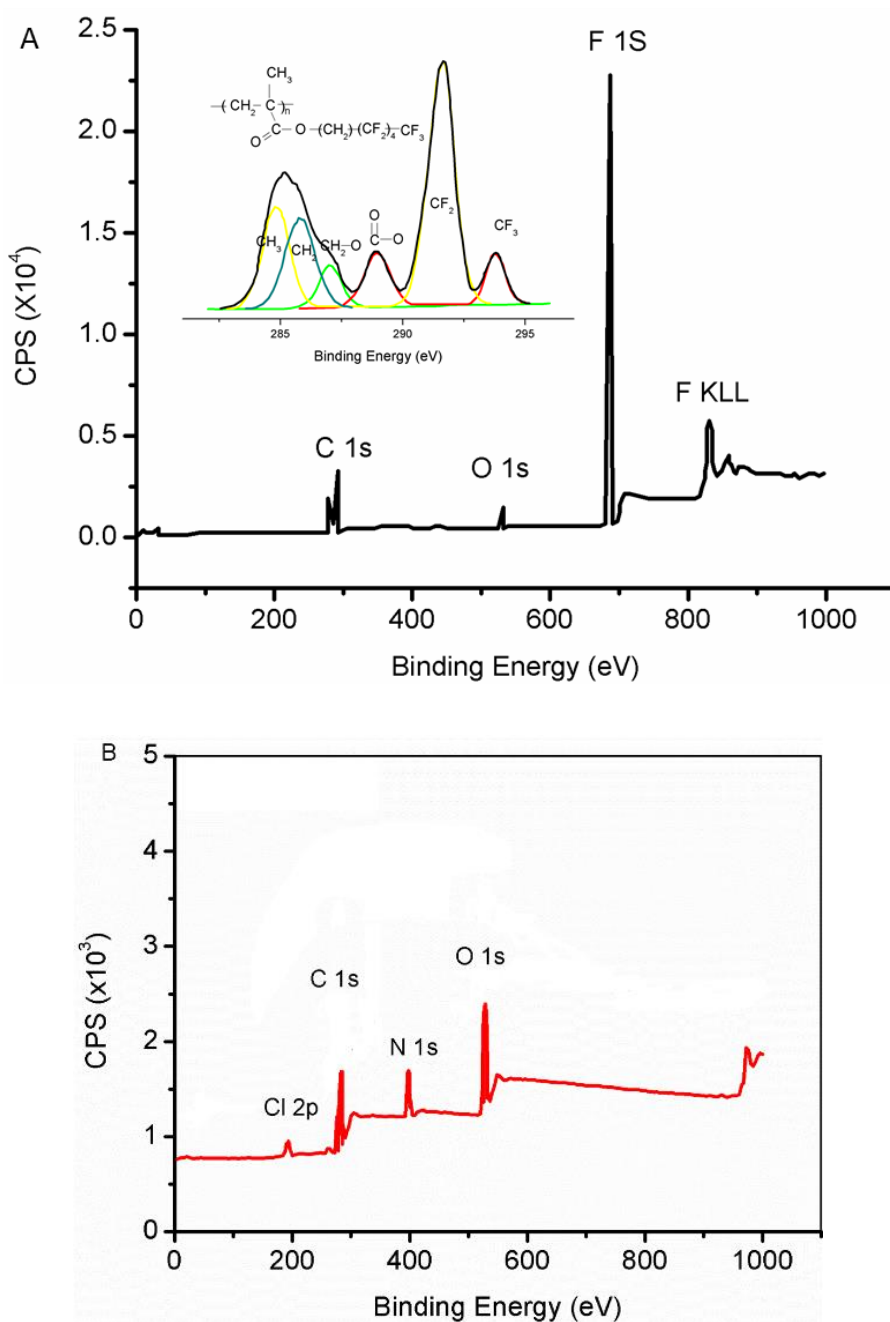


**Fig. 3-8. XPS spectra of two representative polymer coatings growing by SI-ATRP. (A) XPS spectrum of poly(PFMA). (B) high resolution spectra of C 1s. (C) XPS spectrum of PMETAC.**

The described generic post-printing surface modification via SI-ATRP allows the

realization of various functional materials which can be designed with complex structures when incorporating the design flexibility of 3D printing. For example, a micromesh which was designed with a feature size of 400  $\mu\text{m}$  was functionalized to be hydrophobic after the grafting of poly(PFMA), as shown in **Fig. 3-9**. In addition, the surface quality is excellent, no crack or delamination was found. The proposed all-in-one 3D printing method that combines the merits of the building flexibility of 3D printing and the high-compatibility of SI-ATRP surface modification enables an easy approach to functionalize 3D printed structural materials, which are believed to have broad applications in a lot of fields.

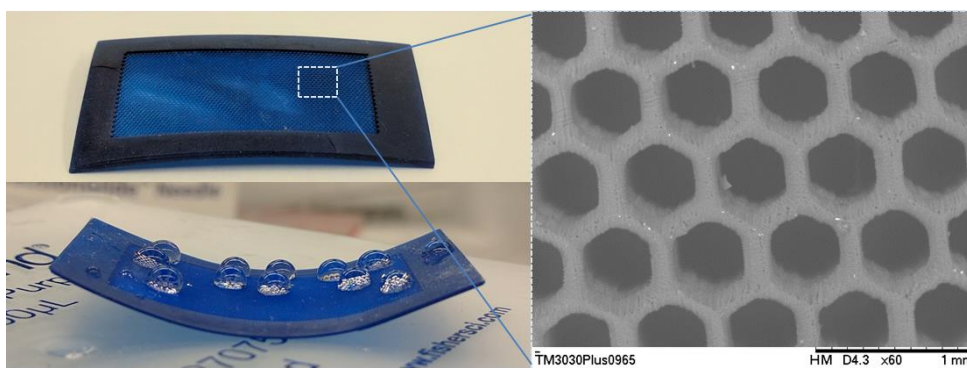


**Fig. 3-9. Hydrophobicity of poly (PFMA) grafted micromesh. Inset is the SEM of hexagonal mesh holes.**

## 3.8 Extending functions based on the polymer grafting

### 3.8.1 Metallization of 3D printed objects

**Preparation of PMETAC-coated object.** The polymerization of METAC was conducted following the procedures described in 3.7.1. Briefly, a mixture of METAC and methanol was prepared under  $\text{N}_2$  protection for 20 min. 2,2-Dipyridyl and CuBr were subsequently added into the solution. An initiator-integrated object was immersed into the resultant solution at 60  $^\circ\text{C}$  for 4 h.

**Electroless Plating (ELP) based PMETAC.** Two representative metal coatings, Ni- and Cu-coating, were deposited to showcase the metallization of 3D printed objects. Typically, the PMETAC-coated samples were immersed into a 5 mM  $(\text{NH}_4)_2\text{PdCl}_4$  aqueous solution for 15 min. After  $\text{PdCl}_4^{2-}$  moieties immobilizing onto the brushes by ion exchange and rinsing thoroughly with water, the samples were immersed into the house-made plating bath to obtain metallic architectures.

The ELP of Ni was prepared as: two plating bath solutions were prepared separately, one consisted of 40 g/L of  $\text{Ni}_2\text{SO}_4 \cdot 5\text{H}_2\text{O}$ , 20 g/L of sodium citrate, and 10 g/L of lactic acid, and the other was 1 g/L of dimethylamine borane (DMAB) in water. The stock solutions were prepared in a 4:1 volume ratio as a final electroless bath.

The Cu plating bath contained a 1:1 mixture of freshly prepared solutions A and B. Solution A consisted of 12 g/L of NaOH, 13 g/L of  $\text{CuSO}_4 \cdot 5\text{H}_2\text{O}$ , and 29 g/L of  $\text{NaKC}_4\text{H}_4\text{O}_6 \cdot 4\text{H}_2\text{O}$ . Solution B was an aqueous solution of 9.5 mL/L of HCHO.

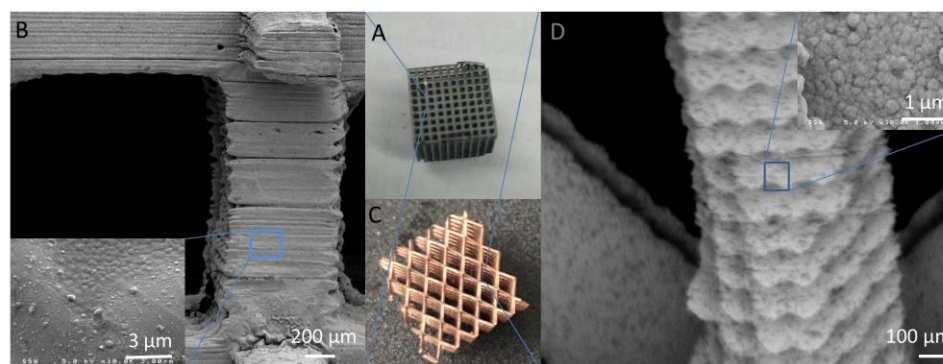


**Fig. 3-10. Ni- and Cu-coated microlattices through polyelectrolyte-brush assisted metal deposition. (A-B) Ni-coated microlattice and SEM image of the Ni coating. (C-D) Cu-coated microlattice and SEM image of the Cu coating.**

**Results and discussion.** Fig. 3-10 shows the resultant Ni- and Cu-coated microlattices.

SEM was conducted to investigate the surface morphology of the metal layer. It is found that the lattice was coated with a layer of Ni (inset of **Fig. 3-10B**) after 1h of ELP, which is composed of dense particles and covers uniformly the entire lattice surface. Also, it shows the lattice was built layer-by-layer, and the connections are excellent, without any cracks or delamination, indicating a robust microlattice. Similarly, a Cu-coated microlattice was also fabricated as **Fig. 3-10C** which is composed of nanoparticles with diameters of ca. 100–200 nm (**Fig. 3-10D**) and present a uniform coverage over the lattice material. Compared with the flat surface in the X and Y directions, the column in the Z direction is rougher with obvious layer patterns, because the polymerization layers were stocked in Z direction during the 3D printing process.

This polyelectrolyte-brush assisted metal deposition is highly dependent on the ELP time [142]. Normally, 15~20 min of ELP can produce a Cu-coated surface with uniform coverage, and the thickness of Cu layer are ca. 140 and 230 nm, respectively, whereas the Cu layer obtained at 10 min of ELP has a thickness of ca. 100 nm, but cannot completely cover the surface [112]. Obvious defects can be found in the Cu layer after ELP of 10 min. This indicates that at least 15 min of ELP is necessary to produce a Cu-coated architecture with a uniform metal coating.

Notably, it is able, assisted with the computer-aided process, to fabricate other desired metallic objects. For example, metallic model of Eiffel towers which have not only the shape but also the details were realized for the first time using a 3D printing approach [112]. Moreover, the polymer core of the metallic architectures can be etched away to obtain ultralight metallic materials, seen as Chapter 6 for more details.

### 3.8.2 Conductive hydrogel enabled by SI-ATRP

**Preparation of initiator-integrated hydrogel.** 4 wt% BrMA was mixed well with a resin base that was composed of Poly(ethylenglycol)diacrylate (PEGDA, 70 wt.%), 29 wt.% H<sub>2</sub>O and 1 wt.% photoinitiator of Phenylbis-(2,4,6-trimethylbenzoyl)-phosphine oxide. Here, the initiator concentration was optimized to be 4 wt.% according to the pre-polymer's proportion. After degassing for 30 minutes in the dark, the customized resin containing initiator was ready for printing. The 3D printing was performed in the same way as that described in 3.4. CAD models of microlattices were first designed and converted to STL files, and then built to hydrogel samples after 3D printing.

**Fabrication of 3D poly(pyrrole-co-formyl pyrrole) (P(Py-co-FPy)) by SI-ATRP.** The preparation of P(Py-co-FPy) layer was carried out according to Abbasian's report [143]. Briefly, 2 M Pyrrole (Py) and 2 M Pyrrole-2-carboxaldehyde (FPy) in chloroform solution (10 ml) were added dropwise into 100 ml of deionized water, and stirred the solution for 30 minutes. Then, an acid catalyst, trifluoroacetic acid (TFA) (6.63 ml, 0.0866 mole), was added into the solution. After a complete dissolution under stirring, CuCl (0.015 g, 0.158 mmol) and bpy (0.07 g, 0.47 mmol) were subsequently added. The system was degassed to remove oxygen by stirring the solution under nitrogen for one hour. The 3D printed initiator-integrated hydrogel samples were immersed into the mixture. After the polymerization was carried out for about 24 hrs at room temperature, the resulted objects were washed with water and methanol for 5min.

**Characterization.** Sample resistivity was measured by using a Keithley-238 High Current Source Measure Unit (voltage range  $\pm 10$  V, step 0.1 V) realizing a two-point contact setup with copper electrodes on the two opposite basal sides. Morphology of the 3D printed materials after the interfacial polymerization of P(Py-co-FPy) was detected by SEM

(Hitachi TM3030Plus).

**Results and discussion.** Optical microscopy and SEM of the P(Py-co-FPy) coated structure are shown in **Fig. 3-11**. A well-defined hydrogel microlattice was fabricated via the functional 3D printing, and it was with good building accuracy. Moreover, the post polymerization of the P(Py-co-FPy) on the structure causes no influence on the printing resolution during the process step, and it clearly shows the structure is without any breaks.

The SEM shows details of P(Py-co-FPy) grafting on the surface. A flowerlike pattern shows up and becomes rougher, and is with big porosity (**Fig. 3-11C, D**). One surmise is that high concentration of FPy and Py monomers in the solution result in a faster polymerization rate, and thus a more uneven distribution of P(Py-co-FPy) was produced [144].

The influence of P(Py-co-FPy) on the resistivity was evaluated by electrical measurements. As plotted in **Fig. 3-12**, the presence of P(Py-co-FPy) decreases the film resistivity of one order of magnitude or more compared with the control film without P(Py-co-FPy) indicating a layer of P(Py-co-FPy) was successfully formed and covered the surface. In addition, the obtained resistivity values are comparable with that in the literature [145], which further evidence that functional 3D printing is capable of forming conductive polymers.

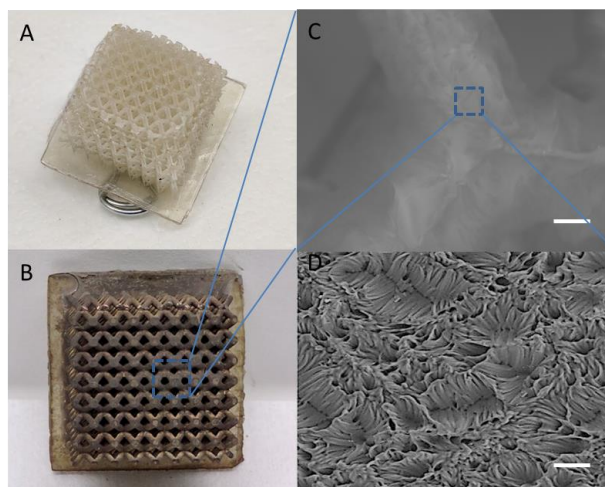


**Fig. 3-11. Functional 3D printed hydrogel-microlattices. (A) 3D printed PEGDA (60%) microlattice. (B) Microlattice with P(Py-co-FPy) grafted. (C-D) High resolution SEM image of the P(Py-co-FPy) brush. Scale bar of C: 200  $\mu\text{m}$ , D: 10  $\mu\text{m}$ .**

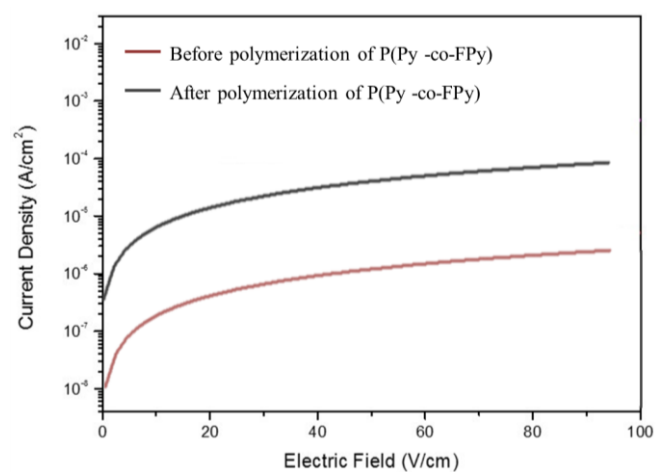


**Fig. 3-12. Semilogarithmic plot of I/V measurements and resistance evaluation for P(Py-co-FPy) coated object (a plate was fabricated via the same procedures as the microlattices).**

### 3.9 Conclusion

In conclusion, a facile and effective initiator-integrated material system was developed to

extend 3D printing's capacity of fabricating functional materials/devices. The initiator-integrated UV-curable resin was prepared by adding an initiator monomer into the resin base, and the SI-ATRP can be initialized to endow the 3D printed materials with tunable surface properties, such as hydrophilicity, metallicity, and conductivity. It is noted that, this approach is versatile for any UV-curable resin that is composed of acrylate-based pre-polymers. That means, taking advantage of 3D printing and SI-ATRP, this initiator-integrated approach can act as an all-in-one 3D printing method feasible to fabricate complex architectures along with obtaining desired functions for various applications. More importantly, this initiator integrated strategy could be compatible with many other surface initiated technology, only by simply selecting a proper initiator with different functional groups. Our following study will further demonstrate that this initiator-integrated strategy is highly effective to 3D print a variety of functional materials/devices, including magnetic robot, cellular materials of high effective strength, ultralight metallic materials and mechanical meta-materials. The proposed functional 3D printing shows a great potential in applications of biomedical science, energy-absorbing, ultralight composites, catalyst support and so forth.

## Chapter 4

### 4 Magnetic objects by i3DP and the structural optimization

The premise of initiator-integrated strategy described in last chapter enables 3D printing to fabricate objects possible for a variety of desired functions. This chapter steps further to use this strategy to fabricate a magnetically driven robot and simultaneously combines the structure topology for effective propulsion. Microrobot with spiral feature was fabricated, and was powered and steered wirelessly using low-strength rotating magnetic fields. The spiral-shaped feature induced a propulsion to the robot which can swim in the fluids. The fluidic kinematics was investigated to optimize the robot's structure. A comprehensive investigation was carried out on the optimization of spiral shape, liquid viscosity and the strategy of magnetic controlling. It is noted here, this Chapter is based on author's publication: Zhang, Dongxing, et al. "Initiator-Integrated 3-D Printing of Magnetic Object for Remote Controlling Application." *IEEE Transactions on Magnetics* 53.5 (2017): 1-9. And all the figures are used with permission from [132].

#### 4.1 Introduction

Magnetically driven micromachines can be employed in a variety of biomedical applications [146-148]. Unlike other micromachines which need onboard batteries or additional controlling accessories, the magnetically actuated machines can be controlled wirelessly, which is especially suitable for minimal invasive applications. Such technology is harmless for living organisms which can benefit the medical application from the reduction of recovery time and infection risks to the increase of

care quality [149, 150]. All the above advantages make the magnetic actuation a promising tool for medical and biological tasks [151].

Recent reports [152-154] have shown the feasibility of external magnetic fields for propelling robotic agents with milli-to-micrometer scale in liquid. They also found the working efficiency depends mainly on the geometries. For instance, a scaffold is always an excellent candidate for cell storage because of its porous three-dimensional (3D) structure [152], and a helical structure is ideal for target-drug delivery [151]. However, recent research mainly focusses on the physical connection between the magnetic material and the matrix, like adhering permanent magnets [155-158], to realize magnetic response. Very few research involves 3D construction, but is using relative complex process, such as e-beam evaporation, to introduce magnetic layer [153, 159-161]. Comprehensive integration of the geometry design and magnetic material was lacking, thus, the strategy to ensure high spatiotemporal guidance and movement trajectories was less explored. The challenges of geometric design, materials spectrum and fabrication process are restricting the application in more widely working conditions. Thus, it is desired to seek for other possible and efficient techniques to fabricate magnetic micromachines.

3D printing technology arises as a popular tool for structure construction benefitting the possibility to create sophisticated, customized and low-cost devices which are either impossible to produce or required complicated procedures and manufacturing facilities [7, 162]. Taking the newly developed direct writing technique for example, although it enables the fabrication of 3D structures of resolution as high as sub-micrometer, the realization of magnetic response is still a big challenge and needs complicated process, such as ALD and e-beam evaporation [152]. Similarly, selective laser sintering (SLS) is feasible to print magnetic objects by incorporating ferromagnetic particles, such as Ni, Co and Fe[163], but the construction resolution and combination of multi-materials

are still big challenges to satisfy the biomedical application. Besides, the surface based technique, such as sputtering, cannot ensure an even coating of magnetic material onto the established 3D structure. In spite of its utilization in industrial rapid prototyping and a few tissue engineering [6] applications, there are few reports about its application in the fabrication of magnetic objects. Therefore, instead of trying hard to develop printable magnetic materials to utilize the advanced 3D printing technology, it is desirable to develop an all-in-one printing method to simultaneously achieve both the geometry construction and magnetic property for the material.

In this study, we aim to adopt the feasible technique described in Chapter 2, which combines 3D printing technology and generic post-surface modification, to in-situ grow magnetic materials onto 3D structures. The proposed initiator-integrated strategy is adopted here to make a magnetically driven robot with desired geometry. The process is illustrated as **Fig. 4-1**. Briefly, a vinyl-terminated initiator was added into a commercial UV curable resin for 3D structure fabrication. After printing, the initiator is embedded into the 3D printed structure to generate surface bound radicals. Because of the uniform distribution of the initiator over the entire structure, the surface of 3D printed object can be modified easily by growing polymer brushes via initiator-enhanced polymerization. The subsequent surface modification is performed by surface-initiated atomic-transfer radical polymerization (SI-ATRP) [134, 135] and electroless plating (ELP) of magnetic materials. Thus, a uniformly distributed coating of magnetic materials is obtained. Because the polyelectrolyte brushes grown via ATRP act as a nano-thick platform to induce the following ELP, the magnetic layers are of excellent adhesion to the substrate [142, 164]. The results demonstrate that the combination of 3D printing and post-printing surface modification provides an efficient method for both construction of complex geometries and innovative functionality, along with the advantage of high-resolution, cost-efficiency and time-saving.



as received except the CuBr was purified by washing through glacial acetic acid.

#### 4.2.2 3D printing and ATRP

A spiral-type swimming robot was designed conceptually to demonstrate the i3DP process. This robot was photo-polymerized as an acrylate-based substrate with spiral blade via 3D printing and the outmost magnetic layer was functionalized from the i3DP technique. When an external rotational magnetic field was applied, it allows the robot rotated and subsequently propels to move linearly because of the existence of the spiral blade. The robot was characterized by the structural parameters (as shown by the schematic model in **Fig. 4-2**), including the height of the spiral  $h$ , the width  $W$ , the pitch  $P$  and the spiral  $\theta$ .

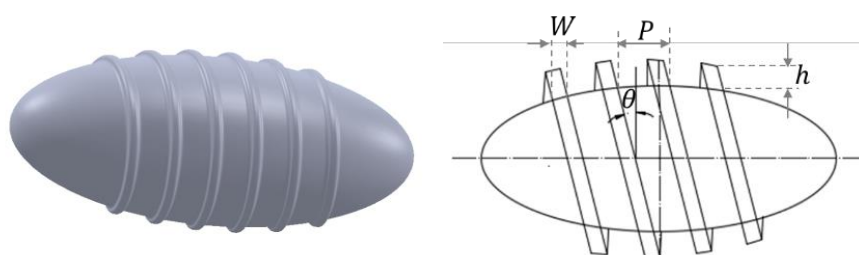


**Fig. 4-2. CAD model of the designed robot and the spiral characteristics.**

The preparation of initiator-integrated UV-curable resin has been introduced in Chapter 3. Briefly, 2-(2-bromoisobutyryloxy)ethylmethacrylate (BrMA) (5 wt%) was mixed well into the resin base and then degassed for 1h in dark. The 3D structure was designed by Solidworks (Dassault Systèmes) and printed layer by layer via a commercial 3D printer (PIC2, Asiga). Our previous results showed that there was no influence of the mixed initiator on the printing process. The printed object was ultrasonically rinsed for 10 min in ethanol to eliminate the adhesive residue on the surface and dried in the air. The initiator-containing structure was ready for the subsequent surface modification to induce functional magnetic material coating.

A layer of functional groups (brushes) was firstly grafted by immersing the sample into

the following solution for 4 h at 60°C. 2-(methacryloyloxy)ethyltrimethyl ammonium chloride (METAC) and methanol were mixed by weight ratio of 1:1, and then the solution was deoxygenized by passing N<sub>2</sub> stream for 20 min. After that, 2, 2-Dipyridyl (24 mg/ml) and CuBr (6 mg/ml) were added into the solution under the protection of N<sub>2</sub>.

The brush-loaded structure was then immersed into an aqueous solution of 5 mM (NH<sub>4</sub>)<sub>2</sub>PdCl<sub>4</sub> for 30 min. The high affinity between METAC and ammonium ions helps the PdCl<sub>4</sub><sup>2-</sup> be immobilized on the brushes. The catalyst of PdCl<sub>4</sub><sup>2-</sup> will assist the subsequent ELP to grow a magnetic layer. Herein, for a specific application of remote controlling under magnetic force, a lab-made multi-alloy (NiCo) magnetic plating bath was prepared for the coating of ferromagnetic material on 3D printed objects with high saturation magnetization (M<sub>s</sub>) and low coercivity (H<sub>c</sub>).

#### 4.2.3 Magnetic control

A permanent-magnet manipulator was set up to carry out the remote-control experiment. The permanent magnet (Grad-42 NdFeB, axially magnetized and 25.4 mm in both length and diameter) was housed in a transparent 3D printed case and connected to a DC motor, seen as **Fig. 4-3**. The magnetic robot was placed in two positions for the magnetic manipulation: beneath the permanent magnet and along the rotation axis of the magnet.

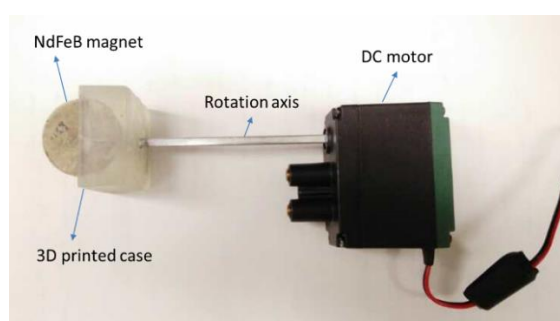


**Fig. 4-3. Magnetic manipulator used to magnetically drive the robot.**

#### 4.2.4 Characterization

X-ray photoelectron spectroscopy (XPS) was conducted by using an Axis Ultra spectrometer (Kratos, UK) to analyse the chemical composition of the 3D object during each procedure. For the spectroscopy, a monochromatic Al  $K\alpha$  radiation resource was utilized by referencing to a binding energy of C 1s at 284.8eV. The morphology of the surface coating was examined by scanning electron microscopy (SEM, Hitachi S-4500) at a 10kV accelerating voltage. A vibrating sample magnetometer (VSM) (730T, Lakeshoper, America) was utilized to measure the magnetic property at room temperature.

### 4.3 Results and discussion

#### 4.3.1 XPS of ATRP Process

XPS spectra were utilized to reveal the process of SI-ATRP. **Fig. 4-4A** clearly shows a characteristic peak of Br rising in the initiator-integrated object which was absent in the object printed by commercial resin. The comparison of Br distribution was also analyzed between the outmost surface and the internal material (2 mm beneath the surface). The results in **Fig. 4-4B** indicate that the initiator distributes in both the outmost surface and the location 2 mm beneath which can verify its existence throughout the whole object. This also guarantees the following polymer brush grafting. The presence of N in **Fig. 4-4C** is attributed to the formation of poly(METAC) coating, and indicates the successful grafting of poly(METAC) on the surface. After ion exchange in  $(\text{NH}_4)_2\text{PdCl}_4$  aqueous solution, Pd 3d<sub>5/2</sub> and 3d<sub>3/2</sub> signaling at 342.5 eV and 337.0 eV respectively (**Fig. 4-4D**) indicate the loading of  $\text{PdCl}_4^{2-}$  moieties due to their high affinity to quaternary ammonium of poly(METAC).

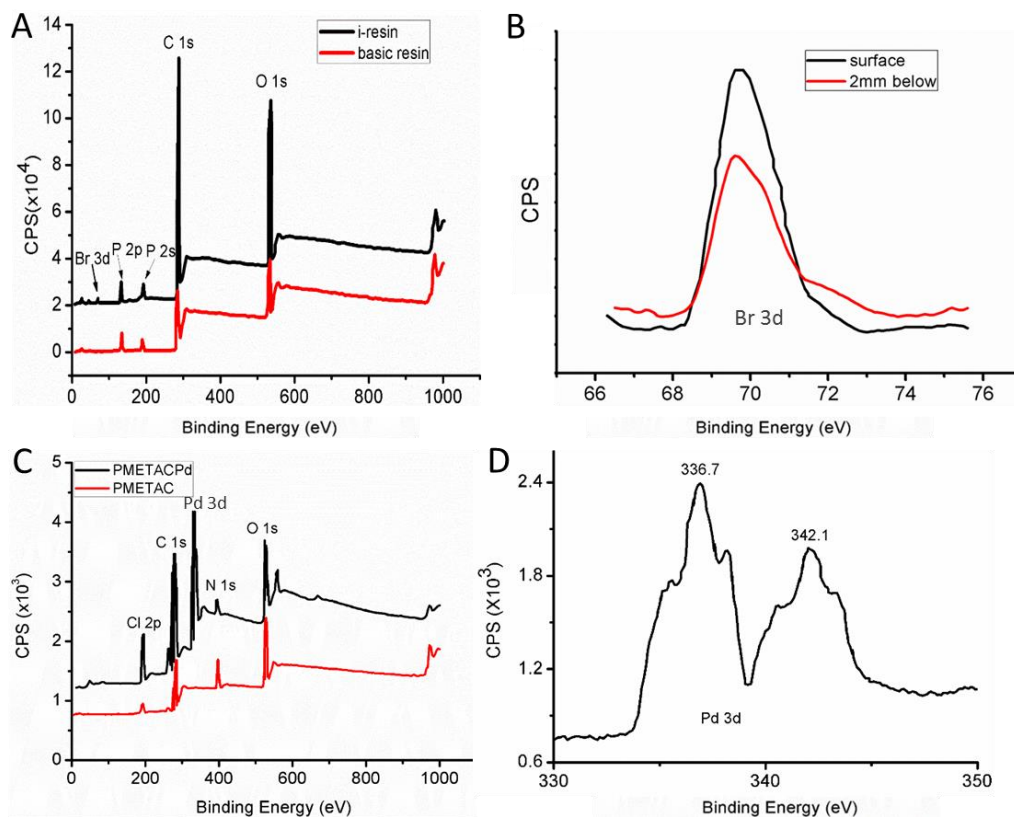


**Fig. 4-4.** XPS survey spectra of 3D printed robots. (A) robot integrated with initiator and regular robot with base resin. (B) High resolution XPS of Br 3d on outmost surface and 2mm beneath. (C) Sample with PMETAC brush before and after ion exchange with  $\text{PdCl}_4^{2-}$ . (D) High resolution XPS spectra in Pd 3d region of poly(METAC) grafted sample after ion exchange.

#### 4.3.2 Magnetism properties

The loaded  $\text{PdCl}_4^{2-}$  moieties act as valid catalytic sites for the subsequent ELP of magnetic coating. **Fig. 4-5** shows the resulted Ni-Co coated robot of ellipsoidal shape with spiral blades on the surface. SEM was used to get the morphology of the magnetic layer. It was found that a dense layer of coating was grown on the surface uniformly after 1h of ELP, shown as **Fig. 4-5B**. As the thickness of the magnetic film highly depends on the ELP time, it is able to control the thickness of magnetic coating by adjusting the reaction duration. In this study, a magnetic coating of 200  $\mu\text{m}$  thickness

was achieved after 12 hours' ELP. This micrometer-level thick layer was composed of uniform particles of ca. 100-200 nm in diameters (inset in **Fig. 4-5B**).

Furthermore, the composition of the magnetic coating was also verified through EDX. The result shown in **Fig. 4-5C** demonstrates the surface consists of 65% Ni, 28% Co, and 7% P. All these evidences strongly suggest a Ni-rich magnetic material was successfully obtained. In addition, a typical hysteresis loop was found through the VSM measurement (Fig. 4-6) which illustrates that the object exhibits soft ferromagnetic behavior. This is in agreement with the fact that Ni-rich alloy coating expresses soft ferromagnetic property[165], and it also verifies the EDX measurement. It is notable here that the ratio of Ni to Co was controllable by adjusting the proportion of Ni in the ELP solution which can subsequently regulate the property for the magnetic coating. Therefore, according to the requirement of magnetic response, it is possible to optimize the property, such as magnetocrystalline anisotropy, based on different magnetic properties of Ni-rich coating or Co-rich one.

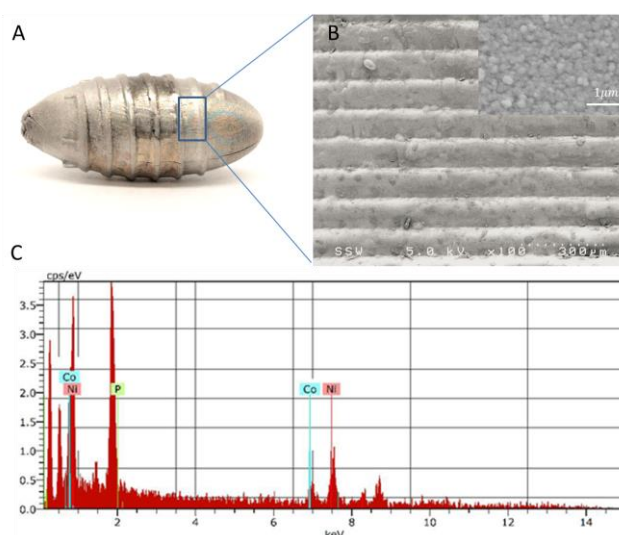


**Fig. 4-5. (A) Magnetic material coated robot with a major axis of 12.5mm and minor axis of 5mm. (B) Surface morphology. (C) The EDX spectrum of the surface coating.**

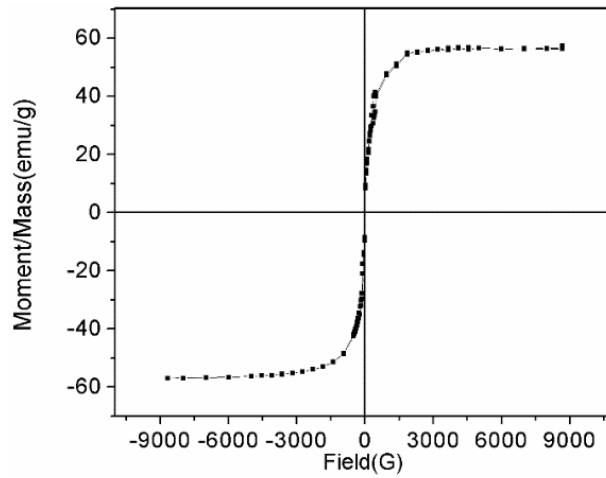


**Fig. 4-6. VSM measurement of the magnetic coating (powder scraped from the surface of i3DPed object)**

#### 4.3.3 Fluidic Kinematics

*Swimming in low-Re liquid.* The magnetic coating on the surface makes the robot able to rotate synchronously along with a rotating magnetic field. Because of the spiral on the body, the rotation will generate forward and backward thrust, resulting in a propelling in linear direction. In general, there is a boundary layer around the swimming machine as shown in **Fig. 4-7**. Within the boundary layer, the fluid is affected by the movement of the machine.

To analyze the swimming behavior in liquid, Navier-Stokes equations [166] is introduced here to define a fluid flow when it is combined with the boundary conditions. For a given fluid, the magnitude of characteristic velocity  $U$  and length  $L$  of the robot can non-dimensionalize the equations in space and time as:

$$\left( \frac{\rho u L}{\eta} \right) \frac{d\tilde{V}}{dt} = -\nabla \tilde{p} + \nabla^2 \tilde{V} \Rightarrow Re = \frac{\rho u L}{\eta} \quad (1)$$

Here  $\rho$  and  $\eta$  are the density and viscosity.  $\tilde{V}$  and  $\tilde{p}$  is the velocity vector field and hydrodynamic pressure scalar field. Reynolds number which presents the interaction

between the inertia and viscosity of the fluid is expressed by this equation. A low  $Re$  flow means a very viscous, slow and small environment and is referred to as creeping flow or Stokes flow around the robot. Thus, there is not a transition to turbulence, even behind bluff bodies. According to the equation (1), the role of time is negligible, and the flow pattern keeps relatively steady and is effectively reversible. Consequently, the reciprocal motion in this study just causes a negligible net movement [167].

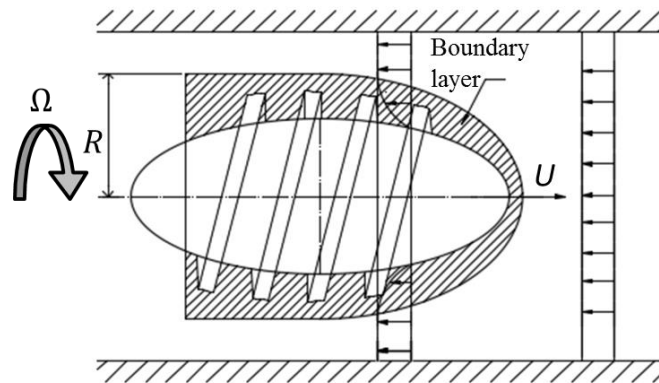


**Fig. 4-7. Flow field around swimming robot.**

**Relationship between the kinematics and robot structure.** Based on the above precondition, in order to optimize the structural parameters of the robot, it is still necessary to set up the relationship between the fluid dynamics and the structural parameters when designing the robot.

A coordinate was established as **Fig. 4-8A**. When the robot starts to rotate, the movement can be decomposed to the axial velocity  $u$  and the radial velocity  $v_a$ , and their components in  $x$  and  $y$  are calculated as:

$$w = v_a \sin \theta - u \cos \theta$$

$$v = v_a \cos \theta - u \sin \theta$$

where,  $w$  is the component of velocity in  $x$  direction, and  $v$  is that in  $y$  direction.  $\theta$  is the angle included angle between the spiral and the vertical direction.

**Fig. 4-8B** shows the schematic of the robot unfolding along with the  $a-a$  cross-section. To simplify the calculation, it is reasonable to neglect the arc influence [166] and consider the surface as flat. Also, we just analysis the pressure contribution in the range of one pitch.  $h_1$  and  $h_2$  are the distance between the robot surface and the tube wall. Because the radius in  $L_1$  and  $L_2$  are different, it results in a different tangential velocity  $v_{a1}$  and  $v_{a2}$ . And the expressions of the components in  $x$  direction are:

$$w_1 = v_{a1} \sin \theta - u \cos \theta, w_2 = v_{a2} \sin \theta - u \cos \theta$$

According to the *Newton inner friction law*, we can get the shear force of  $x$  and  $y$  direction in unit area as[168]

$$f_x = \frac{\tau_{x1}l_1(1-\beta)W + \tau_{x2}l_2\beta W}{L_1l_1 + L_2l_2}, f_y = \frac{\tau_{y1}l_1(1-\beta)W + \tau_{y2}l_2\beta W}{L_1l_1 + L_2l_2} \quad (2)$$

Where,  $\tau_{x1}, \tau_{y1}, \tau_{x2}$  and  $\tau_{y2}$  are the shear stress in  $L_1$  and  $L_2$ , respectively.  $\beta =$  spiral width ( $W$ )/spiral pith ( $P$ ),  $\gamma =$  spiral height ( $h$ )/distance between robot surface and tube wall ( $h_2$ ).  $l_1$  and  $l_2$  stands for the length of contour line along with spiral direction in both  $L_1$  and  $L_2$  area.

When the radius of the robot is  $r$ , it has

$$\frac{l_1}{l_2} = \frac{v_{a1}}{v_{a2}} = \frac{r-h}{r} = 1-\lambda$$

Where,  $\lambda = \frac{h}{r} = \frac{T\gamma}{r}$ .

Thus, according to the calculation results of  $\tau_{x1}, \tau_{y1}, \tau_{x2}$  and  $\tau_{y2}$  in [168], the total thrust force applied on the robot can be calculated as

$$F_a = A(f_y \sin \theta - f_x \cos \theta)$$

$$= \frac{2\pi\eta l}{h_2} \left[ \frac{3\beta(1-\beta)\gamma^2 \cos \theta (r-h_2(1-\gamma)) C_1 C_2}{(1-\beta)C_1 + \beta R(1+\gamma)^3 C_2} - \frac{(1-\beta)(r-h_2\gamma)u - \beta u}{h_2(1+\gamma)} \right] \quad (3)$$

Where,  $C_1 = (r-h_2\gamma)\omega r \sin \theta - ur \cos \theta$ ,  $C_2 = \omega \sin \theta - u \cos \theta$ .  $A$  and  $l$  are the surface area and length of the robot.  $\omega$  is the angle velocity.

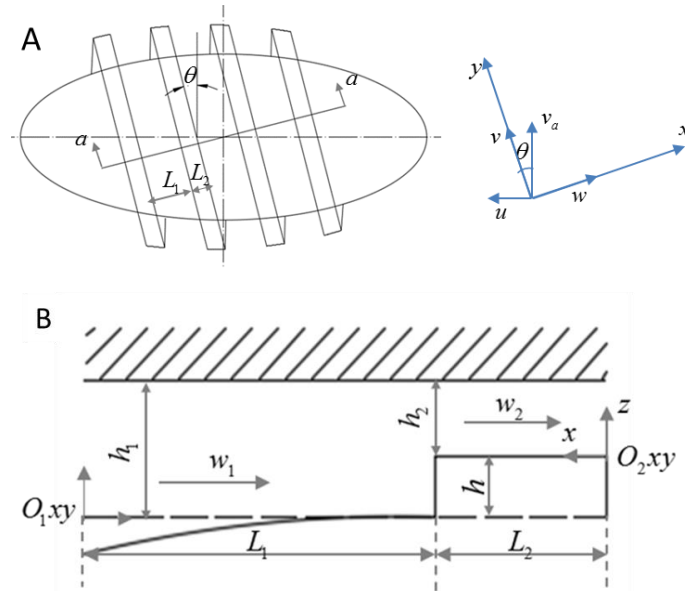


**Fig. 4-8. Kinematic analysis of the robot swimming in liquid.**

#### 4.3.4 Magnetic control

**Swimming behavior activated by rotating magnetic field.** The sum of nonfluidic force  $f$  and torques  $\tau$  acting on the magnetic robot can be described by a transformation of symmetric propulsion matrix [169].

$$\begin{bmatrix} u \\ \tau \end{bmatrix} = \begin{bmatrix} \frac{1}{\alpha + \psi_v} & \frac{-\beta}{\alpha + \psi_w} \\ \frac{\beta}{\alpha + \psi_w} & \lambda + \psi_w - \frac{\beta^2}{\alpha + \psi_v} \end{bmatrix} \begin{bmatrix} f \\ w \end{bmatrix} = A_{2,2} \begin{bmatrix} f \\ w \end{bmatrix} \quad (4)$$

Here,  $u$  and  $w$  are the robot's forward velocity and angular velocity respectively. The matrix parameters  $\alpha$ ,  $\beta$  and  $\lambda$  are related to geometric and environment property, which can be expressed as:

$$\begin{aligned}\alpha &= \frac{2\pi nr_1 (\xi_{//} \cos^2 \theta + \xi_{\perp} \sin^2 \theta)}{\sin \theta} \\ \beta &= 2\pi nr_1^2 (\xi_{//} - \xi_{\perp}) \cos^2 \theta \\ \lambda &= 2\pi nr_1^3 \left( \frac{\xi_{\perp} \cos^2 \theta + \xi_{//} \sin^2 \theta}{\sin \theta} \right)\end{aligned}\quad (5)$$

Here,  $n$  is the number of the spiral on the robot.  $\xi_{//}$  and  $\xi_{\perp}$  are constants denoting the viscous drag coefficients for the spiral structure locally along the length of the axis and normal to the axis, respectively. They present a linear relation with the viscosity of the flow and a complex relation with the geometry of the spiral [169].

The parameters of  $\psi_v$  and  $\psi_w$  in (4) are translational and rotational drag coefficient for the magnetic body, respectively.

$$\begin{aligned}\psi_v &= 6\pi\eta r \\ \psi_w &= 8\pi\eta r^3\end{aligned}\quad (6)$$

According to the symmetric matrix shown in equation (6), the motion behavior can be illustrated by **Fig. 4-9**. A step-out frequency will stop the linear increase of forward velocity along with the frequency. Beyond this frequency, the rotating magnetic field is no longer sufficient to drive the robot rotating synchronously. Thus, the speed decreases drastically.

The magnetic torque  $T_m$  acting on the robot in the rotated magnetic field  $H$  is given by:

$$T_m = \mu_0 VM \times H \quad (7)$$

where,  $M$  is the magnetic moment of the magnetic robot.  $\mu_0 = 4\pi \times 10^{-7} T \cdot m/A$  is the permeability of free space  $V$  is the volume of the robot in  $m^3$ . The component  $T_m$  on the robot is equal to  $\tau$  in equation (4).

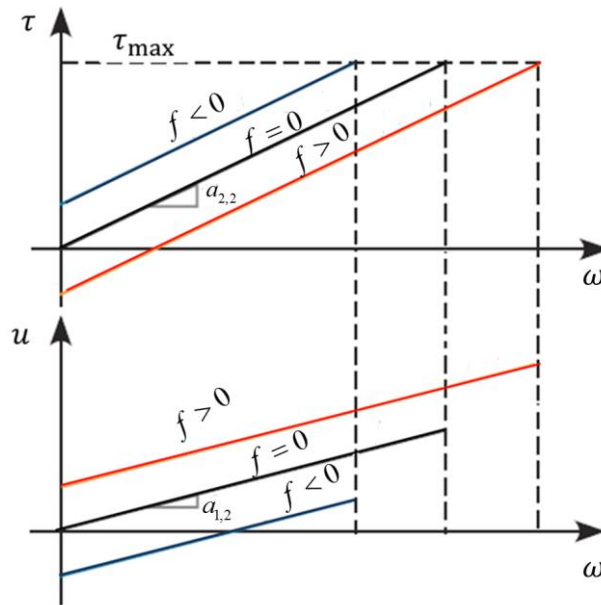


**Fig. 4-9. Qualitative motion behavior of magnetic-driven based on equation (2).**

**$a_{1,2}$  and  $a_{2,2}$  are the entries of matrix  $A$ .**

For the applied magnetic force  $f$  on the robot, it can be simplified as a permanent magnet. Thus, the spatial gradient in applied field at the location of the robot, is given as:

$$f = F = \mu_0 V (m \cdot \nabla) H \quad (8)$$

Here, we can also use magnetic flux density  $B$  to substitute the applied magnetic field in (5) and (6) by a simple translation of  $B = \mu_0 H$ . By taking the combination of (4), (7) and (8) into account, it is found that the rotation frequency of the magnetic field is the primary control input. After an instantaneous equilibrium between the magnetic

torque (7) and rotational fluidic drag torque, the robot rotates synchronously with the rotational magnetic field.

A theoretical magnitude of magnetic field of the manipulator can be described in a simplifying of a point-dipole model. The differentiation can be calculated to get the field gradient[149].

$$|H| = \frac{|\Gamma|}{4\pi|\tilde{p}|^3} \quad (9)$$

$$\frac{d|H|}{d|\tilde{p}|} = \frac{3|\Gamma|}{4\pi|\tilde{p}|^4} \quad (10)$$

Where,  $\Gamma$  is the magnet's magnetic dipole in  $A \cdot m^2$ , and  $\tilde{P}$  is the distance from the 3D printed objects to the dipole in  $m$ . It's easy to calculate the field power of the rotating manipulator repeating in a cycle of  $360^\circ$ , and the average strength acting on the robot mainly depends on the distance.

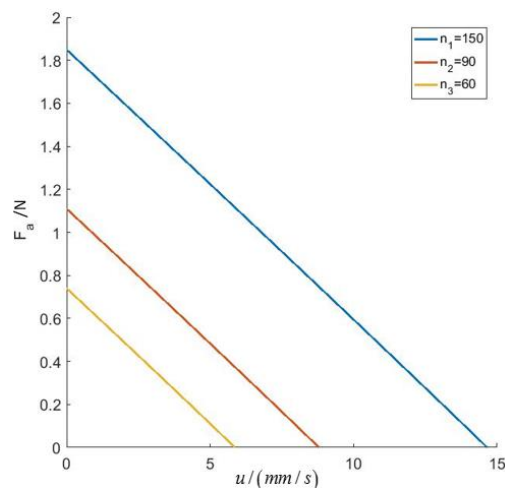
The magnetic field generated by a rotating permanent magnet was used to realize wireless propulsion to this 3D printed robot. The experiment was conducted to verify the ability to manipulate the i3DP robot under the magnetic field. The investigation of magnetic controlling was carried out in two aspects: one is to investigate the effect of the robot's shape on the swimming properties, the other is to analyze the effect of external magnetic field on the swimming properties of the magnetic robot.

#### 4.3.5 Optimization of spiral structure

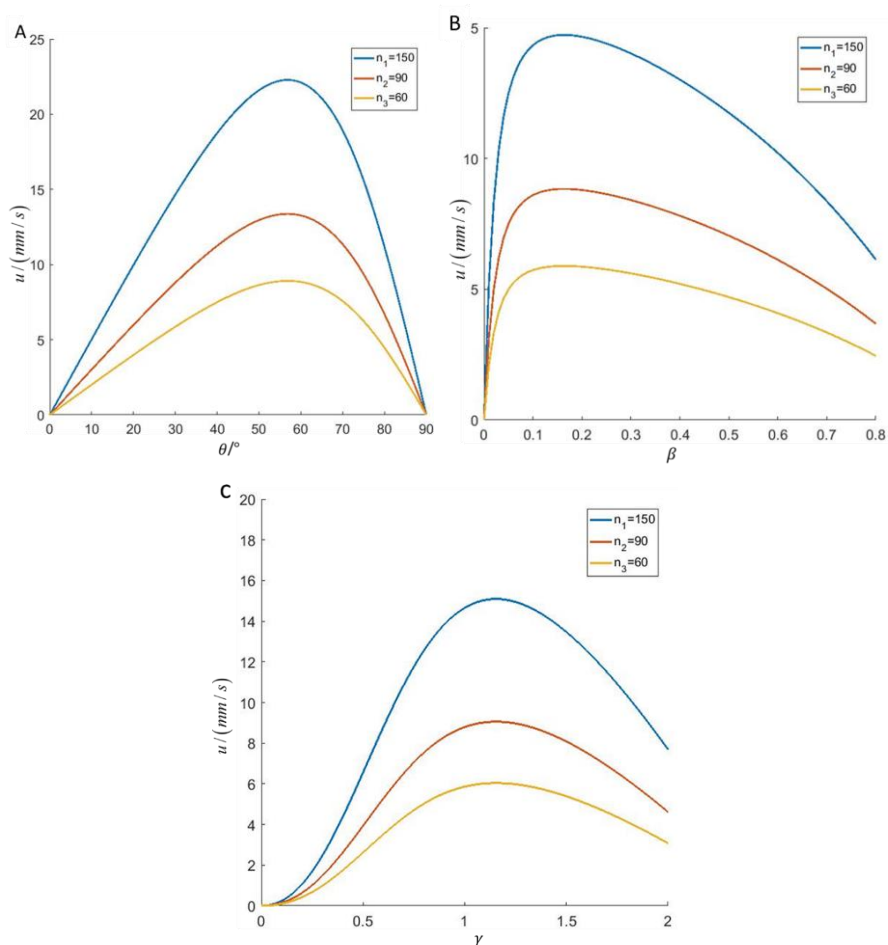
It is notable that the relationship between the thickness of the magnetic coating and the magnetic force is well understood. The interaction volume of magnetic response enhances with the increase of the thickness resulting in a subsequent increase of the magnetic force acting on the robot. Here, all the robots have a constant layer thickness

of 200  $\mu\text{m}$ . Thus, it is reasonable to eliminate the influence of the coating thickness for the magnetic characterization. The global dimension of was fixed as 25 mm of major axis and 10 mm of minor axis. As shown in the schematic of the magnetic robot in Table 1, the spiral is characterized by the pitch  $P$ , height  $h$  and width  $W$ . In order to investigate the effect of these parameters, simulations were conducted by MATLAB to confirm the optimum design of the robot according to (3). Fig. 4-10 shows the relationship between the axial force and the velocity under different rotation speed. It shows the thrust force  $F_a$  decreases with the increase of velocity  $u$ . When  $F_a=0$ , the swimming velocity gets to the maximum. Therefore, the optimum parameters can be determined by plotting their influence on the swimming velocity  $u$  at the situation of  $F_a=0$ .

**Fig. 4-11** shows the influence of spiral angle  $\theta$ , spiral width coefficient  $\beta$  and height coefficient  $\gamma$  on the velocity  $u$  at different rotation speed. When  $\theta$  gets to  $60^\circ$ , the swimming velocity can arrive to the maximum. And the optimum width and height coefficient are 0.15~0.2 and 1.0~1.2, respectively.

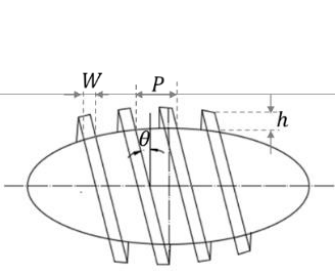


**Fig. 4-10.** The relationship between the thrust force  $F_a$  and swimming velocity  $u$  at three different rotation speeds, 150r/mim, 90 r/min and 60 r/min. The other parameters were set as  $\theta=30^\circ$ ,  $\beta=0.2$ ,  $\gamma=1$ ,  $h_2=2$  mm,  $r=5$  mm,  $\eta=1$  Pa·s,  $l=25$ mm.



**Fig. 4-11. Relationship between the design parameters and the swimming velocity. (A) Spiral angle  $\theta$ , (B) spiral width coefficient  $\beta$  and (C) height coefficient  $\gamma$ .**

**Table 4-1. Series of robots with different spiral shape,  $l=25\text{mm}$ ,  $r=5\text{mm}$ ,  $h_1=4\text{mm}$ . (unit: mm)**

	Number	Angle, $\theta$	Pitch, $P$	Height, $h(\gamma=h/(h_1-h))$	Width, $W(\beta=W/P)$
	M1	30	5	2(1.0)	1(0.2)
M2	60	5	2(1.0)	1(0.2)	
M3	80	5	2(1.0)	1(0.2)	
M4	60	2	2(1.0)	1(0.2)	
M5	60	5	2(1.0)	0.2(0.04)	
M6	60	5	1(0.33)	1(0.2)	
M7	60	5	2.5(1.67)	1(0.2)	

To verify the simulation results, Table 4-1 lists the experimental candidates of different spiral shapes used in the following test. All measurements were conducted radially to the rotating magnetic field by paralleling the robot to the magnet with a distance  $d$  of 10 mm (a maximum 0.08 T magnetic field was acted on the robot). All robots moved in a tube (inner radius 5.4 mm) full of water to simulate the backlash force on the spiral. **Fig. 4-12A** reveals the relationship between the spiral angle and the swimming velocity. It shows a great accordance with the simulation result that the velocity gets to the maximum value at  $\theta = 60^\circ$ , and either smaller or larger angle will decrease the velocity. In **Fig. 4-12B**, when the ratio of pitch ( $P$ ) to width ( $W$ ) is 0.2, it reaches to the fastest swimming velocity, which is consistent with the simulation shown in **Fig. 4-11B**. And it is clear to see that either increasing or decreasing the ratio will reduce the swimming velocity. **Fig. 4-12C** illustrates the relationship between the spiral height and velocity. Because the larger spiral height causes bigger drag force and lower height decreases the active working area, too high and too low height will result in side effects. The robot of spiral height  $h=2.0$  presents the fastest swimming speed which conforms to the simulation shown in **Fig. 4-11C**. Generally, we can see from the measurements that spiral width shows less influence on the swimming velocity than that of spiral angle and height. Also, all the measurements reveal that the velocity was proportional to the rotation rate, which fits with the results shown in **Fig. 4-9** and **Fig. 4-10**.

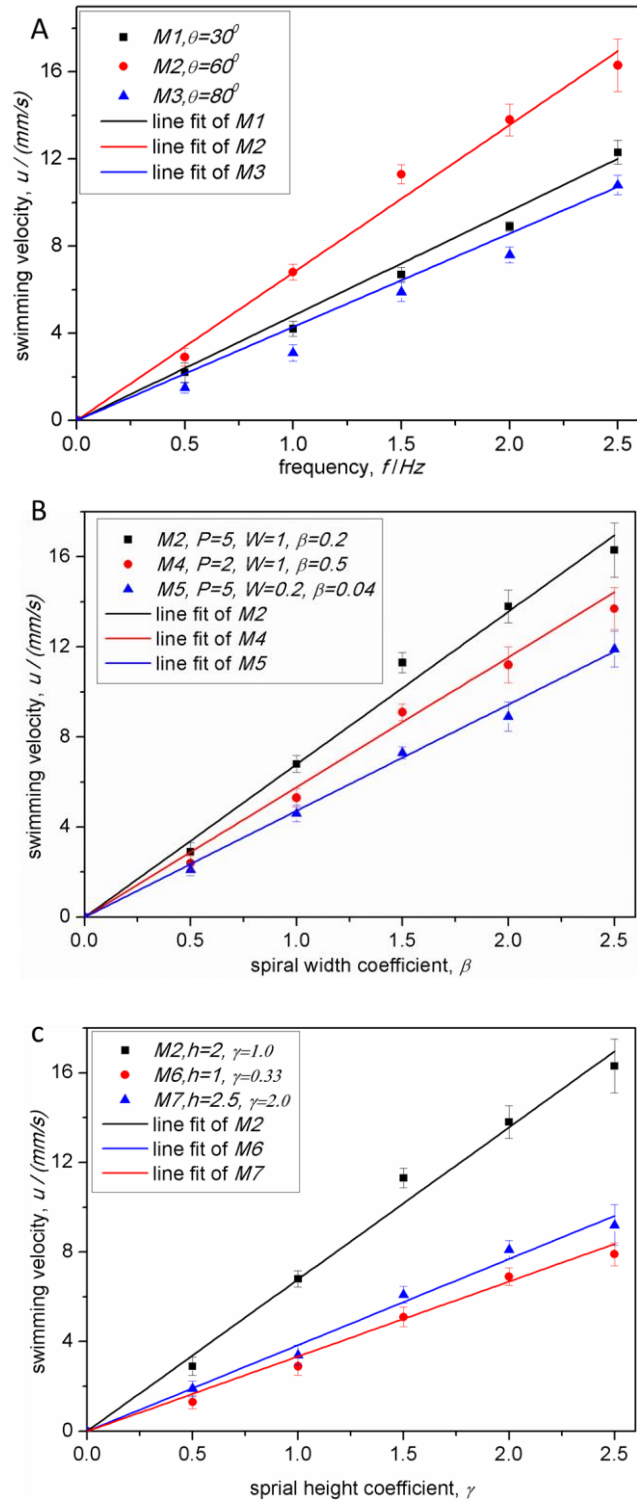


**Fig. 4-12. Effect of spiral shape (A. spiral angle, B. spiral width, C. spiral height) on the swimming velocity.**

#### 4.3.6 Effect of viscosity on the swimming properties.

According to equation (6), translational  $\psi_v$  and rotational drag coefficient  $\psi_w$  are proportional to the viscosity  $\eta$ . Consequently, the viscosity is in a linear relationship with the  $\alpha, \beta, \lambda$  of (5). Therefore, when doubling the viscosity with keeping all other parameters constant, the step-out frequency will be reduced by half and, consequently, halves the maximum velocity. That is, the fluid viscosity affects the maximum velocity concerning inverse proportion.

**Fig. 4-13** depicts the robot (M1) swimming in a plastic lumen via a radial propulsion (distance is 10mm from the robot to the permanent magnet,  $f=1.0\text{Hz}$ ). When there was no liquid in the tube (**Fig. 4-13A**), approximated 60 mm linear movement was measured along the axis in 8 s. For this situation, because the viscosity of air is negligibly small, the backlash is mainly generated by the friction between the robot and the tube wall. It was found that the liquid (**Fig. 4-13B**) can act as lubrication to make the rotation more smoothly. However, due to the increase of the drag force, the movement is slower with the same magnetic force where it took 13 s to finish 55 mm. Furthermore, when this manipulation was performed in the hydrogel of high viscosity, the frictional force caused by the high viscosity will increase the start torque. The magnetically induced torque is not enough to overcome the drag torque, and even high frequency of magnetic field was no longer able to activate the object to rotate.

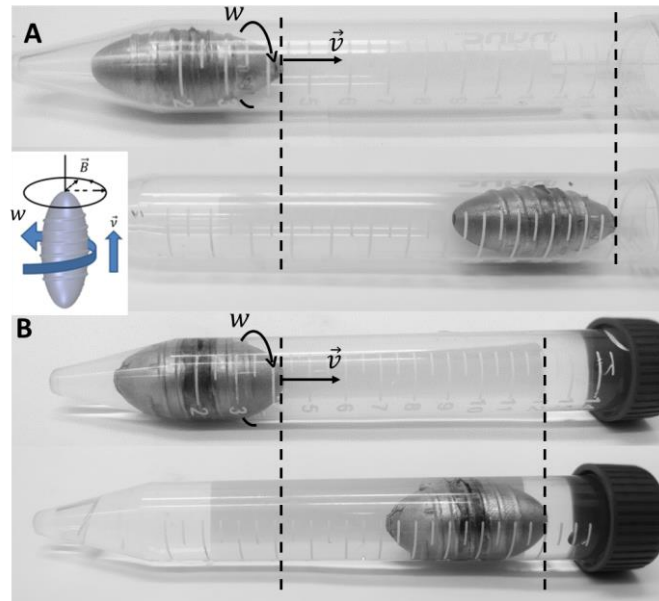


**Fig. 4-13. Robot (M1) rotates along its long axis in an empty plastic tube (A) and full of distilled water (B). The inset shows the schematic of magnetic force applying to the rotor.**

#### 4.3.7 Effect of rotating magnetic field.

To investigate the effect of external magnetic field on the manipulation, two control strategies were used to realize the controlling of the magnetic robot. As shown in **Fig. 4-14**, a permanent magnet rotates radially to produce a rotating magnetic field while the robot was propelled in two methods: along the axis of the rotation and perpendicular to the axis, respectively. External magnetic field induces magnetization to the robot, then drove it to rotate. Because of the existence of spiral structure on the surface, it is effective to transfer the rotation into linear motion in either direction, forward or reverse, by manipulating the rotation direction of the magnetic field. An experimental robot we used here is M2 (swimming in water), of which the spiral has pitch of 5 mm, height of 2 mm and width of 1 mm.

For the axial swimming, two swimming characteristics appear during robot's swimming, namely, step-out and break-away. For the behavior of step-out, it means the

frequency of rotation over which the magnetic field cannot propel the robot anymore. As described above, this behavior can be explained by the symmetry matrix (4). As illustrated by equation (9), the step-out frequency can be calculated indirectly as a function of the distance from the permanent magnet in the control region. As for the break-away behavior, it denotes the frequency over which the propulsion on the robot can overcome the attractive gradient force, and thus the robot can move away from the magnet. Therefore, it is straightforward to speculate that the applying frequency for manipulation is ranging from the break-away to step-out. **Fig. 4-15** shows the relation between rotation frequency and the distance between the manipulator and the robot. It is evident that, during the swimming, the robot always swims above the break-away frequency and below the step-out frequency, which follows the theoretical result of (4). It also shows that when the robot is close to the permanent magnet, break-away occurs at high rotation frequency, but it cannot swim long route before reaching to step-out. When the robot is further away from the magnet, break-away happens at low rotation frequency because of the less propulsion. However, the robot can swim to a farther distance at this situation.

As for the radial swimming, the robot was placed directly beneath the permanent magnet and can rotate synchronously in either forward or backward direction. Also, due to the local minimum in the field gradient, the robot will align itself just below the magnet. Unlike axial swimming, the local minimum in the attractive force can propel the robot at any frequency. That is, no break-away frequency appears during the radial swimming. As shown in **Fig. 4-16**, the magnet can propel the robot at a constant frequency until it is too far from the magnet, which is step-out. The results also show that when the robot starts from a closer distance from the magnet, it is able to swim longer. It is well explained by equation (9) that the magnetic field decreases along with the increase of the distance between the robot and the magnet. Furthermore, compared

to axial swimming, the permanent magnet can be closer to the robot. When the magnet moves at the same velocity as that of the robot, it can propel the robot in a constant magnetic field. In both the axial and radial swimming, the robot presents similar swimming behaviors with other research work with a robot made of permanent magnet [149]. This also states the feasibility of i3DP in fabricating remote controlling objects.

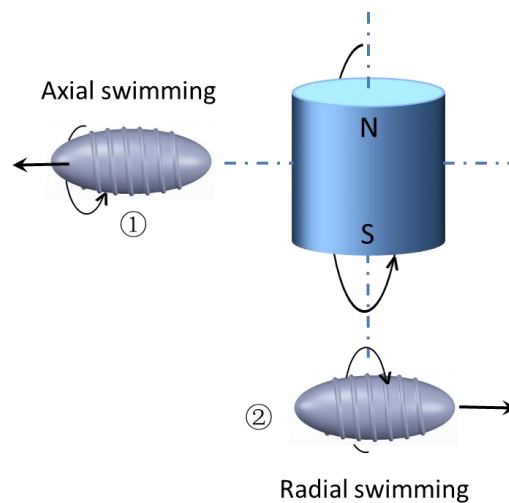


**Fig. 4-14. Axial swimming and radial swimming in rotating magnetic field.**

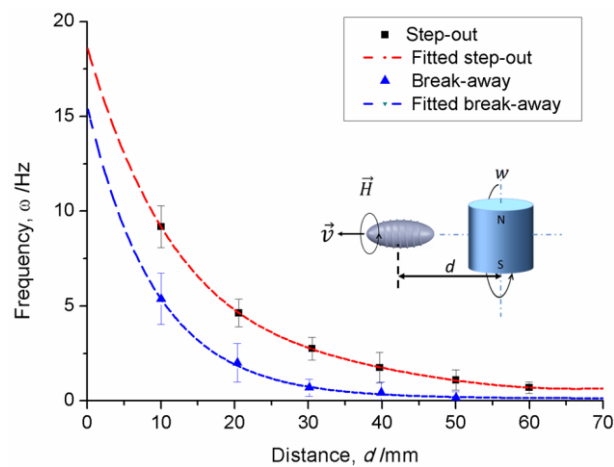


**Fig. 4-15. Axial swimming of the magnetic robot. Red dash line and blue dash line represent the fitted curve of step-out and break-away, respectively.**

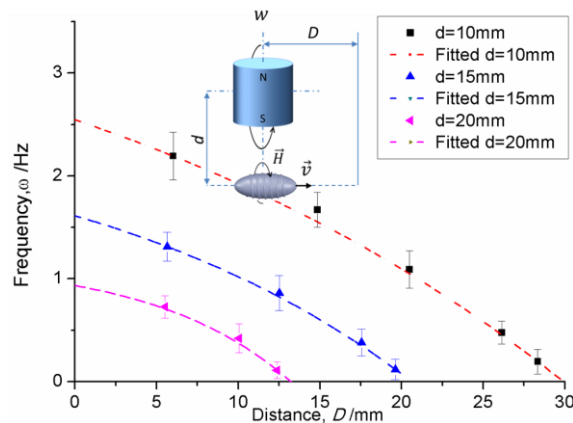


**Fig. 4-16. Frequency of the rotating magnetic field vs. distance of the robot the rotation axis during radial swimming.**

#### 4.4 Conclusion

In summary, a facile and effective approach has been demonstrated to fabricate magnetically manipulated robot by the proposed initiator-integrated 3D printing technique. A layer of bi-alloy magnetic coating was in-situ grown on a 3D structure to generate a magnetic object via surface-initiated ATRP and the subsequent polyelectrolyte-brush-assisted ELP process. A robot with Ni-rich magnetic coating was demonstrated, which exhibited a soft-magnetic property. The magnetic manipulation demonstrated that the ellipsoid robot was successfully magnetized, and rotated synchronously with the magnetic field. The rotational movement can be translated subsequently to linear movement by carefully designing the spiral structure and the strategy of magnetic controlling. According to the kinematic and magnetic analysis, the swimming properties under magnetic control were affected by the spiral shape, liquid viscosity and the controlling manner. Our investigation has shown that the proposed combination of 3D printing for architecture design and surface modification techniques works well for fabrication of remote controlling objects. This technique offers 3D printing with potential application in fabrication of magnetically driven micromachines/systems.

## Chapter 5

### 5 Strength-enhanced cellular materials by i3DP and the optimal design

This chapter mainly focuses on the fabrication of optimized cellular materials which was inspired by the study of magnetic coating described in last chapter. First, octet-truss and pyramidal lattice materials were optimally designed. Effective properties of these two cores were presented and compared. Next, generic post-printing modification was employed to fabricate the metallic ordered lattices. And the strength-enhanced properties were investigated to highlight the influence of nano-metal coating on the mechanical properties.

#### 5.1 Introduction

Nature evolves cellular materials for many situations where low density yet high stiffness and strength are needed [170]. Examples are beaks and bones of birds which consist of thin, solid skins attached to a highly porous and cellular core [171]. The desired properties of low density yet high strength have attracted humankind's long-standing efforts on architected materials. Although ranges of synthetic materials have been developed, such as metal alloys, which are superior to the biological base materials, the developed cellular materials are much less sophisticated than nature's. Foams are the mostly used architectures today because they can be readily manufactured, although they are far from ideal for many applications [172]. However, the pseudo-stochastic cancellous architectures of foams lead to non-uniform mechanical properties, and the local heterogeneous structure makes it difficult to predict the properties and mechanical behaviors of foams.

Emerging highly ordered architectures have been proposed to address the challenge by creating so-called mechanical metamaterials [64]. Their hierarchical structures can result in an efficient distribution of the constituent material [49, 173], and then provide material with the capability to withstand higher mechanical loads [174]. To date, various architected cellular materials have been developed, which have broad potentials in mechanical, optical, electrical, electromagnetic, thermodynamic and acoustic fields. Unique mechanical characteristics were also demonstrated, such as superior stiffness, negative Poisson's ratio, and negative stiffness, etc. [66, 69]. Yet, the key issue is how to design and achieve such structures in a fast, cost-effective, and high throughput way. It is imperative to develop an effective platform for optimal design and fabrication; thus, the geometric parameters can be carefully assigned to meet the desired performance.

The emerging additive manufacturing enables the fabrication of cellular materials with more complex architectures. Very recently, well-controlled 3D cellular structures were fabricated by 3D printing, and simultaneously with unique yet deterministic mechanical properties, for example, ultra-light metallic micro-lattices [175, 176], high-strength ceramic composites [71, 177], and zero thermal expansion lattices [173]. In parallel, computational methods have improved significantly to the design of materials and structures with a complex cellular architecture which is optimized for specific applications.

Here, the feasible functional 3D printing technology described in Chapter 3 was employed to fabricate metallic cellular structures. 3D printing was used to prepare large-scale complex geometries while post-surface modification was used to add detailed metallic features. Two representative core materials, octet-truss and pyramidal cellular structures, were built through this strategy with Ni- and Cu-film coated. To optimize the mechanical properties, the configurations of two lattices were theoretically analyzed and optimized. And the mechanical enhancement after the ELP of metal

coating was also investigated by comparing with polymer-based cellular materials.

## 5.2 Optimal design and the effective properties

**Fig. 5-1** shows the CAD design of truss-assembled lattice materials. **Fig. 5-1A** has an octet-truss structure, while **Fig. 5-1B** is composed of pyramidal cells.  $(x,y,z)$  denotes the Cartesian coordinate system for the cell. For both cells, the structure is characterized by the radius of strut  $D$ , distance between two adjacent nodes  $L$ , and the angle  $\theta$  between the strut and the horizontal plain. The parameter  $L$  is usually used to indicate the size of a representative lattice. Relative density  $\bar{\rho}$  is defined as the ratio of the density of the lattice material to the density of the solid material of which the lattice is made.

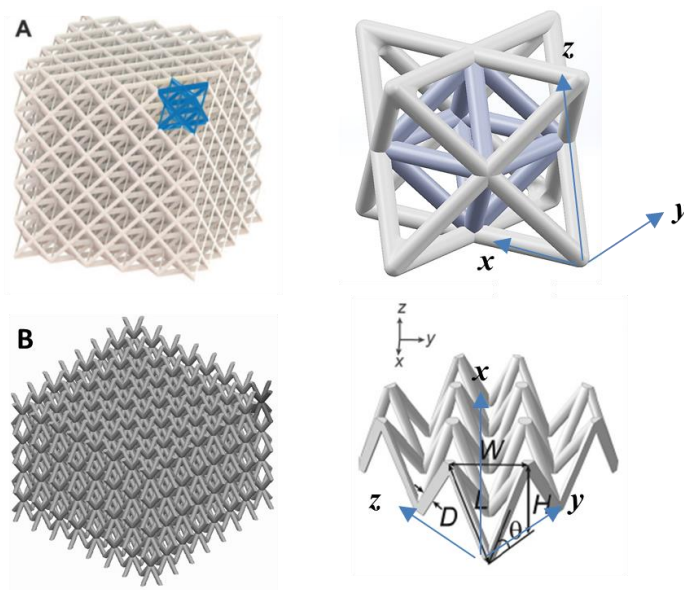


**Fig. 5-1. Cellular materials with octet-truss core (A) and pyramidal core (B).**

### 5.2.1 Effective relative density

The relative density for octet-truss core is:

$$\bar{\rho} = 6\sqrt{2}\pi \left(\frac{D}{L}\right)^2 \quad (1)$$

For pyramidal core, it is:

$$\bar{\rho} = \frac{2\pi}{\cos^2 \theta \cdot \sin \theta} \left( \frac{D}{L} \right)^2 \quad (2)$$

The objective of optimization is to find the optimal structure parameters that minimize the weight of two cores. The relative density of octet-truss core can be determined with a fixed strut aspect ratio-  $D/L$ , while the angle  $\theta$  issues most on the weight efficiency of the pyramidal core. Then the optimization problem requires the minimization of relative density of pyramidal core lattice. Equation (2) can be simplified as:

$$\bar{\rho}_m = C_m \cdot \frac{1}{\cos^2 \theta \cdot \sin \theta} \quad (3)$$

Where  $C_m$  is a constant parameter, as  $2\pi \left( \frac{D}{L} \right)^2$ . The solution to this problem can be addressed through derivation. It has:

$$\bar{\theta} = 35^\circ \quad (4)$$

The result indicates that for pyramidal core lattice, the optimal angle to reach minimal relative density is  $\bar{\theta} = 35^\circ$ .

### 5.2.2 Effective moduli

Another optimization relies on maximizing the stiffness with respect to angle  $\bar{\theta}$ . To eliminate the influence of bending stiffness and strength on the effective stiffness. The strut aspect ratio,  $D/L$ , is assumed to be sufficiently low so that the bending stiffness and strength are negligible. Thus, the materials can be considered as consisting of pin-jointed trusses, which deform in tension or compression only [178]. Under such assumptions, the effective moduli of pyramidal core can be deducted by the following steps according to literature [179]: 1. Apply stress boundary conditions to the surfaces

of the cuboid cell; 2. Calculate the corresponding forces on the node, and then distribute them to every strut in the cell; 3. Analyze the struts deformation; 4. Calculate the cell overall displacement. The effective shear stiffness  $G_{xy}$  and  $G_{xz}$  of pyramidal core can be obtained as:

$$G_{xy} = G_{xz} = \pi \sin \theta \left( \frac{D}{L} \right)^2 E_s \quad (5)$$

Where  $E_s$  is the Young's modulus of strut material.

The optimization problem is defined as the maximization of the ratio of effective stiffness to the relative density, thus:

$$\max \left( \frac{G_{xy}}{\bar{\rho}} \right) = \max \left( \frac{G_{xz}}{\bar{\rho}} \right) = \frac{1}{2} \pi E_s (\sin^2 \theta \cos^2 \theta) \quad (6)$$

Then the optimization result of angle is  $\bar{\theta} = 45^\circ$ . We can step further to get the effective strength as:

$$\frac{\tau_{xy}}{\sigma_y} = \frac{\theta}{\cos \theta} \left( \frac{D}{L} \right)^2 \quad (7)$$

Where  $\sigma_y$  is the yield stress of strut material.

The optimization problem is defined as the maximum ratio of effective strength to relative density.

$$\max \left( \frac{\tau_{xy}}{\bar{\rho}} \right) = \frac{1}{2} \sigma_y \cdot \max (\sin \theta \cos \theta) \quad (8)$$

Then, it is easy to get the optimization result for this project when  $\bar{\theta} = 45^\circ$ .

According, we can get the conclusion that, for pyramidal, when  $\bar{\theta} = 45^\circ$ , it can present the optimal stiffness divided by relative densities, although  $\bar{\rho}$  is slightly larger (about 8.9% higher) than that of  $\bar{\theta} = 35^\circ$ . Therefore, the following discussions in this study will be based on the condition of  $\bar{\theta} = 45^\circ$ .

For the octet-truss core, the effective moduli were deduced as [180], along with the associated coordinate system in **Fig. 5-1A**. **Table 5-1** lists the summary of effective properties of two lattice materials. The effective moduli of octet-truss material is from [180].

**Table 5-1. Effective properties of several lattice materials.**

	Relative density	Effective Young's moduli	Effective shear moduli
Octet-truss	$\bar{\rho}=6\sqrt{2}\pi\left(\frac{D}{L}\right)^2$	$E_{xx} = \frac{1}{4}\bar{\rho}E_s$ $E_{yy} = \frac{1}{8}\bar{\rho}E_s$ $E_{zz} = \frac{1}{8}\bar{\rho}E_s$	$G_{xy} = G_{xz} = \frac{1}{8}\bar{\rho}E_s$
Pyramidal core	$\bar{\rho}=4\sqrt{2}\pi\left(\frac{D}{L}\right)^2$	$E_{xx} = E_{yy} = E_{zz} = \frac{1}{9}\bar{\rho}E_s$	$G_{xy} = G_{xz} = G_{yz} = \frac{1}{12}\bar{\rho}E_s$

### 5.2.3 Comparison of effective properties among various lattice

The effective Young's and shear modulus of two truss structures are plotted as functions of relative density in **Fig. 5-2**. In the figure, the slopes of each line are indicated correspondingly to the property. At low relative density ( $\bar{\rho} < 0.25$ ), all these two truss configurations are usually stronger than those of honeycomb if all moduli are considered [65]. It is because the deformations of lattice materials are governed by stretching or compression of struts while the in-plane deformation of honeycombs is governed by cell wall bending rather than stretching/compression. At the same relative density, pyramidal truss has a higher modulus than octet-truss. Therefore, if high stiffness under low weight is the most important design requirement, the pyramidal

truss is preferred.

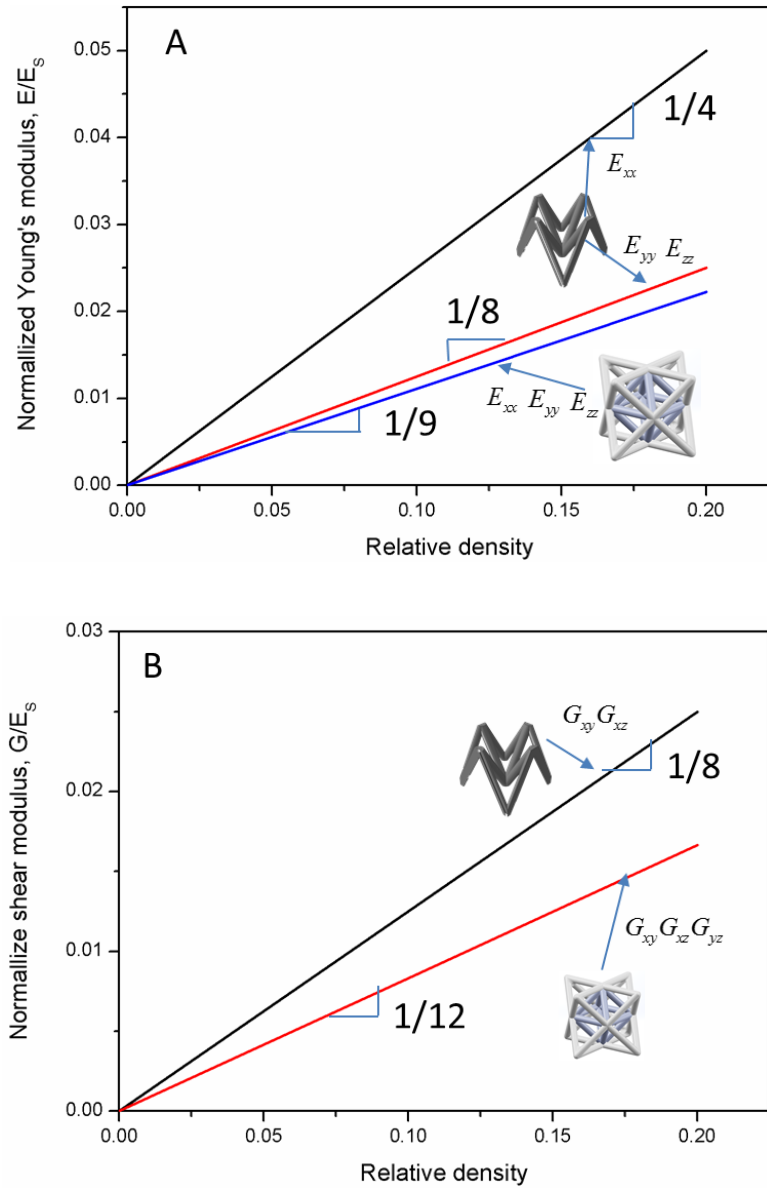


**Fig. 5-2. Comparison of the effective Young's modulus (A) and shear modulus (B) as a function of relative density for octet-truss and pyramidal core structures.**

## 5.3 Metallization via post-printing modification

### 5.3.1 Experimental setup

**Materials.** Commercial 3D printing resin was purchased from Asiga, which is mainly

composed of acrylate-based prepolymers. All other chemicals were purchased from Sigma-Aldrich and used as received except that CuBr was purified by washing through glacial acetic acid.

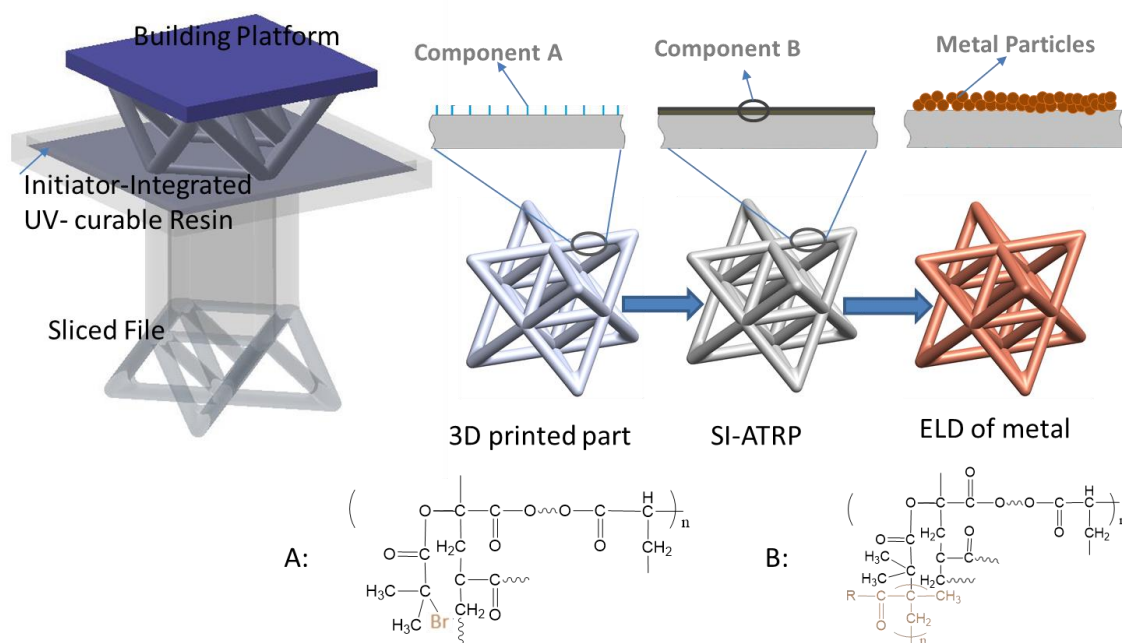


**Fig. 5-3. Schematic illustration of the fabrication of metallic cellular lattices.**

**Both octet-truss and pyramidal lattices are based on the same approach.**

**Initiator-integrated resin and 3D printing.** Metallic lattices were prepared through the proposed functional 3D printing described in Chapter 3. As shown in **Fig. 5-3**, an initiator-integrated UV-curable resin was first prepared, followed by the 3D printing process and the SI-ATRP assisted ELP. Briefly, 5 wt.% BrMA was mixed well into the resin base and then degassed for 1h in dark. 3D structures were designed by Solidworks (Dassault Systèmes) and printed layer by layer via a commercial 3D printer (PIC2, Asiga). Here, both octet-truss and pyramidal cellular architectures were designed following the optimization result from Section 5.2. The strut angle  $\theta$  was designed as  $45^\circ$ . The strut aspect ratio  $D/L$ , was fixed as  $1/4$ . Our previous results showed that there was no influence of the mixed initiator on the printing process, thus the architectures

were printed with a normal setting. The printed objects were ultrasonically rinsed for 10 min in ethanol to eliminate the adhesive residue on the surface and dried in the air. The initiator-containing structures were ready for the subsequent surface modification to induce functional metallic coatings. The polymer octet-truss and pyramidal lattices are shown as **Fig. 5-4A** and **Fig. 5-4D**, respectively.

***Fabrication of metallic octet-truss and pyramidal cellular materials.*** Ni- and Cu-coating were deposited subsequently to obtain metallic cellular architectures. The metallization process was following the procedures described in Chapter 3. Typically, the PMETAC-coated 3D samples were immersed into a 5 mM  $(\text{NH}_4)_2\text{PdCl}_4$  aqueous solution for 15 min. After  $\text{PdCl}_4^{2-}$  moieties immobilizing onto the brushes by ion exchange and rinsing thoroughly with water, the samples were immersed into the house-made plating bath to obtain metallic architectures. The ELP of Ni and Cu was prepared and conducted as the protocols described in Chapter 3.

***Characterization.*** Because this study follows the same metallization protocol as that described in Chapter 3, it is not necessary to detect again the chemical composition during the SI-ATRP process. Therefore, one can read the analysis (i.e., XPS) referring to the previous Chapters. The morphology of the surface coating was examined by SEM (Hitachi TM3030Plus) at a 15 Kv accelerating voltage. The compression tests were carried out on a servo-electric multi-functional test stage (Deben MICROTTEST tensile/compression/bending stages). The test stage is equipped with a standard miniature load-cell in the range 2 N to 200 N, which has accuracy readout of  $\pm 1\%$ , dynamic resolution 0.1% and static resolution 0.05% of the full-scale range. All the compression tests were conducted at a rate of 0.5 mm/min. Load-displacement curves were recorded. Then the relationship between strength and strain were obtained. In the compression tests, the compressive strength is defined as the maximum compressive strength before collapse and the value is the stress at the inflection point of stress strain

curves.

### 5.3.2 Results and discussion

**Metallic cellular materials.** Ni- and Cu- coated metallic lattices were prepared through polyelectrolyte-assisted ELP. Both octet-truss and pyramidal lattices are fabricated as a cube, with an overall dimension of 14 mm × 14 mm × 14 mm for width × length × height. **Fig. 5-4** shows the 3D printed metallic cellular materials with features of octet-truss and pyramidal structure.

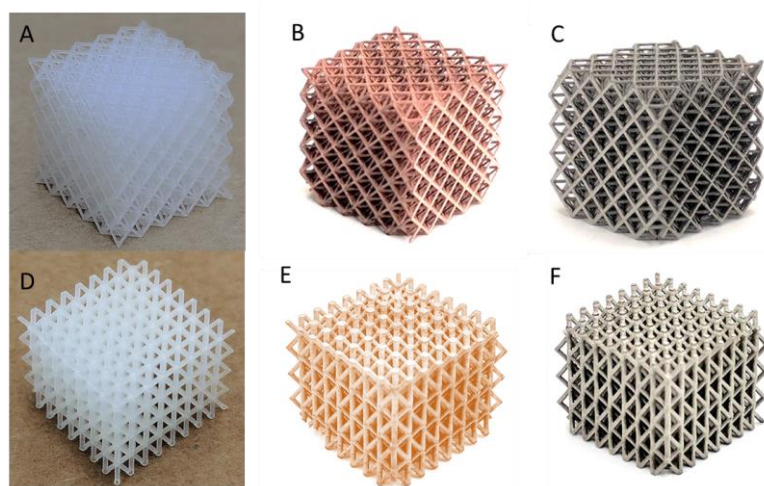


**Fig. 5-4. 3D printed octet-truss cellular materials (A. polymer, B. Cu-coated, C. Ni-coated) and pyramidal cellular materials (D. polymer, E. Cu-coated, F. Ni-coated)**

SEM was conducted to investigate the surface morphology of the Ni layer, as **Fig. 5-5**. It was found that, in the z direction (**Fig. 5-5B**), the lattice was built layer-by-layer, with each layer having a thickness consistent with the set point for printing (50 μm). Importantly, the connections between layers are excellent, without any cracks or delamination, resulting in a robust microlattice. It is evident that, compared to the flat surface in the x and y directions (**Fig. 5-5A**), the column in the z direction is a bit rougher.

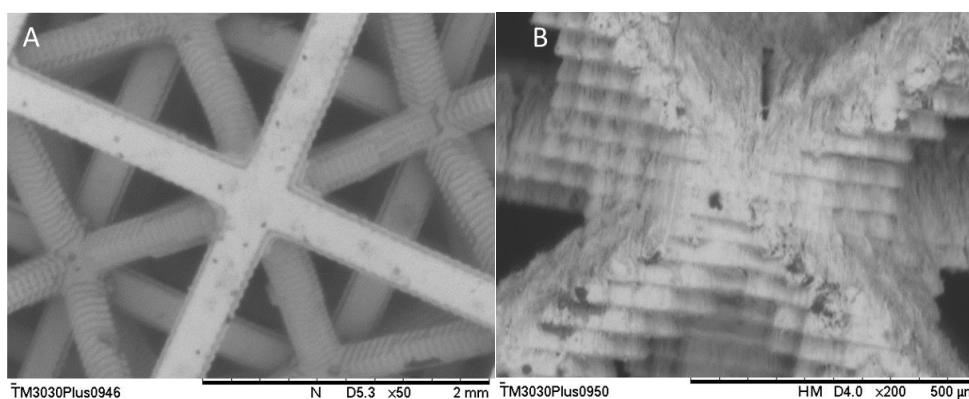
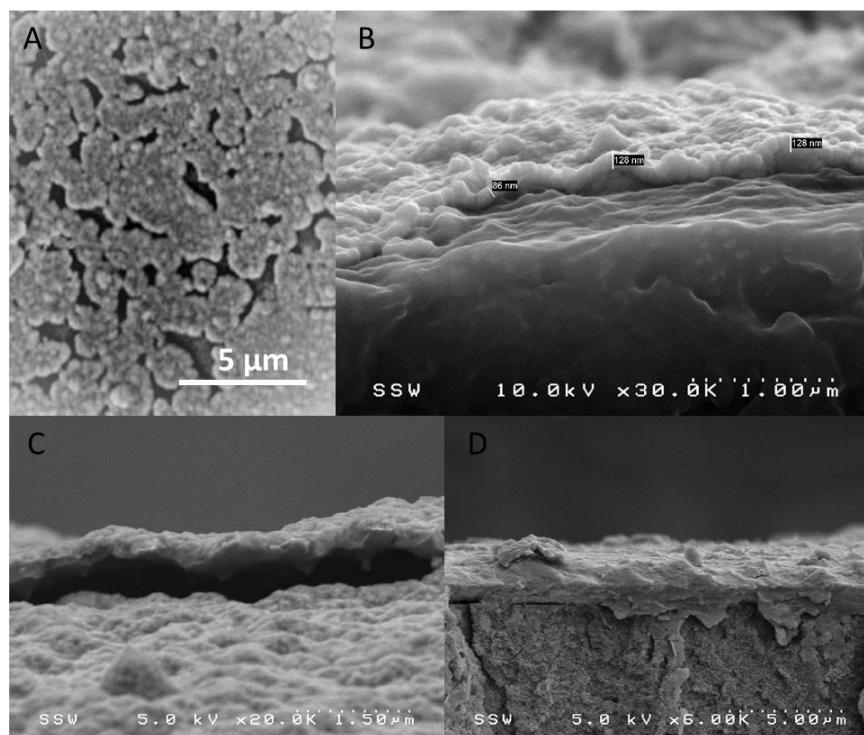


**Fig. 5-5. Surface morphology of Ni-coated octet-truss lattice in the  $z$  (A) and  $x, y$  direction.**

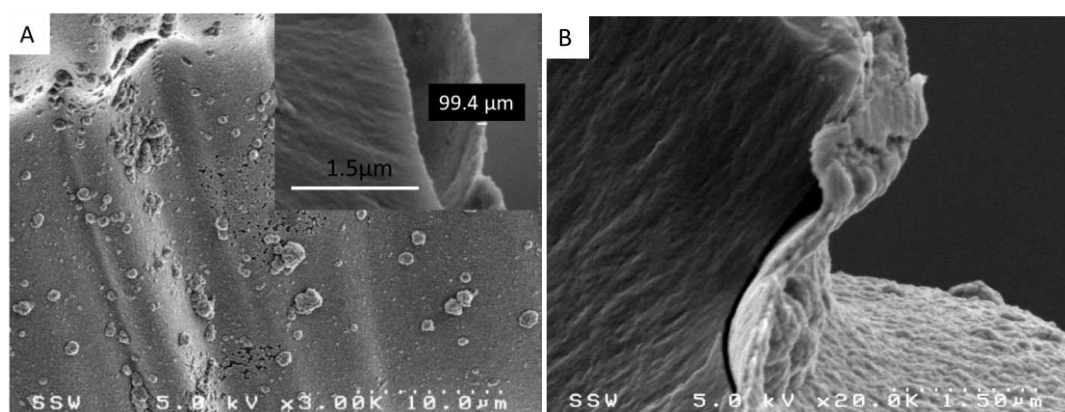
To obtain the influence of metal coating thickness on the mechanical properties. A series of cellular materials are fabricated with different metal thickness. Typically, for this polyelectrolyte-assisted deposition, the obtained metal film is highly dependent on the ELP time [63, 112]. **Fig. 5-6** shows the thickness of Ni-coating upon different ELP time. The coating produced by 15 min of ELP is  $\sim 120$  nm, yet to make a uniform coverage on the microlattice (**Fig. 5-6A** and **B**). While 30 min of ELP can produce a Ni-coated surface with uniform coverage, and the thickness of Ni layer was ca. 300 nm (**Fig. 5-6C**). With increase of the ELP time, a thicker metal layer can be obtained. **Fig. 5-6D** shows the Ni-layer produced after 180 min ELP, which was ca. 1.5  $\mu\text{m}$ . Technically, according to the thickness detected via SEM, it was found the thickness of both Ni- and Cu- presents a linear relationship with ELP time. A function of Ni layer thickness of ELP time can be established approximately as:  $T=8t+23$  (nm), where the  $T$  is the thickness of metal layer, and  $t$  is ELP in a unit of min.

Similarly, the thickness of Cu layer upon ELP time was observed as **Fig. 5-7** [112]. 15 and 20 min of ELP both produced Cu-coated lattices with uniform coverage of metal film, and the thickness of Cu layer was ca. 140 and 230 nm, respectively, whereas the Cu layer obtained at 10 min of ELP was not very dense, with a thickness of ca. 100 nm.

Obvious defects can be found at 10 min of ELP. This indicates that at least 15 min of ELP is necessary to produce a metallic architecture with a uniform Cu coating. And the function of Cu coating thickness to ELP can be calculated as:  $T=13t-38$  (nm).



**Fig. 5-6. SEM images showing the surface of the Ni-coated lattice obtained at 15 min (A, B), 30 min (C), and 180 min (D) of ELP. The thickness of Cu layer is c.a. 120 nm, 300 nm, and 1500 nm, respectively. The Ni film obtained at 15 min of ELP was not uniform and had some defects (A).**



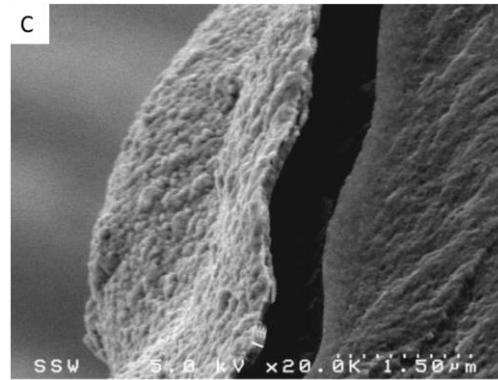


**Fig. 5-7.** SEM images showing the surface of the Cu-coated lattice obtained at 10 min (A, inset shows the thickness), 15 min (B), and 20 min (C) of ELP. The thickness of Cu layer is c. a. 100 nm, 140 nm, and 230 nm, respectively. The Cu film obtained at 10 min of ELP was not uniform and had some defects (A).

*Compression of 3D polymer-based lattices.* To detect the mechanical responses, uniaxial compression experiments were monotonically and cyclically performed on the polymer-based lattices. The mechanical properties of all the lattice structures are summarized in

**Table 5-2**, and the stress-strain curves of octet-truss and pyramidal microlattices are shown in **Fig. 5-8** and **Fig. 5-9**, respectively. It was found that both octet-truss and pyramidal lattices present zigzag stress-stress curves. And both curves are characterized by three peaks, each corresponding to the collapse of a row of units. Octet -truss lattice presents a larger stiffness and compressive strength compared to the pyramidal one, which is consistent with the fact that octet-truss unit is nearly an idealized pin-jointed stretching-dominated structure. The beams are assumed to only experience uniaxial tensile or compressive stresses, and it is the stretching of the horizontal members in tension that will govern the strength and stiffness of the lattice [180, 181], as **Fig. 5-10**.

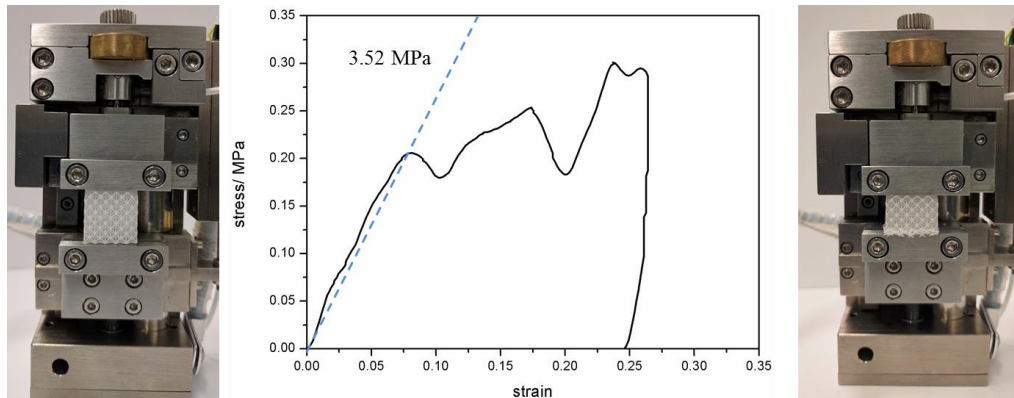


**Fig. 5-8. Compression setup of octet-truss lattice and the stress-strain curve.**

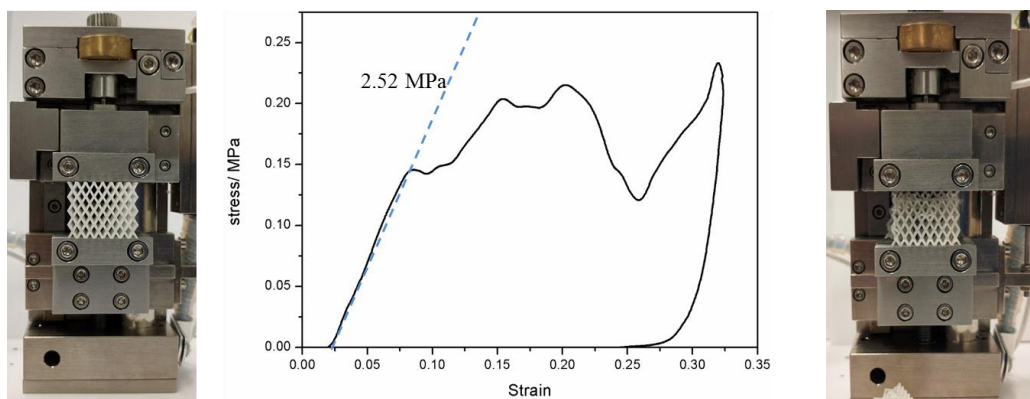


**Fig. 5-9. Compression setup of pyramidal lattice and the stress-strain curve.**

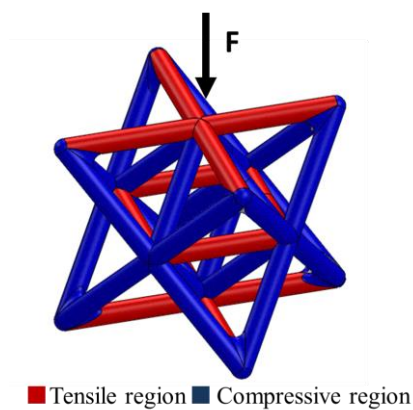


**Fig. 5-10. Simplified representation of idealized stress state in an octet-truss lattice. The solid struts are assumed to only experience uniaxial tensile or compressive stresses.**

When it comes to the effective mechanical properties, the octet-truss lattice is inferior

to the pyramidal lattice in terms of the specific strength and specific modulus. Here, the effective property is defined as the ratio of the mechanical property and the relative density, as **Table 5-1**. As observed in **Fig. 5-11**, although pyramidal lattice has a lower compressive strength and Young's modulus than octet-truss one, the effective strength and Young's modulus are higher due to its lower relative density. **Fig. 5-12** shows the images of octet-truss lattice after compression test that the lattice deformed gradually until fracture and collapse occurred finally with increasing pressure value. **Fig. 5-12B** tells that the fracture happened mainly at nodes.

**Table 5-2** summaries the mechanical properties of all the tested polymer octet-truss lattices and pyramidal lattices.

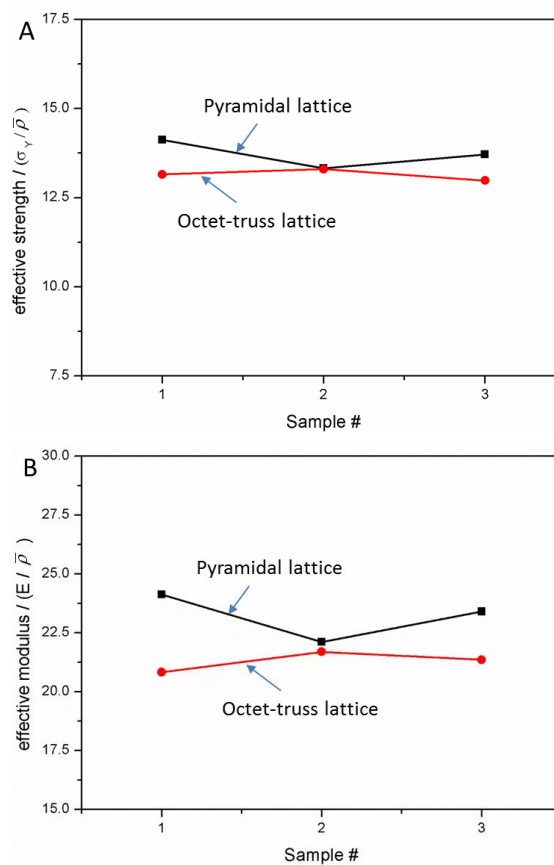


**Fig. 5-11. Comparison of effective properties between octet-truss and pyramidal lattices. (A) comparison of effective strength; (B) comparison of effective Young's**

modulus.

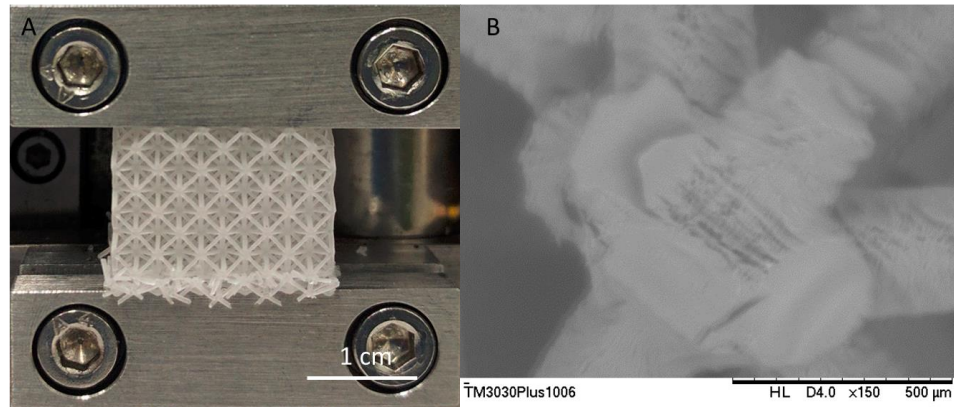


Fig. 5-12. (A) Octet-truss lattice after compression test. (B) SEM image of the fracture status at nodes.

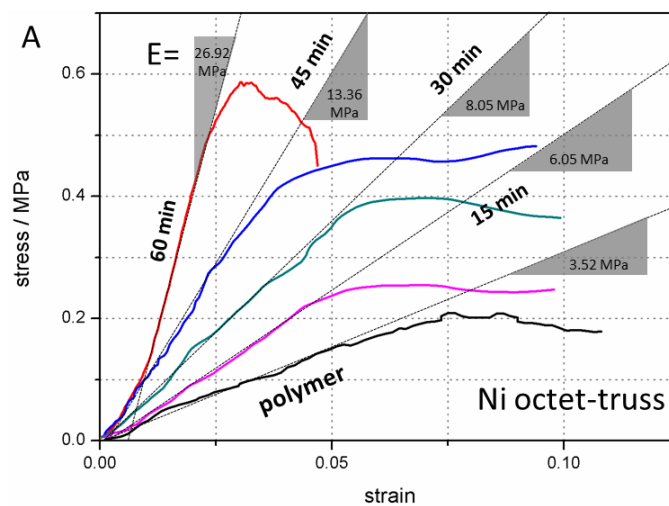
Table 5-2. Summary of lattice properties and the composed bulk material.

	Apparent density, $\rho$ (g/cm <sup>3</sup> )	Relative density, $\bar{\rho}$	Young's modulus, E (MPa)	Compressive strength, $\sigma_Y$ (MPa)	Effective modulus (E / $\bar{\rho}$ )	Effective strength ( $\sigma_Y / \bar{\rho}$ )
Octet-truss 1	0.20	0.169	3.52	2.22	20.83	13.15
Octet-truss 2	0.188	0.159	3.35	2.11	21.69	13.30
Octet-truss 3	0.192	0.162	3.46	2.10	21.36	12.98
Pyramidal 1	0.129	0.109	2.63	1.54	24.13	14.12
Pyramidal 2	0.135	0.114	2.52	1.52	22.11	13.32
Pyramidal 3	0.122	0.103	2.41	1.41	23.40	13.71
bulk	1.18	—	305	25.5	—	—

**Mechanical performance of metallic lattices.** To identify the strength-enhancement of metallic lattices, uniaxial compression test was conducted to the Ni- and Cu-coated octet-truss lattices. For each architecture, lattices after ELP of 15 min, 30 min, 45 min, and 60 min were prepared, and 3 samples for each. The metallic structures' compressive strengths and Young's modulus are described in **Fig. 5-13**. For both Ni- and Cu-coated lattices, Young's modulus and compressive strength increase as the ELP time. For the Ni-coated lattices, Young's modulus increases to 6.05 MPa after ELP of 15 min from 3.52 MPa of pure polymer. When the ELP time increases to 60 min, Young's modulus

can reach to 26.92 MPa, which is around 8 times to that of polymer lattice. It can be explained by that, the high specific strengths of copper and nickel contribute most to carry high compressive force, improving the stiffness and preventing the polymeric cores from an early buckling.

Similarly, the deposition of Cu-coating provides a significant improvement on the mechanical properties. The stiffness increases to 5.6 MPa after ELP of 15 min from 3.52 MPa of pure polymer lattice, and finally reaches to 19.28 MPa after ELP of 60 min. It is noted that, although Cu film is thicker than Ni after the same ELP time, the Cu-coated lattices shows a lower stiffness. The main reason lies in that Ni owns a higher specific stiffness than Cu. Ni which has a density of  $8.91 \text{ g/cm}^3$  almost same as that of Cu ( $8.96 \text{ g/cm}^3$ ), has a Young's modulus almost twice of that of Cu. For both Ni- and Cu-coated lattices, Young's modulus presents an exponential relationship of  $\wedge 3$  with the thickness of metal film, **Fig. 5-13B and D**.



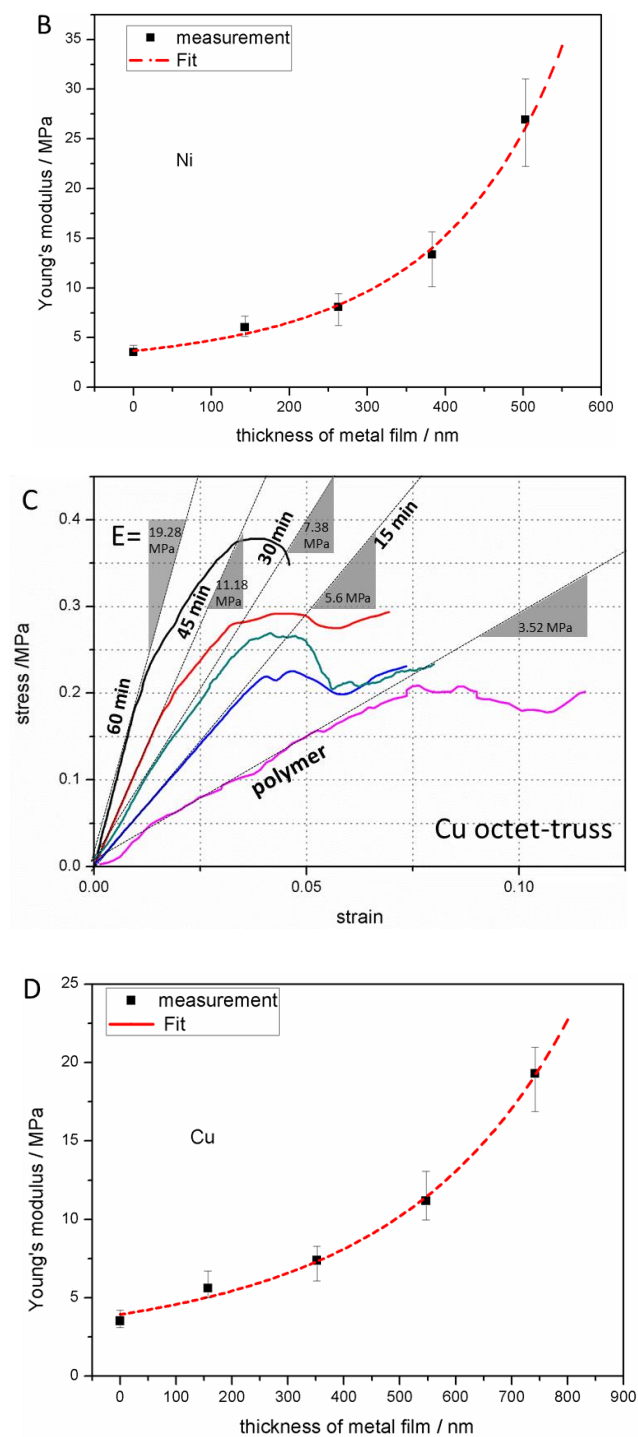


**Fig. 5-13. Strength-enhancement of mechanical properties of the octet-truss lattice. (A) Stress-strain curves of Ni-coated lattices of different ELP time. (B) Young's modulus of Ni-coated lattices vs. the thickness of metal film. (C) Stress-strain curves of Cu-coated lattices of different ELP time. (D) Young's modulus of**

### **Cu-coated lattices vs. the thickness of metal film.**

It is noted that, Ni-coated lattice after 60 min ELP deformed as a bulk material, for which the fracture happens along the plane  $45^\circ$  to the loading direction, as **Fig. 5-14**. That is because, when the metal layer is thick enough, the nodes can bear a higher loading force form fracture than the maximum shear stress action face of the entire material. The material will start to fracture along the maximum shear stress face and finally collapse [65]. With growing layer thickness of the metal film, the failure mechanism changes from buckling to brittle fracture [177].

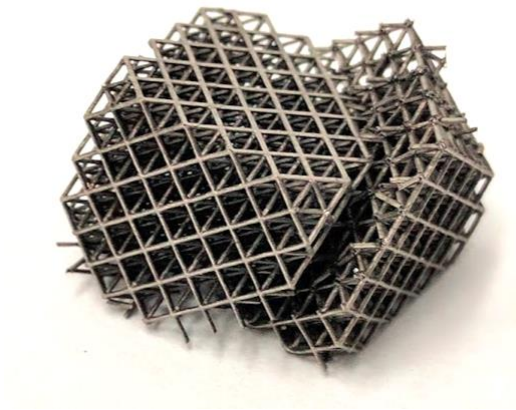


**Fig. 5-14. After 60 min of ELP, the lattice collapses along the maximum shear stress face. When the metal layer is thick enough, the nodes can bear a higher loading force form fracture than the maximum shear stress action face of the entire material. The material will start to fracture along the maximum shear stress face and finally collapse**

All the evidence suggest that the deposition of metal layer has a great improvement on the compressive strengths and Young's modulus, although the ratio of metal thickness to strut radius is only  $\sim 10^{-2}$  even after 1 h of ELP.

### 5.3 Conclusion

Macroscopic properties of cellular materials are determined by both material and structural properties. In this chapter, we theoretically analyzed the mechanical properties of two stretching-dominant structures - octet-truss cellular material and pyramidal cellular. It was found that the pyramidal lattice presents the lowest density with optimal truss angle of  $35^\circ$ , while the effective stiffness reaches to the best at a truss angle of  $45^\circ$ . Although octet-truss can bear a larger compression than pyramidal lattice when having a same loading area, it provides a lower specific stiffness due to its higher density. 3D printing was employed to fabricate the lattices of complex architecture, allowing the verification of the above analysis. Compression tests were conducted to observe and compare the mechanical behaviors, and the results presented a great consistency with the theoretical analysis. By combining the structural optimization and the post-printing modification, Ni and Cu coatings were deposited on the 3D printed polymer lattices, resulting in metallic cellular materials of high effective strength. We also investigated the strength-enhancement of mechanical properties, and understood the relationship between mechanical properties and metal films' thickness in detail. It was found that Young's modulus and thickness of metal films exhibit an approximately exponential relationship. By combining the advantages of 3D printing for the fabrication complex architectures with the generic post-printing modification for surface metallization, it provides opportunities to fabricate more functional materials with novel properties that will have great potentials in fields of tissue engineering, catalyst supports, damping and so forth.

## Chapter 6

### 6 Ultralight, super-elastic, hierarchical metallic meta-materials by i3DP

In this chapter, the proposed method of initiator-integrated 3D printing was employed to create a series of ultralight metallic materials composed of 3D interconnected hollow tubes. This is a further study based on the strength-enhancement described in the last chapter. These metallic materials were characterized with structures spanning three scale orders. The resultant materials can achieve an ultralight density of as low as 5.1 mg/cm<sup>3</sup> and nearly recover after significant compression up to 50%. XPS was utilized to monitor materials preparation during the entire fabrication process. Uniaxial compression was carried out in order to observe the mechanical response upon cyclic loading/unloading. Due to a high compression ratio, the hierarchical structure exhibits superior properties in terms of energy absorption and mechanical efficiency. The relationship of structural parameters and mechanical response was established. The ability to achieve ultralight density < 10 mg/cm<sup>3</sup> and the stable  $\bar{E} \sim \bar{\rho}^2$  scaling through all range of relative density, indicates an advantage over the previous stochastic metal foams. The initiator-integrated 3D printing approach provides an effective platform for fabricating metallic structures with substantial benefits from the hierarchical design and fabrication flexibility to ultralight applications.

#### 6.1 Introduction

It has long been an engineering pursuit to create lightweight and mechanically robust materials. The incorporation of ultralight materials shows tremendous potential in many engineering applications, such as thermal insulation [182-184], battery electrodes [185]

and energy absorption [66]. To date, materials with a density under  $10 \text{ mg/cm}^3$  in ultralight regime have been created, including polymer foams [186], silica aerogels [187, 188], carbon nanotube aerogels [189] and cellulose nanocrystal aerogels [190]. Because metal exceeds at its strength-to-weight ratio among all the possible materials, metallic light-weight structures have recently attracted much research attention. In addition, in compared with the existing ultralight materials of stochastic cells, an optimized cellular structure can achieve lower material density, while simultaneously preserving important mechanical properties such as high material stiffness and good impact resistance due to the high strength within the microstructure [191, 192]. The desired hierarchical structures result in an efficient distribution of the constituent which provides structures with the capability to withstand higher loads [49, 193]. Therefore, metallic cellular materials recently attracted significant interest within the research community.

Different from the most existing ultralight weight materials, such as foams and aerogels, for which the porosity is mainly governed by a random process, target-motivated controlling of the ordered architecture at multiple length scales is a great challenge for current manufacturing. Recently, the newly developed self-propagating polymer waveguides (SPPW) enables the rapid fabrication of large three-dimensional (3D) open-cellular structures with the assistance of exposure masks [67]. Using this method, ultralight cellular materials with the ability to recover from compression were successfully fabricated [67]. However, they still suffer from lacking of structural diversity, the use of a complex process, the requirement of multi-resource of UV, and the necessity to prepare exposure masks. Therefore, it is imperative to develop an effective platform for optimal design, thus the geometric parameters can be carefully controlled to meet various desired performance.

Recent advances in 3D printing have allowed not only the ability to fabricate repetitive

structures similar to SPPW, but also to construct controlled intricate elements. Thus, unique geometries can be created to increase the usefulness of certain materials. However, the creation of hierarchical structures with cross-scale features remains a challenge for even the most advanced 3D printing techniques. Direct laser writing (DLW) which uses a femtosecond laser can print structures at the resolution of tens of nanometers, but it is confined to using photo-resistant materials and printing small structures [193]. Selective laser sintering (SLS) enables a large building areas of some metal materials, but it is hard to obtain high resolution [191]. Therefore, it is desirable to develop an all-in-one method to simultaneously design the geometric architecture and metallic property of the material.

One feasible strategy for building metal materials with hierarchy structures is to integrate 3D printing with controllable and effective methods of surface modification. Recent research has demonstrated success in producing functionalized materials/devices by simple modifications of current 3D printing technology [63, 111-113], and allows construction of intricate structures with functional surface. It is, therefore, promising to employ and extend such hybrid 3D printing techniques to fabricate hierarchical metallic architectures. Herein, we adopt this feasible strategy to fabricate metallic structures with hierarchical features, for which 3D printing is used to construct large-scale complex geometries while post-printing modification is used to add detailed metallic features. Surface modification is achieved with atomic-transfer radical polymerization (ATRP) and the subsequent electroless plating (ELP). Since the polyelectrolyte brushes grown via ATRP act as a nano-thickness platform to induce the following ELP, the metal layers are more securely attached to the substrate compared to traditional ELP induced by physically absorbing catalyst [142, 164].

To demonstrate our proposed method, we successfully constructed metallic cellular materials with features of ordered scales ranging from submicron to centimeter. These

materials are ultra-lightweight with high energy-absorbing efficiency and capable of recovering their original shape after large compression strain up to 50%.

## 6.2 Experimental setup

### 6.2.1 Materials

The UV-curable resin was prepared by mixing acrylate-based monomers consisting of acrylic acid groups with photo-initiator. All the chemicals were purchased from Sigma-Aldrich and used as received except that the CuBr was purified by glacial acetic acid.

### 6.2.2 Fabrication of metallic structures

The fabrication of metallic structures is shown as **Fig. 6-1**. A polymer-temple was first 3D printed via polymerizing the initiator integrated UV-curable resin. The initiator-integrated material was prepared following the instruction described in Chapter 3. Initiator-containing polymer-templates were finally fabricated layer by layer via stereolithography using a commercial 3D printer (PIC2, Asiga).

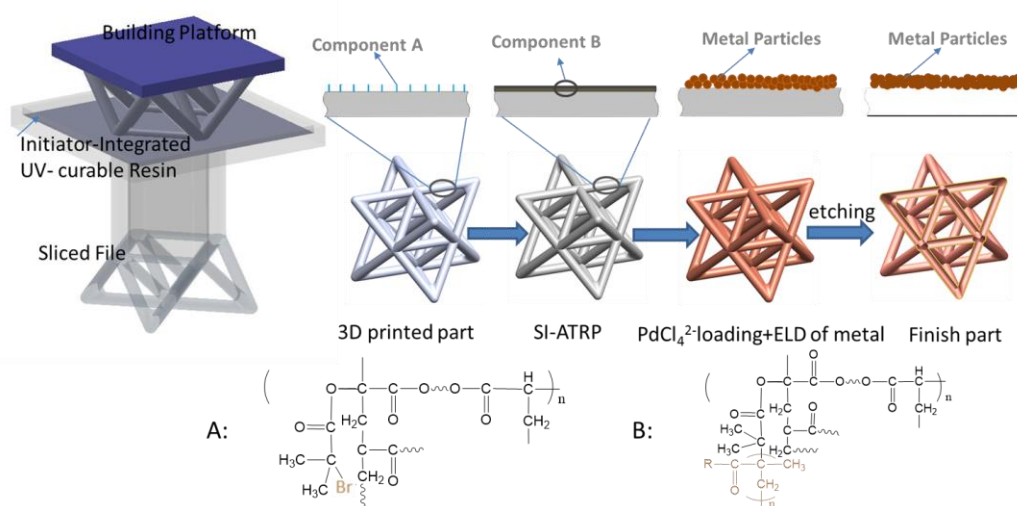


**Fig. 6-1. Schematic illustration of the fabrication of metallic cellular material by initiator-integrated 3D printing and the subsequent surface initiated atomic transfer radical polymerization (SI-ATRP) assisted ELP followed by etching.**

As described in previous chapters and our previous work [112, 132], the metallization was conducted by polyelectrolyte-assisted ELP and a skeleton and metallic lamina on the surface was fabricated successfully following the growth of metallic layer. The removal of the sacrificial template was then carried out through etching the polymer core, and resulted in a hollow, hierarchical and metallic structure.

### 6.2.3 Characterization

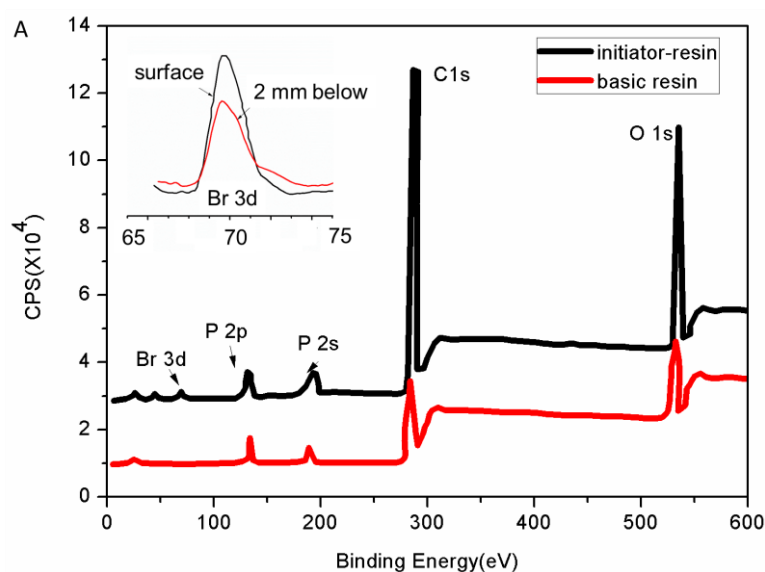
XPS was conducted using an Axis Ultra spectrometer (Kratos, UK) to obtain the chemical composition during each procedure, and measure the effectiveness of SI-ATRP. For spectroscopy, a monochromatic Al  $K\alpha$  radiation resource was utilized with reference to a binding energy of C 1s at 284.8 eV. The morphology of the surface coating was examined by SEM (Hitachi TM3030Plus) at a 15 Kv accelerating voltage. The compression tests were carried out on a servo-electric multi-functional test stage (Deben MICROTTEST tensile/compression/bending stages), which was integrated into the confined space of a SEM chamber (Hitachi TM3030Plus). The test stage is equipped with a standard miniature load-cell in the range 2 N to 200 N, which has accuracy readout of +/-1%, dynamic resolution 0.1% and static resolution 0.05% of the full-scale range. All the compression tests were conducted at a rate of 0.5 mm/min.

## 6.3 Results and Discussion

### 6.3.1 ATRP grafting

XPS spectra have been used to reveal the process of SI-ATRP in Chapter 3. Here I want to emphasize again to guarantee the preparation of initiator-integrated 3D printed objects. **Fig. 6-2A** shows the presence of the Br signature in the initiator integrated sample, which is absent from the sample printed with the original resin. The distribution of Br in the 3D printed object was tested by comparing the Br signal of its inner composition (after 1 mm of material was trimmed from the surface) and the outmost

surface. No obvious difference was observed (inset of **Fig. 6-2A**), which suggests an even distribution of Br within the object. It signifies that the inner distributed Br can also be used to re-initiate the ATRP process, allowing a re-generation of functional polymers and demonstrating a potential application of function self-healing. The successful grafting of poly(METAC) was also confirmed by XPS. The presence of N and Cl (**Fig. 6-2B** and **C**) are attributed to the formation of a poly(METAC) brush. After the ion exchange in  $(\text{NH}_4)_2\text{PdCl}_4$  aqueous solution, Pd signals at 342.5 eV and 337.0 eV (**Fig. 6-2B**) associated with the shift of Cl signal (**Fig. 6-2C**) indicate a successful loading of  $\text{PdCl}_4^{2-}$  due to its high affinity to the quaternary ammonium, which acts as the catalyst to initiate the following metallization. Here, Ni coated 3D objects were fabricated through this approach for the following study.



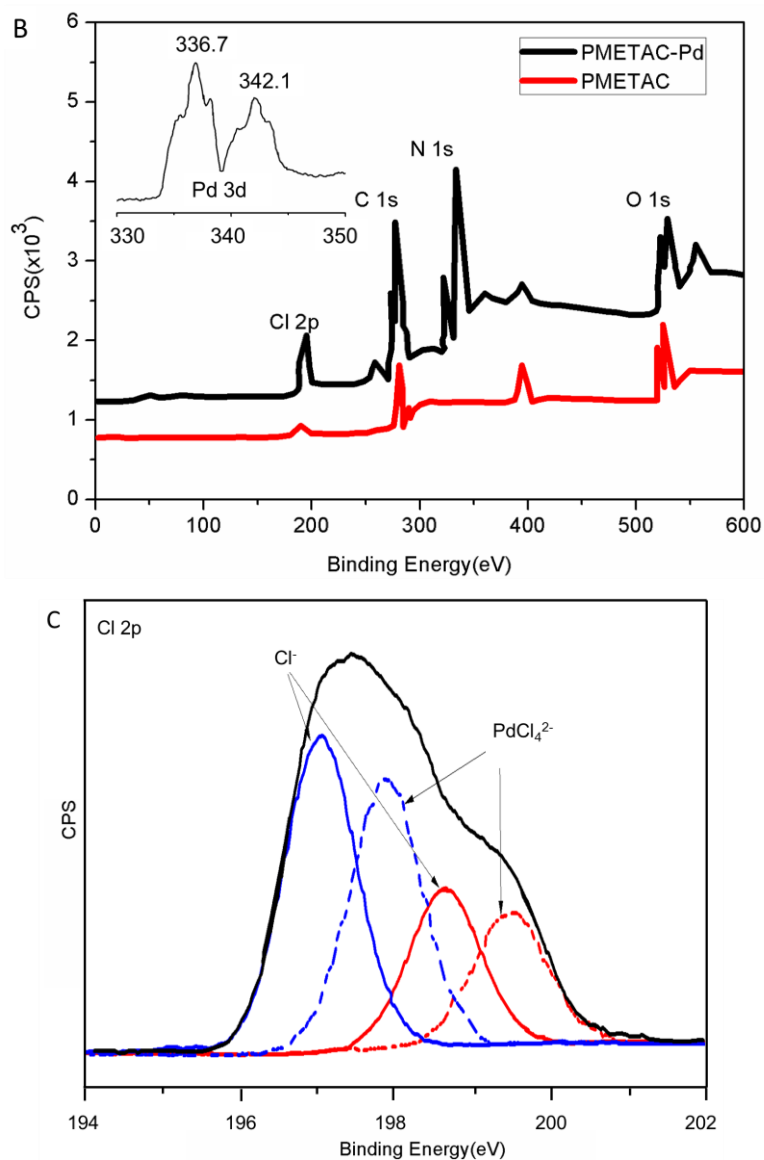


**Fig. 6-2. (A) Comparison of XPS survey spectra of 3D printed samples with and without initiator integrated. The inset is the comparison of high-resolution spectra of Br 3d distributed on the outermost surface and inner part. (B) XPS survey spectra of poly(METAC) before and after an exchange in  $(\text{NH}_4)_2\text{PdCl}_4$  aqueous solution. The inset is the high-resolution spectra of Pd 3d. (C) High resolution spectra of Cl 2p shift after ion exchange for loading  $\text{PdCl}_4^{2-}$  moieties on PMETAC-sample surface.**

### 6.3.2 Structural controlling of the hollow metallic microlattices

After the fabrication of solid polymer-templates using SLA 3D printing, the ATRP-assisted loading of  $\text{PdCl}_4^{2-}$  moieties act as active catalytic sites for the subsequent metallization of the 3D objects. A polymer etching process was then used to obtain ultralight cellular metal architectures. Here, a commercially available Ni bath was used to obtain a thicker metal film (CASEWELL Inc.). The ELP procedures are similar to those described in Chapter 4, but reacted at a high temperature of  $90^\circ\text{C}$ .

Importantly, different from the previously reported method of SPPW which only works for building structures with repetitive units, SLA printing offers more freedom to create flexible and complicated architectures. **Fig. 6-3** showcases a metallic ‘Eiffel Tower’ (**Fig. 6-3A**) etching of a polymer-based template (**Fig. 6-3B**). Its structural hierarchy (**Fig. 6-3C**) further verifies the capabilities of the proposed initiator-integrated 3D printing for freeform fabrication.

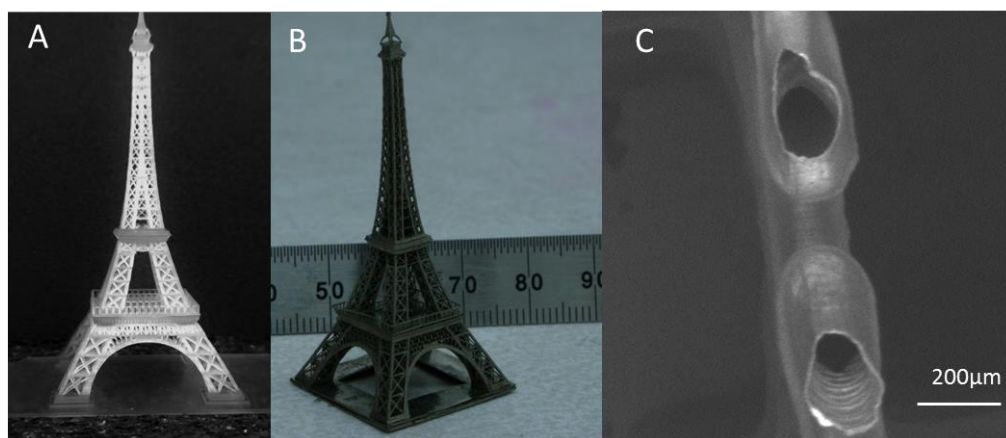


**Fig. 6-3. Metallic ‘Eiffel Tower’ as an example of hierarchical structure composed of hollow Ni-tubes. (A) polymer-template of ‘Eiffel Tower’. (B) Metallic ‘Eiffel Tower’ after ELP and the subsequent etching of polymer core. (C) SEM image of hollow NiP tube.**

To further demonstrate the suitability of this strategy for fabrication of recoverable

lightweight structures, as well as for the corresponding mechanical tests, metallic pyramidal Ni microlattices were prepared (**Fig. 6-4**) consisting of periodic arrays forming octahedral unit cells. Similar to the ‘Eiffel Tower’ above, the hierarchy of the microlattice spans across three distinct length scales from  $\sim\mu\text{m}$  to cm, as shown in **Fig. 6-4C** and **D**. For testing purposes, microlattices with different densities were fabricated via the proposed method, as listed in the **Table 6-1**. Their dimensional characteristics including the strut angle  $\theta$ , strut length  $l$ , diameter  $D$  and metal thickness  $t$ , are described in the schematic of pyramidal lattice (**Fig. 6-5**). The relative density mainly depends on the architecture, while the absolute density is determined by the constitutional material. Besides the structural parameters of truss diameter, length and angle which can be controlled during the CAD design process, one important issue is to control the thickness of the hollow strut. To achieve this, metal layer with various thickness determined by the ELP time can be deposited on the polyelectrolyte-grafted surface to obtain the desired density.

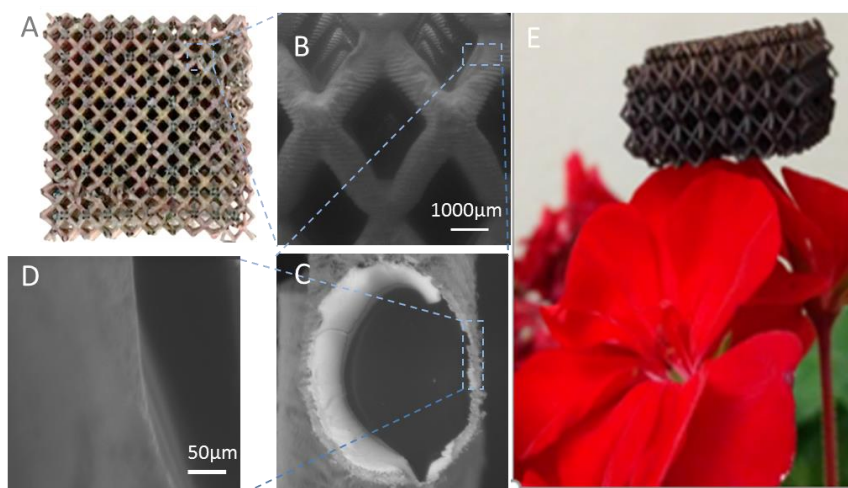


**Fig. 6-4. (A-D). Demonstration of as-fabricated ultralight metallic microlattices along with a breakdown of the hierarchical elements. (E) Ultralight metallic materials suspending on a flower**

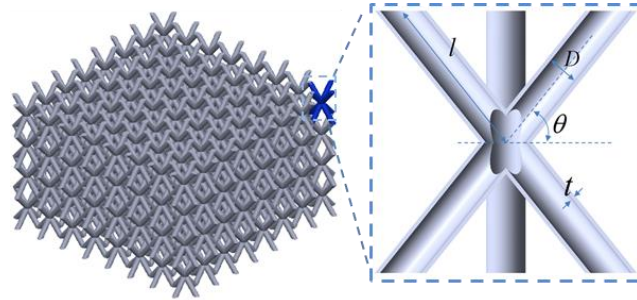


**Fig. 6-5. Structural characteristics of the pyramidal microlattices.**

As observed by SEM images (**Fig. 6-6**), 0.5 and 1 h of ELP both produce Ni coating geometries with uniform coverage, and the thickness of metal layers were c.a. 0.53  $\mu\text{m}$  and 1.52  $\mu\text{m}$ , respectively, while the thickness of Ni layers obtained from 5 min and 10 min of ELP were not dense enough to form an intact layer. This suggests that a minimum of 20 min ELP is necessary to produce Ni-coated architectures. The density  $\rho$  was calculated by measuring the weight and the global dimensions of the lattice while the relative density  $\bar{\rho}$  was calculated by dividing the density of the constitute material (ELPed Ni) with the nominal density  $\rho$  [194]. As listed in **Table 6-1**, the microlattice with 380 nm wall thickness can achieve an ultralight density of 5.1  $\text{mg}/\text{cm}^3$  (ultralight is defined as materials with density less than 10  $\text{mg}/\text{cm}^3$ ). This density is comparable to that of other reported ultralight materials [71] and demonstrates the superiority of the proposed approach for structural adjustability.

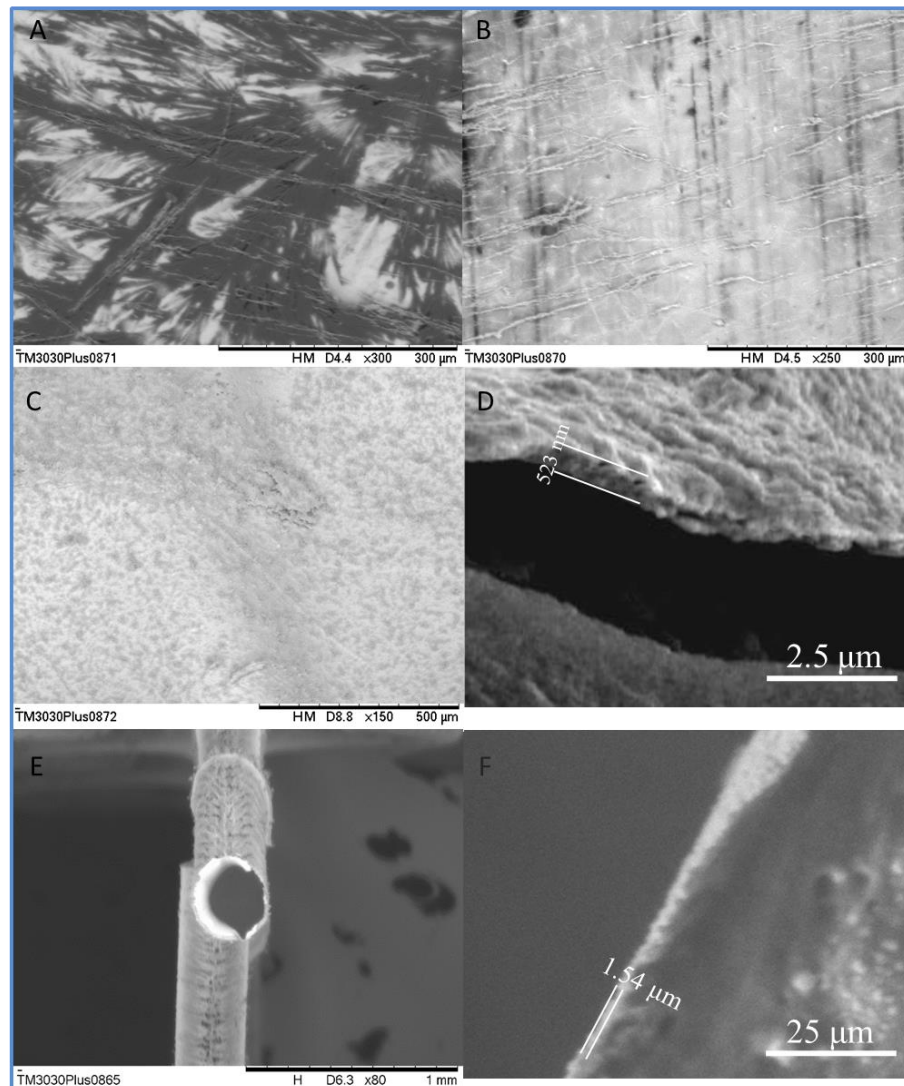


**Fig. 6-6. SEM images showing the surface of the Ni layer obtained at 5 min (A), 10 min (B), 0.5 h (C, D), and 1 h (E, F) of ELD. The thickness of Ni layer is c.a. 530 nm and 1.52  $\mu\text{m}$  after 0.5 and 1 h's deposition. The film obtained at 5 and 10 min of ELP was not uniform and had obvious defects (A and B).**

**Table 6-1. Summary of structural parameters and mechanical properties of the fabricated microlattices.**

Sample#	$t$ ( $\mu\text{m}$ )	$D$ ( $\mu\text{m}$ )	$\varphi = t/D$	$l$ ( $\mu\text{m}$ )	$\theta$ ( $^\circ$ )	$\rho$ ( $\text{mg}/\text{cm}^3$ )	$\bar{\rho}$ (%)	$\sigma_Y$ (kPa)	$E$ (GPa)	$\varepsilon_m$
1	0.32	200	1.6e-3	1000	30	9.7	0.121	2.9	2.2e-4	
2	0.51	200	2.5e-3	1000	30	14.3	0.174	7.1	6.2e-4	
3	0.62	200	3.1e-3	2000	30	7.1	0.086	4.2	2.3e-4	
4	0.83	300	2.8e-3	2000	30	11.3	0.137	4.4	2.58e-4	
5	0.48	300	1.6e-3	1000	45	13.8	0.168	8.6	7.05e-4	
6	1.26	500	2.5e-3	4000	45	25.4	0.310	23.5	12.95e-4	
7	0.38	500	7.6e-4	2000	45	5.1	0.062	1.7	1.24e-4	
8	0.94	300	3.1e-3	2000	60	13.3	0.162	8.9	6.49e-4	0.58
9	7.54	300	2.51e-2	2000	60	91.5	1.115	183.7	195.25e-4	0.112
10	0.50	1000	5e-4	2000	60	6.3	0.077	3.5	2.25e-4	
11	0.97	1000	9.7e-4	2000	60	11.2	0.147	4.8	4.81e-4	0.672
12	1.28	300	4.3e-3	2000	60	22.8	0.278	22.8	20.52e-4	
13	2.54	300	8.8e-3	2000	60	40.3	0.491	51.3	100.51e-4	
14	2.83	300	9.43e-3	2000	60	47.1	0.573	76.2	128.9e-4	0.173
15	7.83	300	2.61e-2	2000	60	97.5	1.147	193.7	205.22e-4	0.058
16	13.2	300	4.4e-2	2000	60	211.4	2.578	932.3	1154.04e-4	
17	2.77	300	9.16e-3	2000	45	51.8	0.631	72.1	119.8e-4	0.241

### 6.3.3 Characterization of mechanical properties

**Mechanical response upon compression.** To detect the mechanical response of microlattices with varying structural parameters, uniaxial compression experiments were monotonically and cyclically performed on the lightweight material, as **Fig. 6-7**. In this study, the microlattices were designed to have densities from 5.1  $\text{mg}/\text{cm}^3$  to 211.4  $\text{mg}/\text{cm}^3$ . The relative densities were calculated to be 0.062 % to 2.58 % by using a reported density of ELPed Nickel 8.2  $\text{g}/\text{cm}^3$ . The structures in all sets of the experiments were compressed uniaxially at a displacement rate of 0.5 mm/min to obtain the engineering stress, strain and overall deformation behaviors. The engineering stress and strain are defined as  $\sigma = F / S_0$  and  $\varepsilon = \Delta L / L_0$ , with  $S_0$  and  $L_0$  as the initial cross-section and length of the compressed sample. The mechanical response was analyzed through the strain-stress curve by extracting the Young's modulus  $E$ , yield stress  $\sigma_Y$ , and the energy loss coefficient  $\lambda = \Delta U / U$  is calculated by dividing the absorbed energy

by the total energy required for compression.

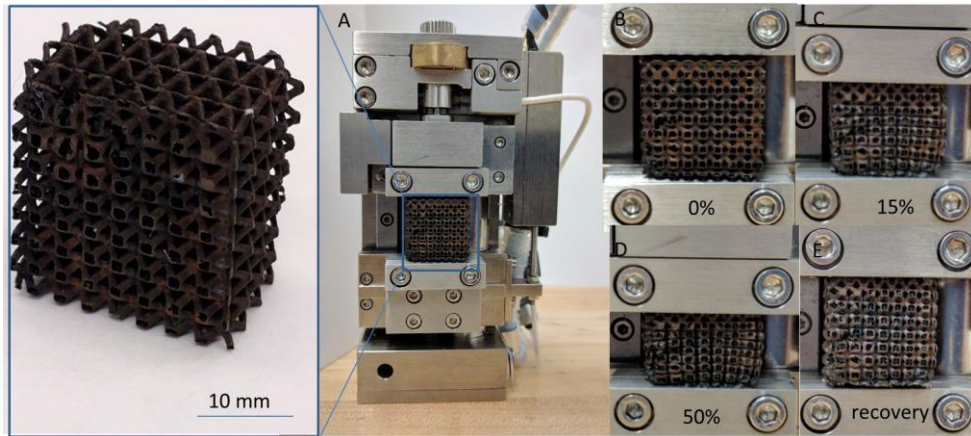


**Fig. 6-7. Cyclic and monotonic uniaxial compression is used to detect the mechanical behavior of the microlattices. (A) Experimental setup, microlattice (sample 12 in Table S1) before compression (B), after 15% compression (C), 50% compression (D), nearly recover to its original shape (E).**

The compressive response of microlattices with different structural parameters is described as **Fig. 6-8**. It shows that all tests present a loading profile consisting of two deformation parts- elastic deformation and the subsequent plastic deformation. Also, all the plastic deformations present a relatively constant plateau. For the unloading process, the mechanical behavior changes dramatically depending on the relative density. As shown in **Fig. 6-8A**, the ultralight lattice with density of  $5.1 \text{ mg/cm}^3$  presents a nearly complete recovery from strains exceeding 50% during the compression results and is referred a typical reversible deformation signature. According to its stress-strain curve, the lattice presents a compress modulus of  $124 \text{ KPa}$  with a yield strength of  $1.7 \text{ KPa}$ . In comparison, the following loading cycles present a decrease in the Young's modulus and compressive stress, which can be explained by the introduction of damage during the first compression cycle. The spreading of node fracture and buckling suffered from the first loading cycle brings the compressive stress in the second loading process down

to  $\sim 2.5 \text{ KPa}$  with elastic modulus of  $\sim 60 \text{ KPa}$ . Noticed that all the releasing process did not present much different and shows self-similarly. The stress initially drops dramatically upon the releasing of the compression and then gradually approaches to zero along with the recovery. Finally, the lattice recovers nearly to its original height after removing the load.

A similar mechanical response happened to the microlattice of  $13.8 \text{ mg/cm}^3$  during the first loading/unloading cycle but with much higher compressive strength. After removing the compression loading, no complete recovery (90%) is achieved after 50% compressive strain. Also, during the following loading/unloading cycles, the sample exhibits much greater mechanical loss compared to the first sample, with both the compressive stress and elastic modulus reduced dramatically. As depicted in **Fig. 6-9**, the yield stress drops to  $\sim 3 \text{ KPa}$  from  $8.6 \text{ KPa}$  and the elastic modulus decreases significantly to  $\sim 600 \text{ KPa}$ . This suggests that the structure suffered heavy irreversible damage during the first cycle. Again, the self-similarity during the loading/unloading cycles following the second one suggests no additional damage is introduced during subsequent compressions.

When the relative density increases further, the compressive behavior becomes similar to that of conventional metal foams, exhibiting a mechanical characteristic with an elastic phase, plateau phase and showing minimal recovery upon unloading. The stress–strain curve of a microlattice with  $40.3 \text{ mg/cm}^3$  density (wall thickness of  $2.54 \mu\text{m}$ ), as shown in **Fig. 6-8C**, shows a typical plastic deformation behavior with the highest yield strength  $\sigma_y = 51.3 \text{ KPa}$  compared to two above samples ( $\sigma_y = 8.6 \text{ KPa}$  and  $\sigma_s = 1.7 \text{ KPa}$ , respectively).

To summarize the change of mechanical properties during the loading/unloading cycles, the evolution of elastic modulus, yield strength, maximum stress and energy loss

coefficient is plotted in **Fig. 6-9**. As observed, the energy loss coefficients of low density samples (**Fig. 6-9A and B**) stabilize to over 0.2, and even the sample of quasi-cellular metal (**Fig. 6-9C**) still has an energy loss coefficient around 0.1. All these results are comparable with other reports [195, 196], and transcend other metallic system, such as bulk nickel and nickel foam ( $\sim 0.02$ ) [195, 197]. In addition, it also clearly shows that all properties in all tests decrease sharply after the first compression cycle and begin to stabilize after the second cycle, which indicates the first cycle induces damage in the sample. All the collective data above suggest that irreversible damage or deformation occur upon the first loading process, and the subsequent cycles just exhibit nearly recoverable elastic deformation. The phenomena can be explained by the nodal fracture occurring after the elastic deformation phase.

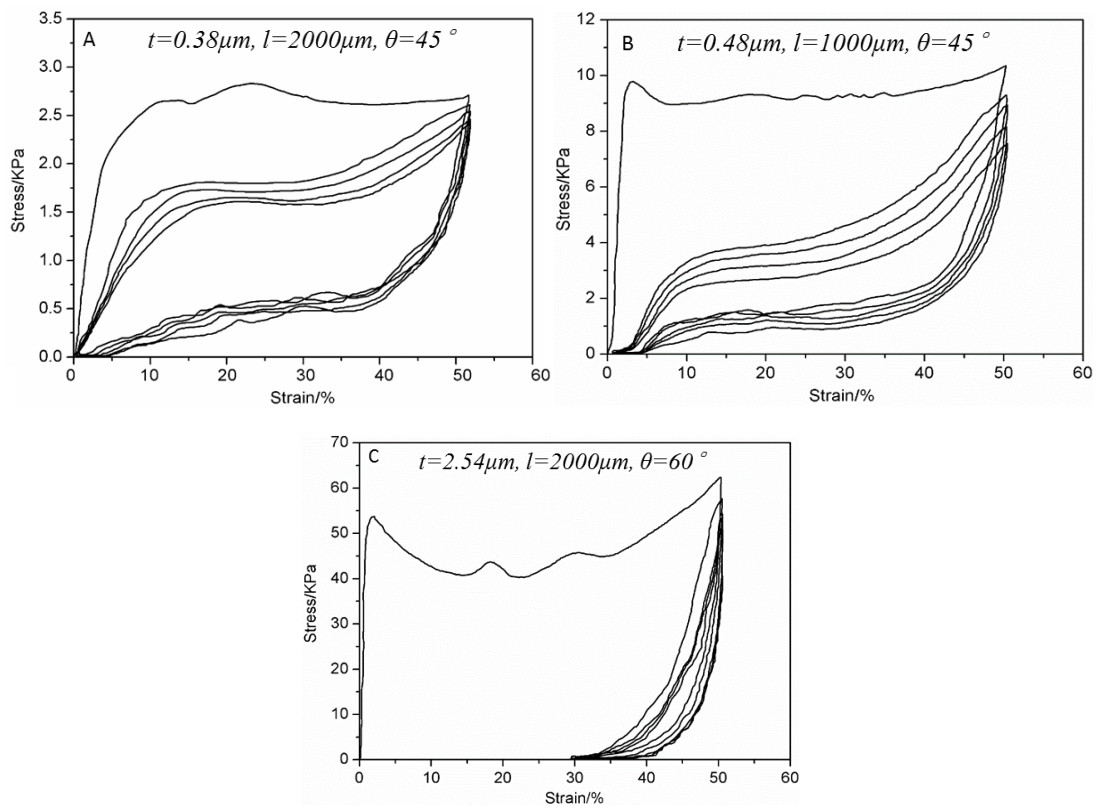


**Fig. 6-8. Mechanical response of microlattices upon loading/unloading cycles (Samples 7, 5, 13 from Table 6.1.) at progressively increasing wall thickness.**

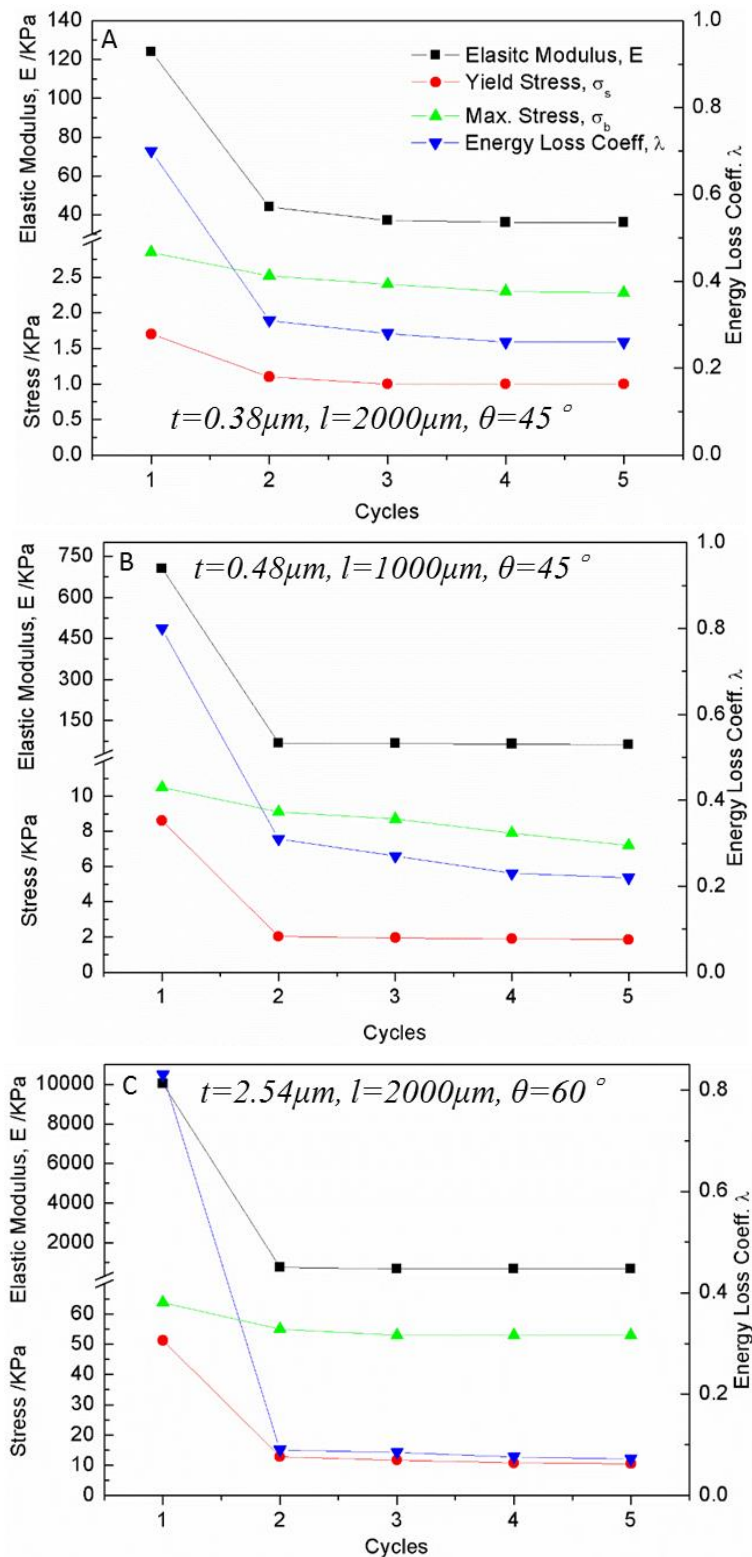


**Fig. 6-9. Mechanical properties evolution of microlattices upon loading/unloading cycles (Samples 7, 5, 13 from Table 5-1) at progressively increasing wall thickness.**

*Analysis of mechanical deformation.* The SEM images of samples, as **Fig. 6-10**, help understand further the deformation mechanism. Two deformation mechanisms are revealed that truss rotates on the node either with partial crack (**Fig. 6-10B and D**) or plastic buckling (**Fig. 6-10E**). Moreover, cracks at nodes are clearly visible after the first compression cycle but absent in the original microlattice (**Fig. 6-10A**), and show no obvious spreading after the second loading/unloading process. This verifies the above assumption that the irreversible cracks are only introduced in the first loading, and subsequent loading cycles only present elastic mechanical behavior. Also, the ligaments remain without cracks extending through the node after the first loading, which enables the strut to rotate around the node.

It is noted that, because the compression was conducted along the printing direction, the printing layer contribute most to the crack due to the stress concentration during compression. When compressing the sample in a direction rotated by 90 degree, it is reasonable to speculate that most of the nodes will suffer from buckling rather than cracking, and the sample will present a similar deformation behavior, for which the only difference lies in the strut angle, because of the structural symmetry.

A. Torrents, et al [195] also verify the above analysis by observing the in-situ deformation process through “freezing” the microlattices using epoxy. They also confirmed that microlattices of thinner wall structure present local plastic buckling, while thicker samples typically show extensive plastic kinking at the nodes. These results indicate that intact ligaments allow extensive rotation of the members without introducing plastic strain, thereby resulting in nearly complete recovery after intensive compression.

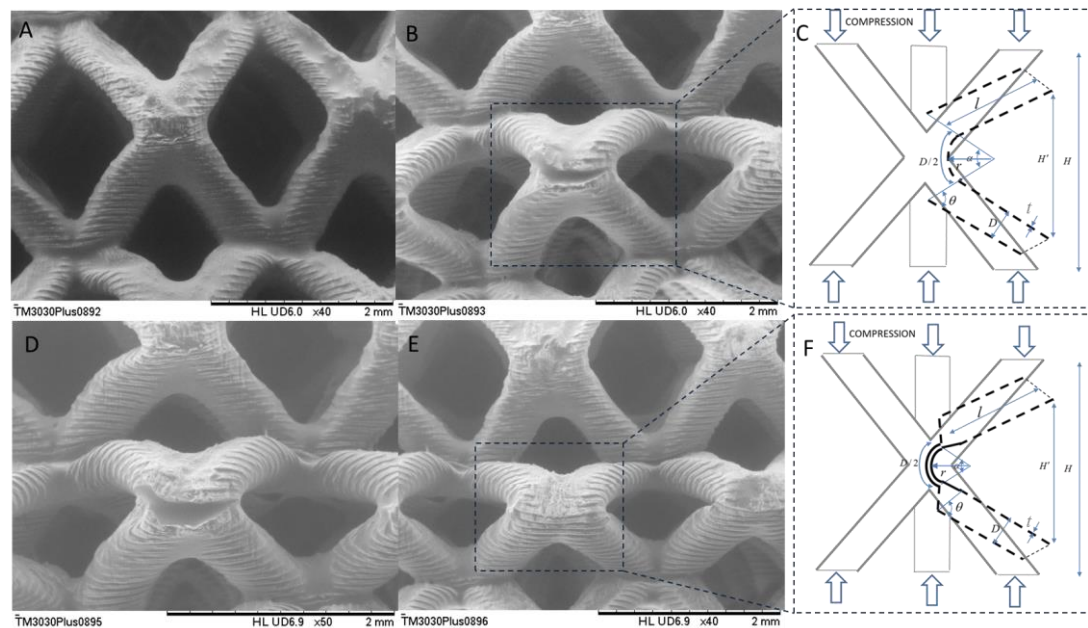


**Fig. 6-10. SEM images of microlattice (sample #11 in Table S1) in cyclic compression testing of 50% strain and two corresponding mechanisms demonstrate the microlattices can bear large global compression without plastic deforming. From left to right, (A) strut of original microlattice, (B) cracking occurs at the node after the first loading cycle, corresponding model of partial fracture of a node with subsequent rotation (C) nearly no enlarging of crack after second loading cycle (D), (E) and (F) show the node rotation of a remnant ligament and the corresponding mechanical model.**

**Computational analysis.** To reveal the influence of structural parameter on the mechanical behavior under conditions of loading, a simple mechanical model is proposed referring to reference [195]. The model predicts the deforming process according to the two aforementioned mechanisms, which takes into account the thickness-to-diameter ratio ( $t/D$ ,  $\varphi$ ) and truss angle  $\theta$ . **Fig. 6-10C** and **F** illustrate the schematic deformation during the compression corresponding to the two rotation mechanisms. Consistent with the above observation and analysis, **Fig. 6-10C** shows the partial fracture of a node with subsequent rotation about a remnant ligament. **Fig. 6-**

**10F** shows the process of elastic buckling at the node followed by rotation. Assuming a uniform deformation during the compression, the rotation occurs by bending a thin film of thickness  $\sim t-2t$  and length of the strut radius. According to **Fig. 6-10C** and **F**, an approximate geometrical relation can be established as:

$$l \cdot \sin\left(\theta - \frac{\alpha}{2}\right) = \frac{H'}{2} \quad (1)$$

Based on the relationship of  $H = 2l \sin \theta$ ,  $H' = H(1 - \varepsilon)$ , we can get:

$$\alpha = 2\left(\theta - \sin^{-1}\left((1 - \varepsilon) \sin \theta\right)\right) \quad (2)$$

The critical condition for elastic recovery can be obtained by approaching the thin film at nodes on the verge of yielding. Based on the geometrical relation and Hook's law that  $\varepsilon = t/r$  and  $\varepsilon = \sigma'_Y / E'$ , we can get the following equation.

$$r = \frac{D}{2\alpha} = \frac{\sigma'_Y}{E't} \quad (3)$$

From (2) and (3), we can obtain the effect of truss characteristics, angle  $\theta$ , thickness  $t$  and the diameter  $D$  on the critical compression strain, as:

$$\varepsilon_{cr} \cdot \sin \theta = 1 - \sin\left(\theta - \frac{\sigma'_Y}{4E'} \cdot \frac{D}{t}\right) \quad \text{or} \quad \varepsilon_{cr} \cdot \sin \theta = 1 - \sin\left(\theta - \frac{\sigma'_Y}{4E'} \cdot \frac{1}{\varphi}\right) \quad (4)$$

Where,  $\sigma'_Y$  and  $E'$  are the compressive yield strength and elastic modulus of the constituent materials, which can be obtained from the measurement of the nanoscale mechanical response of Ni films as reported in literature [195] (as  $\sigma'_Y \sim 2.5$  GPa and  $E' \sim 210$  GPa).

Equation (4) indicates that the critical maximum strain mainly depends on the thickness

ration and truss angle but ignores the effect of truss length. In this study, the length-to-diameter ratio of the strut ranges from 2-8. According to the report [198] that the above two mechanisms still predominate the strut deformation without introducing global instability when this ratio is less than 10, it is not essential to simplify the mechanical model without considering the effect of truss length. By substituting the  $\sigma'_Y$  and  $E'$  into equation (4), the critical relevance of the wall-thickness ratio and truss angle on the maximum compressive strain allowing elastic recovery is determined (**Fig. 6-11**).

The maximum strain decreases with increasing thickness ratio, resulting in a gradual reduction of the recoverability. Thus, the microlattices approach that of traditional cellular metals with solid truss as the ratio increases. Furthermore, the prediction model predicts that truss angle is inversely related to compression tolerance. This is because a smaller truss angle leads to a large inclination of the loading on the strut cross-section resulting in a decrease of shear stress and increasing the likelihood of the strut bending with a large deflection [198]. In addition, the thickness ratio influences the compressive strain exponentially while the truss angle affects the strain approximately linearly. This is in accordance with the fact that the wall-thickness-to-diameter ratio has the most impact on the fundamental local deformation, while the loading angle has more influence on the global loading status. **Fig. 6-11** also compares the experimental data with their corresponding theoretical predictions to verify the accuracy of the mechanical model. With regards to the influence of the thickness ratio and truss angle on the compression tolerance, the experimental results are consistent with the theoretical prediction. Note that microlattices with higher thickness-to-diameter ratio usually conform better to the prediction. This is because the local-buckling deformation model emerges when further decreasing the thickness and becomes the dominant mechanism.

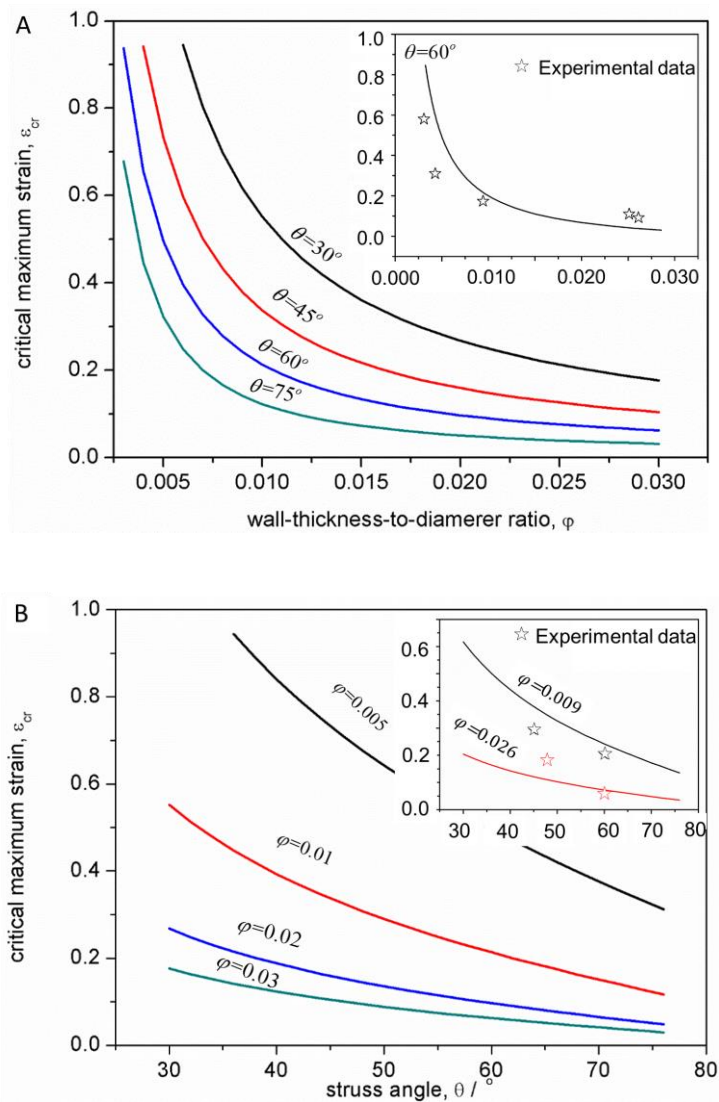


**Fig. 6-11. Critical maximum strain varying with the wall-thickness-to-diameter ratio (A) and truss angle (B) to obtain complete recovery after the compression, insets are the comparison of theoretic prediction and experimental data.**

**Evaluation of the mechanical efficiency.** The mechanical efficiencies of the microlattices can be illustrated by plotting the relative strength and compressive moduli as a function of the relative density. As shown in **Fig. 6-12A**, the compressive strength exhibits two different functional behaviors with regards to the relative density. For microlattices with relative density  $> 0.1\%$ , the compressive strength exhibits approximately a  $\bar{\rho}^{1.9}$  scaling in relation to the relative density, which is comparable to

the reported hollow cellular metals and the open-cell stochastic foams [195, 197]. For relative densities less than 0.1%, although the scaling law changes to  $\bar{\sigma}_Y \sim \bar{\rho}^{2.5}$  because of the emergence of local buckling upon compression of the ultrathin strut, they can bear a larger compressive loading than the traditional ultralight materials with stochastic structures [187] and even the newly developed metal foams [199, 200]. The deformation mechanism shifts from the plasticity-dominated deformation to a local-buckling deformation model [195]. It interprets again that the prediction accuracy of the ultra-small wall-thickness-to-diameter ratio is slightly lower, as **Fig. 6-11**.

The relationship between the elastic modulus and relative density exhibits a  $\bar{E} \sim \rho^2$  scaling, as shown in **Fig. 6-12B**, which is similar to the stochastic metal foams. This scaling law indicates a bending-dominated mechanical behavior to open-cell foams [65]. The reason why a stretching-dominated template (generally has a linear scaling) results in a foam-like scaling for the modulus is: the absence of horizontally linked truss members and the hollow tubes after polymer etching [201]. Most of the deformation is consequently concentrated at the node but not distributed along the truss, as **Fig. 6-10**. In contrast to the most existing ultralight materials [195, 202-204], such as carbon foams, Si aerogels and solid metallic lattice materials, which follow a steeper scaling of  $\bar{E} \sim \rho^3$  due to the inefficient load transfer between ligaments, the hierarchical material presents a stable  $\bar{E} \sim \rho^2$  through all range of relative density. Moreover, no metal foams with stochastic cell have been reported at a relative density below 0.1%, and it is also found that this metallic ultralight microlattice of order cell is among the stiffest materials with densities below 10 mg/cm<sup>3</sup> [205-207].

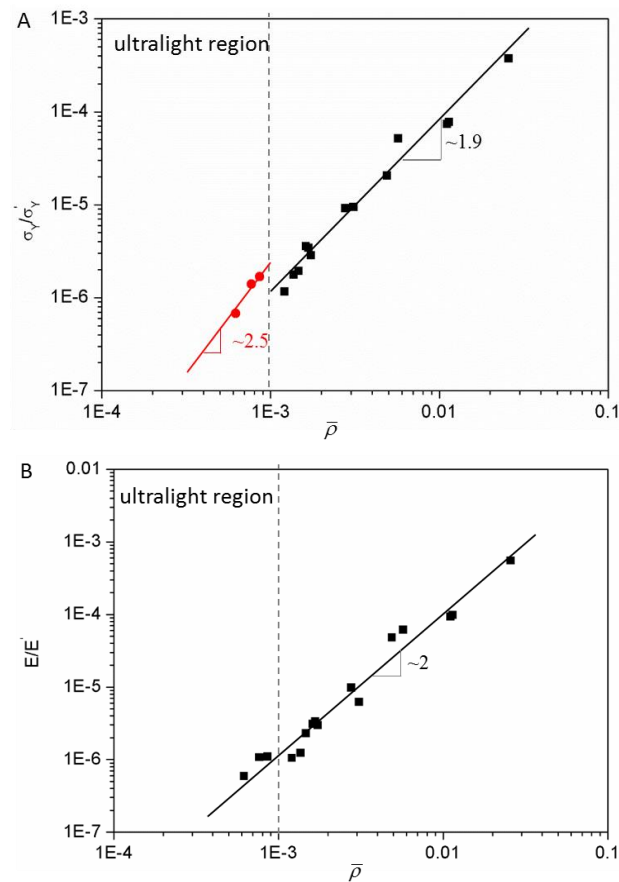


**Fig. 6-12. Evaluation of the mechanical efficiency of the microlattices by plotting the relative compressive strength (A) and elastic modulus (B) as functions of the relative density. The compressive strength scales quadratically with the relative density over the ultralight region but sharply changes to  $\sim \bar{\rho}^{-2.5}$ . For the elastic modulus, the microlattices show a quadratic scaling through the entire range of relative density.**

Importantly, we can further enhance the mechanical properties by either utilizing superior coating materials [201] or carefully designing the lattice topology. For example, adoption of octet-truss lattice can improve the scaling law to  $\bar{E} \sim \rho$ , which will result in a much superior performance [206]. In addition, multiscale metallic metamaterials of higher ordered hierarchy can also allow achieving the maximum strength of a

material for a given density by optimizing the equivalent strength at each hierarchical level [208]. This also highlights the superiority of 3D printing in structural adjustment resulting in a better mechanical property.

## 6.4 Conclusion

In summary, an effective approach has been developed to create ultralight hollow cellular metals with controlled hierarchical structures by a modified 3D printing technology. The superiority of this technology was demonstrated in constructing complex geometries with lattice topology and hierarchical structures spanning multiple length scales. By directly mixing an initiator monomer (Br-containing vinyl-terminated monomer) into the photo-curable resin, a thin metallic coating via surface-initiated ATRP and the subsequent polyelectrolyte-brush-assisted ELP is successfully coated on the 3D printed objects. After etching, metallic structures with complex geometries are achieved and subsequently can be engineered into a thin-walled metallic lattice which is capable of deforming elastically via the node fracture and buckling. In this study, microlattices with a global size of  $\sim 2$  cm and wall thickness of 320 nm to 13.2  $\mu\text{m}$  were fabricated with density ranging from 5.1 to 211  $\text{mg}/\text{cm}^3$ .

Using this novel manufacturing process, we can construct objects from constituent material of high yield stress and truss members of very low aspect ratio, allowing recovery from large compressive strain. These materials exhibit a unique combination of strength and stiffness that optimizes energy absorption and shape recovery after significant compression. In this study, uniaxial compression experiments were carried out to reveal the mechanical behavior of the designed hierarchical microlattices. Two distinct mechanical responses were found to depend on material density, that microlattices of ultralow density ( $<10$   $\text{mg}/\text{cm}^3$ ) exhibit nearly full recovery after large compressive strain, while the microlattices (10 - 50  $\text{mg}/\text{cm}^3$ ) exhibit limited recovery

but with higher compressive strength. As density increases, the deformation behavior of microlattices approaches to that of traditional cellular metals or solid trusses. A mechanical model was established and verified to predict the effect of structural parameters on the compressive response, which can be used to guide the material design. In general, smaller wall-thickness-to-diameter ratio and truss angle allow larger compression without introduction of plastic strain, leading to higher compression tolerance for microlattices.

This fabrication method opens up new possibilities in material design by integrating the advantages of 3D printing for architectural construction with the benefits of surface modification to control the fine structure. This technique also provides an effective approach to fine-tune the mechanical properties through the structural design. Starting from strong but dense brittle base material, the fabrication of an ultralight, energy-absorbing, and recoverable metamaterial was successfully demonstrated.

## Chapter 7

### 7 Mechanical meta-materials by i3DP and the integrated properties

In this chapter, we apply the proposed initiator-integrated material in the fabrication of mechanical meta-materials with negative Poisson's ratio (NPR), which is an extended investigation of metallic cellular materials. Specifically, structural design of auxetic architectures were cooperated with the SI-ATRP initialized modification, allowing the creation of metallic mechanical meta-materials. Three material systems were demonstrated here: 1 polymer, 2 hollow Cu, 3 Cu-polymer composite. It is found that polymer and Cu-polymer composite auxetic materials present an invariable negative Poisson's ratio, while the materials composed of hollow Cu present a tunable ratio. The NPR of hollow Cu material varies with the thickness of metal film. Also, the Cu-polymer shows a significant strength-enhancement to the mechanical properties.

#### 7.1 Introduction

Metamaterials are usually referred to composite materials that can achieve unusual and sometimes even unprecedented effective optical and electromagnetic properties [209-212]. More recently, the concept has been extended to mechanical properties as well. Different kinds of meta-mechanical behaviors have been developed to endow the materials with unique mechanical properties, such as negative modulus, negative compressibility, negative stiff or extremal stiff in certain deformation modes [68, 213, 214]. These materials show promising applications in actuators, amplifiers, micromechanical control, and protective packages. Particularly, the property of zero or even negative Poisson's ratio (NPR) is desirable for materials that subjected to

environments with large compression/tensile fluctuations [173]. Compared to conventional materials, these NPR materials have a precise dimensional tolerance due to their advantages of increased plane strain, tunable density, higher fracture resistance and shear modulus [215].

The NPR materials' unusual equivalent physical properties are dictated by their architectures rather than compositions because the Poisson's ratio (PR) of a given materials can hardly be altered by changing the size of the components. It is therefore that, only elaborately designed structures can result in an effective distribution of the constituent, and then endow material with the capability to perform novel mechanical property. For example, the auxetic materials which are interconnected network-like structures can expand when stretched longitudinally or shrink laterally when compressed uniaxially [216]. Besides the novel property of NPR, carefully designed structure can also make auxetic materials with lower material density than stochastic structures, while preserving some important mechanical properties such as material stiffness and impact resistance due to the efficient distribution of deformation within the structure [177, 217]. However, the instinct constraints of natural material limit the design space and practical applications. The fabrication and controlling of the structure are, therefore, challenging the current manufacturing. As a result, many of the designs of meta-material discussed in the previous studies were only studied theoretically or computationally [218]. All these challenges are motivating the researchers to develop effective fabrication methods that could enable an arbitrarily assigned set of mechanical and physical properties, along with the engineering pursuit of lightweight and mechanically robust materials.

Recent advances in 3D printing made it possible to construct intricate elements. Unique geometries can be created to increase the usefulness of given materials. Here, we adopt the proposed functional 3D printing to fabricate auxetic architectures, aiming to create

mechanical metamaterials with integrated NPR, strength-enhanced and ultralight properties. The SI-ATRP initiated by the integrated initiator helps the deposition of metal layer. After etching the polymer core, ultralight materials composed of hollow tube are obtained.

## 7.2 Experimental setup

### 7.2.1 Materials

The UV-curable resin was prepared by mixing acrylate-based monomers consisting of acrylic acid groups with photo-initiator. All the chemicals were purchased from Sigma-Aldrich and used as received except that the CuBr was purified by glacial acetic acid.

### 7.2.2 Initiator-integrated 3D printing

The preparation of initiator-integrated materials and the fabrication of metallic lattices followed the description in Chapter 3 and 5. Briefly, the initiator-integrated 3D printing material was first prepared by mixing well 5 wt% BrMA into the photo-monomers and then degassed for 1h in dark. 3D structures were designed by Solidworks (Dassault Systèmes) and printed layer by layer via a commercial 3D printer (PIC2, Asiga).

Re-entrant structure was employed to compose auxetic material in this study. As shown in **Fig. 7-1**, the unit cell is characterized by the structural parameters as overhung link  $L_1$ , width  $L_2$  and the re-entrant angle  $\theta$ . Besides, to guarantee the effectiveness of re-entrant, the length-diameter ratio was designed for each inclined beam as  $D/L_2 = 1/4$  so that local buckling can be eliminated [198].

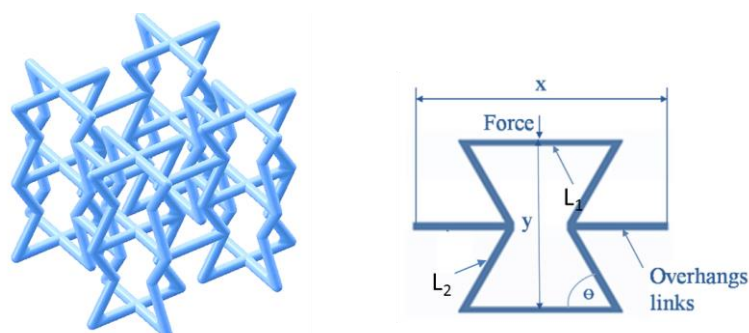


**Fig. 7-1. CAD model of re-entrant structure and the structural parameters**

To investigate the influence of structural parameters on the PR and the mechanical properties. Three material systems were prepared, including polymer lattices, metal-polymer composite lattices and metallic hollow lattices. Except for the polymer lattices which were directly printed through 3D printing, the rest of the materials were synthesized by the initiator-integrated 3D printing and the post-printing technology.

***Fabrication of metallic auxetic materials.*** Cu-coating was deposited subsequently to obtain metallic cellular architectures. The metallization process followed the procedures described in Chapter 3. Typically, the PMETAC-coated 3D samples were immersed into 5 mM  $(\text{NH}_4)_2\text{PdCl}_4$  aqueous solution for 15 min. After  $\text{PdCl}_4^{2-}$  moieties were immobilized to the brushes by ion exchange, the resultant samples were rinsed thoroughly with methanol and immersed into a house-made plating bath (details in Chapter 3) to obtain metallic architectures.

### 7.2.3 Characterization

The compression tests were carried out on a servo-electric multi-functional test stage (Deben MICROTTEST tensile/compression/bending stages). The test stage is equipped with a standard miniature load-cell in the range 2 N to 200 N, and has an accuracy readout of  $\pm 1\%$ , dynamic resolution of 0.1% and static resolution 0.05% of full scale range. All the compression tests were conducted at a rate of 0.5 mm/min.

## 7.3 Results and Discussion

### 7.3.1 Computation of re-entrant structure

An analytical model based on a small deflection assumption was proposed by Warren [219], which neglects the axial deformation of the struts. By establishing equilibrium equations for the unit structure, a set of equations for numerical characterization were used to obtain the PR with different re-entrant angles. It was found that PR varies with the re-entrant angle and only becomes negative at  $\theta \geq 13^\circ$ . Wan et al. [220] proposed a generalized model of the re-entrant lattice structure by considering the case undergoing large deflections. This model is expected to be more accurate in cases when relatively soft materials, such as polymers, are used. The total deformation of the unit cell is obtained by numerically solving a set of elliptical equations. PR is then obtained based on the magnitude of deflection. Unit cell size is included in the analysis along with the re-entrant angle to provide a more comprehensive design guide for these types of structures.

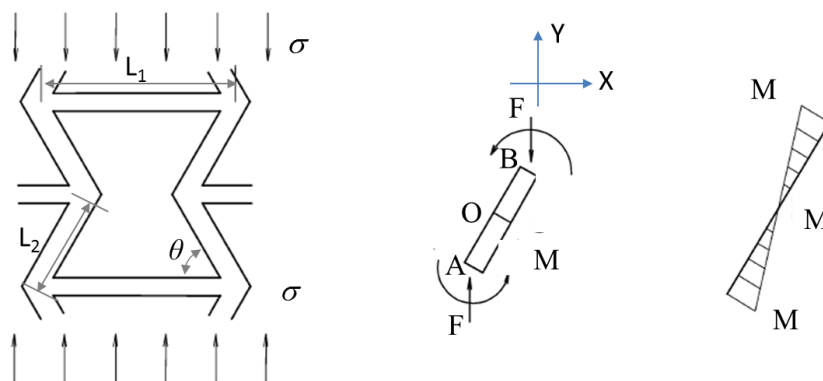


**Fig. 7-2. Deformation of re-entrant cell by inclined cell member bending.**

When the auxetic unite is uniaxially loaded in the Y direction, the cell member bends as shown in **Fig. 7-2**. The loaded stress  $\sigma$  produces force  $F$  on the inclined member, which is paralleling to the Y axis, and can be calculated as [221]:

$$F = \sigma(L_1 - L_2 \cos \theta) r \quad (1)$$

Where  $F$  is the force applied on the inclined member due to  $\sigma$ , N;  $\sigma$  is remote stress applied on the auxetic structure in the Y direction, Pa;  $r$  is the radius of the cell member, m. The equilibrium of the moment is giving the bending moments at the end of the inclined member as:

$$M = FL \sin(45^\circ - \theta) \quad (2)$$

Then the PR under Y direction loading is calculated as the negative transverse strain divided by the axial strain in the loading direction:

$$\nu = -\frac{\varepsilon_{YX}}{\varepsilon_{XX}} = -\frac{L_2 \cos \theta - 4F \sin \delta_x / k_x}{L_1 - L_2 \cos \theta} / \frac{2(2E(\alpha_x) - F(\alpha_x)) / k_x - L_2 \sin \theta}{L_2 \sin \theta} \quad (3)$$

Where  $k_x^2 = F / (E_s I)$ ,  $\delta_x = \arcsin\left(\sin \frac{\beta_x}{2} / \sin \frac{\alpha_x}{2}\right)$ ,  $\alpha_x$  and  $\beta_x$  are bending angles between the tangent of the shape of the inclined member,  $E_s$  is Young's modulus of the constituent material,  $I$  is the second moment of inertia of the cell member.  $F(\alpha_x)$  is an incomplete elliptic integral of the first kind,  $E(\alpha_x)$  is the corresponding bending moment of  $F(\alpha_x)$ .

**PR versus strain and geometries.** As obtained from (3), PR  $\nu$  for loading in Y-direction is expected independent of density, because this large deformation model used here ignores axial compression. **Fig. 7-3** shows that PR in the orthogonal directions versus strain for varying geometry parameters including  $a=L_1/L_2$  and re-entrant angle  $\theta$ . It is found that PR is variable, and has a negative value generally. The magnitude of PR decreases significantly at high strain when the re-entrant cell is under compression in Y-direction. In addition, compressive loading and tensile loading at large deformation

will result in a different variation of Poisson's ratio with strain. For the loading in Y-direction, PR decreases as strain increases when the structure is compressed, and increases as strain increases when the structure is stretched. Importantly, when the re-entrant cell undergoes a compressive stress in Y-direction at large deformation, the sign of PR may switch from negative to positive. It can be explained by that, under compressive loading, if the deformation is large enough the inclined members will contact each other. At this time, the force and the moment distribution will change, indicating that this large deflection model is not suitable for a larger deformation over the critical point of contact [222].

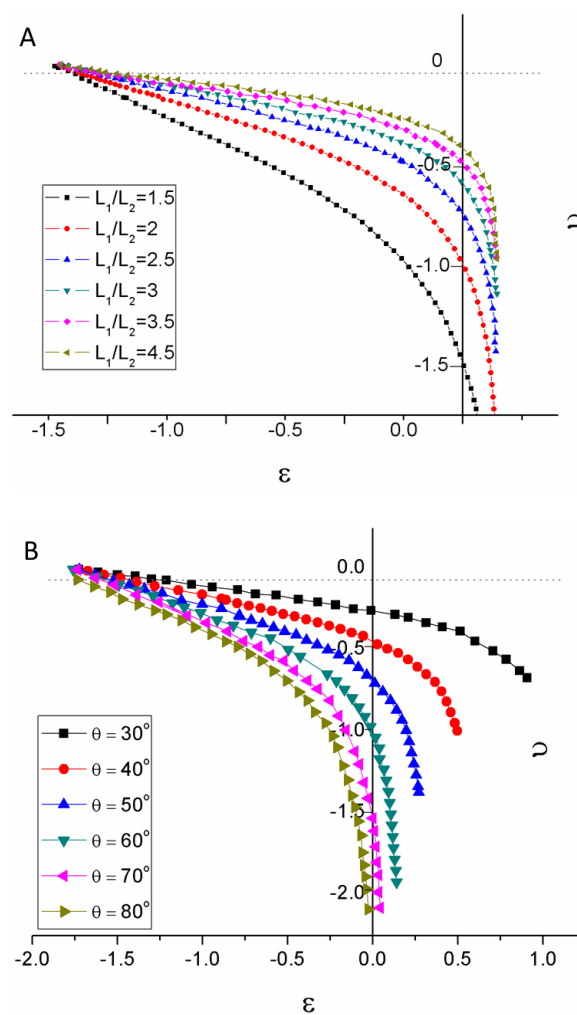


**Fig. 7-3. Poisson's ratios vary with strain for a re-entrant cell with geometric parameters of different  $a$  and re-entrant angle  $\theta$ .**

To investigate the effect of geometry of the re-entrant cell on the PR,  $\nu$  at the limit of small deformation is plotted as **Fig. 7-4**. The Poisson's ratio at the limit value of small deformation is consistent with that reported in literature [222], and a simplified expression using the small deflection assumption was also obtained as:

$$\nu = \frac{\sin^2 \theta}{(L_1 / L_2 - \cos \theta) \cos \theta} = \frac{\sin^2 \theta}{(a - \cos \theta) \cos \theta} \quad (4)$$

Where,  $a$  is the length ratio of struts,  $a = L_1 / L_2$ .

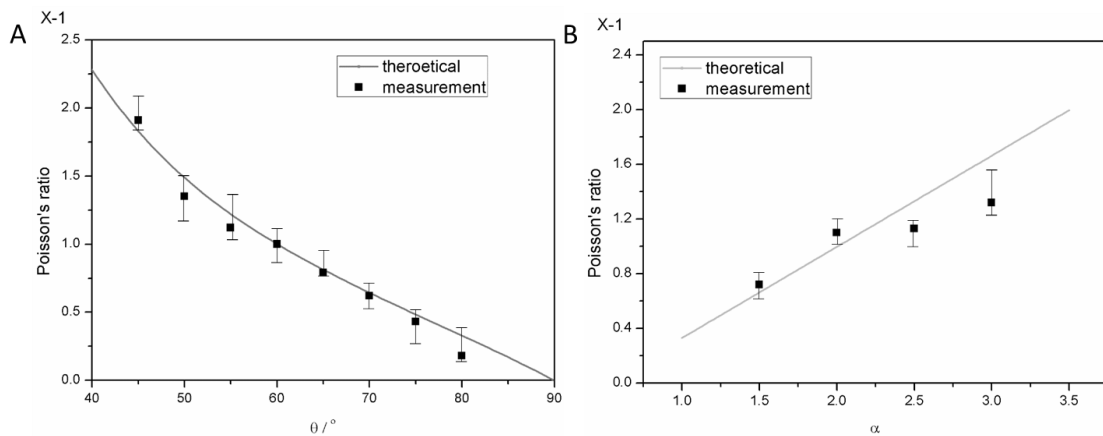


**Fig. 7-4. Relationship of PR with re-entrant angle  $\theta$  (A) and strut ratio  $\alpha$  (B) at the limit value of small deformation.**

From **Fig. 7-3** and **Fig. 7-4**, it is found that PR not only varies significantly with the strain in all cases, but also is influenced significantly by the geometric parameters of the cell. As  $a$  becomes large, the magnitude of  $\nu$  reduces generally with a given value of strain. A reversed tendency occurs for the influence of  $\theta$  on the PR. The sign of PR changes to positive at a critical strain, which, on the other hand, depends on the value of  $a$ .

According to the rule of structural influence on the PR, the following compression tests will focus on the mechanical response to the metal deposition, all the fabricated re-entrant lattices have same geometry parameters,  $\theta = 60^\circ$  and  $a = 2$ .

### 7.3.2 Mechanical properties

Polymer, Cu-coated composite and metallic auxetic structures were fabricated following the proposed initiator-integrated 3D printing. For the composite and auxetic structures, architectures with varying thickness of coating was obtained by controlling the ELP time. Finally, metallic hollow microlattices with hierarchical structures were obtained after etching the polymer core away, as **Fig. 7-5**. The hollow microlattice essentially translates the deposited nanoscale thin film in three dimensions to form a macroscopic material where the base structural elements are hollow tubes. By controlling the reaction time, submicron-thick uniform conformal coating can be achieved, resulting in a metallic cellular material with strength-enhanced property.

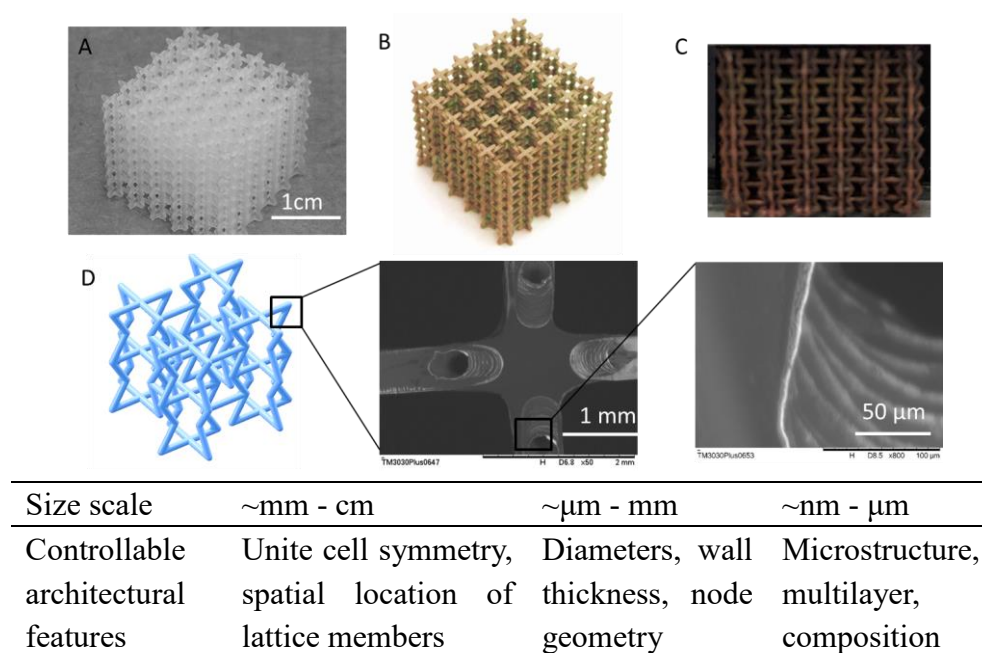


**Fig. 7-5. Auxetic architecture of metallic hollow microlattices after etching of polymer core. (A) Polymer template was fabricated by the initiator-integrated 3D printing. (B) Metallic cellular template was achieved by SI-ATRP-assisted ELP of Cu. (C) Metallic hollow structure was obtained after etching polymer core away. (D) Unit cells along with a breakdown of the relevant architectural hierarchy.**

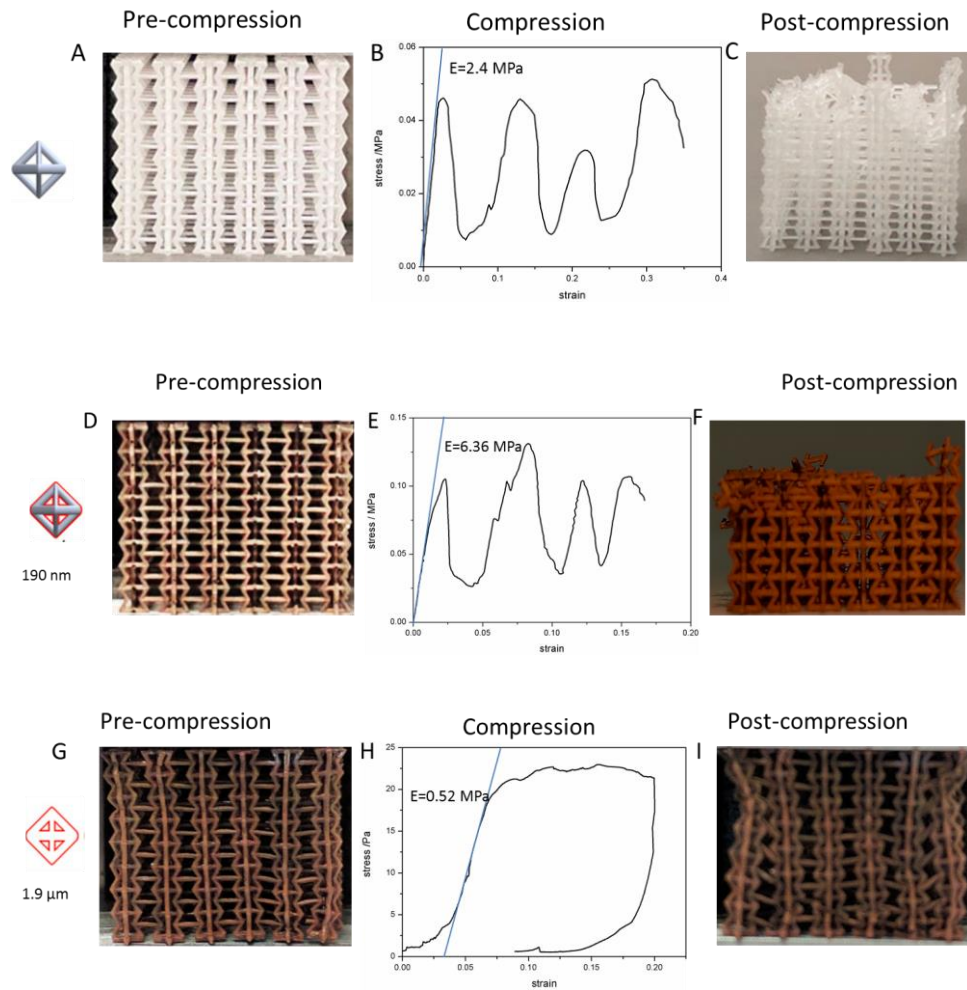


**Fig. 7-6. Compression experiments on the re-entrant lattices of three material systems. (A) Image of the polymer sample before compression. (B) Load displacement data that show compression to 35% strain. (C) Post-deformation of the polymer sample. (D) Image of the composite polymer and 190-nm Cu sample before compression. (E) Load displacement data that show 17.5% strain. (F) Post-deformation image of the composite sample. (G) Image of the hollow 1.9  $\mu\text{m}$  walled Cu sample before compression. (H) Load displacement data that show compression to 20% strain. (I) Post-deformation image of the hollow sample**

The characteristic failure and post-yield deformation of each sample were observed to be correlated with material system and architecture. It was found that the material systems (i.e., polymer, composite, hollow Cu) directly affected the localization of

failure within the hierarchical beams and the global recoverability of the samples, while the architecture strongly influence the global deformation behavior. Mechanical properties of all three material systems with two orders of hierarchy are demonstrated as **Fig. 7-6**.

The post-yield deformations of polymer and composite samples are brittle-like with continuous serrated flow (**Fig. 7-6A-C and D-F**), which is governed primarily by buckling in the inclined beams. The strength-enhancement of composite sample increases significantly the compressive strength and stiffness. After the deposition of ~190 nm Cu coating, the compressive strength increases to 0.1 MPa from polymer's 0.04 MPa. And the stiffness is doubled to 6.36 MPa. As investigated in Chapter 5, the high instinct strength and stiffness of Cu contributes most to the improvement.

The post-yield deformation behavior of hollow metallic samples is ductile-like with continuous stress-strain flow (**Fig. 7-6 G-I**). Similar to the ultralight metallic pyramidal materials in Chapter 6, failure of the re-entrant architecture occurred through a combination of localized elastic beam buckling in the inclined beams, shell buckling in individual hollow tubes, and microcracking at the nodes.

**Table 7-1** lists the mechanical properties of all material systems, and especially the composite and hollow metallic materials with different coating thickness. The hollow Cu samples have the highest average recovery, with samples recovering up to 85–98% of their original height after compressions exceeding 30% strain. Failure in the hollow samples initiated and localized primarily in individual inclined beams. Buckling of these beams creates a compliant region in the horizontal row that accommodates most of the ensuing displacement. Upon unloading, most of the inclined beams within the cross-section of the linked beams remained intact, allowing a significant global recovery. This effect is present in all hierarchical microlattices. The recoverability

mechanism described above is followed the same mechanism as the hollow pyramidal lattices described in Chapter 6.

**Table 7-1. Summary of structural parameters and mechanical properties of the fabricated microlattices.**

Sample#	$t$ ( $\mu\text{m}$ )	$D$ ( $\mu\text{m}$ )	$\varphi =$ $t/D$	$L_2$ ( $\mu\text{m}$ )	$\theta$ ( $^\circ$ )	$\rho$ ( $\text{mg}/\text{cm}^3$ )	$\bar{\rho}$ (%)	$\sigma_y$ (kPa)	$E$ (MPa)	$\varepsilon_m$
polymer	-	500	-	2000	60	130	11.0	43.7	2.4	
polymer	-	500	-	2000	60	123	10.4	45.2	2.23	
polymer	-	500	-	2000	60	137	11.6	44.9	2.37	
composite	0.19	500	3.8e-4	2000	60	143	12.1	117	6.36	
composite	0.47	500	0.9e-3	2000	60	217	18.4	245	20.3	
composite	1.87	500	4.1e-3	2000	60	567	20.3	963	107.4	
composite	2.18	500	4.4e-4	2000	60	613	22.4	1033	117.8	
hollow	0.37	500	7.6e-3	2000	60	4.8	0.054	0.79	0.028	0.53
hollow	1.9	500	4.1e-3	2000	60	41.5	0.463	18.3	0.52	-
hollow	0.50	500	1.0e-3	2000	60	10.3	0.115	2.5	0.093	0.48
hollow	0.91	500	1.8e-3	2000	60	17.6	0.196	9.28	0.19	0.31
hollow	1.22	500	2.4e-3	2000	60	22.8	0.255	17.9	0.32	0.11
hollow	2.18	500	4.4e-3	2000	60	50.4	0.53	23.9	0.61	0.06
hollow	5.72	500	1.1e-2	2000	60	127.6	1.43	218.7	7.05	-

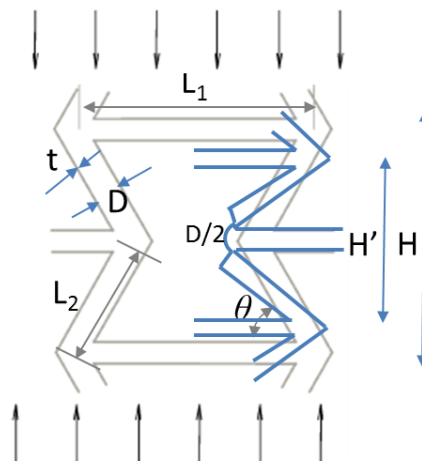


**Fig. 7-7. Mechanical model of inclined beams rotating around the node.**

**Fig. 7-7** shows the process that elastic buckling occurs at the node following by the rotation about the buckling. Assuming a uniform deformation during the compression,

the rotation occurs by bending a thin film of thickness  $\sim t-2t$  and length of the strut radius. For the hollow metallic lattices, a simple mechanical analysis according to **Fig. 7-7** can be established to predict a transition from the elastic recovery regime to the plastic regime at a critical wall-thickness-to-diameter ratio, which is given by:

$$\varepsilon_{cr} \cdot \sin \theta = 1 - \sin \left( \theta - \frac{\sigma_y'}{4E'} \cdot \frac{D}{t} \right) \quad \text{or} \quad \varepsilon_{cr} \cdot \sin \theta = 1 - \sin \left( \theta - \frac{\sigma_y'}{4E'} \cdot \frac{1}{\phi} \right) \quad (5)$$

Where  $E'$  and  $\sigma_y'$  are the yield strength and Young's modulus of ELP Cu.

(more details can be found in Chapter 6)

Equation (5) depicts that the critical maximum strain mainly depends on the thickness ratio and truss angle but ignores the effect of truss length. As stated in Chapter 6, by applying the value into equation (5), it is able to plot the critical relevance of the wall-thickness ratio and truss angle with the maximum compressive strain after which a full recovery can be realized. The maximum strain decreases with the increase of thickness ratio, resulting in a gradual reduction of the recoverability. That means, the microlattices tend to deform as the traditional cellular metals composed of solid truss when the ratio increases further.

As for the truss angle, the prediction suggests that a small truss angle usually get higher compression tolerance. That is because a small truss angle leads to a large inclination of the loading on the strut cross-section resulting in a decrease of the introduction of shear stress and the strut is deformed likely in form of bending with a large deflection [198]. In addition, thickness ratio influences the compressive strain exponentially while the truss angle affects the strain approximately in linear. It is in accordance with the fact that the wall-thickness-to-diameter ratio issues most on the fundamental local deformation, while the global loading status is more sensitive to the loading angle.

### 7.3.3 Poisson's ratio upon metal thickness.

We also investigated the influence of metal layer on the PR by dividing the axial strain in the loading direction with the negative transverse strain. It should be noted that, PR varies significantly with the strain in all cases of geometric parameters as described in 7.3.1. Here, a transient PR is calculated through an approximation method, for which we only take the initial 2.5% uniaxial strain as the effective measurement. The transverse strain is calculated as the ratio of the average contraction after 2.5% uniaxial compression to the width of the sample.

The influence of metal thickness on the PR is plotted in **Fig. 7-8**. Both polymer and composite materials have a fixed PR as  $\sim -1.1$ , which agrees with the computational analysis. The solid polymer beam or metal-coated solid polymer beam undergoes same mechanical response to the uniaxial loading. As analyzed in 7.2.1, the inclined beam will bend around the midpoint and then result in a global contraction. Consequently, for a given geometric parameter of  $L_1/L_2 = 2$ ,  $\theta = 60^\circ$ , and  $L_1/D = 4$ , both polymer and composite material will have a same Poisson's ratio.

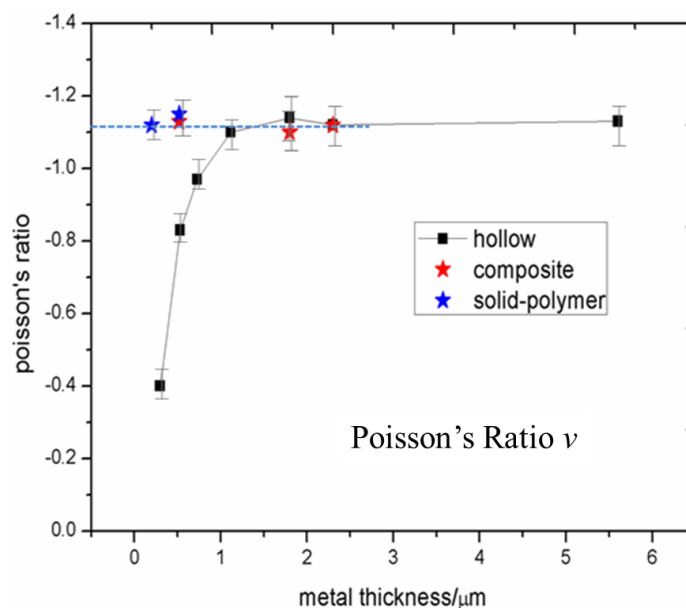


**Fig. 7-8. PR of three material systems versus the thickness metal layer.**

For the hollow Cu lattices, it is noted that PR increases with the increase of metal thickness, and finally stabilizes at  $\sim -1.1$ , which is same as that of the polymer and composite lattices. When the metal film is below  $2 \mu\text{m}$  ( $t/D = 4 \times 10^{-3}$ ), the bending of inclined beams in response to the uniaxial load will not only result in the inclined beam rotating around the node, but also cause a local buckling. The local buckling will reduce the transferring effectiveness of the force in the transverse direction, and accordingly decrease the global contraction of the lattice. In addition, the linking beams will also undergo a local buckling which further decrease the effective PR. The lattices with a thicker metal coating will deform similarly to the polymer and composite lattice due to the inclined and linking beams that are strong enough to eliminate the local buckling.

## 7.4 Conclusion

In summary, mechanical metamaterials-auxetic materials-composed of re-entrant cells were prepared by the initiator-integrated strategy. Ultralight hollow cellular metals were achieved with hierarchical architectures after the etching of polymer core. The advantage of 3D printing in the fabrication of complex geometries incorporating lattice topology benefits the materials of hierarchical structures spanning multiple length scales. In this study, three material systems, i.e. polymer, composite and hollow Cu, were created and compared in terms of the mechanical properties. Among them, hollow microlattices with a global size of  $\sim 2 \text{ cm}$  and wall thickness of  $370 \text{ nm}$  to  $5.72 \mu\text{m}$  are fabricated with density ranging from  $4.8$  to  $127 \text{ mg/cm}^3$ . Furthermore, the transient PR of hollow metallic materials varies with the thickness of metal film, and finally stabilizes at a constant same as that of the polymer and composite materials. These mechanical meta-materials exemplify a new conception of structural design by integrating the advantages of 3D printing in architectural construction with the benefits of surface modification in precise structure controlling.

The numerical analysis shows PR of auxetic lattices are not a constant under large deformation. They vary significantly with the strain and converge to the results predicted by small deformation of flexure within the limit of small strain. At large deformation, the NPR is different in remote compressive loading and tensile loading. A simplified expression was obtained based on the predicted PR at the limit of small strain. Geometric parameters of the re-entrant cell, i.e.,  $L_1/L_2$  and  $\theta$ , have a very significant effect on the magnitude of PR. The sign of PR even changes from negative to positive, when the cell bears a compression, and the deformation is large enough.

In contrast to the brittle-like deformation behavior of polymer and composite lattices, the post-yield deformation behavior of hollow metallic ones is ductile-like with continuous stress-strain flow. The reason is because the failure of hollow lattices occurs through a combination of localized elastic beam buckling in the beams, shell buckling in individual hollow tubes, and microcracking at the nodes. Of all material systems, the hollow metallic samples have the highest average compression recoverability.

## Chapter 8

### 8 New generation of initiator-integrated 3D printable material (i3DP II)

In this chapter, a new generation of 3D printing material, namely i3DP II, was developed and employed to fabricate various metallic structures by directly integrating a catechol-based dopamine as the initiator into the 3D resin followed by the surface-initiated self-polymerization of polydopamine and subsequent electroless plating. This newly developed material can simplify the functionalization process by eliminating the nitrogen/argon protection, since the functional layer of polydopamine comes from a natural oxidation process, and no critical condition is required. The rich catechol groups in polydopamine endow the metal coating with high adhesion stability on the surface of 3D printed object. Complex structures, such as Eiffel towers, micro-stretching-dominated lattices and auxetic lattices were prepared with multifarious metal coatings. The distinct metal coating can offer the 3D printed object with desired properties such as magnetic and high conductivity. The combination of 3D printing's merits in structure design and polydopamine's versatile function in surface modification and the subsequent polymer-assisted ELP of metals, extended the capability of 3D printing as a universal, robust and cost-effective technique to get applications in more practical areas, such as electronics, energy absorption, thermal insulation and others.

#### 8.1 Introduction

3D printing technology provides a powerful tool for the fabrication of sophisticated, bespoke and customized materials/devices, which may be difficult or even impossible for traditional manufacturing routes [223]. Because of its efficient capability of rapidly

converting materials into functional structures, 3D printing has become a revolutionary technology increasingly attracting attention from various fields such as material science, biology, chemistry and engineering [24]. However, the limited range of working materials contradict much of the growing interest in the production of functional materials/devices [224, 225]. Only a few applications have been addressed to date. It is, therefore, imperative to extend the capability of 3D printing to endow the 3D printed materials with more desired properties.

Two possible approaches are suggested to address the challenge, one is developing specific printing strategies together with many different material systems, and the other is developing a new 3D printing material system to produce functional materials/devices. The former is obviously costly and time-consuming, which also requires the support of 3D printer, while the latter is verified to be accessible through an integrated strategy. The recent advances of conjunction of materials with existing 3D printing are opening new areas of applications. This strategy has been preliminarily applied in the fabrication of biochemical products, such as tissue and scaffold engineering. Nevertheless, a major part of the previous work just involves the incorporation of different types of additive into the commercially available resin, mainly focusing on a specific improvement to the matrix [226-229]. Besides, the additive in all these cases strongly affects the printing process in aspects of solution viscosity, light penetration and additive dispersion. It is, therefore, of great significance to develop a robust printing method or material system by optimizing the incorporation of materials with 3D printing instead of solely developing for each.

The newly developed material system described in Chapter 3 gave a great demonstration by incorporating the additive and surface modification. It significantly enhanced the capability of 3D printing in fabrication of various functional materials, such as biocompatible, superhydrophobic, metallic, conductive and antimicrobial. But

the complex experiment procedures and rigorous reaction conditions restrict it available on more applications. Therefore, it is crucial to exploit a robust material system that can serve for a wide variety of demands and only require simple experiment procedures and mild reaction conditions.

Herein, we demonstrate the incorporation of dopamine as an additive with 3D printing to make metallic structures/materials. It presents superiorities in terms of easy-using, environmental friendly and versatility. Metallic cellular materials are used to demonstrate that this approach can not only produce high quality metal coating, but also easily realize an in-situ repair of metal coating. Compared to other methods suggested, including direct 3D printing of metal alloys (i.e., DIW, SLS & EBM) [230-232] and polymer-template directed metallization (SPPW) [67, 206], the proposed approach shows advantages of easy-use, fast-reaction and high resolution. The direct metal 3D printing only involves alloys of moderate-melting-point by high energy beams or metal-nanoparticle suspensions by polymerization, which is relatively costly and time-consuming to specially prepare the working materials. As for the SPPW, although it opens opportunities to fabricate metallic structure indirectly through converting polymer-based templates, its application is limited by fabricating only ordered structure units without horizontal elements. Furthermore, the ELP used in this technique was carried out only by physically absorbed catalysts, which results in a metal layer of weak adhesion.

This study aims to develop a simple and versatile strategy for 3D printing functional materials with desired properties. And taking the fabrication of metallic cellular materials as an example to demonstrate its capacity. In addition to generating high quality metallic coatings, the proposed strategy is also able to locally repair the damage areas by an in-situ growing of polydopamine (PDA) brushes via self-polymerization and the subsequent ELP of metals.

Different from the previous studies of PDA initiated functional coating, this study utilizes the dopamine as the initiator to mix up with UV-curable resin instead of immersing the object into the “have to” freshly prepared dopamine solution. More importantly, it can make the printed objects dominant in the following surface modification. The thin layer of PDA, as an extremely versatile nano-thick platform, can be utilized for secondary reaction to produce tailored functional layers [233, 234]. Especially, the catechol-groups in PDA is of great efficiency to deposit high adherent and uniform polymer brushes or metal coatings. This offers advantages that, on one hand, the 3D printed object itself owns the capability to initiate the following reaction, thus it is easy to realize local generation of desired coating and local repair the damage area; on the other hand, there is no limitation about the preparation of the solution.

The working principle is shown as **Fig. 8-1**, the initiator-integrated resin is polymerized with initiator embedded. Then, the initiator exposed on the surface is polymerized into PDA which acts as a versatile medium to induce the metallic coatings. This approach can provide an effective and robust strategy in fabrication of complex metallic structures by incorporating the surface modification and 3D printing technique. It offers superiorities not only to generate high quality metallic layers, but also to locally repair the surface because the initiator distributed in the 3D printed object is always ready to be initialized.

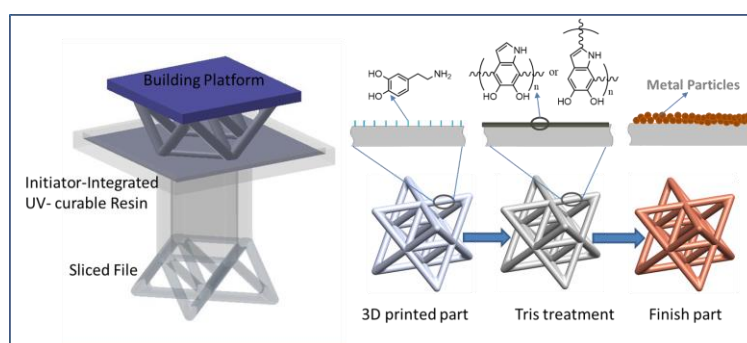


**Fig. 8-1. Schematic illustration of the processing of complex architectures by dopamine-integrated 3D printing with subsequent ELP for the metallic layer.**

## 8.2 Experimental setup

### 8.2.1 Chemicals and materials.

The UV-curable resin was prepared by mixing commercial monomers of 39.5 wt.% di(trimethylolpropane)tetraacrylate, 39.5 wt.% uethoxylated pentaerythritol tetraacrylate and 20 wt.% 2-[(butylcarbamoylethoxy)ethyl acrylate with 1.0 wt.% (2,4,6-Trimethylbenzoyl-diphenyl-phosphineoxide) as photo-initiator. All other chemicals were purchased from Sigma-Aldrich and used as received unless specially indicated.

### 8.2.2 3D Printing of dopamine-integrated architectures

Dopamine hydrochloride was added into the resin base and mixed well to prepare the initiator-integrated UV-curable resin. After degassing for 10 minutes in dark, the customized resin containing 3 wt.% dopamine was ready to print. A DLP 3D printer (PICO2, Asiga) was used to print architectures via photo-polymerizing in a layer-by-layer sequence. During printing, the initiator-added resin was polymerized with same parameters as the commercial resin base. After ultrasonically rinsing for 5 min in ethanol, the printed object was dried by a mild N<sub>2</sub> flow, and post cured by a UV-light for 5 min.

### 8.2.3 In-suit polymerization of PDA

In a typical experiment, dopamine was polymerized to PDA by immersing the 3D printed object into the Tris buffer (pH 8.5) for 2 hours. This needs to be stressed again that the long-time storage of the buffer and the initiator-containing substrate have no negative influence for the following reaction, indicating this method is preponderant to other methods [235, 236]. It was observed visibly that the oxidation polymerization changed the solution color to dark brown, and the object's surface grew a thin layer of black film. After that, the treated object was rinsed with DI water and dried by N<sub>2</sub> flow.

#### 8.2.4 PDA-assisted ELP

The PDA coated object was metallized by immersing in a metal salt solution. For ELP of copper, a solution contained a 1:1 separately prepared solutions A and B. Solution A was prepared in DI water consisting of 30g/L of ethylenediaminetetraacetic acid(EDTA), 15g/L of copper chloride ( $\text{CuCl}_2$ ), and 12 g/L of boric acid ( $\text{H}_3\text{BO}_3$ ). Solution B was 12g/L dimethylamine-borane (DMAB). Immediately before use, solution A was mixed with solution B as 1:1 in volume.

For ELP of Nickel, the solution was prepared consisting of 40 g/L of  $\text{Ni}_2\text{SO}_4 \cdot 5\text{H}_2\text{O}$ , 20 g/L of sodium citrate, 10 g/L of lactic acid in water. A 1g/L DMAB aqueous solution was prepared separately, and was mixed well with the Ni salt solution in a 4:1 volumetric proportion to prepare the final ELP bath.

For the ELP of Ni-Co alloy, the bath contained 0.05 M of  $\text{CoSO}_4 \cdot 7\text{H}_2\text{O}$ , 0.03M of  $\text{NiSO}_4 \cdot 6\text{H}_2\text{O}$ , 0.02M of  $\text{NiCl}_2 \cdot 6\text{H}_2\text{O}$ , 0.02 M of  $\text{NaH}_2\text{PO}_2 \cdot \text{H}_2\text{O}$ , 0.01M of  $\text{NH}_4\text{ReO}_4$ , 0.05M of glycine and sodium citrate as complexing agents, 0.5M of  $\text{Na}_2\text{SO}_4$  as supporting electrolyte, and various additives:  $\text{Ce}_2(\text{SO}_4)_3$  ( $2 \times 10^{-5}$  M), Tergitol 08 (2.5 mL/L), L -ascorbic acid ( $8.5 \times 10^{-3}$  M) and  $\text{C}_7\text{H}_4\text{NNaO}_3\text{S} \cdot 2\text{H}_2\text{O}$  (sodium saccharinate, 0.005 M). The pH was adjusted to 8.6 by adding NaOH. Immediately before use, the resultant solution was mixed with DMAB solution (10g/L) as 1:1 in volume. The PDA-coated surface was dipped into the mixed solution for 2-3 hrs at 30°C.

For the ELP of silver, the solution contained 1:1 separately prepared solutions A and B. Solution A was prepared by adding aqueous ammonia solution (0.2M) dropwise into the aqueous  $\text{AgNO}_3$  (5mM) solution until no brown precipitate generated any more. The solution B was glucose solution of 3mg/ml. Immediately before use, solution A was mixed with solution B as 1:1 in volume. The PDA-coated object was immersed into the resulted solution at ambient temperature. Then the surface was rinsed with DI water

and dried with N<sub>2</sub> gas.

For the ELP of gold, the PDA-modified object was immersed into a freshly prepared solution consisting of 0.01 wt % HAuCl<sub>4</sub> and 0.4 mM hydroxylamine hydrochloride for 24 hr. Then the gold-deposited surface was rinsed with DI water and dried by N<sub>2</sub> gas.

### 8.2.5 Characterization

The morphology of the surface coating was examined by SEM (Hitachi S-4500) at a 10kV accelerating voltage. VSM (730T, Lakeshoper, America) was utilized to measure the magnetic property at room temperature. Electrical conductivity of the deposited metal film was measured using a four-probe method on an M 2400 Keithley High Current Source Measure Unit (voltage range  $\pm 50$  V, step 1 V), and the conductivity was calculated. The data are obtained by multiple measurements on different samples (three for each formulation). Uniaxial tensile tests were carried out using a dynamometer (Deben Microtest) equipped with a load cell of 200N. Flake structures were tested, and at least 3 specimens for each measurement. FTIR spectra were recorded on Nicolet FTIR 6700 spectrophotometer (Thermo Nicolet) under ATR mode. Adhesive peel strength was measured by the use of a cross scotch tape test, according to the ASTM D-3359 using 3M #600 tape [237].

## 8.3 Results and discussion

FTIR analysis was conducted to verify the formation of PDA on the surface of 3D printed object. As observed in **Fig. 8-2**, the original resin presents a typical spectrum of acrylate-based formulation, with signals of O-H, C=O, and C-O appearing at 2917, 1700, and 1203 cm<sup>-1</sup>, respectively, but no signal of N-H shows up. For both the dopamine-integrated resin and PDA-coated sample, signal of N-H (3300-3500 cm<sup>-1</sup>) presents obviously in the spectra indicating the existence of amine group [238, 239].

The shift of the N-H signal from  $3348\text{ cm}^{-1}$  in dopamine-integrated resin to  $3300\text{ cm}^{-1}$  verifies that the amine group changed after the self-polymerization of dopamine. The signal of C-N ranging from  $943\text{-}1034\text{ cm}^{-1}$  also shifts because of the production of secondary amine after the self-polymerization process. All the evidence suggests that PDA was generated after the self-polymerization of dopamine which can act as a versatile medium for the following modification.

Moreover, the very broad signal at  $3300\text{-}3500\text{ cm}^{-1}$  overlapping the H-bonded signals in the FTIR spectrum of sample after self-polymerization indicates that the inner part still contains dopamine which has a potential of re-generating PDA. This characteristic enables the inner part of the initiator-integrated object to repeat the polymerization of PDA and the subsequent modification. That indicates it is possible to locally repair the metal coating in case of damage.

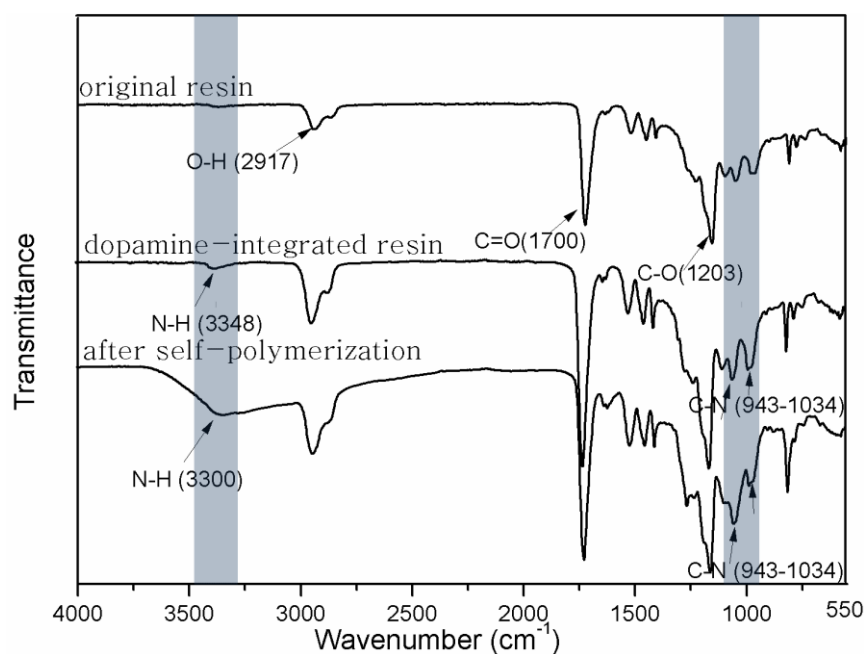


**Fig. 8-2. FTIR spectra of the photo-curable resin before and after the mixture of dopamine**

The universal PDA film is applicable to a broad variety of substrates, from inorganic

and rigid glass, polymeric PET flake, to soft green leaf [235]. Here, we adopt this characteristic into the 3D printing to fabricate a series of complex metallic structures. **Fig. 8-3 A-D** present the resultant Ag-coated microlattice after 30 minutes' deposition. SEM was used to observe the surface morphology of the Ag coating. The surface was deposited with a ~200 nm thick layer of silver which was composed of dense particles. One can also find the layer-by-layer feature of ~ 51  $\mu\text{m}$  in the z direction which was consistent with the printing setting. Furthermore, as observed from the SEM images (**Fig. 8-3 B-C**), the microlattice has no any cracks or delamination, stating the integrated dopamine causes no influence on the printability of the resin.

Moreover, the mechanical test was also conducted to investigate the influence of dopamine on the mechanical properties. Axial tensile test was conducted to qualify the influence on the tensile strength and Young's modulus. As shown in **Fig. 8-4A**, the sample with dopamine integrated showed a typical mechanical behavior of elastic deformation, which was constant with the sample without initiator. In addition, the elongation remains ~0.35 which is relatively unchanged after the addition of dopamine. **Fig. 8-4B** plots the quantitative comparison of the tensile strength and Young's modulus after the integration of the dopamine. It is found that the addition of the initiator causes no obvious effect on the mechanical properties.

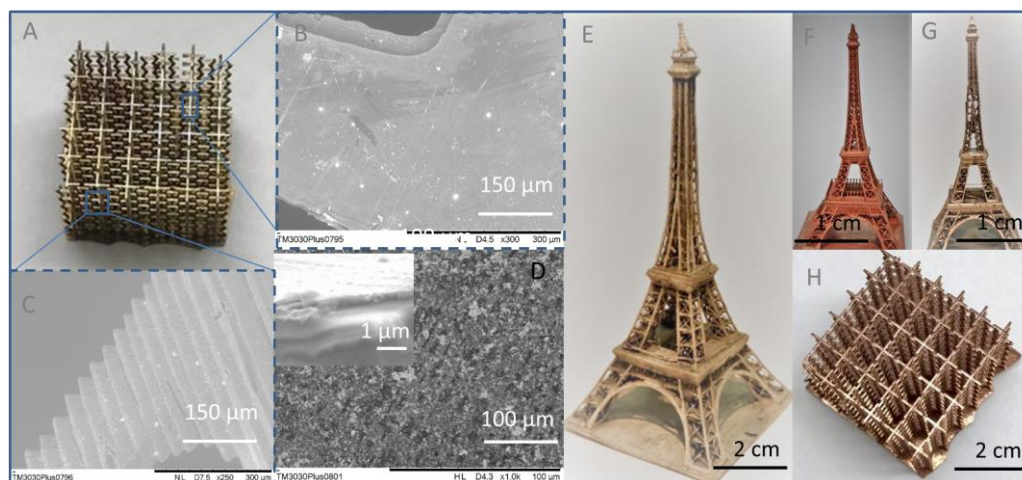


**Fig. 8-3. Optical photographs of complex metallic-architecture fabricated via dopamine-integrated 3D printing. (A-D) Ag-coated Eiffel tower and its surface morphology in the x, y, and z direction, the inset shows the thickness of the Ag coating, scale bar: 1 μm; (E-G) Metallic Eiffel tower of Ni-Co, Cu, and Ni coating, the dimension of the model is 28 × 28 × 72 mm. (H) Microlattice of Au-coating (20 × 20 × 15 mm).**

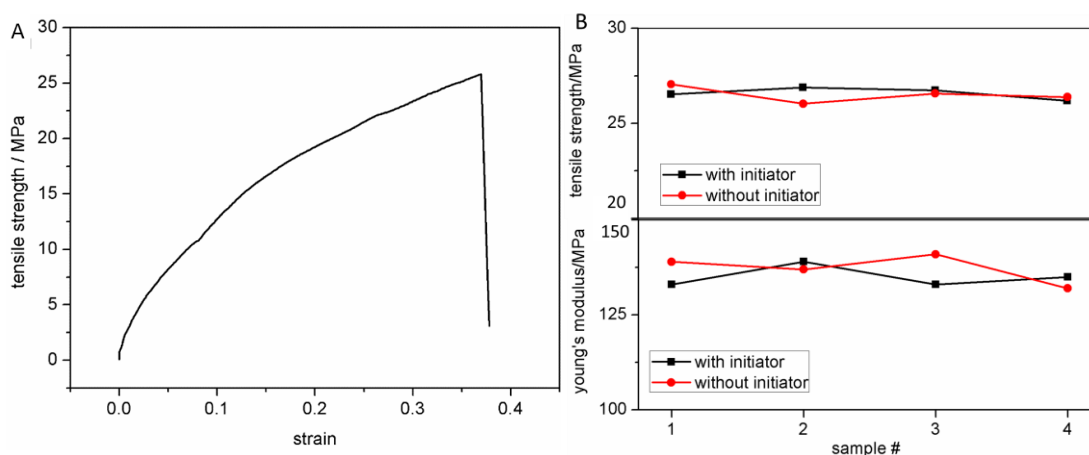


**Fig. 8-4. (A) Deformation behavior of dopamine initiated sample. (B) Comparison of tensile strength of the samples with and without mixture of dopamine-initiator**

Typically, PAD-assisted deposition of metal film is also highly dependent on the ELP

time. To reveal the generation of metal film on the surface of substrate, SEM was conducted to investigate the size and distribution of the silver nanoparticles on the polymerized matrices. Along with reaction time in the silver ELP solution, the 3D sample changed its color from the original clear to brown (the silver nanoparticles formation begins to occur), and finally to a silver-mirror like aspect (**Fig. 8-3A**). **Fig. 8-5** shows the generation process of silver particles reduced by the catalyst layer of PAD. At first, a flat interface was observed which is the polymerized polymer with nano-thick PAD film on it. Then, because of the PDA acts as a layer of catalyst to reduce metal particles in the ELP process, the silver particles began to emerge on the surface (**Fig. 8-5A, B**). Along with the reaction time, a dense layer of silver was deposited and the aggregation obviously shows up (**Fig. 8-5C, D**).

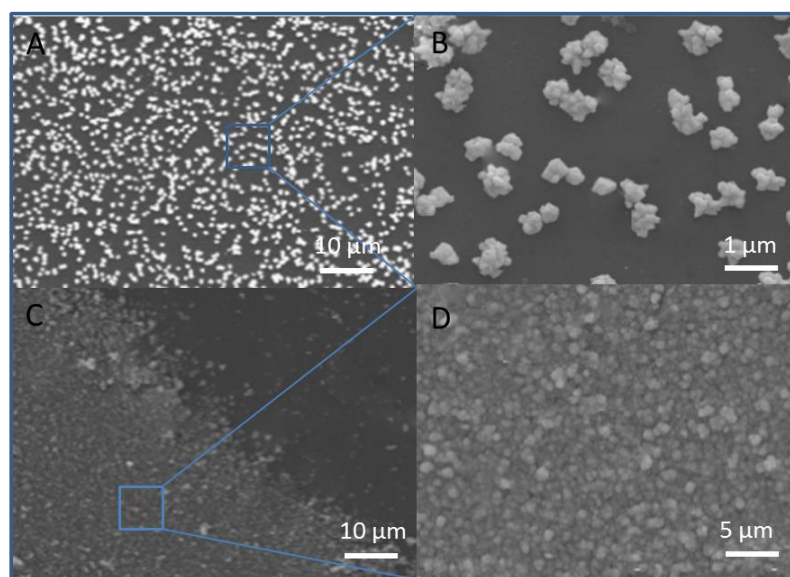


**Fig. 8-5. SEM of the silver film growing on the 3D printed object, the reaction time is 5 min for (A-B) and 30 min for (C-D), respectively.**

Notably, this strategy is also applicable to deposit other metal materials. By utilizing the computer-aided process, we demonstrated various complex metallic objects, including Cu, Ni, and Ni-Co-coated Eiffel tower and Au-coated cellular structures (**Fig.**

**8-3E-H).** In addition, it was found that the thickness of PDA film has no significant influence on the patterning efficiency. The metal film can be achieved regardless of the PDA thickness, which means a very small of dopamine into the UV-curable resin is sufficient to perform the following procedures. This also offers this strategy of advantages of cost- and time-saving. Also, because the PDA acts as a nano-thick adherent polymeric film to induce metal ELP to form metal layers with excellent adhesion to the substrate [236], all the deposited metal films display a robust adhesion on the surface of photo-polymerized polymer. The adhesion was measured through a standard tape test according to ASTM designation F1842-15. Briefly, a lattice pattern with six cuts in two mutual vertical directions was made in the coating to the substrate. Then a pressure sensitive tape was applied over the lattice and removed after 90s of application. The adhesion was evaluated by comparing with the standard illustrations. It was observed that all the coating showed a great adhesion of grade 4, which means only small flakes of the coating were detached at the intersection and less than 5% of the area was affected, as **Fig. 8-6**. This also indicates that approach offers great opportunities for the applications of stretchable and flexible electronics.

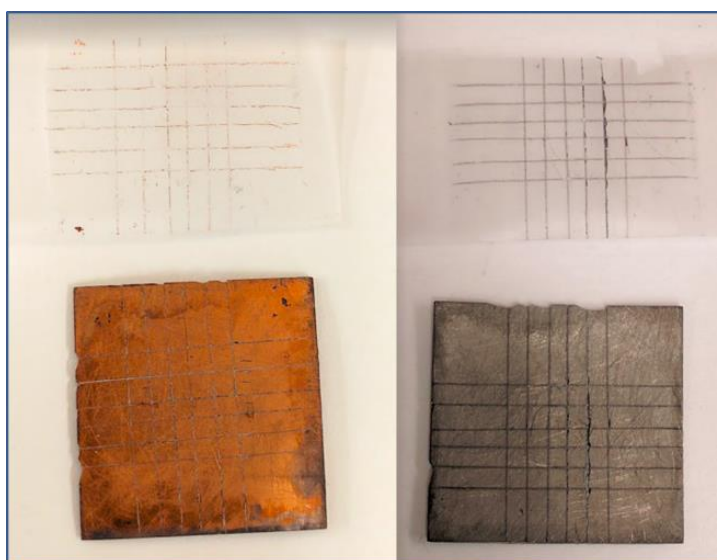


**Fig. 8-6.** Tape test of the Au- and Ag-coated surface to verify the adhesion of the metal coating generated by the dopamine-integrated 3D printing.

The success of metal deposition can offer the 3D printed objects of specific properties. For example, the Ni-Co alloy coating, which consists of 65% Ni, 28% Co, and 4% P (Fig. 8-7), suggests a Ni-rich magnetic material. A typical hysteresis loop was found through the VSM measurement (Fig. 8-8) which illustrates that the object exhibits soft ferromagnetic behavior. This is in agreement with the fact that Ni-rich alloy coating expresses soft ferromagnetic property [165]. It is notable here that the ratio of Ni to Co was controllable by adjusting the proportion of Ni in the ELP solution which can subsequently regulate the property for the magnetic coating. Therefore, according to the requirement of magnetic response, it is possible to optimize the property, such as magnetocrystalline anisotropy, based on the different magnetic properties of Ni-rich coating or Co-rich one. The result indicates that the proposed combination of 3D printing for architecture design and surface modification techniques has a great potential of the application of remote controlling objects. This technique offers 3D printing with potential applications of magnetically driven micromachines/systems.

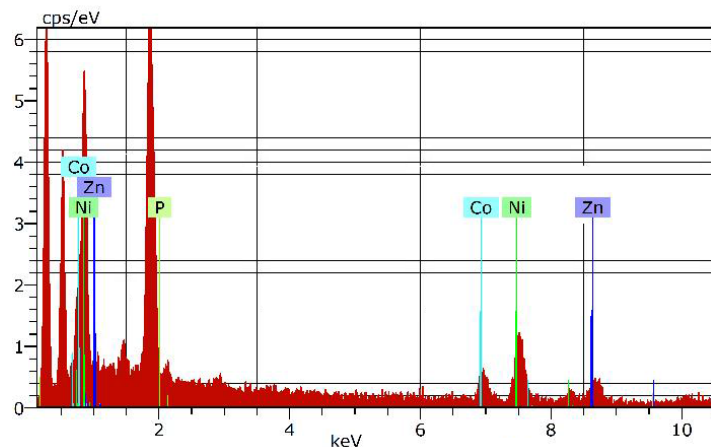


**Fig. 8-7. EDX spectrum of the Ni-Co alloy coating consisting of 65% Ni, 28% Co and 7% P.**

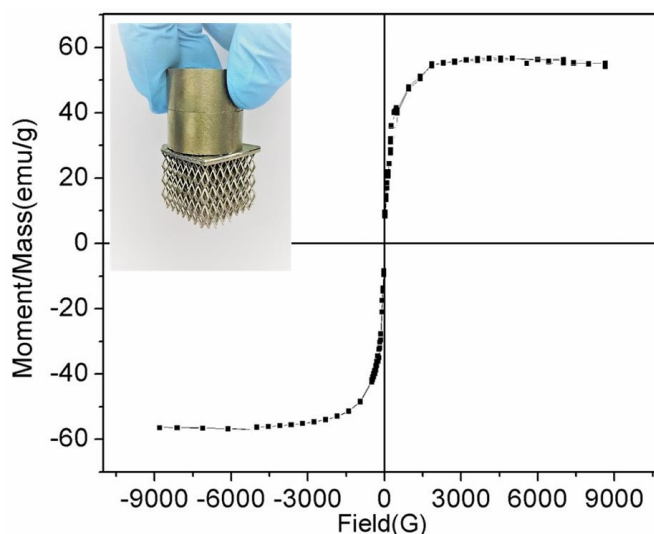


**Fig. 8-8. VSM measurement of the Ni-Co alloy coating. Inset is a cellular structure with Ni-Co alloy coating adsorbed by a magnet.**

Remarkably, this proposed technique is able to regenerate metal coating in case of the damage of existing coating. According to the FTIR spectrum of Fig. 8-2, the inner part still contains dopamine which has potential application of re-generating PDA. This characteristic makes this initiator-integrated object reusable to repeat the polymerization of PDA and the subsequent modification. An electro-circuit was set up as **Fig. 8-9** to demonstrate the re-generation of metal film. A plate with Cu coating, which was prepared using PDA-assisted ELP, was used as an electrode to connect a battery and a LED. As observed, LED was lighted up by connecting the battery through an original Cu-coated plated. After peeling off the middle part of the coating, the circuit was shut down, and LED was turned off. Because of the existence of the unpolymerized dopamine beneath the metal film, it is able to polymerize the dopamine to PDA once again after the damage of the outmost metal film. Thus, a new generated PDA can act repetitively as a functional medium to grow the metal coating. Finally, a new layer of Cu-coating was successfully generated by performing the polymerization of dopamine and the subsequent metal deposition process.

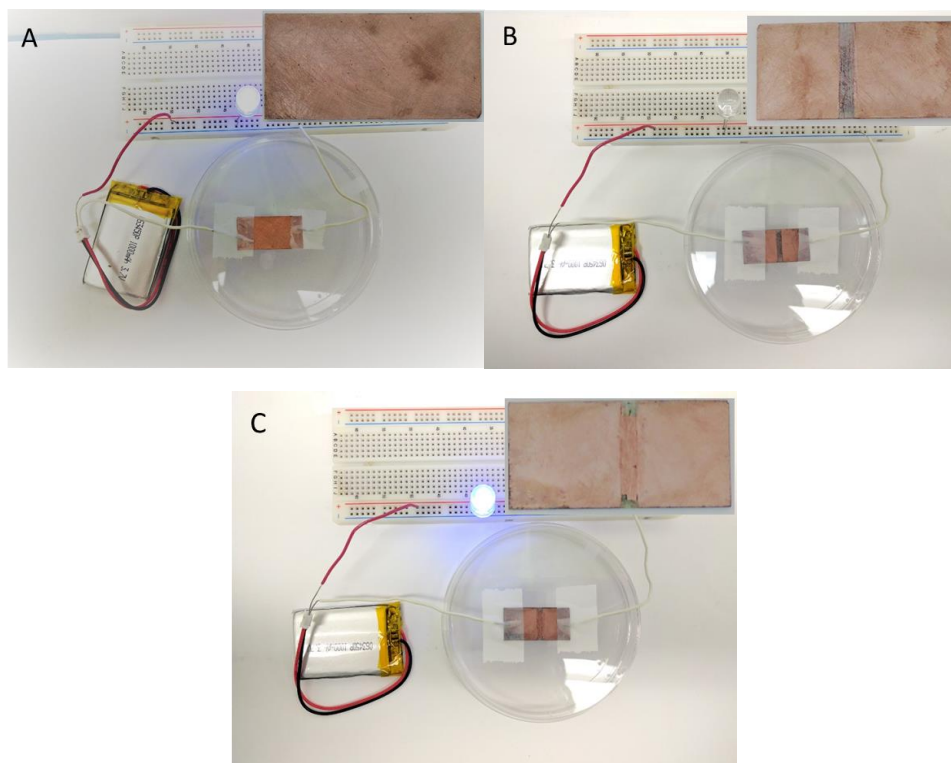


**Fig. 8-9. Demonstration of regeneration of the Cu metal film. (A) A plate with Cu coating was used as electrode to light the LED. (B) After peeling off the coating in middle area, the LED turned down. (C) The Cu coating was regenerated to connect the circuit again. Insets are the electrode made of Cu-coated plate.**

Electrical sheet resistance of the deposited metal films (copper, silver and gold) was measured using a four-probe method, and the conductivity was calculated. The results were listed as **Fig. 8-10**. For the copper film, the sheet resistance was measured to be ca.  $0.08 \Omega/\square$  after 30 min ELP. According to the thickness  $\sim 300\text{nm}$  (**Fig. 8-11A**), the conductivity was calculated as  $3.89 \times 10^7 \text{ S m}^{-1}$  which is  $\sim 65\%$  of the bulk copper material. Similarly, the sheet resistance of silver and gold film was measured as  $0.19$  and  $0.21 \Omega/\square$ , respectively (deposition time is 30 min for both silver and gold). As shown in **Fig. 8-10**, they took a proportion of 53% and 73% of the bulk material, respectively. All the metal films produced by this strategy are of comparable conductivities with the printed electronics described in report [240], indicating a

promising application of electronics. According to the reports [241, 242], it is the difference of surface energy induced by the different microstructures of these three materials that causes the conductivity discrepancy comparing with the bulk materials.

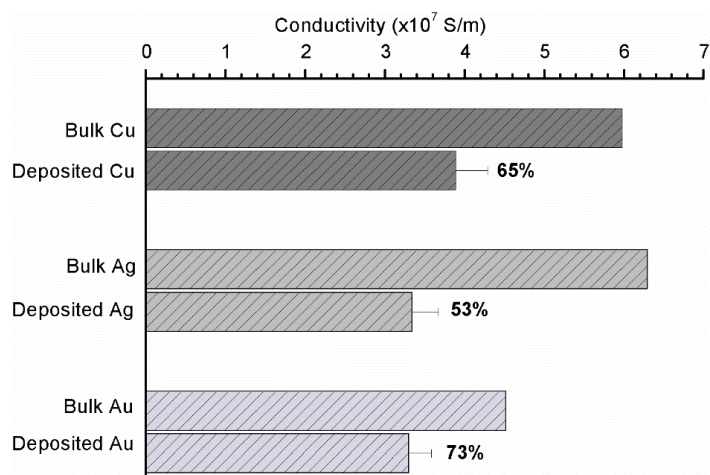


**Fig. 8-10. Comparison of the conductivity of deposited metal coatings and the bulk materials.**

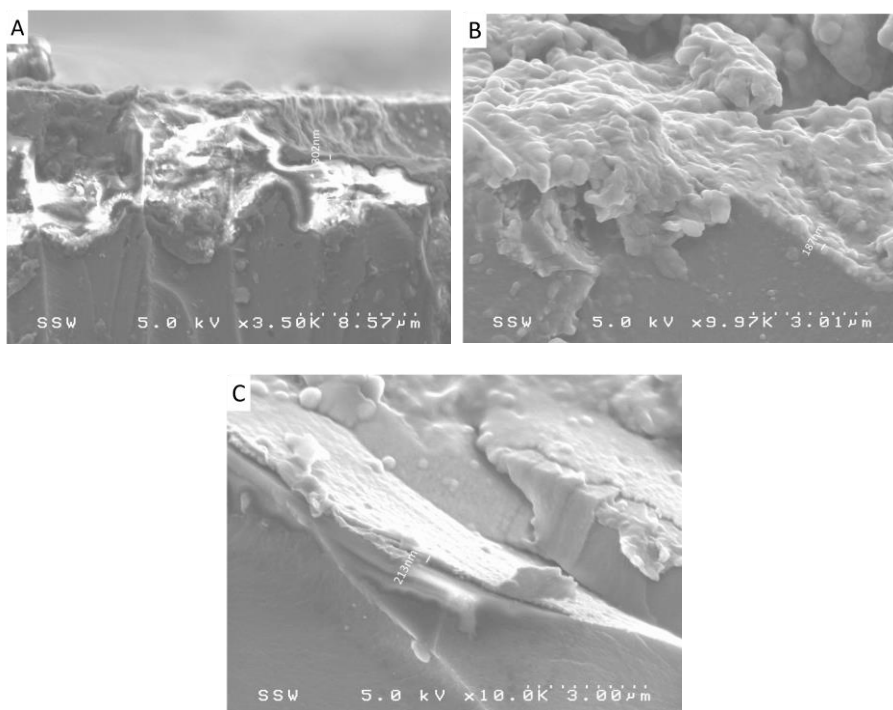


**Fig. 8-11. SEM images showing the thickness of the (A) Cu-coated substrate at 30 min, (B) Ag-coated substrate at 30 min, (C) Au-coated substrate at 30 min.**

## 8.4 Conclusion

In summary, a new generation of initiator-integrated 3D printing material was developed and employed to fabricate metallic structures. By directly mixing dopamine as an initiator into the photo-curable resin, 3D printing technique is able to cooperate with the structural flexibility and the surface modification to generate a variety of complex metallic architectures based on the in-situ growing of PDA and the subsequent ELP process. This strategy makes the 3D printed objects ready at any time to be triggered in the alkali environment for the growth of the desired functional layers on the surface, allowing a self-healing ability of the functional coatings. It also has a potential of fabricating electronics according to the comparable adhesion strength and conductivity of the metal coatings introduced by this approach. Overall, by combining the advantages of 3D printing for geometry construction and the facial PDA layer for inducing metal layers, this approach has greatly extended the capability of 3D printing as a robust and cost-effective technology, and enables this technology to be practical in applications of electronics, energy absorption, catalyst support, and others.

## Chapter 9

### 9 Summary, conclusions, and future directions

#### 9.1 Summary of 3D printing of functional materials

A facile and effective strategy, as described in **Fig. 9-1**, was demonstrated to endow 3D printing's capacity of fabricating functional materials/devices. Post-printing surface modification is used to give the 3D printed materials desirable properties, and structural optimization aims to maximize the functionality.

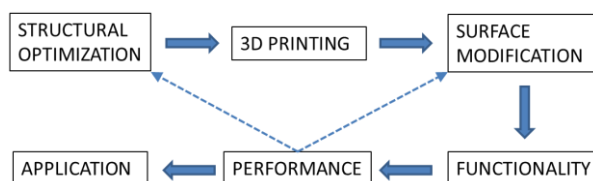


**Fig. 9-1. Workflow of 3D printing functional material through the incorporation of surface modification and structural optimization.**

Following this principle, a reusable filter was first demonstrated for heavy metal ion removal by integrating 3D printing technology with a bio-adsorption method. By combining the advantage of 3D printing in structural design and optimization, with the bio-adsorbent's high efficiency for removing heavy metal ion, it enables a 3D chitosan filter to have a great performance for water treatment. Compared to conventional processes, the fabricated filter offers advantages of simplified manufacturing, customized design and fast treatment. Furthermore, the structurally optimized filter can achieve a considerable adsorption capability up to 13.7 mg/mg in the optimal working condition at  $T = 25^{\circ}\text{C}$  and  $\text{pH} = 5.5$ , which shows promising prospects in a mass application of wastewater treatment. During the cyclical adsorption-desorption processes, the filter's adsorbability remains steadily in repeated filtrations, with only a

slight reduction of  $\sim 2$  mg/g after the first filtration cycle. FTIR spectra indicate that it is the  $-\text{NH}_2$  groups of chitosan that facilitate the adsorption process, implying a compatibility of adsorbing other metal ions. Therefore, the application in this study can be employed for the removal of more kinds of heavy metal ions.

A robust material system – initiator-integrated printable material – was further developed to serve for a wide variety of demands in an all-in-one manner. A bromine-containing acrylate was added into 3D printing resin, which acts as an initiator to allow polymer brushes to grow on the printed surface through surface-initiated atomic transfer radical polymerization (SI-ATRP). The 3D printed materials with easy-to-modify surface allow the fabrication of various functional materials, such as hydrophilic, metallic, and conductive alike. It is noted that, this approach is versatile for any UV-curable resin composed of acrylate-based prepolymers, and any photo-polymerization based 3D printing techniques. That means, taking advantage of both 3D printing and SI-ATRP, it is feasible to use only one material system to fabricate complex architectures with various desired functions. In addition, this initiator-integrated strategy could be compatible with many other surface-initiated technologies, only by simply selecting a proper initiator with different functional groups. Our following studies further verify that this initiator-integrated strategy is highly effective to make 3D printing technology practical in the fabrication of functional materials/devices with novel properties, and shows a great potential in fields of biomedical science, energy-adsorption, and mechanical metamaterials.

Based on the proposed initiator-integrated 3D printing material, magnetically manipulated robot was fabricated via the SI-ATRP assisted ELP. The robot was grafted with a layer of Ni-rich magnetic coating which exhibited a soft-magnetic property. The magnetic manipulation demonstrated that the ellipsoid robot was successfully magnetized, and can rotate synchronously with the magnetic field. The rotational

movement can be translated subsequently to linear movement by carefully designing the spiral structure and the strategy of magnetic controlling. According to the kinematic and magnetic analysis, the swimming properties under magnetic control were affected by the spiral shape, liquid viscosity and the controlling manner. Our investigation has shown that the proposed integrated 3D printing technology works well for fabrication of remote controlling objects. This technique offers 3D printing with a potential application of magnetically driven micromachines/systems.

The combination of surface-initiated modification and structural optimization was employed further to fabricate metallic cellular materials of high effective strength. First, we theoretically analyzed the mechanical properties of two stretching-dominant lattice—octet-truss lattice and pyramidal lattice. It was found that the pyramidal lattices with truss angle of  $35^\circ$  have the lowest density, while the effective stiffness reaches to the best at a truss angle of  $45^\circ$ . Although octet-truss can bear a larger compression than pyramidal lattice when having the same loading area, it provides a lower specific stiffness due to its higher density. 3D printing was employed to fabricate the lattices of complex architecture, for the verification of the above analysis. Compression tests were conducted to observe and compare the mechanical behaviors, and the results were consistent with the theoretical analysis. Next, by combining the structural optimization and the post-printing modification, Ni and Cu coatings were deposited to the 3D printed polymer lattices, obtaining metallic cellular materials of high strength. We also investigated the strength-enhancement effect on mechanical properties, and understood the relationship between mechanical properties and metal films' thickness in detail.

Ultralight metallic cellular materials inspired by the strength-enhancement effect were fabricated by the proposed initiator-integrated 3D printing material. The superiority of 3D printing in the construction of complex geometries incorporating lattice topology benefits the materials of hierarchical structures spanning multiple length scales. A thin

metal layer was successfully coated on the 3D printed objects via SI-ATRP and the subsequent polyelectrolyte-brush-assisted ELP. After etching away the polymer core, metallic structures with complex geometries were achieved, and can be subsequently engineered into a thin-walled metallic lattice which was capable of deforming elastically via the node fracture and buckling. In this study, microlattices with a global size of  $\sim 2$  cm and wall thickness of 320 nm to 13.2  $\mu\text{m}$  were fabricated, and the density ranged from 5.1 to 211  $\text{mg}/\text{cm}^3$ .

This novel manufacturing process enables the fabrication of architectures to have high-yield-stress constituent materials and very low truss member aspect ratio. These structural materials present an unusual mechanical property of strength and stiffness, and take dominance in absorbing energy, and shape recovery after significant compression. Uniaxial compression experiments were carried out to reveal the deformation behavior of the hierarchically designed microlattices. The microlattices of ultralow density ( $<10$   $\text{mg}/\text{cm}^3$ ) exhibit nearly a full recovery after larger compressive strain (50%). When the density increases further, the microlattices tend to deform the same as the traditional cellular metals composited of solid truss. A mechanical model was established to reveal the structural effect on the compressive response, and was used to guide the structural design. Generally, a less wall-thickness-to-diameter ratio or a smaller truss angle allows a larger compression without the introduction of plastic strain, and benefits the microlattices of a higher compression tolerance.

Mechanical meta-materials of NPR were also designed and fabricated through the initiator-integrated material. Ultralight auxetic materials of hierarchical architectures were obtained after etching away the polymer core. Computational analysis was first used to reveal the deformation mechanism. It was found that PR varies significantly with the strain, and converges to the results predicted by small deformation of flexure at the limit of small strain. Geometric parameters of the re-entrant cell, i.e.,  $L_1/L_2$  and

$\theta$ , have a significant effect on the magnitude of PR. A simplified relationship of PR and the structural parameters was obtained based on the predicted data at the limit of small strain. At large deformation, PR is different under remote compressive loading and tensile loading. The sign of PR even changes from negative to positive, when the cell bears an X-direction compression large enough.

In the experimental section, three material systems, polymer, composite and hollow Cu, were created and compared in terms of the mechanical properties. Compared to the brittle-like deformation behavior of polymer and composite lattices, the post-yield deformation behavior of hollow metallic ones is ductile-like with continuous stress-strain flow. This is because the failure of hollow lattices occurs in a combination of localized elastic buckling and shell buckling in individual hollow tubes, and microcracking at the nodes. Of all material systems, the hollow metallic samples have the highest average compression recoverability. It is noted that, the instant PR of hollow metallic materials increases with the thickness of metal film, and finally stabilizes at a constant same as that of the polymer and composite materials. These mechanical meta-materials exemplify a new conception of structural design by integrating the advantages of 3D printing in architectural construction with the benefits of surface modification in the controlling of precise structures.

At last, a new generation of initiator-integrated material (i3DP II) was developed to avoid the  $N_2$  protection. By directly mixing dopamine as an initiator into the photocurable resin, the easy-to-modify surface of the 3D printed object can be generated with a variety of functional coatings. Different from the Br-containing initiator which initiates surface modification requiring an oxygen-free condition, the dopamine-initiator used in this new material generates functional surface naturally due to the oxidative self-polymerization of dopamine. More importantly, this material makes the 3D printed objects ready at any time to be triggered in the alkali environment for the

re-growing of functional layers, and was verified further by locally repairing the damaged surface. It also offers a forward-looking technique on the fabrication of electronics according to the measurements that the metal coatings introduced by this approach present a comparable adhesion strength and conductivity.

## 9.2 Future directions

One goal of this dissertation, and the associated research work, is to establish the working strategy of 3D printing functional materials. I believe this foundation has been established, although many details regarding mechanisms and the fundamental science that makes all this possible still need to be determined. Regarding to the 3D printing technology itself, it is a long way from being possible to print part of large fabrication area and simultaneously with high printing resolution and fast printing speed. If the technology reaches there, magnetically driven robot can be further improved to have small holes containing various drugs, which have great potentials in medical application. Also, large-scale cellular materials can be fabricated with higher order of hierarchy, and nanoscale materials properties can be harnessed, which will give rise to new combinations of properties not seen in bulk-scale materials. In terms of 3D printable materials, although an effective strategy is established in this dissertation, it still requires great efforts to extend the working materials as diverse as that of traditional manufacturing. Specific future directions will be discussed as following, although I believe there are virtually limitless directions this work can take.

The initiator integrated strategy for 3D printing functional materials needs to be further extended and compatible with other kinds of surface initiated technologies by developing more kinds of initiator monomers. In addition, the preparation of initiator-integrated material should be further simplified.

For the specific functional materials mentioned in this study, such as the material that removes metal-ions from wastewater, more work should be focused on extending their working capacity of adsorbing more kinds of metal ions. For future research of the magnetic actuation-based control of microrobots, closed-loop control for non-holonomic mobile microrobots in 3D space should be investigated. The independent control of a microrobot in a group of multiple magnetic microrobots, and the swarm control of a group of magnetic microrobots are also of great challenge in the motion control of microrobots. I have also demonstrated several kinds of functional cellular materials based on the surface modification and structural optimization. However, all the demonstrated materials are limited to contain no more than two constituent materials, far from the point that micro-architectures can be rationally designed and fabricated with different mechanical properties combined. In addition, actual use of mechanical meta-materials for structural application requires a thorough study of their fatigue behavior, which is also proposed as a possible avenue for future research.

At last, the new generation of initiator-integrated 3D printing material still exists a few key issues which must be primarily resolved. The first not-fully addressed issue under study is the polymerization mechanism. There is still a lack of final verdict regarding to the polymerization process, the precise structure, and the components of polydopamine. Additionally, polydopamine is moving towards a programmable material with a great potential for practical use in the future. The main challenge for future success is how to make the best use of its striking properties in the construction of polydopamine-derived hybrid materials, so as to obtain high value products with performance superior to those already in the market.

## References

1. Khoo, Z.X., et al., *3D printing of smart materials: A review on recent progresses in 4D printing*. Virtual and Physical Prototyping, 2015. **10**(3): p. 103-122.
2. Chua, C.K. and K.F. Leong, *3D PRINTING AND ADDITIVE MANUFACTURING: Principles and Applications (with Companion Media Pack) of Rapid Prototyping*. 2014: World Scientific Publishing Co Inc.
3. Bhatia, U., *3D printing technology*. Int. J. Eng. Tech. Res, 2015. **3**: p. 327-330.
4. Frazier, W.E., *Metal Additive Manufacturing: A Review*. Journal of Materials Engineering and Performance, 2014. **23**(6): p. 1917-1928.
5. Huang, S.H., et al., *Additive manufacturing and its societal impact: a literature review*. The International Journal of Advanced Manufacturing Technology, 2013. **67**(5): p. 1191-1203.
6. Bose, S., S. Vahabzadeh, and A. Bandyopadhyay, *Bone tissue engineering using 3D printing*. Materials Today, 2013. **16**(12): p. 496-504.
7. Murphy, S.V. and A. Atala, *3D bioprinting of tissues and organs*. Nature biotechnology, 2014. **32**(8): p. 773-785.
8. Kang, H.-W., et al., *A 3D bioprinting system to produce human-scale tissue constructs with structural integrity*. Nat Biotech, 2016. **34**(3): p. 312-319.
9. Jonathan, G. and A. Karim, *3D printing in pharmaceuticals: A new tool for designing customized drug delivery systems*. International Journal of Pharmaceutics, 2016. **499**(1-2): p. 376-394.
10. Marquardt, T. and E. Zheng, *History of 3D Printing*.
11. Jakus, A.E., *Development and Implementation of Functional 3D-Printed Material Systems for Tissue Engineering, Energy, and Structural Applications*. 2014, Northwestern University.
12. Raya-Rivera, A., et al., *Tissue-engineered autologous urethras for patients who need reconstruction: an observational study*. The Lancet. **377**(9772): p. 1175-1182.
13. Pearce, J.M., et al., *3-D printing of open source appropriate technologies for self-directed sustainable development*. Journal of Sustainable Development, 2010. **3**(4): p. 17.
14. Kruth, J.-P., et al., *Binding mechanisms in selective laser sintering and selective laser melting*. Rapid prototyping journal, 2005. **11**(1): p. 26-36.
15. Berman, B., *3-D printing: The new industrial revolution*. Business Horizons, 2012. **55**(2): p. 155-162.
16. Bogue, R., *3D printing: the dawn of a new era in manufacturing?* Assembly Automation, 2013. **33**(4): p. 307-311.
17. Lipson, H. and M. Kurman, *Fabricated: The new world of 3D printing*. 2013:

John Wiley & Sons.

18. Gretsch, K.F., et al., *Development of novel 3D-printed robotic prosthetic for transradial amputees*. *Prosthetics and orthotics international*, 2016. **40**(3): p. 400-403.
19. *Transplant jaw made by 3D printer claimed as first*.
20. Ventola, C.L., *Medical applications for 3D printing: current and projected uses*. *PT*, 2014. **39**(10): p. 704-711.
21. Wong, K.V. and A. Hernandez, *A review of additive manufacturing*. *ISRN Mechanical Engineering*, 2012. **2012**.
22. *3D printing: the world's first printed plane*. Available from: <https://www.newscientist.com/article/dn20737-3d-printing-the-worlds-first-printed-plane/>.
23. *Obama's speech highlights rise of 3D printing*
24. Tumbleston, J.R., et al., *Continuous liquid interface production of 3D objects*. *Science*, 2015. **347**(6228): p. 1349-1352.
25. Daly, A.C., et al., *3D Bioprinting: 3D Bioprinting of Developmentally Inspired Templates for Whole Bone Organ Engineering (Adv. Healthcare Mater. 18/2016)*. *Advanced Healthcare Materials*, 2016. **5**(18): p. 2352-2352.
26. Almeida, H., et al., *Fibrin hydrogels functionalized with cartilage extracellular matrix and incorporating freshly isolated stromal cells as an injectable for cartilage regeneration*. *Acta biomaterialia*, 2016. **36**: p. 55-62.
27. *LEARN CAD*. Available from: [http://www.3dstuffmakers.com/?page\\_id=2096](http://www.3dstuffmakers.com/?page_id=2096).
28. Petti, F.M., et al., *Digital 3D modelling of dinosaur footprints by photogrammetry and laser scanning techniques: integrated approach at the Coste dell'Anglone tracksite (Lower Jurassic, Southern Alps, Northern Italy)*. *Studi Trentini di Scienze Naturali, Acta Geologica*, 2008. **83**: p. 303-315.
29. Ambrosi, A. and M. Pumera, *3D-printing technologies for electrochemical applications*. *Chemical Society Reviews*, 2016. **45**(10): p. 2740-2755.
30. Leyden, R.N., et al., *Stereolithography method and apparatus*. 1992, Google Patents.
31. Kodama, H., *Automatic method for fabricating a three-dimensional plastic model with photo-hardening polymer*. *Review of scientific instruments*, 1981. **52**(11): p. 1770-1773.
32. *3D Printing Technology Comparison: SLA vs. DLP*. Available from: <https://formlabs.com/blog/3d-printing-technology-comparison-sla-dlp/>.
33. Gibson, I., D.W. Rosen, and B. Stucker, *Additive manufacturing technologies*. Vol. 238. 2010: Springer.
34. Liravi, F., S. Das, and C. Zhou, *Separation force analysis and prediction based on cohesive element model for constrained-surface Stereolithography processes*. *Computer-Aided Design*, 2015. **69**: p. 134-142.

35. Zhu, C., et al., *Highly compressible 3D periodic graphene aerogel microlattices*. Nature Communications, 2015. **6**: p. 6962.
36. Wegst, U.G.K., et al., *Bioinspired structural materials*. Nat Mater, 2015. **14**(1): p. 23-36.
37. *3D Printing Processes - Binder Jetting*. Available from: <https://www.engineersgarage.com/articles/3d-printing-processes-binder-jetting>.
38. *Rapid Prototyping - Selective Laser Sintering*. Available from: <http://www.iotasigma.co.uk/sls.html>.
39. Khoshnevis, B., M. Yoozbashizadeh, and Y. Chen, *Metallic part fabrication using selective inhibition sintering (SIS)*. Rapid Prototyping Journal, 2012. **18**(2): p. 144-153.
40. Bhushan, B. and M. Caspers, *An overview of additive manufacturing (3D printing) for microfabrication*. Microsystem Technologies, 2017. **23**(4): p. 1117-1124.
41. Klein, J., et al., *Additive manufacturing of optically transparent glass*. 3D Printing and Additive Manufacturing, 2015. **2**(3): p. 92-105.
42. Kotz, F., et al., *Three-dimensional printing of transparent fused silica glass*. Nature, 2017. **544**(7650): p. 337-339.
43. Ding, D., et al., *Wire-feed additive manufacturing of metal components: technologies, developments and future interests*. The International Journal of Advanced Manufacturing Technology, 2015. **81**(1): p. 465-481.
44. Malinauskas, M., et al., *Ultrafast laser nanostructuring of photopolymers: A decade of advances*. Physics Reports, 2013. **533**(1): p. 1-31.
45. Obata, K., et al., *High-aspect 3D two-photon polymerization structuring with widened objective working range (WOW-2PP)*. Light: Science & Applications, 2013. **2**(12): p. e116.
46. *Comparison between 3D printing and traditional manufacturing processes for plastics*.
47. Thomas, A., *Functional Materials: From Hard to Soft Porous Frameworks*. Angewandte Chemie International Edition, 2010. **49**(45): p. 8328-8344.
48. Koch, K., et al., *Fabrication of artificial Lotus leaves and significance of hierarchical structure for superhydrophobicity and low adhesion*. Soft Matter, 2009. **5**(7): p. 1386-1393.
49. Lakes, R., *Materials with structural hierarchy*. Nature, 1993. **361**(6412): p. 511-515.
50. Jakus, A.E., et al., *Metallic Architectures from 3D-Printed Powder-Based Liquid Inks*. Advanced Functional Materials, 2015. **25**(45): p. 6985-6995.
51. Eckel, Z.C., et al., *Additive manufacturing of polymer-derived ceramics*. Science, 2016. **351**(6268): p. 58-62.
52. Fu, K., et al., *Progress in 3D Printing of Carbon Materials for Energy-Related*

- Applications*. *Advanced Materials*, 2017. **29**(9): p. 1603486-n/a.
53. Wei, X., et al., *3D Printable Graphene Composite*. 2015. **5**: p. 11181.
  54. Zhu, C., et al., *Highly compressible 3D periodic graphene aerogel microlattices*. 2015. **6**: p. 6962.
  55. Compton, B.G. and J.A. Lewis, *3D-printing of lightweight cellular composites*. *Adv Mater*, 2014. **26**(34): p. 5930-5.
  56. Fantino, E., et al., *3D Printing of Conductive Complex Structures with In Situ Generation of Silver Nanoparticles*. *Advanced Materials*, 2016: p. n/a-n/a.
  57. Chen, N. and Q. Pan, *Versatile Fabrication of Ultralight Magnetic Foams and Application for Oil–Water Separation*. *ACS Nano*, 2013. **7**(8): p. 6875-6883.
  58. Chen, D., et al., *Layer by layer electroless deposition: An efficient route for preparing adhesion-enhanced metallic coatings on plastic surfaces*. *Chemical Engineering Journal*, 2016. **303**(Supplement C): p. 100-108.
  59. Luo, L.-M., et al., *Electroless copper plating on PC engineering plastic with a novel palladium-free surface activation process*. *Surface and Coatings Technology*, 2014. **251**(Supplement C): p. 69-73.
  60. Shu, Z. and X. Wang, *Environment-friendly Pd free surface activation technics for ABS surface*. *Applied Surface Science*, 2012. **258**(14): p. 5328-5331.
  61. Tang, X., et al., *A novel surface activation method for Ni/Au electroless plating of acrylonitrile–butadiene–styrene*. *Surface and Coatings Technology*, 2011. **206**(6): p. 1382-1388.
  62. Wang, M.-Q., et al., *Electroless plating of PVC plastic through new surface modification method applying a semi-IPN hydrogel film*. *Applied Surface Science*, 2013. **277**(Supplement C): p. 249-256.
  63. Wang, X., et al., *i3DP, a robust 3D printing approach enabling genetic post-printing surface modification*. *Chem Commun (Camb)*, 2013. **49**(86): p. 10064-6.
  64. Schaedler, T.A. and W.B. Carter, *Architected Cellular Materials*. *Annual Review of Materials Research*, 2016. **46**(1): p. 187-210.
  65. Gibson, L.J. and M.F. Ashby, *Cellular solids: structure and properties*. 1999: Cambridge university press.
  66. Schaedler, T.A., et al., *Designing Metallic Microlattices for Energy Absorber Applications*. *Advanced Engineering Materials*, 2014. **16**(3): p. 276-283.
  67. Schaedler, T.A., et al., *Ultralight metallic microlattices*. *Science*, 2011. **334**(6058): p. 962-5.
  68. Chen, Y., et al., *Lattice Metamaterials with Mechanically Tunable Poisson's Ratio for Vibration Control*. *Physical Review Applied*, 2017. **7**(2): p. 024012.
  69. Zadpoor, A.A., *Mechanical meta-materials*. *Materials Horizons*, 2016. **3**(5): p. 371-381.
  70. Kadic, M., et al., *On the practicability of pentamode mechanical metamaterials*.

- Applied Physics Letters, 2012. **100**(19): p. 191901.
71. Meza, L.R., S. Das, and J.R. Greer, *Strong, lightweight, and recoverable three-dimensional ceramic nanolattices*. Science, 2014. **345**(6202): p. 1322-6.
  72. Bertoldi, K., et al., *Negative Poisson's Ratio Behavior Induced by an Elastic Instability*. Advanced Materials, 2010. **22**(3): p. 361-366.
  73. Roper, C.S., *Multiobjective optimization for design of multifunctional sandwich panel heat pipes with micro-architected truss cores*. International Journal of Heat and Fluid Flow, 2011. **32**(1): p. 239-248.
  74. Valdevit, L., et al., *Optimal active cooling performance of metallic sandwich panels with prismatic cores*. International Journal of Heat and Mass Transfer, 2006. **49**(21): p. 3819-3830.
  75. Roper, C.S., et al., *Scalable 3D bicontinuous fluid networks: polymer heat exchangers toward artificial organs*. Adv Mater, 2015. **27**(15): p. 2479-84.
  76. Mota, C., et al., *Additive manufacturing techniques for the production of tissue engineering constructs*. Journal of Tissue Engineering and Regenerative Medicine, 2015. **9**(3): p. 174-190.
  77. Melchels, F.P.W., et al., *Additive manufacturing of tissues and organs*. Progress in Polymer Science, 2012. **37**(8): p. 1079-1104.
  78. Kitson, P.J., et al., *3D printing of versatile reactionware for chemical synthesis*. Nat. Protocols, 2016. **11**(5): p. 920-936.
  79. Symes, M.D., et al., *Integrated 3D-printed reactionware for chemical synthesis and analysis*. Nat Chem, 2012. **4**(5): p. 349-354.
  80. Fantino, E., et al., *In Situ Thermal Generation of Silver Nanoparticles in 3D Printed Polymeric Structures*. Materials, 2016. **9**(7): p. 589.
  81. Hu, Y., et al., *Assessing heavy metal pollution in the surface soils of a region that had undergone three decades of intense industrialization and urbanization*. Environmental Science and Pollution Research, 2013. **20**(9): p. 6150-6159.
  82. Fu, F. and Q. Wang, *Removal of heavy metal ions from wastewaters: A review*. Journal of Environmental Management, 2011. **92**(3): p. 407-418.
  83. Li, Z., et al., *A review of soil heavy metal pollution from mines in China: Pollution and health risk assessment*. Science of The Total Environment, 2014. **468-469**: p. 843-853.
  84. Salomons, W., U. Förstner, and P. Mader, *Heavy metals: problems and solutions*. 2012: Springer Science & Business Media.
  85. He, B., et al., *Research progress of heavy metal pollution in China: Sources, analytical methods, status, and toxicity*. Chinese Science Bulletin, 2013. **58**(2): p. 134-140.
  86. Franzetti, A., et al., *Biosurfactant use in heavy metal removal from industrial effluents and contaminated sites*. Biosurfactants: Production and Utilization—Processes, Technologies, and Economics, 2014. **159**: p. 361.

87. Oncel, M., et al., *A comparative study of chemical precipitation and electrocoagulation for treatment of coal acid drainage wastewater*. Journal of Environmental Chemical Engineering, 2013. **1**(4): p. 989-995.
88. Ahmed, M.J.K. and M. Ahmaruzzaman, *A review on potential usage of industrial waste materials for binding heavy metal ions from aqueous solutions*. Journal of Water Process Engineering, 2016. **10**: p. 39-47.
89. Gopi Kiran, M., K. Pakshirajan, and G. Das, *Heavy Metal Removal Using Sulfate-Reducing Biomass Obtained from a Lab-Scale Upflow Anaerobic-Packed Bed Reactor*. Journal of Environmental Engineering, 2015: p. C4015010.
90. Parga, J.R., et al., *Removal of Aqueous Lead and Copper Ions by Using Natural Hydroxyapatite Powder and Sulphide Precipitation in Cyanidation Process*. 2013.
91. Karnib, M., et al., *Heavy metals removal using activated carbon, silica and silica activated carbon composite*. Energy Procedia, 2014. **50**: p. 113-120.
92. Sankararamkrishnan, N., M. Jaiswal, and N. Verma, *Composite nanofloral clusters of carbon nanotubes and activated alumina: An efficient sorbent for heavy metal removal*. Chemical Engineering Journal, 2014. **235**: p. 1-9.
93. Hua, M., et al., *Heavy metal removal from water/wastewater by nanosized metal oxides: a review*. Journal of Hazardous Materials, 2012. **211**: p. 317-331.
94. Mubarak, N., et al., *Removal of heavy metals from wastewater using carbon nanotubes*. Separation & Purification Reviews, 2014. **43**(4): p. 311-338.
95. Wang, H., et al., *Mechanism study on adsorption of acidified multiwalled carbon nanotubes to Pb (II)*. Journal of Colloid and Interface Science, 2007. **316**(2): p. 277-283.
96. Bulgariu, D. and L. Bulgariu, *Equilibrium and kinetics studies of heavy metal ions biosorption on green algae waste biomass*. Bioresource technology, 2012. **103**(1): p. 489-493.
97. Kırbıyık, Ç., A.E. Pütün, and E. Pütün, *Comparative studies on adsorptive removal of heavy metal ions by biosorbent, bio-char and activated carbon obtained from low cost agro residue*. Water Science and Technology, 2015: p. wst2015504.
98. Barakat, M.A., *New trends in removing heavy metals from industrial wastewater*. Arabian Journal of Chemistry, 2011. **4**(4): p. 361-377.
99. Ayoub, A., et al., *Novel hemicellulose-chitosan biosorbent for water desalination and heavy metal removal*. ACS Sustainable Chemistry & Engineering, 2013. **1**(9): p. 1102-1109.
100. Wang, J. and C. Chen, *Chitosan-based biosorbents: modification and application for biosorption of heavy metals and radionuclides*. Bioresource technology, 2014. **160**: p. 129-141.
101. Chen, T., et al., *Performance analysis of Al<sub>2</sub>O<sub>3</sub>/water nanofluid with cationic*

- chitosan dispersant*. *Advances in Materials Science and Engineering*, 2013. **2013**.
102. Zhang, Y., et al., *Porous graphene oxide/carboxymethyl cellulose monoliths, with high metal ion adsorption*. *Carbohydrate Polymers*, 2014. **101**: p. 392-400.
  103. Zhang, N., et al., *Fabrication of highly porous biodegradable monoliths strengthened by graphene oxide and their adsorption of metal ions*. *Carbon*, 2011. **49**(3): p. 827-837.
  104. Kuang, S.-P., et al., *Preparation of triethylene-tetramine grafted magnetic chitosan for adsorption of Pb(II) ion from aqueous solutions*. *Journal of Hazardous Materials*, 2013. **260**: p. 210-219.
  105. Dong, C., et al., *Synthesis of magnetic chitosan nanoparticle and its adsorption property for humic acid from aqueous solution*. *Colloids and Surfaces A: Physicochemical and Engineering Aspects*, 2014. **446**: p. 179-189.
  106. Reddy, D.H.K. and S.-M. Lee, *Application of magnetic chitosan composites for the removal of toxic metal and dyes from aqueous solutions*. *Advances in Colloid and Interface Science*, 2013. **201**: p. 68-93.
  107. Huš, S., M. Kolar, and P. Krajnc, *Separation of heavy metals from water by functionalized glycidyl methacrylate poly (high internal phase emulsions)*. *Journal of Chromatography A*, 2016. **1437**: p. 168-175.
  108. Couck, S., et al., *CO<sub>2</sub>, CH<sub>4</sub> and N<sub>2</sub> separation with a 3DFD-printed ZSM-5 monolith*. *Chemical Engineering Journal*, 2017. **308**: p. 719-726.
  109. Thakkar, H., et al., *3D-Printed Zeolite Monoliths for CO<sub>2</sub> Removal from Enclosed Environments*. *ACS Applied Materials & Interfaces*, 2016. **8**(41): p. 27753-27761.
  110. Thakkar, H., et al., *Formulation of Aminosilica Adsorbents into 3D-Printed Monoliths and Evaluation of Their CO<sub>2</sub> Capture Performance*. *ACS Applied Materials & Interfaces*, 2017. **9**(8): p. 7489-7498.
  111. Zhang, D., et al., *Initiator-integrated 3D Printing of Magnetic Object for Remote Controlling Application*. *IEEE Transactions on Magnetics*, 2017. **PP**(99): p. 1-1.
  112. Wang, X., et al., *Initiator-integrated 3D printing enables the formation of complex metallic architectures*. *ACS Appl Mater Interfaces*, 2014. **6**(4): p. 2583-7.
  113. Guo, Q., et al., *"Paintable" 3D printed structures via a post-ATRP process with antimicrobial function for biomedical applications*. *Journal of Materials Chemistry B*, 2013. **1**(48): p. 6644.
  114. Azizi, N. and M.R. Saidi, *Highly Chemoselective Addition of Amines to Epoxides in Water*. *Organic Letters*, 2005. **7**(17): p. 3649-3651.
  115. Lee, H.S., et al., *Reversible Swelling of Chitosan and Quaternary Ammonium Modified Chitosan Brush Layers: Effect of pH and Counter Anion Size and*

- Functionality*. J Mater Chem, 2012. **22**(37): p. 19605-19616.
116. Funk, C., et al., *Epoxy-functionalized surfaces for microarray applications: surface chemical analysis and fluorescence labeling of surface species*. Surface and Interface Analysis, 2012. **44**(8): p. 890-894.
  117. Salehi, E., et al., *Static and dynamic adsorption of copper ions on chitosan/polyvinyl alcohol thin adsorptive membranes: Combined effect of polyethylene glycol and aminated multi-walled carbon nanotubes*. Chemical Engineering Journal, 2013. **215–216**: p. 791-801.
  118. Bazargan-Lari, R., et al., *Removal of Cu(II) ions from aqueous solutions by low-cost natural hydroxyapatite/chitosan composite: Equilibrium, kinetic and thermodynamic studies*. Journal of the Taiwan Institute of Chemical Engineers, 2014. **45**(4): p. 1642-1648.
  119. He, J., Y. Lu, and G. Luo, *Ca(II) imprinted chitosan microspheres: An effective and green adsorbent for the removal of Cu(II), Cd(II) and Pb(II) from aqueous solutions*. Chemical Engineering Journal, 2014. **244**: p. 202-208.
  120. Zhang, L., Y. Zeng, and Z. Cheng, *Removal of heavy metal ions using chitosan and modified chitosan: A review*. Journal of Molecular Liquids, 2016. **214**: p. 175-191.
  121. Azizian, S., *Kinetic models of sorption: a theoretical analysis*. Journal of Colloid and Interface Science, 2004. **276**(1): p. 47-52.
  122. Wu, F.-C., R.-L. Tseng, and R.-S. Juang, *Kinetic modeling of liquid-phase adsorption of reactive dyes and metal ions on chitosan*. Water Research, 2001. **35**(3): p. 613-618.
  123. Chen, C.-Y., C.-Y. Yang, and A.-H. Chen, *Biosorption of Cu(II), Zn(II), Ni(II) and Pb(II) ions by cross-linked metal-imprinted chitosans with epichlorohydrin*. Journal of Environmental Management, 2011. **92**(3): p. 796-802.
  124. Chen, A.-H., et al., *Comparative adsorption of Cu(II), Zn(II), and Pb(II) ions in aqueous solution on the crosslinked chitosan with epichlorohydrin*. Journal of Hazardous Materials, 2008. **154**(1): p. 184-191.
  125. Laus, R., et al., *Adsorption and desorption of Cu(II), Cd(II) and Pb(II) ions using chitosan crosslinked with epichlorohydrin-triphosphate as the adsorbent*. Journal of Hazardous Materials, 2010. **183**(1): p. 233-241.
  126. Chang, Y.-C. and D.-H. Chen, *Preparation and adsorption properties of monodisperse chitosan-bound Fe<sub>3</sub>O<sub>4</sub> magnetic nanoparticles for removal of Cu(II) ions*. Journal of Colloid and Interface Science, 2005. **283**(2): p. 446-451.
  127. Wan, M.-W., et al., *Adsorption of copper (II) and lead (II) ions from aqueous solution on chitosan-coated sand*. Carbohydrate Polymers, 2010. **80**(3): p. 891-899.
  128. Yuwei, C. and W. Jianlong, *Preparation and characterization of magnetic chitosan nanoparticles and its application for Cu(II) removal*. Chemical

- Engineering Journal, 2011. **168**(1): p. 286-292.
129. Salehi, E., et al., *Novel chitosan/poly(vinyl) alcohol thin adsorptive membranes modified with amino functionalized multi-walled carbon nanotubes for Cu(II) removal from water: Preparation, characterization, adsorption kinetics and thermodynamics*. Separation and Purification Technology, 2012. **89**: p. 309-319.
  130. Zeng, Q.R., et al., *Recycling EDTA solutions used to remediate metal-polluted soils*. Environmental Pollution, 2005. **133**(2): p. 225-231.
  131. Zhou, Y.-T., et al., *Removal of Cu<sup>2+</sup> from aqueous solution by chitosan-coated magnetic nanoparticles modified with  $\alpha$ -ketoglutaric acid*. Journal of Colloid and Interface Science, 2009. **330**(1): p. 29-37.
  132. Zhang, D., et al., *Initiator-Integrated 3-D Printing of Magnetic Object for Remote Controlling Application*. IEEE Transactions on Magnetics, 2017. **53**(5): p. 1-9.
  133. Matyjaszewski, K. and J. Xia, *Atom Transfer Radical Polymerization*. Chemical Reviews, 2001. **101**(9): p. 2921-2990.
  134. Li, Z., et al., *Surface initiated polymerization from integrated poly(dimethylsiloxane) enables crack-free large area wrinkle formation*. Polymers for Advanced Technologies, 2012. **23**(9): p. 1240-1245.
  135. Liu, X., et al., *Tuning the surface chemistry of iPDMS for improved protein microarray performance*. Journal of Materials Chemistry, 2012. **22**(13): p. 6327-6334.
  136. *Roland DG Australia unveils its first DLP 3D printer*. Available from: <http://www.3ders.org/articles/20140903-roland-dg-australia-unveils-its-first-dlp-3d-printer.html>.
  137. Jahn, R. and T. Jung, *Relationship between pigment properties and UV-curing efficiency*. Progress in Organic Coatings, 2001. **43**(1): p. 50-55.
  138. Lee, J.N., C. Park, and G.M. Whitesides, *Solvent Compatibility of Poly(dimethylsiloxane)-Based Microfluidic Devices*. Analytical Chemistry, 2003. **75**(23): p. 6544-6554.
  139. Loguercio, A.D., et al., *Effects of diphenyliodonium salt addition on the adhesive and mechanical properties of an experimental adhesive*. Journal of Dentistry, 2013. **41**(7): p. 653-658.
  140. Liu, J., et al., *A study of shrinkage stress reduction and mechanical properties of nanogel-modified resin systems*. European Polymer Journal, 2012. **48**(11): p. 1819-1828.
  141. Yang, H., et al., *Preliminary Study on Nano Particle/Photopolymer Hybrid for 3D Inkjet Printing*. 2014.
  142. Wang, X., et al., *Stretchable Conductors with Ultrahigh Tensile Strain and Stable Metallic Conductance Enabled by Prestrained Polyelectrolyte Nanoplatfoms*. Advanced Materials, 2011. **23**(27): p. 3090-3094.

143. Abbasian, M., et al., *Versatile method for synthesis of electrically conductive polypyrrole-polystyrene clay nanocomposites using ATRP and chemical polymerisation methods*. Journal of Experimental Nanoscience, 2015. **10**(11): p. 844-858.
144. Jatratkar, A.A., et al., *Consequence of oxidant to monomer ratio on optical and structural properties of Polypyrrole thin film deposited by oxidation polymerization technique*. Journal of Physics and Chemistry of Solids, 2015. **80**: p. 78-83.
145. Hoshina, Y. and T. Kobayashi, *Effect of acidic catalyst on properties of novel conductive copolymer films made of pyrrole and formyl pyrrole*. 2012.
146. Nelson, B.J., I.K. Kaliakatsos, and J.J. Abbott, *Microrobots for minimally invasive medicine*. Annu Rev Biomed Eng, 2010. **12**: p. 55-85.
147. Xu, T., et al., *Magnetic Actuation Based Motion Control for Microrobots: An Overview*. Micromachines, 2015. **6**(9): p. 1346.
148. Rikken, R.S.M., et al., *Manipulation of micro- and nanostructure motion with magnetic fields*. Soft Matter, 2014. **10**(9): p. 1295-1308.
149. Fountain, T.W.R., P.V. Kailat, and J.J. Abbott. *Wireless control of magnetic helical microrobots using a rotating-permanent-magnet manipulator*. in *Robotics and Automation (ICRA), 2010 IEEE International Conference on*. 2010.
150. Yan, L., et al., *Micro- and nanotechnologies for intracellular delivery*. Small, 2014. **10**(22): p. 4487-504.
151. Peyer, K.E., et al., *Magnetic helical micromachines*. Chemistry, 2013. **19**(1): p. 28-38.
152. Kim, S., et al., *Fabrication and characterization of magnetic microrobots for three-dimensional cell culture and targeted transportation*. Adv Mater, 2013. **25**(41): p. 5863-8.
153. Zhang, L., et al., *Artificial bacterial flagella: Fabrication and magnetic control*. Applied Physics Letters, 2009. **94**(6): p. 064107.
154. Marino, H., C. Bergeles, and B.J. Nelson, *Robust Electromagnetic Control of Microrobots Under Force and Localization Uncertainties*. IEEE Transactions on Automation Science and Engineering, 2014. **11**(1): p. 310-316.
155. Parveen, S., R. Misra, and S.K. Sahoo, *Nanoparticles: a boon to drug delivery, therapeutics, diagnostics and imaging*. Nanomedicine: Nanotechnology, Biology and Medicine, 2012. **8**(2): p. 147-166.
156. Mura, S., J. Nicolas, and P. Couvreur, *Stimuli-responsive nanocarriers for drug delivery*. Nature materials, 2013. **12**(11): p. 991-1003.
157. Cheng, R., et al., *Dual and multi-stimuli responsive polymeric nanoparticles for programmed site-specific drug delivery*. Biomaterials, 2013. **34**(14): p. 3647-3657.

158. Petruska, A.J., A.W. Mahoney, and J.J. Abbott, *Remote manipulation with a stationary computer-controlled magnetic dipole source*. IEEE Transactions on Robotics, 2014. **30**(5): p. 1222-1227.
159. Zhang, L., et al., *Characterizing the Swimming Properties of Artificial Bacterial Flagella*. Nano Letters, 2009. **9**(10): p. 3663-3667.
160. Zhang, L., K.E. Peyer, and B.J. Nelson, *Artificial bacterial flagella for micromanipulation*. Lab on a Chip, 2010. **10**(17): p. 2203-2215.
161. Tottori, S., et al., *Magnetic Helical Micromachines: Fabrication, Controlled Swimming, and Cargo Transport*. Advanced Materials, 2012. **24**(6): p. 811-816.
162. Gross, B.C., et al., *Evaluation of 3D printing and its potential impact on biotechnology and the chemical sciences*. Analytical chemistry, 2014. **86**(7): p. 3240-3253.
163. Habijan, T., et al., *The biocompatibility of dense and porous nickel–titanium produced by selective laser melting*. Materials Science and Engineering: C, 2013. **33**(1): p. 419-426.
164. Wang, X., et al., *Grafting of polyelectrolytes onto hydrocarbon surfaces by high-energy hydrogen induced cross-linking for making metallized polymer films*. Chemical Communications, 2013. **49**(41): p. 4658-4660.
165. Kefalas, J., *Effect of Electroplating Parameters on Magnetic Properties of Ni-Co Alloys*. Journal of Applied Physics, 1966. **37**(3): p. 1160-1161.
166. White, F.M. and I. Corfield, *Viscous fluid flow*. Vol. 3. 2006: McGraw-Hill New York.
167. Abbott, J.J., et al., *How Should Microrobots Swim?* The International Journal of Robotics Research, 2009. **28**(11-12): p. 1434-1447.
168. ZHANG Yongshun, Y.H., RUAN Xiaoyan, WANG Nan, GUO Dongming, *Kinematics Characteristics of a New Capsule-type Micro Robot in Intestine [J]*. Journal of Mechanical Engineering, 2009. **45**(8): p. 18-23.
169. Rodenborn, B., et al., *Propulsion of microorganisms by a helical flagellum*. Proceedings of the National Academy of Sciences of the United States of America, 2013. **110**(5): p. E338-E347.
170. Duoss, E.B., et al., *Three-Dimensional Printing of Elastomeric, Cellular Architectures with Negative Stiffness*. Advanced Functional Materials, 2014. **24**(31): p. 4905-4913.
171. Fratzl, P. and R. Weinkamer, *Nature's hierarchical materials*. Progress in Materials Science, 2007. **52**(8): p. 1263-1334.
172. Evans, A.G., et al., *The topological design of multifunctional cellular metals*. Progress in Materials Science, 2001. **46**(3): p. 309-327.
173. Lehman, J. and R.S. Lakes, *Stiff, strong, zero thermal expansion lattices via material hierarchy*. Composite Structures, 2014. **107**: p. 654-663.
174. Hong, S., et al., *3D Printing of Highly Stretchable and Tough Hydrogels into*

- Complex, Cellularized Structures*. *Advanced Materials*, 2015. **27**(27): p. 4035-4040.
175. Jacobsen, A.J., W. Barvosa-Carter, and S. Nutt, *Micro-scale Truss Structures formed from Self-Propagating Photopolymer Waveguides*. *Advanced Materials*, 2007. **19**(22): p. 3892-3896.
  176. Jacobsen, A.J., W. Barvosa-Carter, and S. Nutt, *Micro-scale truss structures with three-fold and six-fold symmetry formed from self-propagating polymer waveguides*. *Acta Materialia*, 2008. **56**(11): p. 2540-2548.
  177. Bauer, J., et al., *High-strength cellular ceramic composites with 3D microarchitecture*. *Proceedings of the National Academy of Sciences of the United States of America*, 2014. **111**(7): p. 2453-2458.
  178. Evans, A.G., *Lightweight Materials and Structures*. *MRS Bulletin*, 2013. **26**(10): p. 790-797.
  179. Deshpande, V.S. and N.A. Fleck, *Collapse of truss core sandwich beams in 3-point bending*. *International Journal of Solids and Structures*, 2001. **38**(36): p. 6275-6305.
  180. Deshpande, V.S., N.A. Fleck, and M.F. Ashby, *Effective properties of the octet-truss lattice material*. *Journal of the Mechanics and Physics of Solids*, 2001. **49**(8): p. 1747-1769.
  181. Fan, H.L., F.N. Jin, and D.N. Fang, *Nonlinear mechanical properties of lattice truss materials*. *Materials & Design*, 2009. **30**(3): p. 511-517.
  182. Zou, J., et al., *Ultralight Multiwalled Carbon Nanotube Aerogel*. *ACS Nano*, 2010. **4**(12): p. 7293-7302.
  183. Nardecchia, S., et al., *Three dimensional macroporous architectures and aerogels built of carbon nanotubes and/or graphene: synthesis and applications*. *Chemical Society Reviews*, 2013. **42**(2): p. 794-830.
  184. Han, X.-H., et al., *A Review of Metal Foam and Metal Matrix Composites for Heat Exchangers and Heat Sinks*. *Heat Transfer Engineering*, 2012. **33**(12): p. 991-1009.
  185. Yuan, W., et al., *Porous metal materials for polymer electrolyte membrane fuel cells – A review*. *Applied Energy*, 2012. **94**: p. 309-329.
  186. Zhang, H.-B., et al., *Tough Graphene–Polymer Microcellular Foams for Electromagnetic Interference Shielding*. *ACS Applied Materials & Interfaces*, 2011. **3**(3): p. 918-924.
  187. Wong, J.C.H., et al., *Mechanical properties of monolithic silica aerogels made from polyethoxydisiloxanes*. *Microporous and Mesoporous Materials*, 2014. **183**: p. 23-29.
  188. Cai, J., et al., *Cellulose–Silica Nanocomposite Aerogels by In Situ Formation of Silica in Cellulose Gel*. *Angewandte Chemie*, 2012. **124**(9): p. 2118-2121.
  189. Bryning, M.B., et al., *Carbon Nanotube Aerogels*. *Advanced Materials*, 2007.

- 19(5): p. 661-664.
190. Yang, X., et al., *Cellulose Nanocrystal Aerogels as Universal 3D Lightweight Substrates for Supercapacitor Materials*. *Advanced Materials*, 2015. **27**(40): p. 6104-6109.
191. Tancogne-Dejean, T., A.B. Spierings, and D. Mohr, *Additively-manufactured metallic micro-lattice materials for high specific energy absorption under static and dynamic loading*. *Acta Materialia*, 2016. **116**: p. 14-28.
192. Meza, L.R., et al., *Resilient 3D hierarchical architected metamaterials*. *Proceedings of the National Academy of Sciences*, 2015. **112**(37): p. 11502-11507.
193. Wendy Gu, X. and J.R. Greer, *Ultra-strong architected Cu meso-lattices*. *Extreme Mechanics Letters*, 2015. **2**: p. 7-14.
194. Schlesinger, M., *Electroless deposition of nickel*. *Modern electroplating*. **4**: p. 667-684.
195. Torrents, A., et al., *Characterization of nickel-based microlattice materials with structural hierarchy from the nanometer to the millimeter scale*. *Acta Materialia*, 2012. **60**(8): p. 3511-3523.
196. Valdevit, L., et al., *Compressive strength of hollow microlattices: Experimental characterization, modeling, and optimal design*. *Journal of Materials Research*, 2013. **28**(17): p. 2461-2473.
197. Ashby, M.F., et al., *Metal foams: a design guide*. 2000: Elsevier.
198. Pingle, S.M., et al., *Collapse mechanism maps for the hollow pyramidal core of a sandwich panel under transverse shear*. *International Journal of Solids and Structures*, 2011. **48**(25–26): p. 3417-3430.
199. Jiang, B., et al., *Ultralight Co/Ag composite foams: Synthesis, morphology and compressive property*. *Scripta Materialia*, 2016. **117**: p. 68-72.
200. Bin, J., et al., *A novel method for synthesizing ultralight silver foams by the silver mirror reaction*. *Materials Letters*, 2016. **173**: p. 80-83.
201. Mieszala, M., et al., *Micromechanics of Amorphous Metal/Polymer Hybrid Structures with 3D Cellular Architectures: Size Effects, Buckling Behavior, and Energy Absorption Capability*. *Small*, 2017. **13**(8): p. 1602514-n/a.
202. Dong, L., V. Deshpande, and H. Wadley, *Mechanical response of Ti–6Al–4V octet-truss lattice structures*. *International Journal of Solids and Structures*, 2015. **60–61**: p. 107-124.
203. Brieland-Shoultz, A., et al., *Scaling the Stiffness, Strength, and Toughness of Ceramic-Coated Nanotube Foams into the Structural Regime*. *Advanced Functional Materials*, 2014. **24**(36): p. 5728-5735.
204. Worsley, M.A., et al., *Mechanically robust and electrically conductive carbon nanotube foams*. *Applied Physics Letters*, 2009. **94**(7): p. 073115.
205. Si, Y., et al., *Ultralight nanofibre-assembled cellular aerogels with*

- superelasticity and multifunctionality*. Nat Commun, 2014. **5**: p. 5802.
206. Zheng, X., et al., *Ultralight, ultrastiff mechanical metamaterials*. Science, 2014. **344**(6190): p. 1373-1377.
  207. Si, Y., et al., *Ultralight Biomass-Derived Carbonaceous Nanofibrous Aerogels with Superelasticity and High Pressure-Sensitivity*. Advanced Materials, 2016. **28**(43): p. 9512-9518.
  208. Zheng, X., et al., *Multiscale metallic metamaterials*. Nat Mater, 2016. **15**(10): p. 1100-1106.
  209. Valentine, J., et al., *Three-dimensional optical metamaterial with a negative refractive index*. Nature, 2008. **455**(7211): p. 376-379.
  210. Chen, H.-T., et al., *Experimental demonstration of frequency-agile terahertz metamaterials*. Nat Photon, 2008. **2**(5): p. 295-298.
  211. Soukoulis, C.M. and M. Wegener, *Optical Metamaterials—More Bulky and Less Lossy*. Science, 2010. **330**(6011): p. 1633-1634.
  212. Chen, H., C.T. Chan, and P. Sheng, *Transformation optics and metamaterials*. Nat Mater, 2010. **9**(5): p. 387-396.
  213. Nicolaou, Z.G. and A.E. Motter, *Mechanical metamaterials with negative compressibility transitions*. Nature materials, 2012. **11**(7): p. 608-613.
  214. Mallikarachchi, H.M.Y.C. and S. Pellegrino, *Quasi-Static Folding and Deployment of Ultrathin Composite Tape-Spring Hinges*. Journal of Spacecraft and Rockets, 2011. **48**(1): p. 187-198.
  215. Valant, M., et al., *Molecular Auxetic Behavior of Epitaxial Co-Ferrite Spinel Thin Film*. Advanced Functional Materials, 2010. **20**(4): p. 644-647.
  216. Liu, Y. and H. Hu, *A review on auxetic structures and polymeric materials*. Scientific Research and Essays, 2010. **5**(10): p. 1052-1063.
  217. Nakajima, H., *Fabrication, properties, and applications of porous metals with directional pores*. Proceedings of the Japan Academy. Series B, Physical and Biological Sciences, 2010. **86**(9): p. 884-899.
  218. Lu, Z.-X., et al., *Novel structure with negative Poisson's ratio and enhanced Young's modulus*. Composite Structures, 2016. **138**: p. 243-252.
  219. Warren, T.L., *Negative Poisson's ratio in a transversely isotropic foam structure*. Journal of Applied Physics, 1990. **67**(12): p. 7591-7594.
  220. Wan, H., et al., *A study of negative Poisson's ratios in auxetic honeycombs based on a large deflection model*. European Journal of Mechanics - A/Solids, 2004. **23**(1): p. 95-106.
  221. Gibson, L.J., et al., *The Mechanics of Two-Dimensional Cellular Materials*. Proceedings of the Royal Society of London. A. Mathematical and Physical Sciences, 1982. **382**(1782): p. 25-42.
  222. Yang, L., et al., *Compressive properties of Ti-6Al-4V auxetic mesh structures made by electron beam melting*. Acta Materialia, 2012. **60**(8): p. 3370-3379.

223. Geissler, M. and Y. Xia, *Patterning: Principles and Some New Developments*. Advanced Materials, 2004. **16**(15): p. 1249-1269.
224. Kim, K., et al., *3D Optical Printing of Piezoelectric Nanoparticle–Polymer Composite Materials*. ACS Nano, 2014. **8**(10): p. 9799-9806.
225. Peterson, G.I., et al., *3D-Printed Mechanochromic Materials*. ACS Applied Materials & Interfaces, 2015. **7**(1): p. 577-583.
226. Villar, G., A.D. Graham, and H. Bayley, *A Tissue-Like Printed Material*. Science, 2013. **340**(6128): p. 48-52.
227. Wei, Q., et al., *Printable hybrid hydrogel by dual enzymatic polymerization with superactivity*. Chemical Science, 2016. **7**(4): p. 2748-2752.
228. Daniela, F.D.C., et al., *Three-dimensional printing of stem cell-laden hydrogels submerged in a hydrophobic high-density fluid*. Biofabrication, 2013. **5**(1): p. 015003.
229. Wu, C., et al., *3D-printing of highly uniform CaSiO<sub>3</sub> ceramic scaffolds: preparation, characterization and in vivo osteogenesis*. Journal of Materials Chemistry, 2012. **22**(24): p. 12288-12295.
230. Wang, J., et al., *Three-Dimensional Printing of Interconnects by Laser Direct-Write of Silver Nanopastes*. Advanced Materials, 2010. **22**(40): p. 4462-4466.
231. Huang, G.-W., et al., *Rapid Laser Printing of Paper-Based Multilayer Circuits*. ACS Nano, 2016. **10**(9): p. 8895-8903.
232. Michael, Z., et al., *Laser sintering of copper nanoparticles*. Journal of Physics D: Applied Physics, 2014. **47**(2): p. 025501.
233. Yang, L., et al., *A Biomimetic Approach to Enhancing Interfacial Interactions: Polydopamine-Coated Clay as Reinforcement for Epoxy Resin*. ACS Applied Materials & Interfaces, 2011. **3**(8): p. 3026-3032.
234. Yang, L., et al., *Polydopamine-coated graphene as multifunctional nanofillers in polyurethane*. RSC Advances, 2013. **3**(18): p. 6377-6385.
235. Zhao, L., D. Chen, and W. Hu, *Patterning of Metal Films on Arbitrary Substrates by Using Polydopamine as a UV-Sensitive Catalytic Layer for Electroless Deposition*. Langmuir, 2016. **32**(21): p. 5285-5290.
236. Lee, H., et al., *Mussel-Inspired Surface Chemistry for Multifunctional Coatings*. Science, 2007. **318**(5849): p. 426-430.
237. *Standard Test Methods for Measuring Adhesion by Tape Test*. 2009, ASTM International.
238. Liebscher, J., et al., *Structure of Polydopamine: A Never-Ending Story?* Langmuir, 2013. **29**(33): p. 10539-10548.
239. Mrówczyński, R., et al., *Electron Paramagnetic Resonance Imaging and Spectroscopy of Polydopamine Radicals*. The Journal of Physical Chemistry B, 2015. **119**(32): p. 10341-10347.
240. Zhang, T., et al., *Fabrication of flexible copper-based electronics with high-*

- resolution and high-conductivity on paper via inkjet printing.* J. Mater. Chem. C, 2014. **2**(2): p. 286-294.
241. Wang, Y., et al., *Thermodynamics versus Kinetics in Nanosynthesis.* Angewandte Chemie International Edition, 2015. **54**(7): p. 2022-2051.
242. Feng, Y., et al., *Achieving Site-Specificity in Multistep Colloidal Synthesis.* Journal of the American Chemical Society, 2015. **137**(24): p. 7624-7627.

## Curriculum Vitae

**Name:** Dongxing, Zhang

**Post-secondary Education and Degrees:** Huazhong University of Science and Technology (HUST)  
Wuhan, Hubei, China  
2006-2010 B.A.

Beijing University of Aeronautics and Astronautics (BUAA)  
Beijing, China  
2010-2013 M.A.

Western University (UWO)  
London, Ontario, Canada  
2013-2017 Ph.D.

**Honors and Awards:** Outstanding graduate  
2010

First-class scholarship  
2007-2010, 2010-2013

Chinese Scholarship Council (CSC) scholarship  
2013-2017

### Publications:

**Zhang, D.**, Xiao, J., Qiu, Y., Yang, J., & Guo, Q. (2017). Initiator-Integrated 3-D Printing of Magnetic Object for Remote Controlling Application. *IEEE Transactions on Magnetics*, 53(5), 1-9.

**Zhang, D.**, Xiao, J., Moorlag, C., Guo, Q., & Yang, J. (2017). Development of ultralight, super-elastic, hierarchical metallic meta-structures with i3DP technology. *Nanotechnology*, 28, 455708-455720.